Characterizing the molecular determinants of neurotransmission using computational and experimental approaches

Inaugural Dissertation
to obtain the academic degree
Doctor rerum naturalium (Dr. rer. nat.)

submitted to the department of
Biology, Chemistry and Pharmacy
of Freie Universität Berlin

by

Andreas Till Grasskamp

March 2020

page intentionally left blank

The work presented in this thesis was conducted under the supervision of Dr. rer. nat. Alexander M. Walter between April 15th, 2015 and March 29th, 2020 at the Leibniz-Forschungsinstitut für Molekulare Pharmakologie, Berlin.

1st Reviewer: Dr. rer. nat. Alexander M. Walter

2nd Reviewer: Prof. Dr. rer. nat. Stephan J. Sigrist

Date of defense: 15.06.2020

page intentionally left blank

“All models are wrong,
but some are useful.”

George Edward Pelham Box

(British Statistician, 1919-2013)

page intentionally left blank

Contents

Summary

The brain is a structure that has fascinated generations of scientists due to its complexity and its relevance in a plethora of biological processes. It is made up of a few hundred nerve cells (so-called neurons) in the worm *C. elegans* (Albertson and Thomson, 1976; White et al., 1986) and can contain up to several hundred billions of nerve cells like in African elephants (Herculano-Houzel et al., 2014). These highly specialized cells communicate with each other at structures termed synapses, where signals are transferred in a highly regulated way, and a majority of synapses communicate via chemicals called neurotransmitters (NTs). The typical chemical synapse can be subdivided into three functionally and morphologically distinct parts: (I) the signal-emitting presynaptic part including the active zone (AZ), where NTs are released from vesicular structures (synaptic vesicles, SVs) within the neuron either following an electrical stimulus (leading to an action potential, AP; AP-evoked release) or spontaneously (i.e. without a corresponding stimulus); (II) the synaptic cleft through which the NT molecules have to diffuse in order to be sensed by (III) the postsynaptic part, which harbors membrane receptors that specifically detect certain kinds of neurotransmitters and allow the signal to propagate electrically or via intracellular signaling cascades. This process of neurotransmission is the physiological basis of all behavior and movement found in animals. In the last few decades, intense research has elucidated many details of neurotransmission and their implications for neurological diseases. However, a considerable amount of questions is still open and unanswered. To contribute to an answer to some of these questions, the work conducted in the framework of this cumulative thesis comprises three interconnected subprojects.

The first subproject aimed to determine how synapses (at the neuromuscular junction formed by nerves terminating on muscles, NMJ) in the invertebrate model organism *Drosophila melanogaster* (commonly known as the fruit fly) engage isoforms of the protein Unc13 to regulate the coupling distance between SVs and the source of calcium influx, which triggers their release. Building a partial computational model of the synapse in conjunction with experimental data of my colleagues, I could substantiate the claim that two *Drosophila* isoforms of the protein localize at different distances from the calcium source and differentially ensure regulated release of SVs (Publication I: Böhme et al., Nature Neuroscience 2016). Using an experimental approach to visualize the release of single SVs at individual synapses and correlating it with protein levels at those synapses, I further contributed to prove that the Unc13A isoform constitutes the main molecular correlate of SV release sites (Publication II: Reddy-Alla et al., Neuron 2017). Parts of these results were then reviewed in Publication III: Böhme et al., FEBS Letters 2018, where I used the model built for Publication I and showed the influence of different coupling distances on synaptic short-term plasticity (which describes how the synapse responds to quickly succeeding stimuli). We further investigated the role of Unc13A in synaptic signaling maintenance on different timescales, where I showed the generally geometric and plastic

patterning of Unc13A at single AZs using a computational approach and STED images acquired by a colleague (Publication IV: Böhme et al., Nature Communications 2019). Using findings from these publications, we then built an advanced stochastic model of synaptic SV release, specifically taking into account the broad distribution of coupling distances found at the AZ. To make our simulations agree with experimental data on short-term plasticity, we found it necessary to include a calcium dependent mechanism that rapidly regulates the number of readily releasable vesicles. These results are shown in Publication V: Kobbersmed et al., eLife 2020.

The goal of the second subproject was to investigate different forms of the cellular membrane signaling lipid diacylglycerol (DAG) and their interaction with a functionally downstream signaling molecule (protein kinase C, PKC), as it is not clear whether or how subtle differences in lipid structure influence kinetics and signaling properties. To this end, our collaborators generated DAGs exhibiting a chemical 'cage' that keeps them from translocating over cellular membranes. These caged compounds were then individually applied to the outside of cells and their biological function restored by acutely removing the cage through a UV laser flash. An intracellular, fluorescently tagged DAG binding protein (a domain of PKC) could then be used to indicate lipid dynamics and protein recruitment in the cell membrane over time. However, due to the temporal convolution of concurrent dynamic processes like trans-bilayer movement, sensor binding/unbinding and metabolism, the exact quantification of kinetic properties required a computational assay that we developed. Using this *in silico* model of lipid dynamics and signaling in a cellular environment, we could show vastly different kinetic properties and lipid-protein interactions only depending on relatively small structural differences. Our computer-aided quantification provided evidence of differential effector protein binding and lipid availability in different parts of the cell. The work and results are shown in Publication VI: Schuhmacher et al., PNAS 2020.

In the third subproject, we set out to determine how spontaneous and AP-evoked SV exocytosis are regulated and whether they are functionally overlapping or separate. Using a genetically encoded calcium indicator, which we expressed in the postsynapse of the *Drosophila* NMJ, we correlated the activity of individual AZs in both release modes with levels of presynaptic proteins, expanding on our findings from Publication II: Reddy-Alla et al., Neuron 2017. Furthermore, we pharmacologically investigated the involvement of different presynaptic voltage gated channels in spontaneous release, and determined the degree of overlap in postsynaptic sensing. This work showed that many presynaptic proteins (e.g. Unc13A) predict both SV release modes, while some show differential influence. We further showed that postsynaptic receptors generally detect NT released via both modes, and that presynaptic voltage-gated Ca^{2+} channels (VGCCs) are involved in the generation of spontaneous SV release. Lastly, we observed that both release modes draw on the same SV pool. The work is shown in Manuscript in preparation: Grasskamp et al.

Zusammenfassung

Aufgrund seiner Komplexität und Wichtigkeit in vielerlei biologischen Vorgängen hat das Gehirn zahlreiche Wissenschaftler-Generationen begeistert. In ihm finden sich wenige hundert (Fadenwurm *C. elegans*; Albertson and Thomson, 1976; White et al., 1986) bis mehrere hundert Milliarden Nervenzellen (Afrikanischer Elefant; Herculano-Houzel et al., 2014). Diese hochspezialisierten Zellen kommunizieren untereinander, indem sie an sogenannten Synapsen Signale übertragen. In chemischen Synapsen geschieht dies durch die Freisetzung und Detektion von chemischen Botenstoffen, den Neurotransmittern (NT). Dieser Prozess ist sehr genau reguliert und wird unter anderem durch drei funktionell und morphologisch trennbare Teile der Synapse möglich gemacht: (I) die Präsynapse beinhaltet aktive Zonen (AZ), wo NT entweder nach einem elektrischen Reiz (der zu einem Aktionspotenzial, AP führt; sog. AP-evozierte Freisetzung) oder spontan (ohne elektrischen Reiz) aus kugelförmigen Strukturen (synaptische Vesikel, SV) freigesetzt werden in den (II) synaptischen Spalt. Durch diesen diffundieren die NT zur nächsten Nervenzelle, der (III) Postsynapse. Hier binden die NT an sehr spezialisierte Detektor-Proteine in der Zellmembran, wodurch das Signal (entweder elektrisch oder durch molekulare Signalkaskaden) weitergeleitet werden kann. Dieser Prozess der Neurotransmission ist die physiologische Entsprechung aller Verhaltensweisen und Bewegungen, zu denen tierische Lebewesen fähig sind. Gründliche Forschung hat in den letzten Jahrzehnten viele Details der Neurotransmission und ihren Einfluss auf neurologische Erkrankungen offengelegt. Nichtsdestotrotz gibt es auch heute noch zahlreiche offene Fragestellungen auf diesem Gebiet. Um zur Lösung einiger dieser Fragestellungen beizutragen, wurde die Arbeit, die dieser kumulativen Dissertation zugrunde liegt, in drei miteinander verwobenen Teilprojekten durchgeführt.

Das erste Teilprojekt diente der Fragestellung, wie zwei Isoformen des Proteins Unc13 in Synapsen (an neuromuskulären Verbindungen zwischen Nerv und Muskel, NMJ) der Taufliege *Drosophila melanogaster* die Entfernung von SV zur Quelle des Kalziumeinstroms (welcher zur Freisetzung der SV führt) reguliert. Mithilfe eines computergestützten, teilweisen Modells der Synapse und gepaart mit experimentellen Daten meiner Kollegen, konnte ich die Beobachtung untermauern, dass zwei Isoformen dieses Proteins in verschiedenen Entfernungen (sog. Kopplungsdistanzen) zur Kalzium-Quelle sitzen. Dort regulieren sie auf unterschiedliche Weise die Freisetzung der SV (Publication I: Böhme et al., Nature Neuroscience 2016). Anhand eines experimentellen Ansatzes, der die Freisetzung von SV an einzelnen Synapsen sichtbar macht und mit dem Vorkommen von synaptischen Proteinen in Verbindung bringt, konnte ich dann helfen zu beweisen, dass die Isoform Unc13A festlegt, wo exakt SV freigesetzt werden (Publication II: Reddy-Alla et al., Neuron 2017). Teile der vorhergehenden Erkenntnisse wurden dann in Publication III: Böhme et al., FEBS Letters 2018 besprochen. Hierfür habe ich das Computermodell aus Publikation I genutzt um zu zeigen, dass verschiedene Kopplungsdistanzen sehr unterschiedliche Einflüsse auf die Kurzzeitplastizität (also die Reaktion der Synapse auf schnell aufeinanderfolgende Reize) der Synapse haben. Im weiteren Verlauf haben wir untersucht, welche Rolle Unc13 bei der Aufrechterhaltung der Signalübertragung über verschiedene Zeiträume spielt. Hierbei habe ich anhand von computergestützten Berechnungen und hochauflösenden STED-Bildern eines Kollegen gezeigt, dass Unc13A generell geometrisch und dynamisch an der AZ angeordnet ist (Publication IV: Böhme et al., Nature Communications 2019).

Aufbauend auf den vorhergehenden Ergebnissen haben wir daraufhin ein erweitertes, stochastisches Modell von SV-Freisetzung erstellt. Dabei haben wir insbesondere einbezogen, dass die Verteilung von SV um die AZ sehr breit gestreut ist. Um unsere Simulationen mit Experimenten zu synaptischer Kurzzeitplastizität in Einklang zu bringen, mussten wir daher annehmen, dass ein Kalzium-abhängiger Mechanismus existiert, der sehr schnell die Anzahl der zur Freisetzung verfügbaren SV reguliert. Die Ergebnisse sind unter Publication V: Kobbersmed et al., eLife 2020 zu finden.

Die Zielsetzung des zweiten Teilprojektes behandelte die Untersuchung verschiedener Formen des zellulären Membran-Signal-Lipids Diacylglycerol (DAG) hinsichtlich ihrer Eigenschaften und Interaktionen mit einem funktionell nachgeschalteten Signalmolekül (Proteinkinase C, PKC). Es ist bisher nur wenig bis gar nicht erforscht, ob minimale Unterschiede in der Struktur eines Lipids Einflüsse auf Eigenschaften wie Dynamik und Signalweiterleitung haben. Zu diesem Zweck haben Kollegen verschiedene Formen von DAG erstellt, die aufgrund eines chemischen „cage“ nicht ohne Weiteres zur Bewegung durch die Zellmembran fähig sind. Gibt man diese von außen auf Zellen, kann man dann durch einen hochenergetischen UV-Laserpuls den „cage“ zerstören und die biologische Beweglichkeit wiederherstellen. Ein in der Zelle befindliches Protein mit fluoreszentem Label (eine Domäne von PKC) bindet dann an die DAG-Moleküle, die sich ohne „cage“ in die Zelle hineinbewegen. Dieser Ansatz kann dazu genutzt werden, kinetische Informationen dieses Prozesses auszulesen. Da aber gleichzeitig mehrere Prozesse wie Membran-Translokation, Sensor-Bindung und Verstoffwechselung den Fluoreszenzverlauf beeinflussen, benötigten wir einen computergestützten Ansatz zur Bestimmung der einzelnen kinetischen Eigenschaften jedes Lipids. Anhand dieses *in silico* Modells von Lipid-Dynamik und Signalweiterleitung in der Zelle konnten wir den sehr unterschiedlichen Einfluss kleinster struktureller Unterschiede auf kinetische Parameter und Lipid-Protein-Interaktion genau bestimmen. Mit dieser quantitativen, computergestützten Analyse haben wir gezeigt, dass die verschiedenen Lipide unterschiedliche Auswirkungen auf Zielproteine haben und unterschiedlich über Teile der Zelle verteilt sind. Eine genaue Beschreibung und Erklärung der Arbeit befindet sich im Kapitel Publication VI: Schuhmacher et al., PNAS 2020.

Für das dritte Teilprojekt nahmen wir uns vor, herauszufinden, wie spontane und AP-evozierte SV-Freisetzung genau reguliert sind und ob sie funktionell unterschiedlich oder ähnlich sind. Wir haben daher einen fluoreszenten Kalzium-Reporter verwendet, den wir durch genetische Steuerung im postsynaptischen Muskel der NMJ von *Drosophila* herstellen ließen. Mithilfe dessen konnten wir die Aktivität einzelner Synapsen mit der Menge verschiedener Proteine korrelieren, womit wir die Ergebnisse aus Publication II: Reddy-Alla et al., Neuron 2017 erweiterten. Des Weiteren haben wir durch pharmakologische Beeinflussung die Rolle verschiedener spannungsabhängiger Membran-Kanäle in spontaner SV-Freisetzung untersucht und herausgefunden, wie stark postsynaptische Rezeptoren beim Detektieren beider Modi funktionell überlappen. Wir konnten zeigen, dass einige präsynaptische Proteine (z.B. Unc13A) für beide Freisetzungsmodi wichtig sind, während manche nur einen Modus beeinflussen. In unseren Experimenten sahen wir, dass die meisten postsynaptischen Rezeptoren zur Detektion beider Modi dienen, und dass spannungsabhängige Kalziumkanäle (VGCC) für spontane SV-Freisetzung wichtig sind. Zuletzt konnten wir zeigen, dass beide SV-Freisetzungsmodi die gleichen Vorräte von SV nutzen. Diese Ergebnisse sind im Kapitel Manuscript in preparation: Grasskamp et al. aufgeführt.

1 Introduction

Neuroscientific research has led to a number of fascinating discoveries such as the molecular underpinnings of memory formation by Eric Kandel (Kandel, 2012) or the description of grid cells, which constitute part of the neural navigation system that allows the brain to find and memorize its place in its three-dimensional environment, by John O'Keefe and Edvard & May-Britt Moser (Kandel, 2014). While science can, by those unacquainted, sometimes be misunderstood as self-serving due to its partially abstract nature, many (if not most) advancements in modern medicine stem from efforts in basic research on biopharmaceutical, biomedical, or related topics. This includes the discovery of vaccines in the face of life-threatening bacterial infections (e.g. anthrax and diphtheria) or viral diseases (such as polio and smallpox), as well as the testing of substances and materials for their risk to induce genetic mutations and abnormal cell-proliferation (i.e. tumors). In many fields of basic neuroscientific research, molecular and physiological properties of signal transmission in cells and organisms are investigated to help understand basic mechanisms and pathological conditions of the nervous system.

The main difficulties in understanding brain function stem from the utter diversity, complexity, and miniature size of the involved components, as is the case with most biological processes. On one end of the scale, we can look at the nervous system as a whole and trace connections between different functional parts, trying to infer their role in behavior. On the other end of the scale, we can try to investigate single atoms or molecules, and their role in nerve cell communication. Technological advances in the past decades have given us the tools to investigate the brain on a cellular and molecular level, and to reproduce network activity in computer simulations. While both fields, and all neuroscientific fields of research in between, are vigorously expanding and delving ever deeper into details, it will in the end be an integration of all fields that may show us how the brain achieves consciousness and its vital responsiveness to changing environmental conditions.

With this introductory part of my written work, I aim to briefly delineate the groundwork that has enabled my colleagues and me to contribute to the field by investigating cellular signaling and neurotransmission in peripheral synapses of the fruit fly *Drosophila melanogaster* through experimental and computational work. Where appropriate, I will link the primary sources, and otherwise refer the inclined reader to reviews on specific subtopics. For many of the points I will make here, more detailed information is provided in the discussion at the end of this thesis.

1.1 Early attempts in understanding the brain

Whether for spiritual or medical reasons, the human brain has been the subject of surgical procedures since prehistoric times. The act of trepanation, where an aperture in the skull is

created, is viewed today as possibly the first act of neurosurgery. In some instances, signs point to sustained injuries warranting cerebral decompression as early as 5000 B.C. (Petrone et al., 2015), and likely even earlier. While not all cases can be attributed to a purely medical intention, studies have shown the post-operative healing of the inflicted cranial wounds (Moghaddam et al., 2015). It is evident from such cases that medical attention for the brain did not originate in modern times. However, understanding the role of the brain has not followed the same pace. While it is common in science journalism to jokingly cite ancient Greek philosopher Aristotle (384 – 322 B.C.) for his claim that the brain was merely a device for heat dissipation ("The brain [...] tempers the heat and seething of the heart." Aristotle and Ogle, 1911:652b26-27) and the cause for frontal baldness ("[...] the front part goes bald because the brain is there." Aristotle and Peck, 1943:784a1-2), we today still struggle to understand conscious thought and the exact neural processes that govern animal behavior.

Aristotle's arguably misguided, "cardiocentric" view was preceded by Greek philosopher Alcmaeon of Croton (5th century B.C.), who was a proponent of the "encephalocentric" view in which the brain serves as the mediator of cognitive processes (Crivellato and Ribatti, 2007). Other famous supporters of this theory were Hippocrates of Cos (~460 – 370 B.C.) and Plato (~427 – 347 B.C.), who saw its potential as the "seat of the rational soul" and "source of emotional, moral and aesthetic activities" (Crivellato and Ribatti, 2007). Plato even saw the body as a "servant" of the brain. It was Claudius Galenus of Pergamon (better known as Galen; ~129 – 216) who most vigorously fought for the dominance of the encephalocentric view, and he based his views on anatomical findings that all nerves emerged from the brain and spinal cord (Crivellato and Ribatti, 2007). For several centuries, his considerations supported the view that "psychic pneuma" flowing through the nerves conveyed thought and sensation, which was only corrected beginning in the 17th century, as explained later.

1.2 Visualizing the brain: single cells or continuous tissue?

The first researchers more widely credited with putting considerable effort into understanding nervous system structure and wiring were Santiago Ramón y Cajal (1852 – 1934) and Camillo Golgi (1843 – 1926), who investigated the complex networks of neurons. They were later jointly awarded the Nobel Prize in Physiology or Medicine. However, they came to different conclusions about the nature of neuronal wiring (Bock, 2013). Golgi held the opinion that all the tissue he could visualize with his silver-nitrate staining was a continuous network or *reticulum*. Following the concepts of Matthias Schleiden and Theodor Schwann, who found that separate cells made up all living organisms (Baluska et al., 2004), Cajal opposed Golgi's theory by claiming that the central nervous system (CNS) was made up of small, anatomically separate units. While using an only slightly altered version of Golgi's silver-nitrate method of staining nervous tissue (Jones, 2007), Cajal was therefore a proponent of the "neuron doctrine". Among other claims, it states that nervous cells in the brain are anatomical units and not a continuous *reticulum*. The term *neuron*, which is

the universally used term for individual nervous cells until today, was coined by German researcher Heinrich Wilhelm Gottfried von Waldeyer-Hartz (1836 – 1921) (Fodstad, 2001), who studied Golgi's and Cajal's work. The term *synapse* (from Greek συναψις, conjunction), which is today used to refer to the connection points between anatomically distinct neuronal cells, stems from the work of Charles Sherrington (1857 – 1952) (Bennett, 1999) where he tried to describe the nature of a connection between separate units.

1.3 The electrical nature of neuronal signal propagation

We know today that electrical impulses travel along elongated nerve cell protrusions, or axons and dendrites (*Fig. 1*), to propagate a signal from one neuron to the next, or to a muscle. However, the electrical nature of nerve conduction was not known until experiments like the famously serendipitous ones conducted by Luigi Galvani (1737 – 1798) brought it to light by showing the influence of electrical stimulation on muscle contraction in frog legs. Instead, "animal spirits" had been thought to flow through the nerves and mediate their function as theorized by Greek/Roman physician Galen (Cobb, 2002), but this had been debunked through slightly harrowing yet insightful experiments by Jan Swammerdam (1637 – 1680) (Cobb, 2002). He observed that removing a frog's heart did not immediately eliminate its ability to swim, but removal of the brain did. However, mechanical stimulation of the nerve was still able to elicit twitching in the leg muscles, and any "animal spirits" should have escaped the nerve by then. Further, he did not observe an increase in muscle volume upon contraction, which was another concept imposed by Galen's views. Although unknowingly, he may have even preceded Galvani in electrically stimulating a nerve and observing the contractions induced by that.

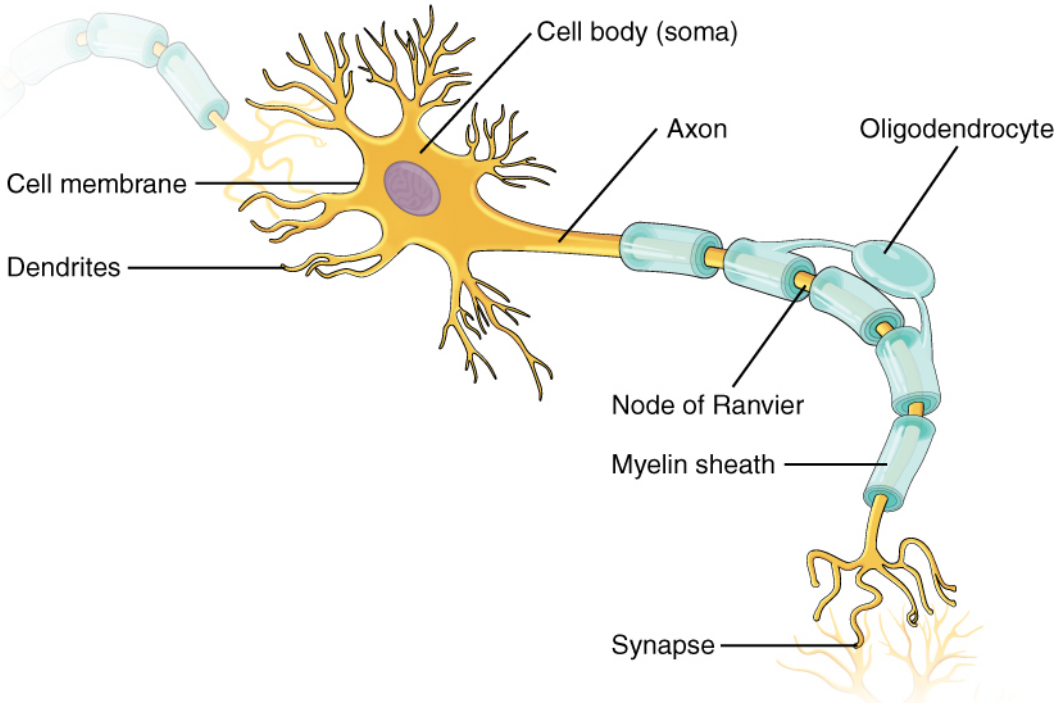

Fig. 1 Structure of a myelinated vertebrate neuron.
From: Betts et al., 2013; CC BY 4.0

Work by Emil Du Bois-Reymond (1818 – 1896) and Hermann von Helmholtz (1821 – 1894) later provided a first estimate of the speed of electrical signal propagation in frog nerves, measuring values between 25 and ~43 meters per second (at nerve lengths of 5–6 cm and signal durations between 1.4-2 ms depending on environmental temperature; Helmholtz, 1850) (Cobb, 2002). Based on Walther Nernst's (1864 – 1941) work on the thermodynamics of electrode potentials, connecting potentials with the concentrations of ions, Helmholtz's assistant Julius Bernstein (1839 – 1917) then formulated the "Membrane Hypothesis". It states that, at rest, the nerve cell membrane is a selective barrier for positively charged potassium ions, which can leave the cell following their concentration gradient. Therefore, a potential difference is generated because no counteracting concentration gradient could be equilibrated to compensate this loss of positive charges (Carmeliet, 2019). Bernstein stated that changes in the permeability for all ions then led to a self-propagating action potential (AP, *Fig. 2*), however without knowing which ions were involved and how the permeability changed for these. It was Charles Ernest Overton (1865 – 1933) who first hypothesized that, in conjunction with intracellular potassium concentrations, the extracellularly higher concentration of sodium ions , and changes in membrane permeability for both ions, would play a role in the depolarization of the membrane (Häusser, 2000; Carmeliet, 2019).

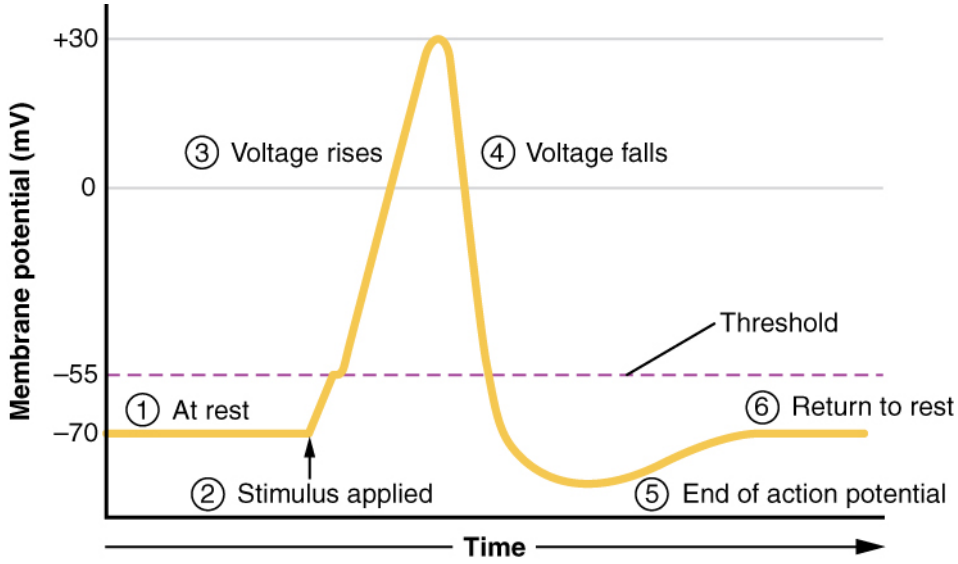

Fig. 2 Time course of an action potential.
From: Betts et al., 2013; CC BY 4.0

Together, these observations determined the two major ions involved in the generation of an AP, and this theory was later validated and refined by the seminal work of Alan Lloyd Hodgkin (1914 – 1998) and Andrew Fielding Huxley (1917 – 2012). Together with Bernard Katz (1911 – 2003), who aided in the theoretical explanation of the AP, they determined the flow of ions over the membrane during APs in squid giant axons in voltage clamp experiments, which allow the measurement of compensatory ionic currents over the membrane upon changes in membrane polarization (Hodgkin and Huxley,

1939; Hodgkin and Katz, 1949; Häusser, 2000). Doing so, they proposed the "Ionic Theory" which in essence combined the work of Bernstein and Overton to prove that the AP consisted of two major components: the initial depolarization of the nerve was due to a self-propagating increase of the membrane's permeability to sodium ions (leading to a net inward movement, owing to the opening of voltage-dependent sodium channels and the electrochemical gradient of sodium), and the subsequent repolarization was due to an increased outward movement of potassium ions. They showed that, while the "resting" membrane had a negative potential of around -70 mV (*Fig 2.*; depending on the electrochemical gradients of mainly sodium and potassium), a threshold potential had to be reached for the membrane depolarization to become a self-propagating AP, meaning that the generation of an AP was binary: only depolarizing events reaching this threshold would lead to the generation and propagation of the AP. A refractory period of few milliseconds ensures that the AP travels away from its point of initiation, since no new AP can be generated by the previously used sodium and potassium ion channels for this short period of time. But, as the depolarization induced by the AP passively spreads to other nearby ion channels, the AP can be iteratively generated at other points of the membrane and travel along the axon. Today we know that the membrane uses an energy-demanding process where ion transporters (Na^+/K^+-ATPases) exchange sodium and potassium ions against their concentration gradients (constituting up to 50% of the brain's energy demand; Erecińska and Silver, 1994). This helps maintain the physiological membrane state at rest, although fast action of these transporters is not necessary for the membrane's ability to generate an AP.

Nerve cells in different organisms show different ways of optimizing their conduction velocity along the axon, notably by increasing the diameter (as in the famous squid giant axon optimized for flight response) as electrical resistance decreases along the axon, or by wrapping the axon in an electrically insulating (i.e. increasing electrical resistance across the membrane) fatty myelin sheath formed by glial oligodendrocytes in the vertebrate CNS (*Fig. 1*) and by Schwann cells in the PNS (Bear et al., 2012). In myelinated axons, the AP "jumps" (a nearly lossless electrotonic spread due to low membrane capacitance and high electrical membrane resistance) between nodes of Ranvier forming along the axon, where ions can cross the membrane in local confinement and generate the next AP (Bear et al., 2012). This process is known as saltatory signal propagation, and it achieves its high conduction speed by only necessitating the generation of APs at higher distances, while the attenuation of longitudinally propagating current is prevented by the myelin sheath, which decreases membrane capacitance and increases electrical resistance across the membrane.

1.4 Signal conversion and transmission at the chemical synapse, and the molecular determinants of neurotransmission

Chemical synapses are the main connecting points between nerve cells, and they are needed to relay the electrical signal propagated as an AP to the next cell. However, this transmission is not electrical like the AP, but relies on chemicals. The chemical synapse can be subdivided into three parts based on its morphologically distinct compartments (*Fig. 3*). The synaptic part of the signal-emitting cell, where SVs reside and the AP arrives prior to SV release, is called the presynapse or presynaptic compartment. It is of particular importance to my doctoral work, and its structure and function will be explained in more detail below. The synaptic part of the signal-receiving cell, which senses presynaptic neurotransmitter release with specialized membrane receptors, is termed postsynapse, or postsynaptic compartment. Together, the pre- and postsynaptic part form the third part of the synapse by leaving a synaptic cleft of few tens of nanometers, through which the released neurotransmitter must diffuse in order to target pre- and postsynaptic receptors. The presynaptic part of the electron dense meshwork observed in electron microscopy (EM) (*Fig. 4*) is called the active zone (AZ), as it constitutes the synaptic part where synaptic vesicles (SVs) dock to the membrane and fuse upon arriving stimuli. "Docked" SVs are those seen as the closest to the membrane surrounding the AZ in EM, and docking is a necessary step in preparing an SV for fusion (Verhage and Sørensen, 2008).

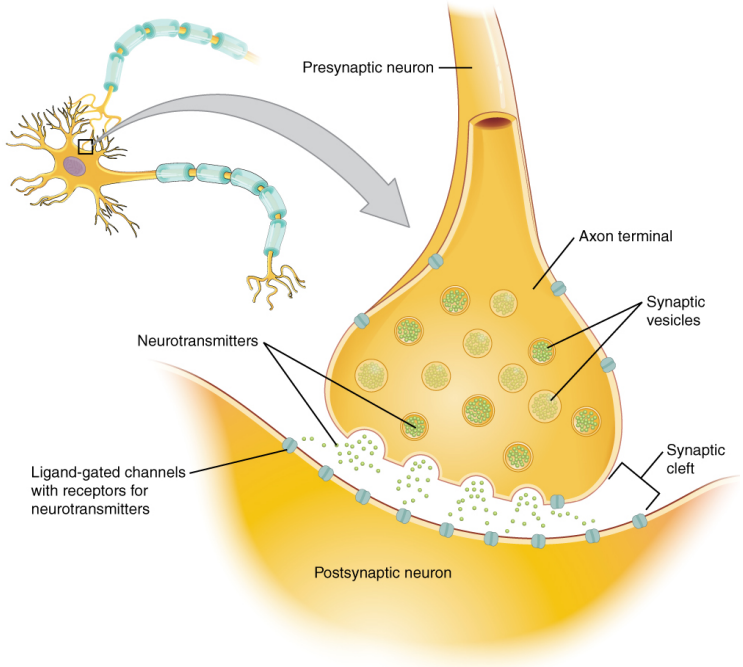

Fig. 3 Schematic morphology of a chemical synapse.
From: Betts et al., 2013; CC BY 4.0

Bernard Katz and Paul Fatt found in the early 1950s that, even without electrical stimulation of the nerve, they could still detect stochastically occurring "quantal" events when measuring the "end-plate potential" by intracellular recordings in the frog muscle (Fatt and Katz, 1952; Augustine and Kasai, 2007), which they already attributed to the presynaptic release of defined amounts of acetylcholine. Otto Loewi (1873 – 1961) had found this substance (although under a different name, "Vagusstoff" or "vagus substance") to be responsible for signal transmission from the Vagus nerve to the heart, and it was therefore the first identified neurotransmitter (NT) (Hyman, 2005). Importantly, he found that this substance alone was able to elicit the same response in the frog's heart tissue (slowing down its contractions) as when he stimulated the Vagus nerve. The numerous NTs we know of today comprise amino acids like glutamate, gamma-aminobutyric acid (GABA) and glycine, monoamines such as serotonin, dopamine, and epinephrine, as well as peptides such as oxytocin and vasopressin (Hyman, 2005).

Not long after the experiments of Fatt and Katz, it was determined that the quantal events they had found made up the large responses evoked by nerve stimulation and measured in the muscle (del Castillo and Katz, 1954). This work crucially furthered our knowledge about neurotransmission at chemical synapses, which we today know to be the major mediator of signal transmission between nervous cells, or at neuromuscular endplates. It provided us with the knowledge that, at the typical chemical synapse, the signal is converted from an electrically propagated one into a chemical one. Later observations by George Palade (1912 – 2008) and Sanford Palay (1918 – 2002) using high-resolution EM of fixed tissue showed membranous structures (SVs) at the end of nerve cell terminals, (see *Fig. 4* for examples) and these were quickly brought into connection with the quantal hypothesis of release (Heuser, 1989; Wells, 2005). Ever since the observation of quantal release, and the observation that summation of this quantal release underlies the response to nerve stimulation by Fatt, Katz, and del Castillo (Fatt and Katz, 1952; del Castillo and Katz, 1954), it has been hypothesized that a mechanism must exist which restricts SV release to defined release sites. Fluctuation analysis has since shown that a defined amount of SVs can be released upon stimulation with a certain release probability pV_r, and that the measured response size results from the product pV_r*q*N (q - quantal size; N - number of release sites) (Scheuss and Neher, 2001). The molecular correlate of release site formation has since been found to be Unc13 (Reddy-Alla et al., 2017; Sakamoto et al., 2018), as described later.

An intrinsic property of the synapse is the coupling of SVs to the source of Ca^{2+}-influx, the voltage-dependent calcium channels (or voltage-gated calcium channels, VGCCs). SVs are released with a certain vesicular release probability pV_r when their main Ca^{2+}-dependent release sensor synaptotagmin-1 (Syt-1) triggers membrane fusion through the SNARE complex (see below). Ca^{2+}-triggering of fusion is not a binary process (i.e. a single Ca^{2+} ion does not trigger fusion), as Syt-1 possesses several Ca^{2+} binding C2-domains and fusion can happen even when not all of the vesicular Ca^{2+}-binding sites (possibly and likely consisting of multiple Syts) are occupied by Ca^{2+} (Lou et al., 2005). Several Ca^{2+} sensors (like Doc2 and Syt-7) may cooperate in SV fusion (Walter et al., 2011). Still, pV_r increases with the amount of available Ca^{2+} (Meinrenken et al., 2002). Therefore, the coupling distance crucially influences pV_r by determining how much Ca^{2+} reaches the SV, and hence the sensor(s) triggering fusion. It can be tested by applying a slow Ca^{2+} buffer (like EGTA) to the synapse and measuring response strengths (e.g. by postsynaptic recordings). If the coupling is loose (i.e. SVs are localized far away from the Ca^{2+} source), release will be decreased by EGTA application, while its effect on release will be less pronounced in tightly coupled synapses.

EM has generally been a tremendous aid in resolving the components of the synapse. Besides showing the existence of SVs at synaptic terminals (*Fig. 4*) and the general structure of the synapse, EM has served to identify and visualize particularly electron-dense parts of the synapse (Zhai and Bellen, 2004; Ackermann et al., 2015), where a dense network of proteins resides close to or directly on the pre- and postsynaptic membranes. Many of these proteins have been identified and characterized, as I will lay out below.

At the postsynapse, the signal conveyed by presynaptic SV exocytosis is converted back into an electrical one by specialized membrane channel proteins called ionotropic receptors, which become permeable to certain ions (like Ca^{2+}, K^{+}, Na^{+}, or Cl^{-}) upon opening. Apart from these fast-acting, ion conductive channels, the class of metabotropic, G-protein coupled receptors (GPCRs) mediates slower modulatory actions via the intracellular GTP-binding protein signaling cascade. Presynaptic metabotropic glutamate receptors (mGluRs) have been implied in the regulation of glutamate release, ethanol dependence, and stress (Bahi et al., 2012; Peterlik et al., 2016). Ionotropic NT receptors on the membrane of the postsynaptic cell open upon the binding of NTs and, depending on their ion species conductivity, lead to de- or hyperpolarization of the postsynaptic membrane (Snyder, 2009). Therefore, NT release from the presynaptic cell can lead to excitation (excitatory postsynaptic potential, EPSP) or inhibition/attenuation (inhibitory postsynaptic potential, IPSP) of postsynaptic signal propagation, respectively increasing or decreasing the likelihood that the postsynaptic neuron will propagate the signal in form of an AP. A major system for inhibitory transmission uses GABA and $GABA_A$ receptors (whereas $GABA_B$ receptors are metabotropic), and it constitutes an important target for anticonvulsant and anxiolytic drugs (Lydiard, 2003; Schousboe et al., 2014). The most well-established excitatory transmission system (defined by its depolarizing effect on the postsynaptic cell, see above) in vertebrates uses glutamate, and its respective ionotropic receptors have been classified by their susceptibility to substances like NMDA (IUPAC: (2R)-2-(Methylamino)butanedioic acid or N-methyl-D-aspartate), Kainic acid, and AMPA (IUPAC: 2-Amino-3-(3-hydroxy-5-methyl-isoxazol-4-yl)-propanoic acid.

This synaptic signal conversion, from electrical to chemical and back, establishes an important control point in nerve cell communication, as it allows the defined release of chemicals and the majority of fast signal propagation only in one direction. Slow, GPCR-mediated action may be a bidirectional modulator of activity through pre- and postsynaptic metabotropic receptors, and a presynaptic localization of ionotropic receptors has been described (MacDermott et al., 1999). These might be involved in a feedback regulation mechanism to rapidly modulate the membrane potential of the firing cell, and thus increase or decrease its excitability.

As described, signal conversion at the synapse is initiated when the AP, having travelled from the cell body (or *soma*) along the axon to the synaptic endpoint, depolarizes the membrane and leads to the opening of VGCCs. These channels are permeable to Ca^{2+} ions, which are much more highly concentrated in the extracellular space than inside the cell due to their vital role in cell signaling processes (Carafoli and Krebs, 2016). Ca^{2+} concentrations within the cell (low ten to hundred nM in neurons) are strictly regulated, e.g. by active Na^{+}/Ca^{2+} exchangers removing it from the intracellular space, and a large intracellular store of Ca^{2+} is the endo-/sarcoplasmic reticulum which can release Ca^{2+} when ryanodine- or IP_3-receptors are activated (Ca^{2+}-induced Ca^{2+} release) (Grienberger and Konnerth, 2012). In the extracellular space, Ca^{2+} concentrations are typically much higher by a

factor of >10000, reaching millimolar values (Breitwieser, 2008). Ca^{2+} ions will therefore follow their electrochemical gradient downwards into the cell upon opening of VGCCs. Once inside the presynapse, Ca^{2+} will diffuse and bind to calcium sensors (e.g. Syt-1) located on the surface of SVs (Brose et al., 1992; Geppert et al., 1994), via so-called C2 domains. When Ca^{2+} binds to synaptotagmin-1, this protein interacts with phospholipids in the cell membrane and SNARE (soluble N-ethylmaleimide sensitive factor attachment protein receptor) proteins (Südhof, 2012). Normally, the membranes of SVs and the cell would not fuse due to constraints imposed by the energy required for lipid bilayer fusion (Jahn and Fasshauer, 2012). This energy barrier of SV fusion can be overcome by the formation of the SNARE complex, which is built from vesicular vSNAREs located on SVs, such as the vesicle-associated membrane protein VAMP/synaptobrevin, and from target tSNAREs located on the cell membrane, such as SNAP25 (synaptosomal nerve-associated protein 25) and syntaxin-1 (Syx-1) (Südhof, 2012). The working model is that these proteins bend the membranes by "zippering" their domains together into alpha-helical bundles and drawing them close, until both membranes are forced together and fuse. This opens a fusion pore and allows NT to leave the SV, diffuse across the synaptic cleft, and bind to ionotropic and/or metabotropic postsynaptic receptors, where another electrical or G-protein mediated signal is generated (Südhof, 2013).

The function of presynaptic proteins necessary for signal propagation and SV release can be investigated using neurotoxic substances found in nature, like Tetrodotoxin (TTX) occurring in puffer fish and blue-ringed octopus, among others (Makarova et al., 2019). This toxin specifically blocks the function of Na^{+} channels and prevents the generation of an AP (Narahashi, 2008). It therefore blocks NT at a very early stage, before directly influencing the exocytosis of SVs. Other toxins like tetanus neurotoxin (TeNT) or botulinum neurotoxin (BoNT) directly cleave the SNARE-proteins Syx-1, SNAP-25, and synaptobrevin/VAMPs (TeNT only) at different sites and depending on the toxin serotype (Dong et al., 2019), and therefore interfere with neurotransmission by reducing or preventing the ability of SVs to release their NT into the presynaptic cleft (Pellizzari et al., 1999).

The probability of SV fusion upon Ca^{2+} influx into the presynaptic terminal, pV_r, critically depends on the distance between the source of Ca^{2+} influx and the SV itself (see above) (Meinrenken et al., 2002; Böhme et al., 2018; Walter et al., 2018). In *Drosophila*, the central ELKS/CAST-homologous cytomatrix protein Bruchpilot (BRP) regulates the clustering of VGCCs at the AZ (Kittel et al., 2006) together with RIMs (Rab3-interacting molecules) (Han et al., 2011). In electron micrographs of neuromuscular endplate synapses, this protein is visible as an electron-dense area termed the a "T-bar", while synaptic structures differ in other animals and synapse types (*Fig. 4*). BRP also tethers SVs to the presynaptic membrane via few amino acids at its C-terminus (Hallermann et al., 2010) and interacts with the NT-release factor complexin (Scholz et al., 2019). Tethered SVs are then recruited to the AZ by RIMs, which (among a large number of other interactions, e.g. with RIM-BP, ELKS, Piccolo, Bassoon, SNAP25, Munc-13 and Liprin-α) simultaneously interact with

calcium channels and the SV membrane proteins Rab3 and Syt-1, although this latter interaction is controversial (Schoch et al., 2002; Mittelstaedt et al., 2010; Südhof, 2013). These recruited vesicles, which are ultrastructurally seen as very close to the presynaptic membrane, are the ones identified as docked in EM (as described earlier). The synaptic protein (M)unc-18 (M for mammalian, conserved in invertebrates), member of the Sec1/Munc-18 like protein family, has the ability to bind Syx-1 in its closed (inactive) conformation and therefore shield it from SNARE complex formation. Therefore, the fusion of tethered SVs needs to be prepared by a process called "priming", which induces fusion competence in docked SVs (Weimer et al., 2003; Verhage and Sørensen, 2008). Primed vesicles are those most amenable to fusion-inducing stimuli, and the pool of these SVs is therefore termed the "readily releasable pool" or RRP (Kaeser and Regehr, 2017). This RRP makes up ~5% of all SVs, and is replenished from the recycling pool, which itself makes up ~15% and is fed off the larger resting pool containing all other SVs (~85%) (Alabi and Tsien, 2012).

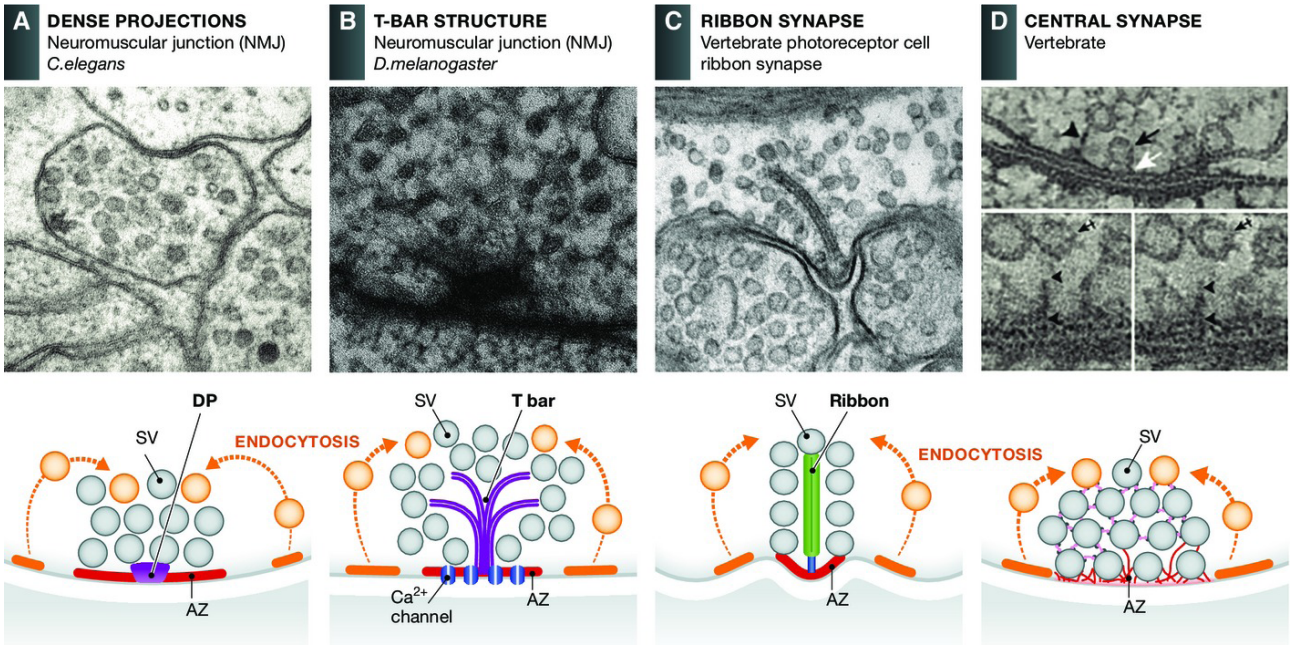

Fig. 4 Electron micrographs and cartoons of synapses in different organisms.
From: Ackermann et al., 2015; Licensed from John Wiley and Sons, License Nr. 4797741122216

The release factor (M)Unc13 (mammalian uncoordinated 13; identified in *C. elegans*; Brenner, 1974; Brose et al., 2000) seems to be essential for this process, as it binds Syx-1 and opens it up to initiate SNARE complex formation (Hammarlund et al., 2007; Magdziarek et al., 2020). Unc13, like most other essential synaptic proteins, is highly evolutionarily conserved, and mammals possess at least three genes for its production (Munc13-1, Munc13-2, and Munc13-3). Munc13-1 and Munc13-3 are specifically expressed in neurons and neuroendocrine cells, while two isoforms of Munc13-2 exist in either brain-exclusive (bMunc13-2) or ubiquitous (ubMunc13-2) form (Brose et al., 2000). In *Drosophila*, at least two isoforms (Unc13A and Unc13B) are expressed by the same gene, differing in their N-terminal composition and their location in respect to the AZ center, where the VGCCs reside (Böhme et al., 2016).

While *Drosophila* Unc13s seemingly lack the most N-terminal C2 domain (C2A) responsible for RIM-interaction in mammals (although a lack of interaction between these two proteins in *Drosophila* is unlikely due to its importance), the *Drosophila* Unc13A isoform possesses several identified functional domains that are highly similar to those found in mammalian Unc13s (Böhme et al., 2018). A domain that seems to be responsible for binding calmodulin, which preferably interacts with ubMUnc13-2 in the presence of Ca^{2+} (Junge et al., 2004), is important for synaptic short-term plasticity in (M)Unc13-1 (Lipstein et al., 2012; Lipstein et al., 2013). Furthermore, Unc13s in mammals, *Caenorhabditis* and *Drosophila* harbor a highly conserved phorbol-ester (PdBu/PMA)-sensitive C1 domain, activation of which in Munc13-1 facilitates NT (Basu et al., 2007). Phorbol esters serve as diacylglycerol (DAG)-analogs, and this domain is therefore likely responsible for actions induced by the membrane signaling lipid DAG that is formed by PLC-mediated $PI(4,5)P_2$ (another signaling lipid) cleavage at the membrane. In addition, there are two C2 domains (C2B and C2C, named by their appearance from N- to C-terminal ends), one of which (C2B in Munc13-2) has been shown to bind calcium and phosphoinositides such as $PI(4,5)P_2$ (Shin et al., 2010; Böhme et al., 2018). The C1-domain of protein kinase C (PKC) can interact with C2-domains of other proteins (like (M)Unc18; Genç et al., 2014) and maintain their active state by phosphorylation (Brose et al., 2000), and the C1-domain of *C. elegans* Unc13 (and likely of all other Unc13 homologs due to the high grade of conservation) is functionally similar to that of PKC (Silinsky and Searl, 2003). An autoinhibitory interaction between C1 and C2B-domains in *C. elegans* has been shown to negatively influence pV_r (Michelassi et al., 2017), and therefore regulates a Ca^{2+} dependent role of Unc13 in SV release. The large MUN domain, which is the minimal part required for priming, mediates the interaction between (M)Unc13 and Syx-1 (Yang et al., 2015). Together, the C1, C2B, C2C and MUN domains comprise the essential and most conserved part ('core') of most known Unc13s in mammals and invertebrates (Dittman, 2019). The N-terminal part of *Drosophila* Unc13A has been proven vital for its specific localization, while the C-terminal part generates the previously mentioned release site (Reddy-Alla et al., 2017). Besides interacting with the SNARE protein Syx-1, and binding Ca^{2+} and membrane lipids (all known and supposed functions are reviewed in Dittman, 2019), Unc13 therefore positions SVs at specific coupling distances to the VGCC cluster and primes them for release. Further confirmation of these findings later came from experiments in mammalian neurons (Sakamoto et al., 2018).

1.5 Lipid membrane components and their role in neurotransmission

Apart from the proteinaceous components acting in SV release, like (M)Unc13, Syt-1 and the SNARE proteins, the composition of the cellular membrane seems to determine parameters of neurotransmission, as is already implied in the role of DAG in Unc13 activity regulation described above (also see Böhme et al., 2018). Biological membranes, such as those of the eukaryotic cell and its organelles/compartments (like nucleus, endoplasmic reticulum, Golgi apparatus, SVs, and

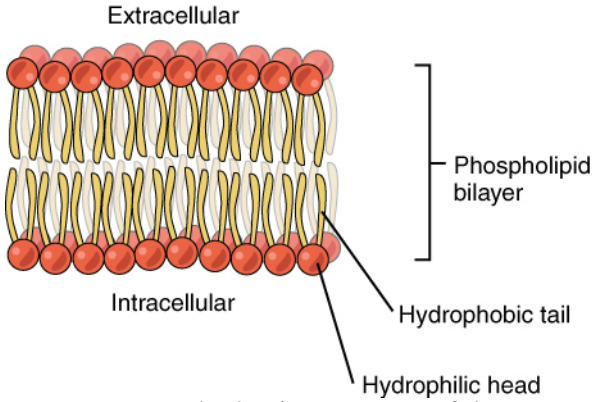

Fig. 5 The basic structure of the membrane lipid bilayer.
From: Betts et al., 2013; CC BY 4.0

lysosomes), are typically composed of lipids in an asymmetrical bilayer (*Fig. 5*; Casares et al., 2019). The cell membrane bilayer is made of two "leaflets" of lipids, ordered by their hydrophilicity and lipophilicity (i.e. how well their parts are soluble in polar solvents like water or in fat/oil and nonpolar solvents like benzene or hexane). This means that the hydrophilic/polar headgroups of the main membrane components like sterols (e.g. cholesterol), glycerophospholipids (e.g. PI(4,5)P_2), and sphingolipids (e.g. sphingomyelin) (Alberts, 2008; Borroni et al., 2016) are oriented towards the aqueous milieu of the extracellular or intracellular space, while the lipophilic/nonpolar tail groups (typically fatty acids) are shielded from water by orienting towards other lipophilic components. This leads to the aggregation of lipids in bilayers, even in artificial experimental conditions (Alberts, 2008). Based on their composition, membranes are relatively fluid, and lipids can freely diffuse laterally along the membrane surface or perform dynamic movement like "flip-flop" across the membrane to the respective other leaflet and back.

This separation of cellular compartments and the cell itself from the outside constitutes an important barrier to regulate concentrations of different molecules, like ions and proteins. The importance of ion separation in neuronal cells has been described in an earlier section explaining the electrical nature of signal propagation in the nervous system, where specialized ion channels in the otherwise impermeant lipid membrane allow the regulated exchange of charged ions. The lipid milieu of the cell membrane also determines how metabotropic and ionotropic NT receptors are embedded in the membrane, as they interact with cholesterol and contain transmembrane domains that anchor them in the lipid bilayer (Khelashvili and Weinstein, 2015; Borroni et al., 2016). Lipids can non-randomly accumulate to form "rafts" in the membrane, which may serve to keep location-specific proteins (like those used in postsynaptic NT sensing) in the physiologically relevant place (Allen et al., 2007; Borroni et al., 2016).

Influences of lipid-protein interactions on hormone and neurotransmitter secretion have been described (Ammar et al., 2013). Specifically, PI(4,5)P_2 has been shown to influence the transport and exocytosis of secretory vesicles (Martin, 2012; Walter et al., 2017). This is less surprising when taking into consideration that many synaptic proteins, like the ones described earlier, exhibit lipid binding C2-domains (e.g. Syt-1 and Unc-13) or interact with lipid-dependent enzymes like PKC (e.g. Unc-18). Therefore, the recruitment of SVs to, and their fusion with, the membrane at the active zone is easily conceivable to depend on membrane lipids like PI(4,5)P_2. The binding of Ca^{2+}-bound Syt-1 C2B-domains to PI(4,5)P_2-rich regions to induce NT exocytosis is likely an enhancing factor in

neurotransmission (Martin, 2012, 2015). It thus becomes clear that the study of lipid-protein interactions can give great insight into physiological mechanisms of neurotransmission, and an important as well as specific role of lipids is obvious. For these reasons, and as advancements in biochemical synthesis of specific lipids and recombinant proteins have facilitated the study of lipid-protein interactions, a part of my thesis is dedicated to this topic and has been published in Schuhmacher et al. (2020).

The study of lipids is inherently difficult due to their volatile nature and the complex pathways by which they are synthesized and metabolized *in vivo* (van Meer et al., 2008). Approaches to get a grip on lipid properties in the membrane include the generation of artificial membrane systems like grand unilamellar vesicles (GUVs), the depletion of cholesterol using cyclodextrin, electron microscopy, atomic force microscopy, X-ray diffraction, and molecular dynamics simulations (Owen, 2015). Fluorescent phospholipid analogs and dyes can be used to optically trace the localization of lipids, although interference with normal membrane structure cannot be excluded (Owen, 2015). If it is desired to capture the dynamic movement of lipids, and their interaction with other components of the cell, it is vital to be able to control the exact amounts and locations of these lipids. A recent approach where biologically inactive, caged lipids are loaded onto cells and can be turned into the native, biologically active forms has targeted exactly this need (Nadler et al., 2013; Nadler et al., 2015; Walter et al., 2017). Here, membrane lipids were chemically linked to a coumarin cage, which could be removed by a UV laser flash. Therefore, the controlled release of defined amounts of native lipid species became feasible.

The $PI(4,5)P_2$-metabolite DAG is an important second messenger in the cell, with the abilities to recruit protein kinase C (Gallegos and Newton, 2008) and activate TRP-channels (Hardie, 2007). It is formed when GPCR-mediated PLC-activity leads to the cleaving of $PI(4,5)P_2$ into IP_3 and DAG. The inability of caged DAG to translocate over the membrane allows a relaxation experiment, in which lipids are initially present at a specific location (the outer membrane leaflet in Schuhmacher et al., 2020) and an intracellular fluorescent reporter protein is recruited to the membrane only when the uncaged compound is translocating over the membrane. This method in conjunction with quantitative measurements of the reporter protein and of the caged lipid allow inferences about lipid dynamics and lipid-protein interactions, which we performed using a mathematical model in Schuhmacher et al. (2020). Generally, the study of lipid-protein interactions remains a challenging issue and employing the existing methods in nervous tissue will be necessary to fully understand the synaptic relevance of lipid-protein interactions.

1.6 Synaptic plasticity: the system responds to changing demand

One of the most important properties of the nervous system is its ability to plastically regulate synaptic connection strengths. On a short timescale, this enables e.g. controlled and rapid muscle contractions, as well as fine movement. On longer time scales, this is important for the activity-dependent strengthening or weakening of synaptic connections that play a role in differentially used neural pathways. One of the most famous examples is that of hippocampal long-term potentiation (LTP) found in 1973 (Siegelbaum and Kandel, 1991), which is almost undeniably implied in memory formation, and which relies on pre- and postsynaptic mechanisms of second-messenger induced molecular processes (like an increase in postsynaptic ionotropic receptor levels).

This synaptic ability to scale its transmission strength is limiting to the rate of SV release under rapid AP succession at the presynapse, as the RRP consists of under 5% of all SVs (Alabi and Tsien, 2012), and coupling distances even within the RRP can vary widely and obey exclusion zones around the VGCC cluster (Vyleta and Jonas, 2014; Keller et al., 2015; Böhme et al., 2018; Kobbersmed et al., 2020). Therefore, depending on the synapse type (e.g. loose/tight coupling), the present buffers (like ATP) and their saturation kinetics, as well as the speed of Ca^{2+} clearance, SV release upon repetitive stimulation within few milliseconds will either decrease (short-term depression, STD) or increase (short-term facilitation, STF) in comparison to initial release at the "naïve" synapse. This is commonly measured as the paired-pulse ratio PPR, which results from dividing the second response amplitude by the first response amplitude measured in electrophysiological experiments. Another measure that can be taken from this short-term plasticity behavior is the size of the readily releasable pool, as release will reach a steady state of depletion and replenishment after a certain number of stimuli (Kaeser and Regehr, 2017). While RRP depletion is inherent in SV release, mechanisms of replenishment are less clear. Possible explanations of replacing depleted SVs to maintain or increase release include the increase of pV_r e.g. by upregulating the influx of Ca^{2+} through VGCCs, by activating other Ca^{2+}-sensors that act on the second release phase due to accumulating Ca^{2+}, or the rapid priming of docked SVs (Fioravante and Regehr, 2011). Actin- and Myosin-dependent mechanisms of RRP replenishment have been proposed (Miki et al., 2016), and Ca^{2+}/CaM-interactions with Unc13 show roles in regulating STF (Lipstein et al., 2013). In one of our recent publications, we have shown a role of Ca^{2+}-dependent regulation of the RRP in STP at the *Drosophila* NMJ, which could not be explained by a mere upregulation of pV_r (Kobbersmed et al., 2020).

The sustained modification of synaptic connections on timescales above a few hundreds of milliseconds requires changes in pre- and/or postsynaptic molecular composition (Davis, 2013; Davis and Müller, 2015). The scaling of synaptic activity in response to increased demand is called homeostatic plasticity in which the synapse senses the demand (by as of yet unknown pathways) and induces mechanisms like the upscaling of presynaptic SV release (Davis, 2013; Davis and Müller, 2015). Presynaptic mechanisms may include the scaling of VGCC numbers, while the postsynapse

may contribute to plasticity by regulating the number of ionotropic receptors available for generating a response to presynaptically release NT (Voglis and Tavernarakis, 2006). The involvement of different molecules can be investigated by pharmacologically interfering with their function (e.g. blocking ionotropic glutamate receptors with the wasp toxin Philanthotoxin; Piek, 1982; Eldefrawi et al., 1988, or the synthetic compound MK-801; Clineschmidt et al., 1982). Furthermore, plasticity can be investigated on a longer timescale by genetically mutating/removing ionotropic glutamate receptors. In a recent publication (Böhme et al., 2019) we have used both approaches to investigate the molecular mechanisms underlying homeostatic plasticity at the Drosophila NMJ.

1.7 Spontaneous neurotransmission

While nerve stimulation leads to the temporally confined, synchronous exocytosis of many SVs, the experiments of Fatt and Katz (1952) saw the unprovoked release of single SVs (without eliciting an AP), a mechanism of release termed spontaneous exocytosis (as opposed to AP-evoked exocytosis following a stimulus). The reason for this stochastic and seemingly unregulated mode of neurotransmission is elusive. It has been seen as a byproduct of the presynaptic release machinery due to “leaking” (Xu et al., 2009; Walter et al., 2014), while some studies claim a role in development (Huntwork and Littleton, 2007; Ataman et al., 2008; Choi et al., 2014), release modulation (Carter and Regehr, 2002), and synapse maintenance (McKinney et al., 1999). Release sensors apart from Syt-1, the deletion of which leads to increased spontaneous NT in *Drosophila* (Littleton et al., 1993; Littleton et al., 1994), have been implied in spontaneous release, like the double C2-domain protein Doc2β (Groffen et al., 2010), and recent results by the same group further distinguish Doc2 protein function from Syt-1 (Díez-Arazola et al., 2020). Further, distinct SV pools and postsynaptic receptors have been implied to separately control spontaneous and evoked SV release (Atasoy et al., 2008; Andreae et al., 2012; Crawford and Kavalali, 2015), even at distinct active zones (Melom et al., 2013; Peled et al., 2014; Walter et al., 2014). Spontaneous release has been shown to depend on intracellular Ca^{2+} concentrations (Nosyreva and Kavalali, 2010; Wierda and Sørensen, 2014), as it could be reduced by BAPTA (a fast Ca^{2+} buffer) treatment. Additionally, some studies state that it also scales with extracellular Ca^{2+} concentrations (Xu et al., 2009; Vyleta and Smith, 2011). Furthermore, spontaneous release can be modulated by intracellular signaling molecules like the DAG-analogous phorbol esters (PdBu, PMA) or cyclic monophosphates (AMP, GMP) that target protein kinases C, A, and G, respectively (Publicover, 1985; Malenka et al., 1987; Arancio et al., 1995; Capogna et al., 1995).

1.8 Investigating synapses at the *Drosophila* neuromuscular junction

The investigation of molecular neurotransmission determinants requires a biological model system that is easily accessible for optical and physiological measurements, as well as to genetic

Fig. 6 The fruit fly *Drosophila melanogaster*.
Source: https://commons.wikimedia.org/wiki/File:Drosophila_melanogaster_Proboscis.jpg; CC BY-SA 4.0

modifications. If inferences regarding human physiology and pathologies are desired, this model system should possess the same genes and components that control and organize neurotransmission in humans. While neurotransmitter substances like serotonin and its receptors have seemingly been found in sponges (although the validity of these results is disputed; Leys, 2015), and several evolutionarily early organisms, like sponges (porifera) and comb jellies (ctenophora), possess forms of Unc13 (Dittman, 2019), none of these systems allow the investigation of neurotransmission due to the lack of a nervous system with synaptic connections. Apart from the most widely used vertebrate model systems (rat - *Rattus norvegicus*, mouse - *Mus musculus*, zebrafish - *Danio rerio*), the evolutionarily more recent (i.e. compared to fungi, choanoflagellates, and porifera) and simple enough invertebrate model systems preferably used by neuroscientists and geneticists today are the nematode *Caenorhabditis elegans*, whose hermaphrodite form has a nervous system made up of 302 neurons (Albertson and Thomson, 1976; White et al., 1986), and the arthropod *Drosophila melanogaster* which served as the model organism in this thesis (*Fig. 6*). Both organisms are genetically well-characterized, and their keeping and husbandry require little resources and effort (especially compared to the mentioned vertebrate models). The fruit fly shows a fast generational turnover, with times between oviposition and eclosion of the adult ranging between ~10-12 days depending on environmental conditions like temperature and humidity.

Drosophila genome studies have revealed that up to 75% of human disease-related genes have orthologs (genes of the same evolutionary origin) in the fruit fly, with conserved domains showing 80-90% nucleic acid identity (Pandey and Nichols, 2011). This allows inferences regarding some of the basic mechanisms of physiology and pathology across species. Progress in *Drosophila* genetics gained traction in 1910, when Thomas Hunt Morgan (1866 – 1945) discovered the *white* gene, a mutation of which leads to a change in compound eye pigmentation from red to white in males (Bellen et al., 2010). Further important discoveries included the observation that genetic mutations could be induced by radiation (X-rays; 1927) and ethyl methanesulfonate (EMS; 1968) (Bellen et al., 2010). An EMS-induced mutation in the Unc13 gene has been used in our experiments to study synaptic function in Unc13A-mutant flies (*unc13A*^{null}; Böhme et al., 2016). One of the most widely used genetic toolboxes for *Drosophila* is the UAS/Gal4-system (Brand and Perrimon, 1993). It allows the tissue-specific expression of a gene by mating flies that ubiquitously contain a gene under the

control of an upstream activating sequence (UAS) with flies that contain a tissue-specific promoter and the Gal4-gene. When Gal4 is expressed in the targeted tissue, it binds to the UAS-sequence of the gene of interest, and that gene can then be expressed (via transcription into mRNA and translation into an amino acid chain/polypeptide) into the desired protein (Brand and Perrimon, 1993).

During its development, the holometabolous *Drosophila* passes several stages, three of which are the larval instar stages (1st – 3rd instar) characterized by foraging and growth. The larva of *Drosophila* is easily accessible to research at the synapse level, as its motoneuronal bundles emerging from the CNS innervate muscles at the transparent body wall. Every symmetrical larval segment contains a very regular pattern of body wall muscles, each of which is innervated by different types of motoneurons, forming different types of NMJs (Keshishian et al., 1996). Type I NMJs (morphologically and functionally divisible into Ib (big) and Is (small)) use glutamate as the main neurotransmitter, which differs from vertebrate NMJs where acetylcholine is the major neurotransmitter (Jan and Jan, 1976; Menon et al., 2013). Type II and III NMJs of *Drosophila* predominantly use neuromodulatory peptides like octopamine and tyramine.

Due to the transparence of the larval body wall, 3rd instar larvae can be used for live-imaging of synaptic development in the intact animal. Genetically expressed, fluorescently labelled synaptic proteins can be visualized over several hours, enabling observations of NMJ development and synapse maturation. In our work, we often choose to dissect the animal and make it accessible to electrophysiological and/or optical measurements. Current clamp recordings make use of a single sharp electrode that is inserted into the muscle close to the NMJ, where neurotransmission events lead to a change in membrane potential, which can then be measured (Bykhovskaia and Vasin, 2017). Additionally, two-electrode voltage clamp recordings can be used to keep the membrane potential at a defined value and measure the current needed to maintain it during neurotransmission events (Bykhovskaia and Vasin, 2017).

Since the molecular cloning of the green fluorescent protein from the jellyfish *Aequorea victoria* (Prasher et al., 1992), fluorescent probes like it have been used extensively for the investigation of cellular processes. While probes that exhibit continuous fluorescence are extremely useful, conditional fluorescence can be used to visualize temporally confined processes. An insightful optical approach that can be applied at the *Drosophila* NMJ is the imaging of presynaptic Ca^{2+} transients using Oregon green BAPTA (OGB) (Macleod et al., 2002; He and Lnenicka, 2011). This allows the measurement of Ca^{2+}-influx and -buffering dynamics in the presynapse, two properties that influence the short-term plasticity of the synapse, which can be measured with controlled stimulation and postsynaptic electrophysiological recordings.

Other approaches that utilize conditional fluorescence *in vivo* include the investigation of spatial protein interactions or colocalization by Förster resonance energy transfer (FRET), where fluorescence

of one fluorophore is only induced by the spatial proximity to a second fluorescent molecule emitting light at a wavelength that excites the former fluorophore (Dunst and Tomancak, 2019). Similarly, split GFP-probes can be used in bimolecular fluorescence reconstitution assays to trace spatial interactions between proteins in *Drosophila* (Hudry et al., 2011). A conditional green fluorescent probe for the detection of glutamate release at the *Drosophila* NMJ, iGluSnfr, has recently been developed and shows promise for the investigation of NT in this model (Marvin et al., 2013). Furthermore, voltage sensitive dyes and proteins exist to visualize changes in membrane polarization, essentially allowing optical electrophysiology, like Arclight (Cao et al., 2013)

In my work, to quantify synaptic mechanisms of signal transmission at individual AZs, I have made use of flies pre- and postsynaptically expressing the genetically encoded Ca^{2+}-indicator (GECI) GCaMP (Nakai et al., 2001). This circularly permuted form of GFP transiently emits green light when Ca^{2+} binds to the included calmodulin domain and this in turn wraps around the included CaM-binding M13-domain of the myosin light chain kinase (Akerboom et al., 2009), as this closes the chromophore (the part of the fluorophore which is responsible for electron transition and light emission) off from solvent-induced protonation and leads to fluorescence increase (Akerboom et al., 2009). This sensor has been successfully used in *Drosophila* to visualize neurotransmission, and it has been significantly improved over recent years (Tian et al., 2009; Akerboom et al., 2012; Chen et al., 2013; Yang et al., 2018; Dana et al., 2019). Several labs have used GCaMP to characterize the molecular determinants underlying release heterogeneity at the fly NMJ (Peled and Isacoff, 2011; Melom et al., 2013; Peled et al., 2014; Muhammad et al., 2015; Newman et al., 2017). This way, it could be shown that AP-evoked SV release critically depends on levels of BRP at the presynapse, and that the larval *Drosophila* NMJ consists of many synapses of heterogeneous maturity and composition, which hence differ in their participation in neurotransmission (Melom et al., 2013; Peled et al., 2014; Muhammad et al., 2015). For the results presented in this thesis, I made use of GCaMP to dissect the overlap between mechanisms involved in evoked and/or spontaneous release (Grasskamp et al., manuscript in preparation), specifically regarding regulation at the single AZ level.

1.9 Combining experimental data with computational methods

Due to the inaccessibility of many molecular functions and signaling pathways, experimental data is not always readily interpretable by the human brain. Therefore, increasingly elaborate computational analysis of data has proven valuable in augmenting biological experimentation. Moore's law (first published as "Cramming more components onto integrated circuits" - Moore, 1965) states that the number of transistors on a chip doubles roughly every two years (Brock and Moore, 2006). Although the law will face its supposedly inevitable demise within the next few years as predicted by its own pioneer (Moore, 2020), tapping into the exponential increase in computational power over the last decades has allowed the scientific community to make progress undreamt of by researchers before the advance of the modern computer as predicted by Alan Turing (1912 - 1954)

(Turing, 1937). Today's supercomputers have aided in problems no human brain could reasonably hope to solve alone, just like the microscope has brought about a level of understanding no human eye could have achieved in its current form. Machine learning approaches that rely on considerable computational power have seemingly surpassed trained physicians in recognizing retinal pathologies (Fauw et al., 2018). The controversial "Human Brain Project" (www.humanbrainproject.eu) seeks to build a complete digital version of the brain, although its "Blue Brain Project" predecessor (starting in 2005) has failed at the task. Still, the flow of progress in computer-aided neuroscience is far from running dry.

Due to the proven superiority of functionalized silicon in performing numerical operations, it lends itself to the investigation of cellular processes based on experimental observations. The beginnings of computational neuroscience saw the simulation of APs based on Hodgkin's and Huxley's work, and modern desktop processors are capable of computing the AP faster than it occurs in the squid giant axon (Moore, 2010).

Formulating a biological concept and translating it into a form that the computer will be able to process requires breaking it down into its basic components. For a cellular process, that can be the amount of a substance that is present in the cytoplasm at any point in time before being modified or removed, and the speed with which these processes happen. In my work, I have used systems of differential equations that calculate exactly this: The change of molecule states over time from a known initial state, assuming specific reactions that happen with unknown speeds or rate constants. In one computer model, I simulated intracellular, presynaptic increases of Ca^{2+} and subsequent SV release following nerve stimulation and optimized the simulations so that they would agree with experimental measurements gathered by my colleagues (Böhme et al., 2016). A good optimization approach is signified by exploring a large set of possible parameters to avoid finding a solution of the problem that does not represent physiological conditions and should be designed with as many known (i.e. measured) parameters as possible. All unknown parameters should be constrained within a reasonable range. The described approach in Böhme et al. (2016) represents a deterministic model, where everything happens very reproducibly and without random processes. Opposed to this, and more in line with biological reality (although considerably more computationally demanding), is the simulation of stochastic processes (used in Kobbersmed et al., 2020). Stochastic processes in the cell include spontaneous SV exocytosis, VGCC gating, and many more on the basis of single molecules (Bracciali et al., 2008).

As the quality of a computer model still heavily relies on the problem as defined by the scientist, it is important not to overstate the role of the computer in neuroscientific research; however, its sheer speed will continue adding value to scientific progress. And with the advancement of machine "intelligence" and neural networks, even the design of models might soon be performed by the computer itself.

1.10 Aims of the presented work

With the experiments and conclusions presented in this thesis, both *in vitro* and *in silico*, I aimed to contribute to the characterization of the molecular underpinnings that direct synaptic signal transmission. To do so, my goals were the following:

(1) I wanted to develop a computational method that utilizes Ca^{2+} simulations and an allosteric model of Ca^{2+}-driven SV exocytosis to explain and support experimental findings that showed the differential release coupling in *Drosophila* by two isoforms of Unc13 (Böhme et al., 2016).

(2) Additionally, I aimed to contribute to detailing the role of Unc13 as the molecular release site correlate by performing optophysiological experiments in wild-type and Unc13A mutant flies, showing that scaling of evoked and spontaneous release did not directly depend on BRP itself, but on BRP-mediated recruitment of Unc13A (Reddy-Alla et al., 2017).

(3) My computational work furthermore aimed at showing how molecular release site components of the AZ are added to scale release upon postsynaptic disturbances of neurotransmitter detection (Böhme et al., 2019).

(4) Reviewing the work of recent years in characterizing the molecular components of synaptic transmission and plasticity, I wanted to show how well different synaptic protein domains are conserved over evolution in different organisms, and how differential SV-VGCC coupling influences short-term plasticity in a computational model of the *Drosophila* synapse (Böhme et al., 2018).

(5) Taking into account how broadly SVs are distributed at the *Drosophila* synapse, my computational work set out to build an improved model of SV release by implementing different release sensors and a way to simulate stochastic SV release (Kobbersmed et al., 2020).

(6) Elaborating on the investigation of SV release at the level of individual AZs, I wanted to determine the molecular determinants of spontaneous and evoked SV release, and their overlap on the pre- and postsynaptic level (Grasskamp et al., manuscript in preparation).

(7) Honoring the crucial role of membrane lipids in cellular signal transmission, and using mathematical modeling of lipid kinetics in living cells, I further aimed to determine how subtle structural differences between acyl side-chains of various DAG species contributed to their differential interaction with the C1 domain of PKC, a cellular signaling protein (Schuhmacher et al., 2020).

2 Publications

This part of the thesis encompasses a chronological register of all relevant publications or work in preparation to which I contributed during the course of my doctoral work. All publications (except for the manuscript in preparation) underwent a peer-review process, and each publication is prefaced by a detailed list of my contributions.

2.1 List of publications

Publication I: Böhme MA*, Beis C*, Reddy-Alla S*, Reynolds E*, Mampell MM, **Grasskamp AT**, Lützkendorf J, Bergeron DD, Driller JH, Babikir H, Göttfert F, Robinson IM, O'Kane CJ, Hell SW, Wahl MC, Stelzl U, Loll B, Walter AM, Sigrist SJ - *Active zone scaffolds differentially accumulate Unc13 isoforms to tune Ca^{2+} channel–vesicle coupling*, Nature Neuroscience, 2016
Permalink: https://doi.org/10.1038/nn.4364

Publication II: Reddy-Alla S*, Böhme MA*, Reynolds E, Beis C, **Grasskamp AT**, Mampell MM, Maglione M, Jusyte M, Rey U, Babikir H, McCarthy AW, Quentin C, Matkovic T, Bergeron DD, Mushtaq Z, Göttfert F, Owald D, Mielke T, Hell SW, Sigrist SJ, Walter AM - *Stable Positioning of Unc13 Restricts Synaptic Vesicle Fusion to Defined Release Sites to Promote Synchronous Neurotransmission*, Neuron, 2017
Permalink: https://doi.org/10.1016/j.neuron.2017.08.016

Publication III: Böhme MA, **Grasskamp AT**, Walter AM - *Regulation of synaptic release-site Ca^{2+} channel coupling as a mechanism to control release probability and short-term plasticity*, FEBS letters, 2018
Permalink: https://doi.org/10.1002/1873-3468.13188

Publication IV: Böhme MA*, McCarthy AW*, **Grasskamp AT**, Beuschel CB, Goel P, Jusyte M, Laber D, Huang S, Rey U, Petzoldt AG, Lehmann M, Göttfert F, Haghighi P, Hell SW, Owald D, Dickman D, Sigrist SJ, Walter AM - *Rapid active zone remodeling consolidates presynaptic potentiation*, Nature Communications, 2019
Permalink: https://doi.org/10.1038/s41467-019-08977-6

Publication V: Kobbersmed JRL, **Grasskamp AT**, Jusyte M, Böhme MA, Ditlevsen S, Sørensen JB, Walter AM - *Rapid regulation of vesicle priming explains synaptic facilitation despite heterogeneous vesicle:Ca^{2+} channel distances*, eLife, 2020
Permalink: https://doi.org/10.7554/eLife.51032

Publication VI: Schuhmacher M, **Grasskamp AT**, Barahtjan P, Wagner N, Lombardot B, Schuhmacher JS, Sala P, Lohmann A, Henry I, Shevchenko A, Coskun Ü, Walter AM, Nadler A - *Live-cell lipid biochemistry reveals a role of diacylglycerol side-chain composition for cellular lipid dynamics and protein affinities*, Proceedings of the National Academy of Sciences, 2020
Permalink: https://doi.org/10.1073/pnas.1912684117

Manuscript in preparation: **Grasskamp AT**, Jusyte M, McCarthy AW, Walter AM - *Molecular and functional interdependence of spontaneous and action potential evoked neurotransmission at individual synapses*

** equal contributions*

2.2 Permissions to archive and reuse

The rights and permissions to reproduce and publish the listed publications within this thesis, in print and online (non-commercially and according to the respective publisher terms and conditions), have been acquired from or provided by the publishers as detailed below. Importantly, it is stated whether the publisher's version/PDF can be used in the publicly available electronic version of this thesis according to data available from SHERPA/RoMEO publisher copyright policy & self-archiving repository (www.sherpa.ac.uk/romeo), or from the publishers themselves. It follows that the publications in Nature Neuroscience (Springer Nature) and FEBS Letters (John Wiley and Sons) will not be included in the publicly available online version of this thesis.

Springer Nature (Böhme et al., *Nature Neuroscience* 2016): "Ownership of copyright in original research articles remains with the Author, and provided that, when reproducing the contribution or extracts from it or from the Supplementary Information, the Author acknowledges first and reference publication in the Journal, the Author retains the following non-exclusive rights: To reproduce the contribution in whole or in part in any printed volume (book or thesis) of which they are the author(s)." SHERPA/RoMEO: "Publisher's version/PDF cannot be used."

Elsevier (Reddy-Alla et al., *Neuron* 2017): "As an Elsevier journal author, you have the right to Include the article in a thesis or dissertation (provided that this is not to be published commercially) whether in full or in part, subject to proper acknowledgment; see the Copyright page for more information. No written permission from Elsevier is necessary. This right extends to the posting of your thesis to your university's repository provided that if you include the published journal article, it is embedded in your thesis and not separately downloadable." (Source: https://www.elsevier.com/about/policies/copyright/permissions)

John Wiley and Sons (Böhme et al., *FEBS Letters* 2018): I have acquired the right to reuse this publication non-commercially in print and electronic form through license number 4747050813038 (copyright.com). SHERPA/RoMEO: "Publisher's version/PDF cannot be used."

Springer Nature (Böhme et al., *Nature Communications* 2019): "This is an open access article distributed under the terms of the Creative Commons CC BY license, which permits unrestricted use, distribution, and reproduction in any medium, provided the original work is properly cited. You are not required to obtain permission to reuse this article." SHERPA/RoMEO: "Author can archive publisher's version/PDF."

National Academy of Sciences (Schuhmacher et al., *PNAS* 2020): "PNAS authors need not obtain permission for the following cases: (…) to include their articles as part of their dissertations." SHERPA/RoMEO: "Publisher's version/PDF may be used"

eLife (Kobbersmed et al., *eLife* 2020): "This article is distributed under the terms of the Creative Commons Attribution License (CC BY 4.0), which permits unrestricted use and redistribution provided that the original author and source are credited." The version used here is an author layout of the accepted manuscript and not the PDF version offered by the publisher.

2.3 Publication I: Böhme et al., Nature Neuroscience 2016

Full bibliographical reference

Böhme MA*, Beis C*, Reddy-Alla S*, Reynolds E*, Mampell MM, Grasskamp AT, Lützkendorf J, Bergeron DD, Driller JH, Babikir H, Göttfert F, Robinson IM, O'Kane CJ, Hell SW, Wahl MC, Stelzl U, Loll B, Walter AM, Sigrist SJ (2016) - *Active zone scaffolds differentially accumulate Unc13 isoforms to tune Ca^{2+} channel–vesicle coupling*, Nature Neuroscience 19(10):1311–1320. doi:10.1038/NN.4364. * *equal contributions*

Permalink: https://doi.org/10.1038/nn.4364

Author contributions

M.A.B., S.R.-A., A.M.W. and S.J.S. conceived the project. M.A.B. and M.M.M. performed all confocal and in vivo imaging experiments and analyzed the data. M.A.B. performed STED experiments and analyzed the data. C.B., S.R.-A. and E.R. performed all electrophysiological experiments, and C.B. and E.R. analyzed the data. J.L., U.S. and J.H.D. performed and analyzed Y2H experiments. M.C.W. and B.L. contributed to the Y2H experiments and analysis. C.B. and D.D.B. performed HPF experiments and C.B. analyzed the data. **A.T.G. performed modeling and simulation**. H.B. and M.M.M. created antibodies and isoform-specific mutants. I.M.R. and C.J.O. performed the EMS screen. F.G. and S.W.H. developed and built the STED microscope. M.A.B., A.M.W. and S.J.S. wrote the paper with input from all coauthors.

Contribution details

For the work shown in this publication, I combined simulations of spatial and temporal calcium dynamics (using the tool CalC developed by Victor Matveev, see Matveev et al., 2002) in the presynaptic terminal with a mathematical model that describes calcium-driven SV release. I integrated the automated use of CalC into several MATLAB scripts and simulated postsynaptic measurements of electrical stimulation of the motoneuron, as they were acquired by my colleagues in electrophysiological two-electrode voltage clamp experiments. Optimizing parameters of SV release, like the coupling distance of SVs to the AZ center and the influx of calcium into the presynapse, and repetitively comparing my simulations to the measurements of my colleagues, I found that these measurements could be explained by the existence of two distinct SV release pathways. These findings were made stronger by the fact that the model could not only explain the wildtype situation, but also reproduced findings from a mutant lacking the Unc13A isoform. The distances of these release pathways to the AZ center matched with findings from super-resolution STED microscopy. In conclusion, this work enabled the development of a model describing the position of two SV release pathways at the *Drosophila* synapse mediated by two isoforms of the protein Unc13. The results of this computational study are shown in Figure 7, panels b-j.

2.4 Publication II: Reddy-Alla et al., Neuron 2017

Full bibliographical reference

Reddy-Alla S*, Böhme MA*, Reynolds E, Beis C, Grasskamp AT, Mampell MM, Maglione M, Jusyte M, Rey U, Babikir H, McCarthy AW, Quentin C, Matkovic T, Bergeron DD, Mushtaq Z, Göttfert F, Owald D, Mielke T, Hell SW, Sigrist SJ, Walter AM (2017) - *Stable Positioning of Unc13 Restricts Synaptic Vesicle Fusion to Defined Release Sites to Promote Synchronous Neurotransmission*, Neuron 95(6):1350-1364.e12. doi:10.1016/J.NEURON.2017.08.016. * *equal contributions*

Permalink: https://doi.org/10.1016/j.neuron.2017.08.016

Author contributions

S.R.-A., M.A.B., S.J.S., and A.M.W. conceived the project. M.A.B., M.M.M., M.J., and U.R. performed confocal and in vivo imaging experiments and analyzed the data. **A.T.G.** and M.J. **performed GCaMP experiments and analyzed the data.** M.A.B. performed STED experiments and M.A.B. and **A.T.G. analyzed the data.** S.R.-A., E.R., C.B., M.J., and Z.M. performed electrophysiological experiments and E.R., C.B., M.J., A.W.M., and Z.M. analyzed the data. M.A.B., C.B., C.Q., D.D.B. and T.M. performed HPF experiments, and C.B., **A.T.G.**, and M.M. **analyzed the data**. M.M.M., H.B., T.M., and D.O. created cDNA constructs. F.G. and S.W.H. developed and built the STED microscope. S.R.-A., M.A.B., S.J.S., and A.M.W. wrote the paper with input from all co-authors.

Contribution details

For this paper, we collaborated with several groups in determining the essential synaptic release factor Unc13 as a protein that defines the site of SV release. To achieve this, we combined genetics, electrophysiology, high resolution STED- and electron microscopy, and live-imaging of SV release events with single AZ resolution. To support the findings of this publication, I (together with my colleague Meida Jusyte) performed live-imaging of individual SV release events using a green fluorescent calcium indicator (GCaMP5G) that was expressed only in the postsynaptic muscle and genetically targeted to the muscle membrane. Correlating the number of individual SVs released at single AZs with the AZ levels of several proteins, I found that Unc13A, BRP, and Syx1A, but not Unc18, scale with levels of evoked SV release at the average *Drosophila* synapse (Figure 1, panels I-L). I further determined that the genetic removal of the Unc13A protein decreased the dependence of spontaneous and evoked SV release on the BRP scaffold, matching the notion of Unc13 as the release site determining factor (Figure 2, all panels). My experimental work was essential to fulfill the requirements set by the reviewers during the peer-review process. Furthermore, I performed essential computational analysis of (1) STED imaging data to show the position of Unc13A labels in relation to BRP/RBP (Figure 3, panel A) and of (2) EM imaging data to quantify the distribution and amount of docked vesicles in control animals and genetic mutants lacking the N-term of Unc13A (Figure 4, panels O-S).

page intentionally left blank

2.5 Publication III: Böhme et al., FEBS Letters 2018

Full bibliographical reference

Böhme MA, Grasskamp AT, Walter AM (2018) - *Regulation of synaptic release-site Ca^{2+} channel coupling as a mechanism to control release probability and short-term plasticity*, FEBS letters 592(21):3516–3531. doi:10.1002/1873-3468.13188.

Permalink: https://doi.org/10.1002/1873-3468.13188

Author contributions

M.A.B. and A.M.W. conceptualized and wrote the manuscript with contributions from A.T.G. Additionally, A.T.G. performed all protein sequence alignments, and simulated synaptic Ca^{2+} dynamics and SV release.

Contribution details

In this review, we compiled and discussed the findings of numerous research groups regarding the factors determining the coupling distance between SVs and Ca^{2+} channels. This synaptic property contributes to the capability of the synapse to scale SV release levels under rapid and sustained stimulation, a process known as synaptic short-term faciliation (STF). By comparing how functional domains of proteins involved in several steps of SV exocytosis are evolutionarily conserved in vertebrates and invertebrates, and by simulating the influence of varying coupling distances on synaptic short-term plasticity, we aimed to provide an overview of the relevant recent research.

For this publication, I performed work on two separate computational topics. Firstly, I generated the protein sequence alignments shown in Figure 1 and Figure 5 using Clustal Omega (Madeira et al., 2019) to determine and visualize the evolutionary conservation of functional domains between human Munc13-1, RIM1, RIM-BP2, ELKS1 and $Ca_v2.1$, and their homologues in three other species (*M. musculus*, *C. elegans* and *D. melanogaster*). Secondly, I performed the simulations shown in Figure 2 based on the model developed for Böhme et al., 2016. Expanding on the former findings, I could show the influence of different coupling distances on SV release probabilities, intracellular calcium transients and short-term plasticity of release. This contribution makes up 3 of the 5 figures in this review. In addition, I aided in the progress of the review by finding adequate sources and writing parts of the text.

2.6 Publication IV: Böhme et al., Nature Communications 2019

Full bibliographical reference

Böhme MA*, McCarthy AW*, Grasskamp AT, Beuschel CB, Goel P, Jusyte M, Laber D, Huang S, Rey U, Petzoldt AG, Lehmann M, Göttfert F, Haghighi P, Hell SW, Owald D, Dickman D, Sigrist SJ, Walter AM (2019) - *Rapid active zone remodeling consolidates presynaptic potentiation*, Nature Communications 10(1085). doi:10.1038/S41467-019-08977-6. * *equal contributions*

Permalink: https://doi.org/10.1038/s41467-019-08977-6

Author contributions

M.A.B., S.J.S. and A.M.W. conceived the project. M.A.B., A.W.M., C.B.B., P.G. and A.G.P. performed fly husbandry and maintenance. M.A.B., M.J., M.L. and P.G. performed confocal and/or STED imaging experiments and M.A.B., P.G. and **A.T.G. analyzed the data**. A.W.M., M.J. and P.G. performed electrophysiological experiments and analyzed the data. U.R. performed live-imaging experiments and analysis. P.H. provided reagents and suggested additional experiments. **A.T.G** and A.M.W. **developed software codes for image alignment and averaging and A.T.G analyzed the data**. P.G. and D.D. conceived and performed translation block experiments. C.B.B. performed adult Drosophila brain antibody staining and imaging. C.B.B. and S.H. performed behavioral experiments and data analysis. S.H. performed Western blots. D.L. and D.O. planned and performed in vivo two-photon live calcium imaging. F.G. and S.W.H. developed and built the STED microscope. M.A.B., S.J.S., and A.M.W. wrote the paper with input from all co-authors.

Contribution details

My contribution to this study was a purely computational effort. I translated work initiated by Alexander M. Walter in ImageJ/Fiji to MATLAB code. Based on this, I developed several distinct methods to show the underlying geometry of different proteins at the active zone. One of those methods was used to generate the data shown in Figure 2, all panels except panel a. To acquire the number of clusters and the average geometry in one category, several hundred images were loaded into MATLAB and categorized by the number of found clusters, or local maxima of fluorescence intensity. Within one category, all cluster positions were then altered by rotation around the image center such that the distances between clusters were minimal. This involved the development of an optimization procedure using a genetic algorithm, which improves outcomes through mechanisms supposed to resemble evolution. Applying the determined optimal rotation angles to the original images, and generating an average projection of the rotated images then revealed the shown geometrical series. Furthermore, this method was used to determine the differences in cluster numbers between control animals and those treated with the use-dependent glutamate receptor blocker PhTx. The increase in cluster numbers upon PhTx treatment in wild type animals, and upon glutamate receptor deletion in mutant animals, supports the observations of plastic synaptic adaptations from other forms of image analysis and electrophysiological experiments performed by my colleagues.

nature COMMUNICATIONS

ARTICLE

https://doi.org/10.1038/s41467-019-08977-6 OPEN

Rapid active zone remodeling consolidates presynaptic potentiation

Mathias A. Böhme[1,2,3], Anthony W. McCarthy[1], Andreas T. Grasskamp[1,2], Christine B. Beuschel[2,3], Pragya Goel[4], Meida Jusyte[1], Desiree Laber[5], Sheng Huang[3], Ulises Rey[3,6], Astrid G. Petzoldt[3], Martin Lehmann[1], Fabian Göttfert[7], Pejmun Haghighi[8], Stefan W. Hell[7], David Owald[5], Dion Dickman[4], Stephan J. Sigrist[2,3] & Alexander M. Walter[1]

Neuronal communication across synapses relies on neurotransmitter release from presynaptic active zones (AZs) followed by postsynaptic transmitter detection. Synaptic plasticity homeostatically maintains functionality during perturbations and enables memory formation. Postsynaptic plasticity targets neurotransmitter receptors, but presynaptic mechanisms regulating the neurotransmitter release apparatus remain largely enigmatic. By studying *Drosophila* neuromuscular junctions (NMJs) we show that AZs consist of nanomodular release sites and identify a molecular sequence that adds modules within minutes of inducing homeostatic plasticity. This requires cognate transport machinery and specific AZ-scaffolding proteins. Structural remodeling is not required for immediate potentiation of neurotransmitter release, but necessary to sustain potentiation over longer timescales. Finally, mutations in Unc13 disrupting homeostatic plasticity at the NMJ also impair short-term memory when central neurons are targeted, suggesting that both plasticity mechanisms utilize Unc13. Together, while immediate synaptic potentiation capitalizes on available material, it triggers the coincident incorporation of modular release sites to consolidate synaptic potentiation.

[1] Leibniz-Forschungsinstitut für Molekulare Pharmakologie (FMP), 13125 Berlin, Germany. [2] NeuroCure Cluster of Excellence, Charité Universitätsmedizin, 10117 Berlin, Germany. [3] Institute for Biology/Genetics, Freie Universität Berlin, 14195 Berlin, Germany. [4] Department of Neurobiology, University of Southern California, Los Angeles, CA 90089, USA. [5] Institut für Neurophysiologie, Charité Universitätsmedizin, 10117 Berlin, Germany. [6] Department of Theory and Biosystems, Max Planck Institute of Colloids and Interfaces, Science Park Golm, 14424 Potsdam, Germany. [7] Department of Nanobiophotonics, Max Planck Institute for Biophysical Chemistry, 37077 Göttingen, Germany. [8] Buck Institute for Research on Aging, Novato, CA, USA. These authors contributed equally: Mathias A. Böhme, Anthony W. McCarthy. These authors jointly supervised this work: Stephan J. Sigrist, Alexander M. Walter. Correspondence and requests for materials should be addressed to S.J.S. (email: stephan.sigrist@fu-berlin.de) or to A.M.W. (email: awalter@fmp-berlin.de)

Neurotransmitter-laden synaptic vesicles (SVs) release their content at presynaptic active zones (AZs) in response to Ca^{2+} influx through voltage gated channels that respond to action-potential (AP) depolarization. Neurotransmitter binding to postsynaptic receptors subsequently leads to their activation for synaptic transmission. Modulation of transmission strength is called synaptic plasticity. Long-term forms of synaptic plasticity are major cellular substrates for learning, memory, and behavioral adaptation[1,2]. Mechanisms of long-term synaptic plasticity modify the structure and function of the presynaptic terminal and/or the postsynaptic apparatus. AZs are covered by complex scaffolds composed of a conserved set of extended structural proteins. ELKS/Bruchpilot (BRP), RIM, and RIM-binding protein (RBP) functionally organize the coupling between Ca^{2+}-channels and release machinery by immobilizing the critical (M)Unc13 release factors in clusters close to presynaptic Ca^{2+}-channels and thus generate SV release sites, at both mammalian and *Drosophila* synapses[3–12]. Whether and how discrete AZ release sites and the associated release machinery are reorganized during plastic changes remains unknown.

One crucial form of presynaptic plasticity is the homeostatic control of neurotransmitter release. This process, referred to as presynaptic homeostatic potentiation (PHP), is observed in organisms ranging from invertebrates to humans, but is perhaps best illustrated at the larval neuromuscular junction (NMJ) of *Drosophila melanogaster*[13,14]. Here, PHP requires the core AZ-scaffolding proteins RIM, RBP and Fife[15–17] and physiologically coincides with the upregulation of SV release sites[17,18]. Yet it is unknown how these AZ-scaffolds mediate release site addition, which downstream molecules are needed for PHP, whether AZ-scaffold independent reactions occur, and whether these mechanisms extend to other forms of plasticity, e.g., during learning in the central nervous system.

Here, we combine genetic and electrophysiological analysis to reveal a molecular sequence that triggers structural remodeling of AZ scaffolding proteins (BRP/RBP), and which ultimately leads to Unc13 addition within minutes. Using super-resolution light microscopy, we identify a modular AZ nano-architecture built by these proteins (which correspond to SV release sites) that rapidly extends by incorporating additional modules for plasticity. This rapid remodeling critically depends on the core AZ scaffolding proteins RBP/BRP, but neither on the early AZ assembly factors Liprin-α/Syd-1, nor on RIM or Fife. Additionally, AZ-remodeling was abolished in transport mutants previously shown to promote BRP/RBP transport. Strikingly, rapid addition of AZ nano-clusters was not required for the immediate expression of PHP on a minutes' timescale, but was essential to sustain potentiation thereafter. We identify Unc13A as a direct molecular target for PHP in experiments where Unc13A was delocalized from the AZ scaffolds. This mutant displayed sizable synaptic transmission but completely lacked PHP and AZ-remodeling. The same interference in mushroom body Kenyon cells of the *Drosophila* brain eliminated short-term memory, indicating that Unc13A is also a plasticity target in the central nervous system. In summary, we show that synapses capitalize on the available AZ material for immediate potentiation, but coincidently undergo release site addition via modular building blocks to consolidate stable synaptic potentiation. Thus, our work lays a foundation that will help to understand the mechanisms of a likely conserved presynaptic plasticity process that is important for dynamically adjusting and stabilizing neurotransmission across multiple timescales.

Results

Homeostatic plasticity regulates AZ protein levels. As a robust paradigm for assessing presynaptic plasticity over different time scales, we focused on PHP, which is well characterized at *Drosophila* NMJs[13]. To induce plasticity on a timescale of minutes, postsynaptic ionotropic glutamate receptors were partially blocked using the non-competitive open-channel blocker Philanthotoxin-433 (PhTx)[19] (Fig. 1a–d). This reduces postsynaptic sensitivity to neurotransmitter release from single SVs (reflected in a reduction of the amplitude of spontaneously occurring "minis", single SV fusion events, Fig. 1b). Initially, this also leads to a proportional decrease in AP-evoked transmission, but in under 10 min, PHP increases the number of SVs released per AP (quantal content). This compensates for the postsynaptic interference, resulting in AP-evoked transmission comparable to baseline levels (Fig. 1b)[19]. To identify molecular adaptations during plasticity, we investigated whether the levels of any of the evolutionarily conserved AZ proteins were altered. We accordingly immunostained against BRP, RBP, Unc13A (we focused on Unc13A, the Unc13 isoform dominating evoked SV release at *Drosophila* NMJ synapses[4]; flybase: unc-13-RA), Syx-1A, Unc18, and Syd-1 (as motoneuronally expressed Syd-1-GFP) (Fig. 1c; Supplementary Fig. 1a). In agreement with previous observations[18,20], we found that 10 min of PhTx treatment increased AZ BRP-levels by about 50% (Fig. 1c, d). In addition, we found that RBP, Unc13A, and Syx-1A increased by about 30%, 60%, and 65%, respectively (Fig. 1c, d). The AZ levels of RBP/BRP, Unc13A/BRP, and Syx-1A/BRP scaled proportionally over all AZ sizes (Supplementary Fig. 1b; Ctrl, black lines). This proportionality was preserved upon PhTx treatment (Supplementary Fig. 1b; PhTx, blue lines). Notably, the AZ-levels and distribution of the essential Sec1/(M)Unc18 family protein Unc18—which was recently found to function in PHP[21]—were unaffected (Fig. 1c, d), demonstrating specific up-regulation of a subset of AZ proteins. Another AZ protein, the assembly factor Syd-1, even displayed a slight reduction upon PhTx (Supplementary Fig. 1a), further underscoring a high degree of specificity.

To verify that these AZ-adaptations were specific to functional glutamate receptor interference, and to address their relevance over a longer time window, we investigated larvae bearing mutations in a glutamate receptor subunit (Fig. 1e–h). Deletion of the high-conductance receptor subunit IIA (GluRIIA) resulted in a similarly reduced postsynaptic sensitivity to single SV fusion events (Fig. 1f) as PhTx treatment (Fig. 1b). Because under these circumstances PHP also increases quantal content to achieve similar AP-evoked transmission (Fig. 1f), *gluRIIA* mutants have extensively been used to investigate long-term PHP (over the 3–4 days of larval development)[22,23]. Immunostainings against BRP, RBP, Unc13A, and Syx-1A confirmed their (in this case larger) elevation on this longer timescale (compare Fig. 1g, h with 1c, d) (100%, 70%, 400% and 200%, respectively, compared to 50%, 30%, 60%, and 65% upon PhTx treatment). Unlike the stoichiometric increase observed for BRP/Unc13A within minutes, this long-term PHP revealed enhanced Unc13A AZ-incorporation (Supplementary Fig. 1c). Another distinction was a remarkable reorganization and eight-fold increase of Unc18 (Fig. 1g, h; Supplementary Fig. 1d, e). Our data hence imply that considerable AZ restructuring occurs within minutes of PHP induction, which is further enhanced across longer-lasting timescales.

Rapid addition of release site modules during PHP. We next sought to investigate how the altered levels of AZ proteins during PHP affected their nanoscopic topology by super-resolution STED microscopy (*x-y* resolution ~30–40 nm). As noted before, planar AZs revealed clearly distinguishable individual Unc13A/BRP/RBP spots arranged in a ring-like geometry[4–7] (Fig. 2a). It was recently shown by single molecule imaging that these individual clusters likely contain several (probably few tens of)

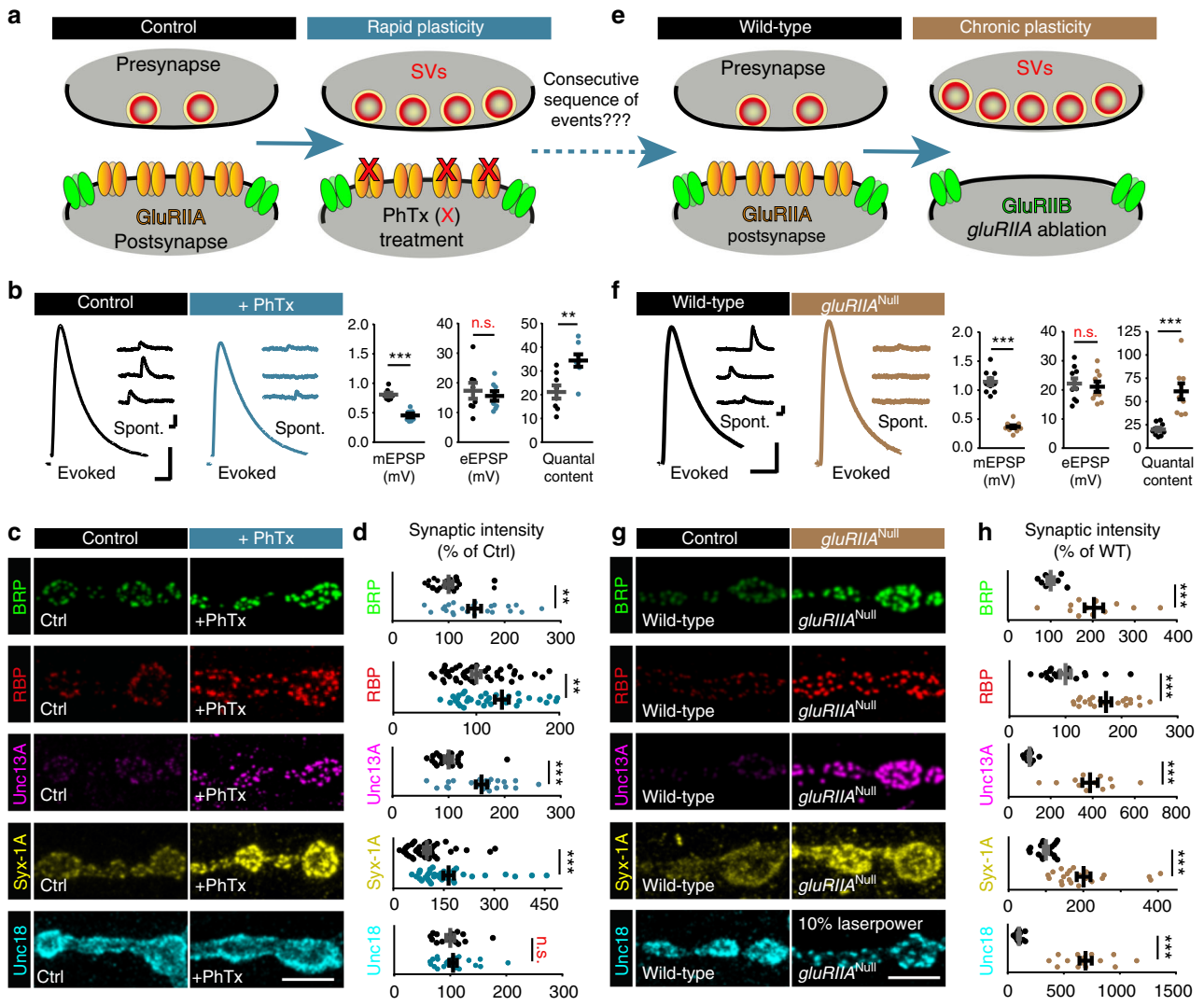

Fig. 1 Rapid homeostatic plasticity regulates AZ protein levels. **a** Sketch of investigated conditions for rapid plasticity: control synapses (left) are compared with rapid plasticity (10 min of PhTx (red "X"); right). Rapid plasticity increases the number of SVs released (red). **b**, **f** Representative traces of eEPSP (evoked), mEPSP (spont.) and their quantification in Ctrl (black) and PhTx (blue) treated (**b**) or wild-type (black) and *gluRIIA*^{Null} (brown) (**f**) cells. **c**, **g** NMJs labelled with indicated antibodies in Ctrl (black) and PhTx (blue) treated (**c**) or in wild-type (black) and *gluRIIA*^{Null} (brown) (**g**) animals. **d**, **h** Quantification of BRP, RBP, Unc13A, Syx-1A, and Unc18 AZ-levels in % of Ctrl in Ctrl (black) and PhTx (blue) treated (**d**) or in % of wild-type (WT) in wild-type (black) and *gluRIIA*^{Null} (brown) (**h**) animals. **e** Sketch of investigated conditions for chronic plasticity: wild-type synapses (left) are compared with *gluRIIA*^{Null} mutants. Chronic plasticity greatly increases the number of SVs released. See also Supplementary Fig. 1. Source data as exact normalized and raw values, detailed statistics including sample sizes and *P* values are provided in the Source Data file. Scale bars: **b**, **f** eEPSP: 25 ms, 5 mV; mEPSP: 50 ms, 1 mV; **c**, **g** 5 µm. Statistics: Student's unpaired *T*-test was used for comparisons in (**b**) and ((**f**) eEPSP) and Mann–Whitney *U* test for all other comparisons. $^{**}P \leq 0.01$; $^{***}P \leq 0.001$; n.s., not significant, $P > 0.05$. All panels show mean ± s.e.m.

molecules in the case of BRP[24]. We detected the number of clusters per AZ in single AZ-images, which was largely heterogeneous for all three proteins, with a simple peak detection algorithm (Fig. 2c–e (black bars)). However, in all cases the cluster number per AZ increased upon PhTx-treatment (Fig. 2c–e (blue bars)), and slightly increased further in *gluRIIA*^{Null} mutants (Supplementary Fig. 2a; brown bars). With increasing AZ-cluster number the AZ diameter (measured from the AZ center to the center of the clusters) also increased in both conditions (Supplementary Fig. 2b, c), consistent with previous STED analysis performed on BRP-rings[18]. Notably, the observed remodeling only affected cluster numbers, and did not alter their intensities (Supplementary Fig. 2b, c). Consequently, the first conclusion of our analysis is that PHP increases the number of Unc13A/BRP/RBP nano-clusters per AZ within minutes.

We also wanted to investigate whether the overall AZ-topology changed upon cluster incorporation. Notably, averaging of STED-images was recently used to generate a three-dimensional model of an average synapse, displaying the mean protein localization at high resolution[25]. Thus, to compare the overall single AZ-topology, AZ images were centered, sorted by the number of clusters, aligned by rotation, and averaged. Two different alignment methods were used. In the first procedure, images were simply rotated such that the cluster with the highest intensity was positioned at the top (Supplementary Fig. 3a and Methods for details). Even though this procedure only targeted a single pixel per image (the position of the brightest cluster), the remaining (lower intensity) clusters were often found in similar relative positions, such that averaging revealed a simple polygonal geometrical series (Supplementary Fig. 3a), demonstrating some

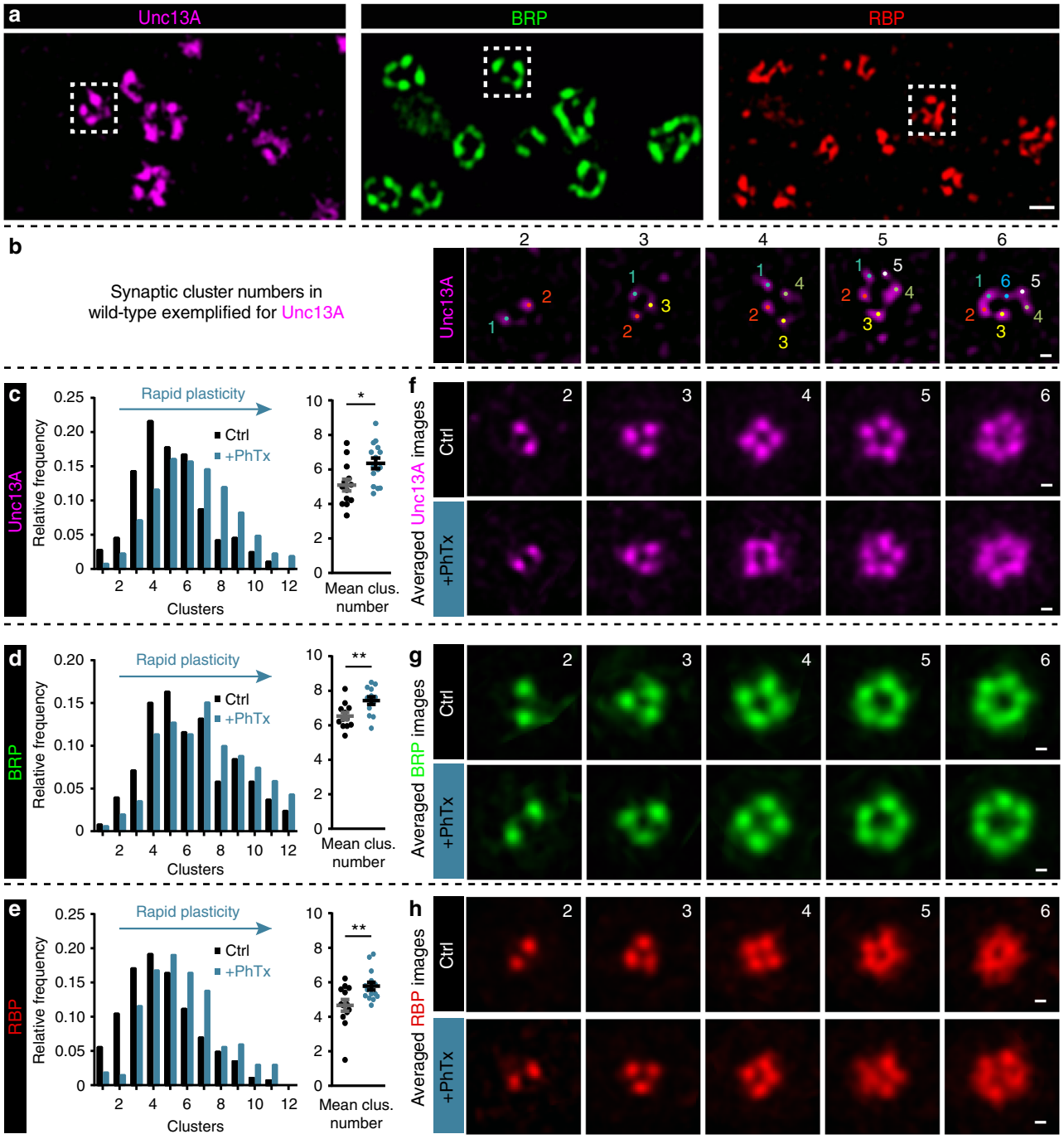

Fig. 2 Rapid plasticity alters Unc13A/BRP/RBP AZ protein cluster number. **a** STED microscopy images containing several AZs with variable numbers of protein clusters of Unc13A (magenta), BRP (green) and RBP (red). Dashed white boxes mark one AZ example used for the cluster number counting. **b** Example AZs with 2–6 Unc13A clusters, marked by colored dots and used for cluster number counting. (**c**–**e**, left) Frequency distribution of Unc13A (**c**), BRP (**d**), and RBP (**e**) modules per AZ either without (Ctrl, −PhTx; black) or with PhTx (+PhTx; blue) treatment. **f**–**h** Average of rotated STED images stained against Unc13A (**f**), BRP (**g**), and RBP (**h**) with 2–6 modules either without (Ctrl) or with PhTx (+PhTx) treatment. See also Supplementary Figs. 2–4. Source data as exact values, detailed statistics including sample sizes and *P* values are provided in the Source Data file. Scale bars: **a** 200 nm; (**b**, **f**–**h**) 50 nm. Statistics: Mann-Whitney *U* test. $^{*}P \leq 0.05$; $^{**}P \leq 0.01$. Panels (**c**–**e**) show NMJ-wise means of AZ-mean ± s.e.m.

regularity. In a more refined analysis, we simultaneously considered the position of all clusters per AZ (Supplementary Fig. 3c and Methods for details) which also revealed a simple geometrical pattern for Unc13A, BRP, and RBP (Fig. 2f–h and Supplementary Fig. 3c). This stereotypical arrangement was best seen for AZs containing two to six clusters but less clear for AZs containing more than that (which could mean that these are less regular; Supplementary Fig. 2d, e). This arrangement was unaltered upon PhTx-treatment or *gluRIIA* ablation (Fig. 2f–h and Supplementary Fig. 4a–c). Notably, the results of these averaging approaches did not necessarily result in specific patterns, as neither random categorization of the single AZ images nor applying this methodology to Syx-1A and Unc18 (which are diffusely distributed at the AZ) resulted in regular but instead in highly irregular/random fluorescence patterns (Supplementary Figs. 3b and 2f, g). This also demonstrates that structural features are only conserved

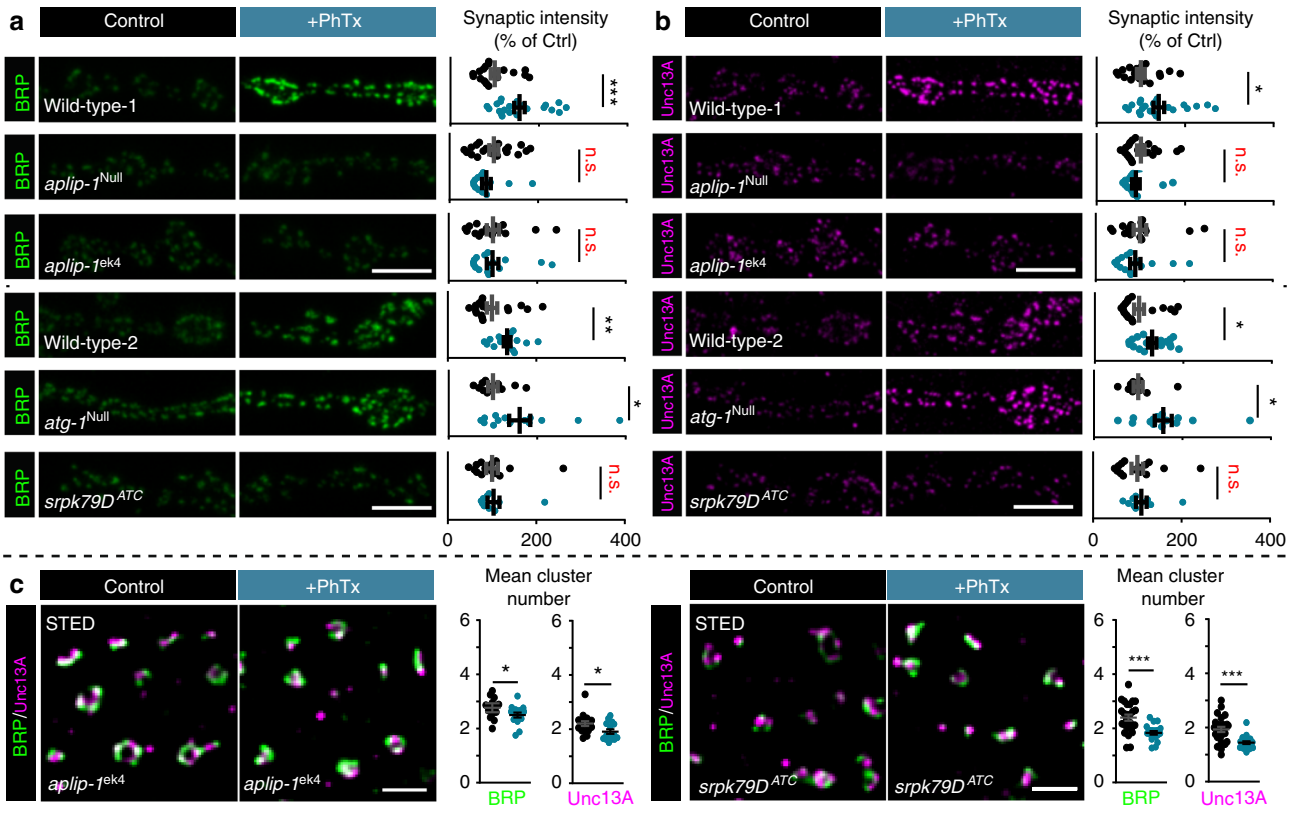

Fig. 3 Rapid AZ-remodeling during PHP requires Aplip-1 and Srpk79D. **a**, **b** Muscle 4 NMJs of segment A2-A5 from third instar larvae and quantification of synaptic levels of wild-type—1, *aplip-1*^{Null}, *aplip-1*^{ek4}, wild-type-2, *atg1* and *srpk79D*^{ATC} labelled with the indicated antibodies without (Ctrl; black) and with 10 min of PhTx (+PhTx; blue) treatment. Two independent experiments were performed, wild-type-1 was used as control for *aplip-1*^{Null} and *aplip-1*^{ek4} while wild-type-2 was used for *atg1*^{Null} and *srpk79D*^{ATC}. **c** Average BRP and Unc13A cluster number per AZ either without (Ctrl, −PhTx; black) or with PhTx (+PhTx; blue) treatment in *aplip-1*^{ek4} and *srpk79D*^{ATC}. See also Supplementary Figs. 5, 6 and Movie 1. Source data as exact normalized and raw values, detailed statistics including sample sizes and *P* values are provided in the Source Data file. Scale bars: **a**, **b** 5 µm; **c** 500 nm. Statistics: Mann-Whitney *U* test. * $P \leq 0.05$; ** $P \leq 0.01$; *** $P \leq 0.001$; n.s., not significant, $P > 0.05$. All panels show mean ± s.e.m.

across AZs containing the same number of clusters. It should be noted that only the average images (Fig. 2f–h; Supplementary Fig. 4) depend on this procedure, while detecting the effects of PhTx or *gluRIIA* ablation on cluster numbers (Fig. 2c–e; Supplementary Fig. 2a) was fully independent of this.

Thus, these findings imply that complexes of the core AZ-scaffold form discrete nano-modular structures, which correspond to SV release sites, and that rapid presynaptic plasticity triggers their fast AZ-incorporation which is even further enhanced over longer-timescales.

Impairing BRP/RBP transport disrupts rapid AZ-remodeling. The remarkable remodeling of AZ material within the short timeframe of PhTx-treatment (minutes) raised the question of how this is mechanistically achieved. We first considered whether local presynaptic protein translation could be required[26]. However, treatment of larvae with 50 µg/ml of the translation blocker cycloheximide (prior and during PhTx-treatment) did not disrupt structural remodeling of BRP or vGlut (vesicular glutamate transporter) at AZs (Supplementary Fig. 5a), consistent with remodeling being translation-independent. Moreover, the functional increase in quantal content remained expressed in the presence of the blocker (Supplementary Fig. 5b), consistent with previous reports[19,20].

Because active kinesin-dependent protein transport is required for long-term homeostatic plasticity in *gluRIIA*^{Null} mutants[27], we asked whether BRP/RBP transport mechanisms might be employed for AZ remodeling. For this, we investigated proteins involved in BRP/RBP transport by their mutation which causes abnormal BRP/RBP accumulation in the moto-neuronal axons, such as Atg1 (Unc-51)[28], serine–arginine (SR) protein kinase at location 79D (Srpk79D[29,30]), and App-like interacting protein (Aplip-1, Jip1 or JNK interacting protein in mammals), a selective RBP transport-adaptor[31] (Fig. 3a, b). While we observed clear PhTx-induced BRP-/Unc13A-upscaling in wild-type controls as well as in *atg1* mutants (Fig. 3a, b), remodeling was fully absent upon null-mutation of *srpk79D*, *aplip-1*[32] or in animals bearing an Aplip-1 point mutation that selectively prevents kinesin light chain interaction (*aplip-1*^{ek4})[33] (Fig. 3a, b). Additionally, STED microscopy revealed that *aplip-1*^{ek4} and *srpk79D*^{ATC} mutants appeared to contain fewer BRP/Unc13A clusters per AZ on average than wild-type (compare Fig. 2c, d with Fig. 3c) and fully lost the capacity to increase cluster numbers upon PhTx-treatment (even a decrease was observed, Fig. 3c). We also discovered that upon motoneuronal Aplip-1 or Srpk79D knock-down, Unc13A-GFP co-accumulated with aberrant axonal BRP aggregates (Supplementary Fig. 5c, d). Interestingly, a partial co-accumulation of BRP/Unc13A-GFP (but to a lower extent in comparison to the knock-downs) was also present in the control situation, in line with an at least partial co-transport that we occasionally observed in live-imaging experiments (Supplementary Fig. 5c–g; Movie 1).

We further wanted to elaborate on the involvement of active protein transport during PhTx-induced AZ-remodeling by interfering with the cytoskeletal tracks used for short-range

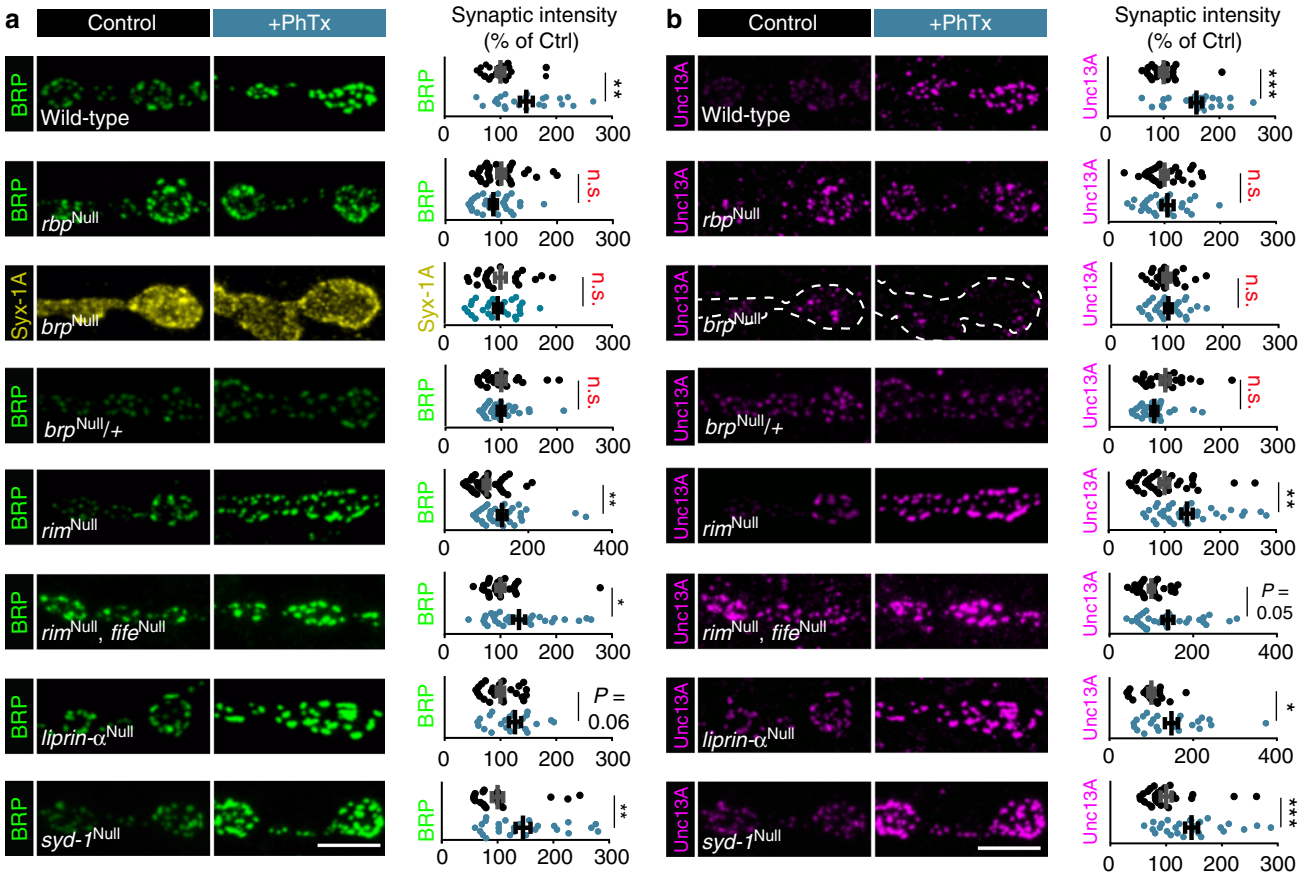

Fig. 4 Rapid AZ-remodeling during PHP requires BRP and RBP. **a**, **b** Confocal images and quantification of synaptic intensities of muscle 4 NMJs of abdominal segment 2–4 from third instar larvae at wild-type, *rbp*^{Null}, *brp*^{Null}, *brp*^{Null}/+, *rim*^{Null}, *rim*^{Null}/*fife*^{Null}, *liprin-α*^{Null}, and *syd1*^{Null} NMJs labelled with the indicated antibodies without (control; black) and with 10 min PhTx (+PhTx; blue) treatment. For wild-type, images and data were adapted and replotted from Fig. 1. Please note, although wild-type controls were performed in parallel to every mutant genotype to check for functional AZ-remodeling upon PhTx-treatment in each set of experiments, we do not show all WT-control here due to space limitations. Therefore, AZ-protein levels should not be compared between genotypes. Source data as exact normalized and raw values (also of additional Wild-type controls for genotypes where PhTx-treatment failed to induce AZ-remodeling), detailed statistics including sample sizes and *P* values are provided in the Source Data file. Scale bars: 5 µm. Statistics: Mann–Whitney *U* test. $^{*}P \leq 0.05$; $^{**}P \leq 0.01$; $^{***}P \leq 0.001$; n.s., not significant, $P > 0.05$. All panels show mean ± s.e.m.

transport using Latrunculin B (an actin polymerization blocker). While the AZ levels of BRP/Unc13A were already slightly enhanced by Latrunculin B treatment (Supplementary Fig. 6a, b), PhTx-treatment failed to induce the typical increase of the AZ levels of these proteins (in fact a reduction was observed, Supplementary Fig. 6a, b). Thus, the actin cytoskeleton and active BRP/RBP transport are required for rapid AZ remodeling.

Rapid homeostatic AZ-remodeling depends on BRP and RBP. We next investigated which of the evolutionarily conserved core AZ scaffolding proteins are required for rapid AZ-remodeling. Loss of RBP fully blocked the rapid, PhTx-induced increase of BRP/Unc13A (Fig. 4a, b). BRP was also essential, because the typical increase in Syx-1A and Unc13A observed upon PhTx treatment was abolished (Compare Fig. 4a, b with Fig. 1c, d). Notably, BRP-amounts appear to be rate-limiting because PhTx-induced AZ-remodeling was blocked in larvae heterozygous for a *brp* null allele (*brp*^{Null}/+) (Fig. 4a, b). In contrast, null mutation of RIM, which abolished PHP[17], did not interfere with AZ-remodeling (Fig. 4a, b). Furthermore, the simultaneous deletion of RIM and Fife (a possible RIM homologue which is required for PHP[15,34]) did not interfere with AZ-remodeling. Thus, RIM and Fife appear to act downstream of BRP/RBP and are non-essential for AZ-remodeling (Fig. 4a, b).

AZ assembly is initiated by the conserved scaffolding proteins Liprin-α and Syd-1, which both regulate AZ size[35–39]. We reasoned that AZ growth —as observed here during plasticity— may capitalize on the same molecular machinery as de novo AZ formation, and therefore tested whether BRP/Unc13A-scaling depended on those proteins. However, *liprin-α*^{Null} and *syd-1*^{Null} mutants revealed normal PhTx-induced BRP/Unc13A-scaling (Fig. 4a, b), indicating that these factors are dispensable. Thus, systematic investigation of evolutionarily conserved AZ scaffolding proteins reveals a selective dependence on the core AZ-scaffolds BRP and RBP for structural remodeling during plasticity.

AZ-remodeling is required for chronic -but not rapid- PHP. Several studies have shown that presynaptic release positively correlates with AZ-size[7,40–43]. Therefore, we expected that the increase of AZ-BRP/Unc13A observed upon PhTx treatment would functionally increase presynaptic release (Fig. 1a–d). However, it is not entirely obvious whether the AZ-remodeling (which continues beyond the minutes' timescale during long-term PHP (Fig. 1e–h)) would be essential for rapid PHP. For instance, loss of RBP was shown to occlude both AZ remodeling (Fig. 4) and the functional increase in quantal content[16], suggesting a pivotal role in both adaptations. Yet PHP and AZ-remodeling do

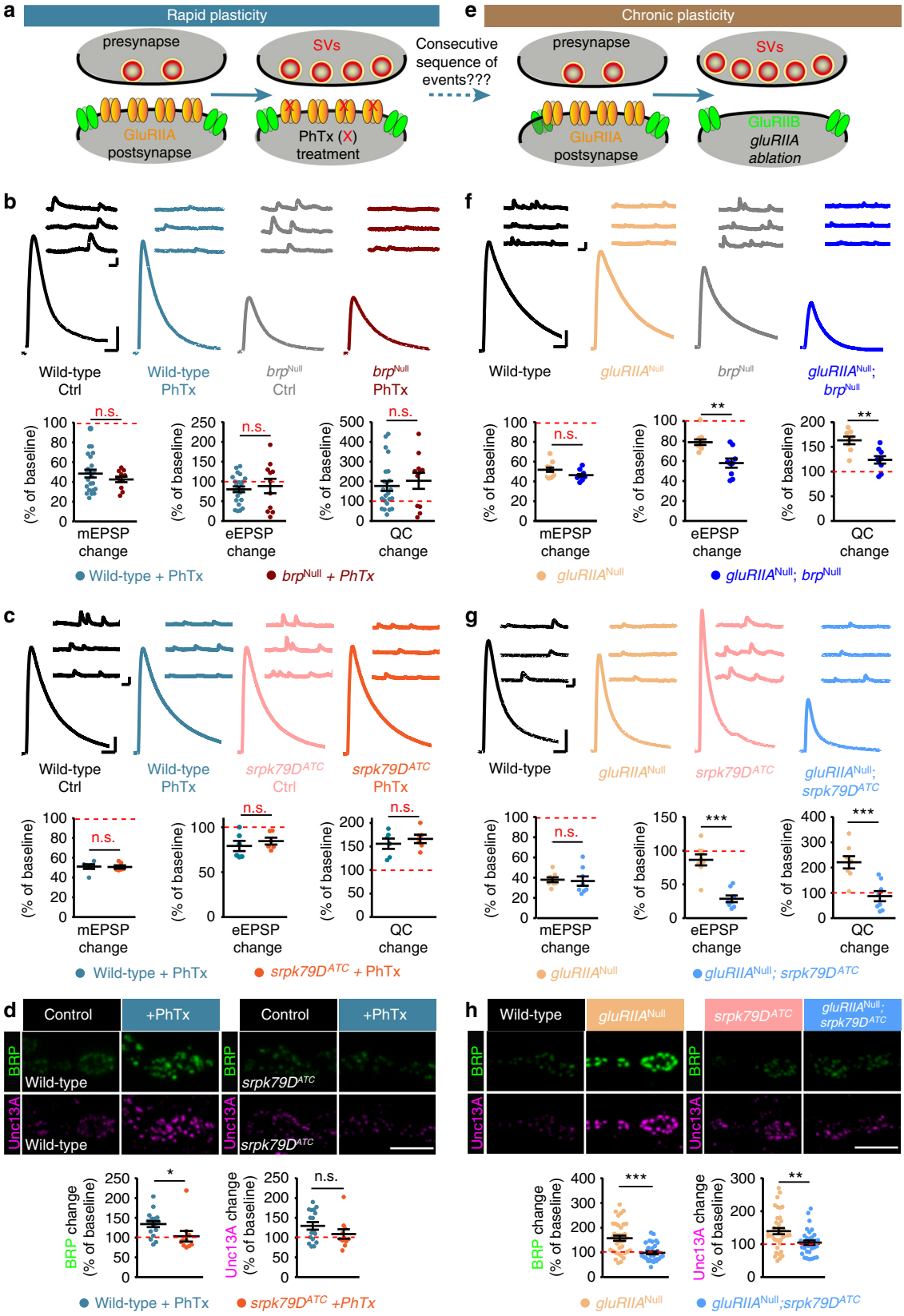

not go hand-in-hand in the case of RIM (and Fife) mutants, whose AZs remodel, but which cannot express PHP (increased quantal content[15,17]). These observations prompted us to systematically investigate the relevance of AZ-remodeling for the rapid induction and sustained expression of PHP.

We first investigated the dependence of rapid PHP on the rapid remodeling of Unc13A/Syx-1A in *brp*^{Null} larvae. Strikingly, AZ-remodeling was blocked (Fig. 4a, b), but functional PHP expression (an increased quantal content) persisted at levels comparable to the wild-type/control situation (Fig. 5a, b). In

Fig. 5 AZ-remodeling sustains NT-release potentiation over longer timescales. **a** Sketch of investigated conditions for rapid plasticity: control synapses (left) are compared with rapid plasticity (10 min of PhTx (red "X"); right). Rapid plasticity increases the number of SVs released (red). **b**, **c** (left) Representative traces of eEPSP (evoked) and mEPSP (spont.) of the indicated genotypes with and without PhTx-treatment. (Right) Quantifications of percentage change of mEPSP amplitude, eEPSP amplitude and quantal content (QC) upon PhTx-treatment. Values are divided by the corresponding measurement in the absence of PhTx for each genotype (dashed red line corresponds to 100%/no change). **d** (left) Confocal images of muscle 4 NMJs of abdominal segment 2–5 from third instar larvae at wild-type and *srpk79D*^{ATC} NMJs labelled with the indicated antibodies without (control; black) and with 10 min PhTx (+PhTx; blue) treatment. (Right) Quantification of percentage change of synaptic BRP and Unc13A levels in wild-type (blue) and *srpk79D*^{ATC} (orange) upon PhTx-treatment compared to baseline of control treatment for each genotype (dashed red line). Data are modified from Fig. 2. **e** Sketch of investigated conditions for chronic plasticity: wild-type synapses (left) are compared with *gluRIIA*^{Null} mutants. Chronic plasticity greatly increases the number of SVs released. **f**, **g** Same as in (**b**, **c**) but compared to baseline of each control genotype. **h** Same as in (**d**) but compared to baseline fluorescence values of wild-type for *gluRIIA*^{Null} and *srpk79D*^{ATC} for *gluRIIA*^{Null};*srpk79D*^{ATC}. See also Supplementary Fig. 7. Source data as exact normalized and raw values, detailed statistics including sample sizes and *P* values are provided in the Source Data file. See also Supplementary Figure 10 and 11 for non-normalized values. Scale bars: eEPSP: 25 ms, 5 mV; mEPSP: 50 ms, 1 mV; **d**, **h** 5 µm. Statistics: Student's unpaired *T*-test was used for comparisons in ((**b**) quantal content change), (**f**), (**g**) and Mann–Whitney *U* test for all other comparisons. $^{*}P \leq 0.05$; $^{**}P \leq 0.01$; $^{***}P \leq 0.001$; n.s., not significant, $P > 0.05$. All panels show mean ± s.e.m.

addition, mutants of Srpk79D (whose AZs also do not undergo PhTx-induced AZ-remodeling; Fig. 3a, b and replotted in Fig. 5d) were likewise able to increase their quantal content (Fig. 5c), showing that AZ remodeling can be uncoupled from rapid PHP expression. Thus, even though AZ-remodeling occurs on a similar time-scale, it is not required to rapidly enhance the quantal content in these cases.

We next investigated whether elevation of the AZ protein levels was required to consolidate the increased quantal content over chronic time-scales in *gluRIIA*^{Null} mutants (Fig. 5e–h). Indeed, PHP was severely impaired in *brp*^{Null}, *gluRIIA*^{Null} double mutants (Fig. 5f). In an otherwise wild-type background, the increase in quantal content (upon *gluRIIA*-null mutation) was much larger than when BRP was additionally deleted (Fig. 5f). We could ensure that the impairment was not due to the overall reduced release in *brp*^{Null} mutants, as a loss to compensate for the *gluRIIA* ablation was also seen in *srpk79D*^{ATC} mutants (which had synaptic transmission comparable to wild-type cells (Fig. 5g), no AZ-remodeling upon PhTx-treatment (Fig. 3a, b), intact PHP upon PhTx-treatment (Fig. 5c) and severely impaired PHP expression in *gluRIIA*^{Null} (Fig. 5g)). Importantly, AZ-remodeling was also fully blocked in *gluRIIA*^{Null}; *srpk79D*^{ATC} double mutants (Fig. 5h). An intermediate behavior was seen in the case of the *aplip-1*^{ek4} mutant, (Supplementary Fig. 7), possibly because other transport adapters might compensate in this situation. Together, this suggests that PHP rapidly increases neurotransmitter release through modulation of the available AZ components, but in addition immediately induces AZ-remodeling to ensure its consolidation.

Presynaptic potentiation requires Unc13A. We next sought to identify the molecular substrate of PHP. Previous experiments established a requirement for the α1 subunit of the voltage gated Ca^{2+}-channel Cacophony (Cac)[19,44]. In line with this, the levels of Cac as well as the Ca^{2+}-influx increase upon PhTx treatment (Fig. 6a, b)[44,45]. We furthermore investigated Unc13A. A slight PhTx-induced BRP-/RBP-scaling persisted upon Unc13A loss, but was weaker than in the wild-type situation (Fig. 6a, b), possibly due to slightly elevated BRP/RBP-AZ-levels already in the non-PhTx-treated *unc13A*^{Null} situation[4]. Notably, Cac-levels were still increased, even to a slightly larger extent than in the wild-type situation (Fig. 6a, b). However, functional PHP, the increase in quantal content, was completely lost (Fig. 6c, d). This indicates that Unc13A—like RIM and RBP[16,17]—plays an essential role in the plastic enhancement of NT release during PHP.

Rapid PHP and learning rely on the Unc13A N-terminus. The observation that Unc13A is essential for PHP is fully consistent with the previous findings that RIM and RBP are required[16,17], because these proteins likely function in Unc13A AZ recruitment and activation (see discussion). As in other species (*M. musculus*/*C. elegans*), this interaction depends on the (M)Unc13 N-terminus[4,46–50]. To investigate the functional relevance of the Unc13A N-terminus for rapid PHP and AZ-remodeling, we used an Unc13A mutant lacking the N-terminal AZ-localization sequence (named C-term-GFP; Fig. 6e), which uncouples Unc13A from the central BRP/RBP scaffold[7] (and therefore supposedly also uncouples SV fusion from a possible regulatory function of RIM —see discussion). Importantly, the magnitude of AP-evoked synaptic transmission in these mutants was largely restored compared to the detrimental effect of *unc13*^{Null} mutation (compare Fig. 6h (C-term-GFP; grey traces) with Fig. 6h (full-length Unc13A-GFP; black traces) and ref. [7]). However, in contrast to control larvae (*unc13*^{Null} with full-length Unc13A-GFP rescue; Fig. 6f–i), C-term-GFP mutants (*unc13*^{Null} with C-term-GFP rescue; Fig. 6f–i) completely lacked AZ-remodeling (Fig. 6f, g) (note that BRP levels were already enhanced in the non-PhTx-treated group, Supplementary Fig. 8a, b), Furthermore, unlike in control larvae, no rescue of evoked transmission and no increase in quantal content was seen upon PhTx treatment, indicating that C-term mutants were deficient of functional PHP (Fig. 6h–i). This demonstrates a dependence of PHP on the Unc13A N-terminus.

Although synapses vary tremendously in their excitability, input/output relationship, and transmitter type, the presynaptic release machinery is remarkably conserved in most systems and across species[9]. We wondered whether the principles of rapid presynaptic adaptation of the peripheral nervous system might be utilized in other synapse types and in other forms of plasticity, like the ones involved in learning and memory formation. Because short-term memory functions on timescales comparable to the PhTx-induced rapid homeostatic plasticity[51], we investigated whether the Unc13A C-term mutant also exhibited learning deficits.

We specifically expressed C-term-GFP either alone, or while simultaneously knocking down endogenous full-length Unc13A (Unc13A-RNAi), in mushroom body Kenyon cells (KCs). KC output synapses undergo learning-induced plasticity and are required for the formation of short-term memories[52]. Knock-down of endogenous Unc13A and expression of C-term-GFP were confirmed using antibodies against GFP (labelling C-term-GFP but not endogenous protein) and the Unc13A N-terminus (labelling the endogenous protein but not C-term-GFP where the N-terminal epitope is deleted) (Fig. 7a). Additionally, we confirmed the strong efficacy of the Unc13A-RNAi via Western blot (knock-down in the entire brain using the pan-neuronal elav-Gal4 driver; Supplementary Fig. 9a).

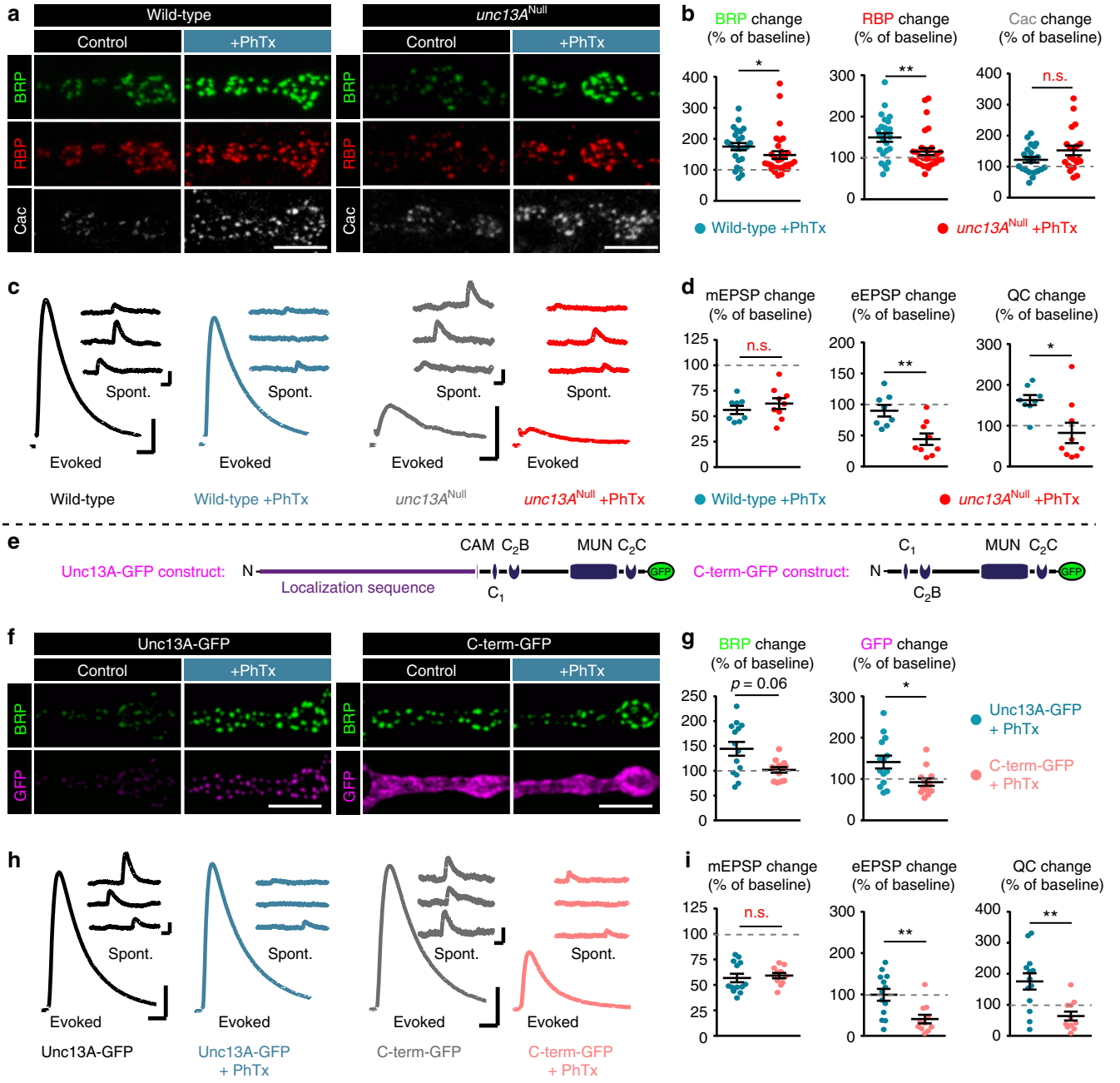

Fig. 6 Unc13A and its N-terminus are critical for rapid PHP and AZ-remodeling. **a** Confocal images of muscle 4 NMJs of abdominal segment 2–5 from 3rd instar larvae at wild-type (left) and *unc13A*^{Null} (right) NMJs labelled with the indicated antibodies without (control; black) and with 10 min PhTx (+PhTx; blue) treatment. **b** Quantification of percentage change of synaptic BRP, RBP and Cac AZ-levels in wild-type (blue) and *unc13A*^{Null} (red) upon PhTx-treatment compared to the same measurement in the absence of PhTx for each genotype (dashed grey line indicates 100%/no change). **c** Representative traces of eEPSP (evoked) and mEPSP (spont.) in wild-type and *unc13A*^{Null} animals without (Ctrl; black or grey) and with 10 min PhTx (+PhTx; blue or light red) treatment. **d** Quantifications of percentage change of mEPSP amplitude, eEPSP amplitude and quantal content (QC) in PhTx-treated wild-type (blue) and *unc13A*^{Null} (light red) cells compared to the same measurement obtained without PhTx for each genotype. Traces for (**c**) were replotted from Fig. 1. **e** Left: Full-length Unc13A construct used in rescue experiments of *unc13*^{Null} animals. Functional domains for AZ localization, Calmodulin- (CAM), lipid-binding (C1, C2B, C2C) and the MUN domain relevant for SV release are shown. Right: Schematic of Unc13A construct lacking the N-terminal localization sequence (C-term-GFP rescue). **f**–**i** Same as in (**a**–**d**) for cells re-expressing Unc13A-GFP (blue) or C-term-GFP (light red) in the *unc13*^{Null} background. See also Supplementary Figure 8. See also Supplementary Figure 10 for non-normalized values. Source data as exact normalized and raw values, detailed statistics including sample sizes and *P* values are provided in the Source Data file. Scale bars: **a**, **f** 5 µm; **c**, **h** eEPSP: 25 ms, 5 mV; mEPSP: 50 ms, 1 mV. Statistics: Student's unpaired *T*-test was used for comparisons in ((**d**) mEPSP, eEPSP change), ((**i**) mEPSP change) and Mann–Whitney *U* test for all other comparisons. $^{*}P \leq 0.05$; $^{**}P \leq 0.01$; n.s., not significant, $P > 0.05$. All panels show mean ± s.e.m.

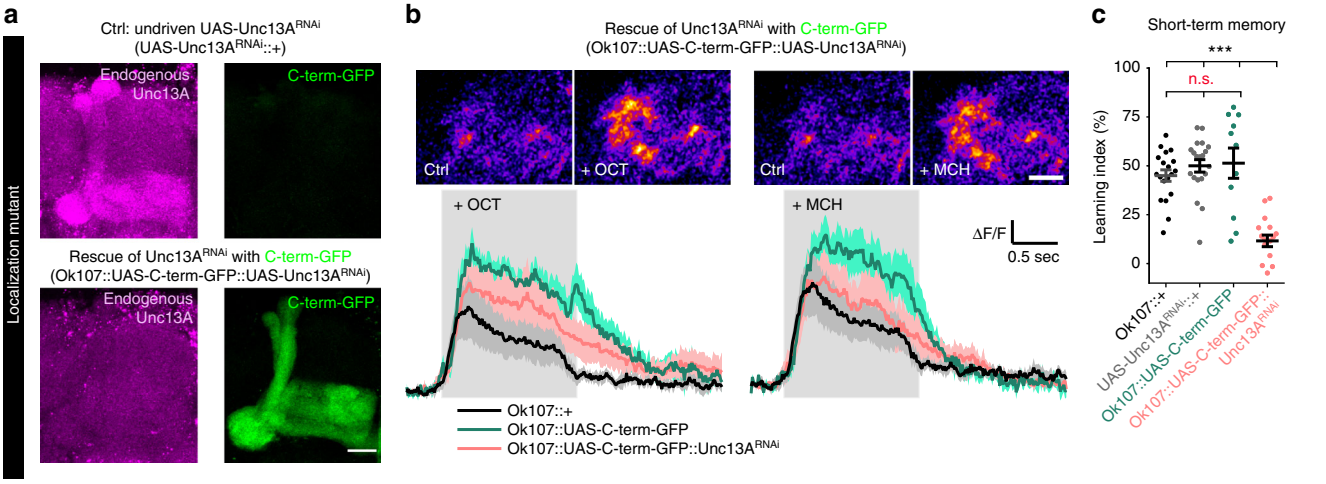

Fig. 7 Mutants incapable of PHP impair short-term memory. **a** Confocal images of adult *Drosophila* mushroom-body regions of control (top; undriven UAS-Unc13A^{RNAi} (UAS-Unc13A^{RNAi}::+)) and rescue of driven UAS-Unc13A^{RNAi} with C-term-GFP (bottom; Ok107::UAS-C-term-GFP::UAS-Unc13A^{RNAi}) brains labelled with the indicated antibodies. **b** Averaged odor responses measured at the level of presynaptic boutons of M4/6 (MBON-β′2 mp/MBON-γ5β′2a/MBON-β2β′2a) mushroom body output neurons (compare ref. [54] or ref. [89]). Above: sample images of two-photon recordings from M4/6 cells (20 frames averaged respectively) before and after odor onset. Grey shading indicates the time at which the odor was applied. Left panels OCT and right MCH response. Below: averaged odor responses. Five responses per odor were averaged per animal. Solid lines show mean responses ($n = 5$–6 animals per genotype). Shaded areas represent the SEM. **c** Short-term memory scores after mushroom body-specific C-term-GFP rescue after Unc13A downregulation via locally driven RNAi expression (Ok107::UAS-C-term-GFP::Unc13A^{RNAi}) compared to controls expressing the driver, but not the RNAi (Ok107::+), the RNAi without driver (UAS-Unc13A^{RNAi}::+) or mushroom body-specific overexpression of the C-term-GFP construct (Ok107::UAS-C-term-GFP). See also Supplementary Fig. 9. Source data as exact raw values, detailed statistics including sample sizes and P values are provided in the Source Data file. Scale bars: **a** 20 µm; **b** 10 µm. Statistics: nonparametric one-way analysis of variance (ANOVA) test, followed by a Tukey's multiple comparison test. ***$P \leq 0.001$; n.s., not significant, $P > 0.05$. All panels show mean ± s.e.m. For representative images experiments were repeated twice with at least 6–7 brains per genotype

Because the C-term-GFP construct largely rescued the detrimental effect of *unc13* null mutation at the NMJ[7], we predicted that general transmission from KCs should be functional for both the C-term-GFP and the C-term-GFP/Unc13A-RNAi conditions. To verify this, we performed in vivo two photon Ca^{2+}-imaging (GCaMP6f) experiments in adult flies to assess odor-evoked responses at the M4/6 (MBON-β′2 mp/MBON-γ5β′2a/MBON-β2β′2a) mushroom body output neurons, a postsynaptic circuit element directly downstream of KCs[53,54]. Indeed, robust Ca^{2+} transients in response to odor stimulation were observed in all genetic constellations tested (Fig. 7b). We conclude as a result that KC output synapses expressing C-term-GFP or C-term-GFP/Unc13A-RNAi are functional under naive conditions. Together with the finding that naive odor avoidance was not statistically different between all these groups (Supplementary Fig. 9b), this allowed us to test whether either condition would interfere with learning and memory.

We assessed short-term memory in adult *Drosophila* using classical aversive olfactory conditioning. Flies were trained by pairing an odor with an electric shock and learning was scored by subsequently assaying avoidance of that odor[55]. All control groups showed similarly robust memory performance, while the relevant C-term-GFP/Unc13A-RNAi mutant (where endogenous Unc13A is knocked down and replaced by the C-term mutant incapable of PHP (Fig. 6e–i)) showed severe short-term memory impairments (Fig. 7c). Whether these impairments are indeed a consequence of the loss of a similar plasticity mechanism as the one observed at the NMJ or whether they are also related to differences in the synaptic transmission profile (e.g., short-term plasticity which is also affected in this mutant[7]) remains to be established. Nevertheless, our data clearly indicate that Unc13A is a target for similar forms of plasticity (Unc13A-RNAi knockdown also impaired short-term memory, Supplementary Fig. 9b, c). Thus, our data imply that structural, functional, and behavioral adaptations are linked and that different forms of presynaptic plasticity may converge on Unc13A.

Discussion

Synapses are able to modify their transmission strength by undergoing plastic changes. This synaptic plasticity is crucial for neuronal circuit adaptation including learning and memory processes[1,56]. Molecular mechanisms for postsynaptic plasticity have been defined in considerable detail[2]. However, presynaptic mechanisms also modulate transmission strength in many synapse types and species[13,51,57]. Homeostatic plasticity is a well-studied form of presynaptic plasticity at the *Drosophila* NMJ where an enhancement of AP-evoked neurotransmitter release counterbalances decreased postsynaptic receptor sensitivity. A number of relevant signaling molecules and pathways, including BMP signaling, CaMKII signaling, TOR signaling, proteasomal degradation, and trans-synaptic signaling are required for this[13,19,58–60]. These factors appear to converge on two principal avenues to enhance presynaptic transmitter release, via increased Ca^{2+} channel amounts and AP-induced Ca^{2+} influx[44,45,61] and secondly via an increase in the number of releasable SVs and their associated release sites[17,18,61]. Nevertheless, some conditions were observed where Ca^{2+} influx or Ca^{2+}-channel levels were increased but the quantal content was not (Fig. 6a–d and ref. [17]), suggesting that release site addition or activation is a required contributor. On the minutes' time-scale, structural AZ-remodeling was observed, yet whether and how this contributes to the enhancement of NT-release remained unclear[18].

In the present study, we uncover a sequence of presynaptic molecular events that mediate AZ-remodeling (Fig. 8). We identify the presynaptic cytomatrix as a highly dynamic structure that can add discrete nano-modules of core proteins within minutes. In the initial phase of this structural remodeling, RBP

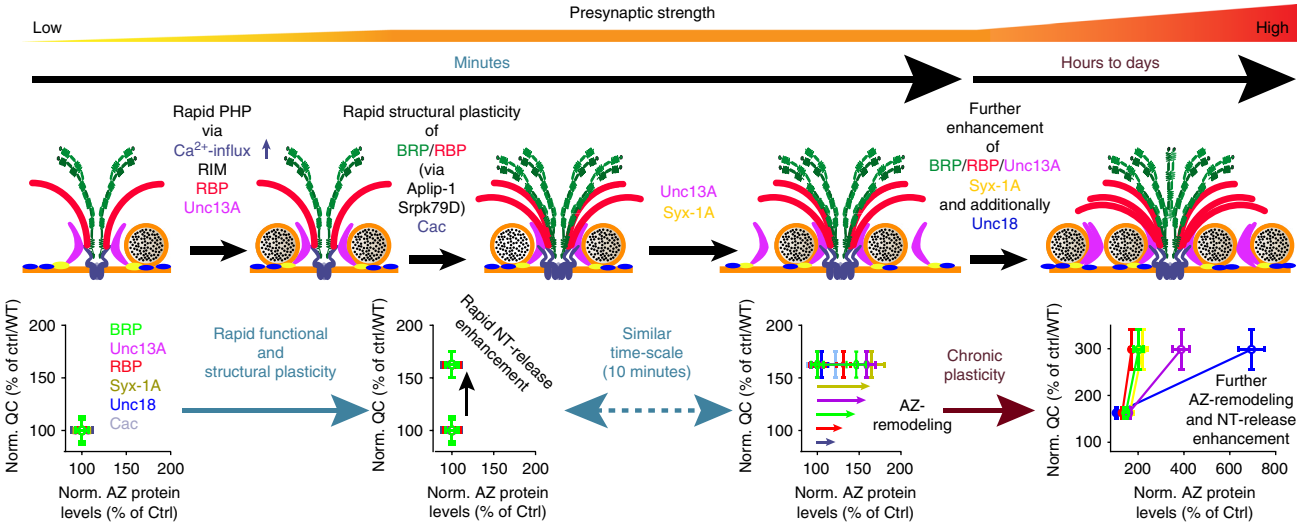

Fig. 8 Sequence of events enabling rapid and sustained homeostatic plasticity Top row: Illustration of AZ modes addressed. Bottom row: Plot of normalized quantal content (QC) vs. AZ protein levels of experiments performed in Fig. 1 normalized to either Ctrl (−PhTx) for rapid plasticity or wild-type for chronic plasticity. In the basal activity mode (left), BRP (green), RBP (red), Syx-1A (yellow), Unc18 (blue) and Unc13A (magenta) provide two SV release sites at the Ca^{2+}-channel (Cac; light blue). However just one release site is active (occupied by SV). (Second left) During the rapid functional plasticity phase the quantal content (and thus neurotransmitter (NT) release) is rapidly enhanced within minutes via mechanisms involving altered Ca^{2+}-influx as well as RIM, RBP and Unc13A. On a comparable time-scale (minutes), BRP and RBP are incorporated in a pre-existing AZ in an Aplip-1/Srpk79D dependent manner and additionally Cac-levels also increase (third cartoon). The BRP/RBP incorporation enhances AZ levels of Unc13A/Syx-1A providing an additional release sites (fourth left). This rapid structural AZ-remodeling is not required for the rapid functional plasticity but directly acts on the consolidation of the release enhancement. (Right) On longer time-scales, chronic plasticity then further enhances the AZ-levels of BRP, RBP, Syx-1A in a conserved stoichiometry, while Unc13A and Unc18 increase out of scale, increasing the number of release sites and thus transmitter release/quantal content activity even further

and BRP are needed as their loss occludes an increase in Syx-1A- and Unc13A levels (Fig. 4). Somewhat unexpectedly, although AZ-remodeling occurs on the same minutes' time-scale, it is dispensable for the rapid potentiation of NT-release during PhTx-induced PHP (e.g., brp^{Null}, $aplip\text{-}1^{ek4}$ or $srpk79D^{ATC}$) (Fig. 6). However, the remodeling is essential for the long-term consolidation of the potentiation (the capacity to restore the AP-evoked response in $gluRIIA^{Null}$ mutants was severely impaired when combined with brp^{Null} or $srpk79D^{ATC}$) (Fig. 6).

Thus, the rapid release enhancement appears to capitalize on AZ-material that is already present, for example by increasing Ca^{2+} influx[44] and by the activation of already present but dormant release sites consistent with PHP depending on RIM, RBP, and Unc13A (refs.[16,17]and this study). Interestingly, the rapid potentiation coincides with the accumulation of BRP, Cac, RBP, Unc13A, Syx-1A, and (later) Unc18 in the AZ, which is required to consolidate and possibly extend the release enhancement. Therefore, the synapse utilizes two coincident programs which together ensure immediate rescue and also supply the synapse with backup-material in the form of BRP/RBP/Unc13A nano-modules in case the disturbance should persist.

Notably, recent work using STED microscopy to characterize hippocampal synapses also identified AZ nano-modules by clusters of Bassoon, vGlut, and Synaptophysin, and observed a scaling of vGlut and Synaptophysin upon chemically induced LTP[62]. This nicely aligns with the structural AZ-remodeling described here, suggesting an evolutionarily conserved process that tunes synaptic transmission by adding nano-modular structures to both sides of the synapse. In addition, activity dependent alterations in Syx-1A nano-clusters were also recently described[63], further pointing to the AZ being a highly dynamic structure which adapts to different environmental demands.

How does the AZ scaffold remodel within minutes? While local protein translation is required for some forms of plasticity[64], acute translation block did not interfere with PhTx induced AZ-remodeling (Supplementary Fig. 5a). However, we found evidence that effective AZ protein transport and a functional cytoskeleton is a precondition here: The BRP/RBP transport adaptor/regulator proteins Aplip-1 and Srpk79D were required for rapid enhancement of BRP/RBP AZ levels (and loss of Aplip-1-mediated BRP/RBP transport impaired short-term memory (Supplementary Fig. 9d, e)). Moreover, acute actin-depolymerization prevented the PhTx-induced BRP/Unc13A addition into AZs, further supporting a crucial role for their transport and in line with a recent study where *Drosophila* Mical, a highly conserved, multi-domain cytoplasmic protein that mediates actin depolymerization, was shown to be necessary for PHP[59].

Considering the short timeframe of this adaptation, long-range transport appears unlikely. Instead, we favor the idea that Aplip-1 and Srpk79D function to engage an AZ-proximal reserve pool of components for rapid integration. This pool could originate from a local reservoir in the distal axon or terminal, or even between AZs, from which plasticity may trigger integration into established AZs[18]. Transport processes may fill or empty the reservoir. Between AZs, the reservoir could be composed of diffusely distributed proteins falling below the detection limit[65], or could reflect a local rearrangement of material (note the reduction of AZs containing few AZ-protein modules after PhTx treatment (Fig. 2c–e) or upon *gluRIIA* ablation (Supplementary Fig. 2a)). Reducing the amount of BRP (by removing one gene copy) blocked the rapid structural adaptation (Fig. 4a, b), possibly because all available material was required to build AZs of proper functionality leaving no material for the reservoir. Regardless of the specific molecular mechanism, guided active transport along the cellular cytoskeleton or rearrangements of the cytoskeleton itself appear to serve a general function in synaptic plasticity in multiple species[59,66–68].

RIM and RBP are established targets for multiple forms of presynaptic plasticity in several synapse types and species[10,16,17,57]. Here, we additionally identified a critical role for

Unc13A (Fig. 6). In fact, with our data we can infer the interrelation between these factors in presynaptic plasticity. RIM proteins are known to activate (M)Unc13s in several species[46–48,69,70]. While *C. elegans* and mouse (M)Unc13 proteins interact via an N-terminal C2A domain with RIM, no such domain is known for *Drosophila*, but the principal functional interaction may well be conserved (via another region of the N-term). This was directly tested by an Unc13A mutant, whose N-term was deleted[7]. This mutant largely rescued the severe loss of synaptic transmission in the *unc13*^{Null} condition with AP-evoked transmission comparable to the full-length Unc13A rescue (compare black with grey traces in Fig. 6h). However, this mutant completely lacked the capacity to undergo PHP, consistent with a required RIM/RBP/Unc13A interplay for plasticity. Furthermore, expressing the same mutant in the *Drosophila* memory center, the mushroom body, severely impaired short-term memory formation (Fig. 7), pointing to a relevance of the RIM/RBP/Unc13 plasticity module in the *Drosophila* central nervous system.

Thus, the morphological and molecular similarities between long-term sensitization in the famous sea slug *Aplysia*, presynaptic LTP in the mammalian brain, and homeostatic plasticity or learning in *Drosophila* indicate that the sequence of molecular events we describe here might be highly conserved.

Methods

Fly husbandry, stocks, and handling. Fly strains were reared under standard laboratory conditions[71] and raised at 25 °C on semi-defined medium (Bloomington recipe). For RNAi experiments flies and larvae were kept at 29 °C. For experiments both male and female third instar larvae or flies were used. The following genotypes were used: Wild-type: +/+ (*w*^{1118}). *gluRIIA*^{Null}: *df(2 L)cl*^{h4}*/df(2 L)gluRIIA&IIB*^{SP22} (A22);*GluRIIB-GFP/+* or *AD9/df(2 L)cl*^{h4} *or gluRIIA*^{SP16}*/gluRIIA*^{SP16}. Supplementary Fig. 1a: Ok6::Syd-1-GFP: *Ok6-Gal4/+;UAS-Syd-1-GFP/+*. Transport mutants: Figs. 3, 5; Supplementary Fig. 7: *aplip-1*^{Null}: *aplip-1*^{ex213}/Df(3L)BSC799; *aplip-1*^{ek4}: *aplip-1*^{ek4}/Df(3L)BSC799; *atg-1: atg1*^{ey07351}*/Df(3L)BSC10*; *srpk79D*^{ATC}: *srpk79D*^{ATC}/srpk79D^{ATC}. Supplementary Fig. 5c: Ctrl: *Ok6-Gal4/+;UAS-Unc13A-GFP/+*; *aplip-1-RNAi*: *Ok6-Gal4/+; UAS-Unc13A-GFP/UAS-Aplip-1-RNAi;* Supplementary Fig. 5d; Ctrl: *Ok6-Gal4/+; UAS-Unc13A-GFP/+*; srpk79D-RNAi: *Ok6-Gal4/+; UAS-Unc13A-GFP/UAS-srpk79D-RNAi*. Intravital imaging: Movie 1 and Supplementary Fig. 5e–g: Ok6/+; UAS-Unc13A-GFP/UAS-BRP-D3-Straw. Figures 4, 5: *rbp*^{Null}: *rbp*^{Stop1}*/rbp*$^{S2.01}$; *brp*^{Null}: *brp*$^{Δ6.1}$*/brp*^{69}; *brp*^{Null}/+: *brp*^{69}/+; *rim*^{Null}: *rim*$^{ex1.103}$/Df(3R)ED5785; *rim*^{Null}, *fife*^{Null}: *rim*$^{ex1.103}$, *fife*^{ex1027}*/rim*$^{ex1.103}$, *fife*^{ex1027}; *liprin-α*^{Null}: *liprin-α*^{F3ex15}*/liprin-α*^{R60}; *syd-1*^{Null}: *syd-1*$^{1.2}$*/syd-1*$^{3.4}$. Figure 5: *gluRIIA*^{Null}, *brp*^{Null}: *gluRIIA*^{SP16}, *brp*$^{Δ6.1}$*/gluRIIA*^{SP16}, *brp*^{69}; *gluRIIA*^{Null}, *srpk79D*^{ATC}: AD9/*df(2L)cl*^{h4}; *srpk79D*^{ATC}*/srpk79D*^{ATC}. Supplementary Fig. 7: *gluRIIA*^{Null};*aplip-1*^{ek4}: AD9/*df(2L)cl*^{h4};*aplip-1*^{ek4}*/Df(3L)BSC799*. Figure 6; Supplementary Fig. 8: *unc13A*^{Null}: *EMS7.5/P84200; For UAS-Cac-GFP in unc13A*^{Null}: *Ctrl: Ok6-Gal4, UAS-Cac-GFP/+*; *unc13A*^{Null}: *Ok6-Gal4, UAS-Cac-GFP/+;;EMS7.5/P84200;* Unc13A-GFP: *elav-GAL4/+;;UAS-Unc13A-GFP/+;P84200/P84200;* C-term-GFP: *elav-GAL4/+;;UAS-C-term-GFP/+; P84200/P84200*. Learning and memory: Fig. 7; Supplementary fig. 9: Ok107::+: *Ok107-Gal4/+*; Ok107::Aplip-1^{RNAi}: *UAS-Aplip-1-RNAi/+; Ok107-Gal4/+*; MB247::+: *MB247-Gal4/+*; MB247::Aplip-1-RNAi: *MB247-Gal4/UAS-Aplip-1-RNAi*; UAS-Unc13A^{RNAi}::+: *UAS-Unc13A-RNAi/+*; Ok107::UAS-C-term-GFP: *UAS-C-term-GFP/+; Ok107-Gal4/+*: Ok107::UAS-C-term-GFP::Unc13A^{RNAi}: *UAS-C-term-GFP/UAS-Unc13A-RNAi; Ok107-Gal4/+*; Ok107::UAS-Unc13A^{RNAi}: *UAS-Unc13A-RNAi/+; Ok107-Gal4/+*. Figure 7b: Ok107::+: *VT1211-LexA::LexAop-GCaMP6f/+;;Ok107-Gal4/+*; Ok107::UAS-C-term-GFP: *VT1211-LexA::LexAop-GCaMP6f/+;UAS-C-term-GFP/+; Ok107-Gal4/+*; Ok107::UAS-C-term-GFP::Unc13A^{RNAi}: *VT1211-LexA::LexAop-GCaMP6f/+; UAS-C-term-GFP/UAS-Unc13A-RNAi; Ok107-Gal4/+*. Western blot, Supplementary Fig. 9a: elav::+: *elav-Gal4/+*; UAS-Unc13A-RNAi::+: *UAS-Unc13A-RNAi/+*; elav::UAS-Unc13A^{RNAi}: *elav-Gal4/+;;UAS-Unc13A-RNAi/+*.

Stocks were obtained from: *A22*[22]; *AD9, df(2L)cl*^{h4}, *gluRIIA*^{SP16} [23]; GluRIIB-GFP[72]; *Ok6-GAL4*[73]; *rbp*^{Stop1}, *rbp*$^{S2.01}$ [6]; *rim*$^{ex1.103}$ [17]; *fife*^{ex1027} [34]; *liprin-α*^{F3ex15}, *liprin-α*^{R60} [38]; *UAS-Syd-1-GFP*; *syd-1*$^{1.2}$, *syd-1*$^{3.4}$ [39]; *brp*$^{Δ6.1}$ [36]; *brp*^{69} [5]; EMS7.5, *UAS-Unc13A-GFP*[4]; *UAS-BRP-D3-Straw*[72]; *UAS-Cac-GFP*[74]; *elav-Gal4*[75]; *UAS-Unc13A-RNAi, UAS-C-term-GFP*[7]; *aplip-1*^{ex213} [32]; *aplip-1*^{ek4} [33]; *srpk79D*^{ATC} [29]; *Ok107-Gal4*[76]; *MB247-Gal4*[77]. *P84200* was provided by the Drosophila Genetic Resource Center (DGRC). The *aplip-1*^{ek4}; Df(3L)BSC799; *atg1*^{ey07351}; Df(3L)BSC10; Df(3R)ED5785 lines were provided by the Bloomington *Drosophila* Stock Center. *UAS-Aplip-1-RNAi* and *UAS-srpk79D-RNAi* from VDRC.

Immunostaining. Larvae were dissected and stained as described previously[39]. The following primary antibodies were used: guinea-pig Unc13A (1:500[4]); mouse Syx1A 8C3 (1:40; Developmental Studies Hybridoma Bank, University of Iowa, Iowa City, IA, USA; AB Registry ID: AB_528484); mouse Unc18/Rop 4F8 (1:500; Developmental Studies Hybridoma Bank, University of Iowa, Iowa City, IA, USA; AB Registry ID: AB_1157869; mouse GFP 3E6 (1:500, Thermo Fisher Scientific Inc., MA, USA, A-11120; AB Registry ID: AB_221568), mouse Nc82=anti-BRP^{C-term} (1:100, Developmental Studies Hybridoma Bank, University of Iowa, Iowa City, IA, USA; AB Registry ID: AB_2314865); rabbit BRP^{Last200} (1:1000[78]); rabbit RBP^{C-term} (1:500[6]); guinea-pig vGlut; (1:2000[79]). Except for staining against RBP, Syx1A and Unc18, where larvae were fixed for 10 min with 4% paraformaldehyde (PFA) in 0.1 mM phosphate buffered saline (PBS), all fixations were performed for 5 min with ice-cold methanol. The glutamate receptor blocker PhTx-433 (Sigmal-Aldrich, MO, USA) was prepared as a 4 mM stock solution either in DMSO (final DMSO concentration, 0.5%) or dH_2O. Rapid pharmacological homeostatic challenge was assessed by incubating semi-intact preparations in 20 µM PhTx diluted in HL3 (see below) containing 0 or 1.5 mM $CaCl_2$ for 10 min at room temperature[19]. Controls were treated in the same way but were incubated either in pure HL3 or HL3 containing 0.5% DMSO (in dependence of how PhTx stock solution was prepared) for 10 min. After incubation, the dissection was completed and the preparation was rinsed three times with fixative solution. During the dissection, extreme care was taken to avoid excessive stretching of body wall muscles, as this may significantly impair induction of homeostasis[19].

For translation block experiments semi-intact preparations were pre-incubated in HL3 containing 50 µg/ml Cycloheximide (Chx; Sigmal-Aldrich, MO, USA) dissolved in DMSO for 10 min, a concentration previously shown to block protein synthesis in Drosophila[80]. Rapid pharmacological homeostatic challenge was then assessed by incubating semi-intact preparations in 20 µM PhTx (or a similar volume of H_2O in control experiments) diluted in HL3 (see below) containing 50 µg/ml Chx for 10 min at room temperature. For actin-depolymerization experiments semi-intact preparations were pre-incubated in HL3 containing 15 µM Latrunculin B (Abcam, UK) in DMSO for 10 min. For control experiments larvae were incubated with a solution containing a similar volume of DMSO. Rapid pharmacological homeostatic challenge was then assessed by incubating semi-intact preparations in 20 µM PhTx (or a similar volume of H_2O in control experiments) diluted in HL3 (see below) containing 15 µM Latrunculin B in DMSO (or DMSO alone in control experiments) for 10 min at room temperature. Afterwards, prepping and staining procedures were performed as described above/below. Control animals were always reared in parallel and treated identically in all experiments.

Secondary antibodies for standard immunostainings were used in the following concentrations: goat anti-HRP-Cy5 (1:250, Jackson ImmunoResearch, PA, USA); goat anti-HRP-647 (1:500, Jackson ImmunoResearch 123–605–021, PA, USA); goat anti-rabbit-Cy3 (1:500, Jackson ImmunoResearch 111–165–144, PA, USA); goat anti-mouse-Cy3 (1:500, Jackson ImmunoResearch 115–165–146); goat anti-mouse or anti guinea pig Alexa-Fluor-488 (1:500, Life Technologies A11001/A11073, CA, USA). Larvae were mounted in vectashield (Vector labs, CA, USA). Secondary antibodies for STED were used in the following concentrations: goat anti-mouse or rabbit Alexa594 (1:500, Thermo Fisher Scientific Inc. A11032/A11037, MA, USA); goat anti-mouse Atto590 (1:100); goat anti-rabbit Atto590 (1:100); goat anti-guinea pig star635 (1:100); goat anti-rabbit star635 (1:100); goat anti-mouse or rabbit Atto647N (1:250; Active Motif; 15038/15048). Atto590 (ATTO-TEC AD 590–31) and star635 (Abberior 1–0101002–1) coupled to respective IgGs (Dianova). For STED imaging larvae were mounted in Mowiol (Max-Planck Institute for Biophysical Chemistry, Group of Stefan Hell) or ProLong Gold (Life-Technologies, CA, USA) on high-precision glass coverslips.

For Western blots[81], adult flies were dissected in cold Ringer's solution and homogenized in Lysis buffer (1× PBS, 0.5%Triton, 2%SDS, 1× Protease inhibitor, 1× Sample buffer) followed by full-speed centrifugation at 18 °C. One brain's supernatant for each group was subjected to SDS-PAGE and immunoblotted according to standard procedures. The following antibodies were used: guinea-pig Unc13A (1:2000[4]) and mouse Tubulin (1:100,000; Sigmal-Aldrich, MO, USA; Cat# T9026, AB Registry ID: AB_477593). Antibodies obtained from the Developmental Studies Hybridoma Bank were created by the NICHD of the NIH and maintained at The University of Iowa, Department of Biology, Iowa City, IA 52242.

Image acquisition, processing, and analysis. Confocal microscopy was performed with a Leica SP8 microscope (Leica Microsystems, Germany). Images of fixed and live samples were acquired at room temperature. Confocal imaging of NMJs was done using a *z*-step of 0.25 µm. The following objective was used: 63 × 1.4 NA oil immersion for NMJ confocal imaging. All confocal images were acquired using the LAS X software (Leica Microsystems, Germany). Images from fixed samples were taken from muscle 4 of third instar larval 1b NMJs (segments A2–A5) or nerve bundles (segments A1–A3). Images for figures were processed with ImageJ software to enhance brightness using the brightness/contrast function. If necessary, images were smoothened (0.5 pixel Sigma radius) using the Gaussian blur function. Confocal stacks were processed with ImageJ software (http://rsbweb.nih.gov/ij/). Quantifications of AZs (scored via BRP) were performed following an adjusted manual[82], briefly as follows. The signal of a HRP-Cy5 antibody was used as template for a mask, restricting the quantified area to the shape of the NMJ. The original confocal stacks were converted to maximal projections, and after background subtraction, a mask of the synaptic area was created by applying a certain

threshold to remove the irrelevant lower intensity pixels. The segmentation of single spots was done semi-automatically via the command "Find Maxima" embedded in the ImageJ software and by hand with the pencil tool and a line thickness of 1 pixel. To remove high frequency noise a Gaussian blur filter (0.5 pixel Sigma radius) was applied. The processed picture was then transformed into a binary mask using the same lower threshold value as in the first step. This binary mask was then projected onto the original unmodified image using the "min" operation from the ImageJ image calculator. For spots/µm² the number of spots was divided by the size of the mask of the synaptic area.

For colocalization analysis (Pearson correlation coefficient) the ImageJ plugin "JACOP" (http://rsb.info.nih.gov/ij/plugins/track/jacop2.html) was used. To determine the synaptic protein levels, a custom-written ImageJ script was used that detects the locations with highest local maxima in pixel values to generate regions of interests (ROIs) and sets a point selection at each. The intensities were then measured and all selections were deleted, leaving intensity values and (x, y) locations in the results list. The results list was then used to create a circle of size = 5 pixels (pixel size 100 nm) centered around each (x, y) location and the integrated density within these ROIs was measured and taken for further calculations. The same ROIs were then used in the channel containing signals of the co-stained protein. For scatter plots, co-stainings of BRP either with RBP, Unc13A or Syx-1A with or without PhTx-treatment or wild-type and *gluRIIA*^{Null} were used. The AZ numbers were counted (number of BRP spots) and the local synaptic levels of both co-stained proteins were measured. AZs were then sorted into five bins (AZ number divided by five) depending on their synaptic BRP levels and then the respective second channel intensities distributed to the appropriate bin. Binned BRP levels were then plotted against binned levels of the second channel.

STED microscopy. Two-color STED images were recorded on custom-built STED-microscopes[83,84], which either combine two pairs of excitation laser beams of 595 nm and 635 nm or 595 nm and 640 nm wavelength with one STED fiber laser beam at 775 nm. All STED images were acquired using Imspector Software (Max Planck Innovation GmbH, Germany). STED images were processed using a linear deconvolution function integrated into Imspector Software (Max Planck Innovation GmbH, Germany). Regularization parameters ranged from $1e^{-09}$ to $1e^{-10}$. The point spread function (PSF) for deconvolution was generated by using a 2D Lorentz function with its half-width and half-length fitted to the half-width and half-length of each individual image. For Fig. 3c, dual-color STED imaging with time-gated detection was performed using a commercial Leica SP8 TCS STED microscope (Leica Microsystems, Germany) equipped with a 100× NA 1.4 objective (HC PL Apo CS2; Leica Microsystems, Germany). Briefly, the system includes an inverted DMi8 CS microscope equipped with a 100× pulsed white light laser (WLL; ~80-ps pulse width, 80-MHz repetition rate; NKT Photonics, Denmark) with a STED lasers for depletion (pulsed) at 775 nm. Detection of Alexa594 after excitation at 594 nm and emission detection of 604–650 nm and Atto647 after excitation at 640 nm at emission of 656–751 nm was performed in frame sequential mode. Time-gated detection with Hybrid detectors was set from 0.3–6 ns for both dyes. Raw data were deconvolved with Huygens Professional software (Scientific Volume Imaging) using a theoretical PSF automatically computed based on pulsed-wave STED optimized function and the specific microscope parameters. Default deconvolution settings were applied. Images for figures and for finding high-intensity clusters (see below) were processed with ImageJ software to remove obvious background or neighboring AZs (if required), enhance brightness/contrast and smoothened (0.5 pixel Sigma radius) using the Gauss blur function.

Classification and alignment of single AZs. All analysis described below was done using MATLAB R2016b (Mathworks Inc., Natick MA, USA) with optional toolboxes, which are indicated in the respective sections. Classification of individual AZs was achieved by using a custom script to detect the position of cluster centers (local intensity maxima) in the images where speckles of neighboring AZs were removed (only for Unc13A, BRP, RBP), while the averaging procedure described hereafter was performed on the corresponding raw images. This code retains only pixels above a defined grey value threshold. For the analysis of Unc13A stainings shown in Fig. 2f, a threshold value of 25 was used (18 for BRP, RBP, Syx-1A, and Unc-18). All pixel values in the image below this threshold value were set to zero to remove background noise. We then identified the positions of high-intensity pixel clusters as local intensity maxima in the images. This was achieved by finding local maxima in the vertical and horizontal pixel lines. First, the function searched the first derivative (using the function diff) of all pixel columns for zero values and the changes in the surrounding slopes were considered to identify local maxima. The same procedure was then applied in pixel rows, but only for those pixel column values associated with a local maximum in the previous step. All single pixels that were associated with a maximum in both a row and a column were detected using the function intersect. To prevent detection of the same cluster more than once, a defined minimum distance of clusters was used (50 nm for BRP, Unc13A, Syx-1A and 20 nm for RBP) and only the local maximum with the highest intensity value was considered. All subsequent translation and averaging procedures were performed on corresponding raw images of the same AZs using the determined classification and positions of clusters. The non-cleaned AZs were sorted by the number of protein clusters detected this way. To calculate the center of mass of all coordinates, the means of all x- and y-coordinates were taken according to equations (1) and (2).

$$\mathrm{Sx} = n^{-1} \cdot \sum_{1}^{n} x_{\mathrm{obs}}(n) \tag{1}$$

$$\mathrm{Sy} = n^{-1} \cdot \sum_{1}^{n} y_{\mathrm{obs}}(n) \tag{2}$$

where (Sx, Sy) is the (x, y)-coordinate center of mass in the initial image, n is the number of identified clusters, and $x_{\mathrm{obs}}(n)$ and $y_{\mathrm{obs}}(n)$ are the positions of the n-th cluster in the present image. To align the center of mass to the center of the image, the necessary shift (Δx and Δy) of the original coordinates was calculated according to Eqs. (3) and (4) and used subsequently in Eqs. (5) and (6).

$$\Delta x = 0.5 \cdot \mathrm{imsize}(x) - \mathrm{Sx} \tag{3}$$

$$\Delta y = 0.5 \cdot \mathrm{imsize}(y) - \mathrm{Sy} \tag{4}$$

$$x_{\mathrm{centered}}(n) = x_{\mathrm{obs}}(n) + \Delta x \tag{5}$$

$$y_{\mathrm{centered}}(n) = y_{\mathrm{obs}}(n) + \Delta y \tag{6}$$

In Eqs. (3) and (4), "imsize" refers to the size of the image in x or y dimension. The resulting coordinates x_{centered} and y_{centered} represent cluster coordinates after shifting the original coordinates x_{obs} and y_{obs}. The same translation was applied to the corresponding AZ image (using the function imtranslate, part of the 'Image Processing' toolbox). Clusters were ranked in a counter-clockwise sequence in all images (see illustration in Fig. 2b; Supplementary Fig. 3c) by sorting them for increasing angle between the image center and the cluster location in relation to the vertical midline ($x = 26$).

To align protein cluster coordinates between all investigated AZs, central rotation (around the image center, $x_{\mathrm{middle}} = y_{\mathrm{middle}} = 26$), was done using the operation in Eq. (7).

$$\begin{pmatrix} x_{\mathrm{rotated}}(n) \\ y_{\mathrm{rotated}}(n) \end{pmatrix} = \left[\begin{pmatrix} x_{\mathrm{centered}}(n) \\ y_{\mathrm{centered}}(n) \end{pmatrix} - \begin{pmatrix} x_{\mathrm{middle}} \\ y_{\mathrm{middle}} \end{pmatrix} \right] \cdot \begin{pmatrix} \cos(\alpha) & -\sin(\alpha) \\ \sin(\alpha) & \cos(\alpha) \end{pmatrix} + \begin{pmatrix} x_{\mathrm{middle}} \\ y_{\mathrm{middle}} \end{pmatrix} \tag{7}$$

To find the optimal angle to overlay all AZs, a cost reflecting the sum of distances between cluster positions of the same rank in all images was minimized. The cost function was defined as described in Eq. (8).

$$\mathrm{cost} = \sum_{n=1}^{\mathrm{totClusters}} \sum_{m=1}^{\mathrm{totImgs}} \sum_{l=1}^{\mathrm{totImgs}} \left(\left(x_{\mathrm{rotated}}(n,m) - x_{\mathrm{rotated}}(n,l) \right)^2 + \left(y_{\mathrm{rotated}}(n,m) - y_{\mathrm{rotated}}(n,l) \right)^2 \right) \tag{8}$$

In Eq. (8), n is the cluster number, totClusters is the total cluster number of the respective category of images, m and l are particular AZ images in the stack of images from one category, and totImgs is the total number of AZ images in that category. The squared Euclidean distances were calculated using the function pdist, which performs the operation shown in Eq. (8).

The optimal rotation angle was found using a genetic algorithm function (ga, part of the 'Global Optimization' toolbox). The rotation angles evaluated were constrained in a range from −180 to 180 degrees. For faster optimization, parallelization (setting the option 'UseParallel' to 'true'; this requires the 'Parallel Computing' toolbox) was employed to evaluate 500 individual cost functions per generation. Cluster coordinates from all images in one category were rotated simultaneously. A single individual in the genetic algorithm represented a set of rotation angles for each image. The convergence criterion (TolFun) was left at the default value (a relative cost value change of $<10^6$ over 50 generations). The output of this optimization was a vector containing all rotation angles that led to the best overlap of cluster coordinates. Finally, these rotations were then applied to the centered original AZ images. All images aligned this way were then combined in a stack and an average image was generated by calculating the mean intensity of all image pixels. For better illustration of the AZ structure, pixel intensities were linearly scaled such that the highest intensity pixel had a value of 255. The procedure was only performed if more than two images existed in the same cluster number class for at least 5 consecutive cluster number classes. The histograms shown in Fig. 2c–e and Supplementary Fig. 2a were generated by counting the number of images in each cluster number class, and dividing each value by the total amount of images detected in all classes. The mean cluster intensity shown in Supplementary Fig. 2b, c was calculated by taking the average image intensities per category and subtracting the mean intensity of each category from the next higher one. These differences in mean intensity between subsequent categories were then further averaged.

To investigate the AZ structure in an approach independent of the cluster-distance minimization procedure described above, we repeated the averaging in a different way as follows. We developed a MATLAB code for AZ centering and alignment by rotation of the highest intensity pixel to identical angles and therefore

similar positions, which yielded qualitatively similar results (Supplementary Fig. 3a). Again, high-intensity clusters were detected in AZ images cleaned from clusters belonging to bordering AZs, and all translations and rotations were then performed on unretouched images. The center of mass of the found cluster coordinates was calculated and the image shifted so that the center of mass of the coordinates was in the center of the 51 by 51 pixel space ($x = y = 26$; see Eqs. (1) to (6)). Only the position of the brightest pixel was then considered for rotation. To determine the angle by which to rotate each image to place this highest intensity pixel to the same fixed position (on the vertical midline between the two top image quadrants—the "twelve o'clock" position), the x and y distances to the center of rotation (equal to the center pixel of the image $x = y = 26$) were calculated to find the length (l) of the hypotenuse and the opposite side of the right triangle using pdist. The angle α in degrees was then calculated by taking the inverse sine in degrees of this value (MATLAB function asind), as shown in Eq. (9).

$$\alpha = \sin^{-1}\left(\frac{l_{\text{opposite side}}}{l_{\text{hypotenuse}}}\right) \quad (9)$$

In cases where the brightest peak was located above the horizontal midline, the adjacent side of the triangle was the vertical midline. In cases where the brightest peak was located below the horizontal midline, the angle was calculated with the horizontal midline being the adjacent side, and 90° were added to the final angle value. Additionally, in cases where the brightest peak was located to the right of the vertical midline, the angle was multiplied with −1. To generate the results shown in Supplementary Fig. 3b, which shows the averaging of AZ images within randomly assigned categories, we generated a number of random category values and then proceeded with the averaging procedure described above. For this, we reproduced the distribution of category values from the AZ dataset according to the histogram values of the category vector as follows. A histogram of the category vector was generated (MATLAB function histogram) with a bin width of 1, yielding the absolute amount of AZs per category. A cumulative sum vector was calculated from these histogram values (MATLAB function cumsum). For each position in the category vector, we then chose a random number between 0 and 1 and multiplied it by the number of images. We then found the first position in the cumulative sum vector that was larger than this random value. The position found was equal to the assigned category. This resulted in a randomly assigned category vector with a similar distribution of categories as the original vector.

In vivo live imaging and analysis. In vivo imaging of intact *Drosophila* larvae was performed as previously described[85]. Briefly, third instar larvae were put into a drop of Voltalef H10S oil (Arkema, Inc., France) within an airtight imaging chamber. Before imaging, the larvae were anaesthetized with 20 short pulses of a desflurane (Baxter, IL, USA) air mixture until the heartbeat completely stopped. For assessing axonal transport, axons immediately after exiting the ventral nerve cord were imaged for 5 min using timelapse confocal microscopy. Kymographs were plotted using a custom-written ImageJ script.

Induction of homeostatic plasticity and electrophysiology. Third-instar larvae were selected and placed individually on a Sylgard block. Using a very sharp pin, the tail of the larva was pinned between the posterior spiracles, in the absence of solution. The head was pinned, making sure not to stretch the larva, so that the animal was relatively loose between the two pins. A small horizontal incision was made in the dorsal cuticle at the tail with a sharp scissors. The larva was cut vertically from the tail incision in an anterior direction (towards the head), continuing beyond the head pin. Great care was taken not to stretch the cuticle or animal during this process. Forty microliters of a 20 µM PhTx in modified hemolymph-like solution (HL3[86]; composition (in mM): NaCl 70, KCl 5, $MgCl_2$ 10, $NaHCO_3$ 10, trehalose 5, sucrose 115, HEPES 5, $CaCl_2$ 0, pH adjusted to 7.2) was pipetted into the abdominal cavity with minimal force, making sure to fill the abdomen. After 10 min incubation, the preparation was completed without rinsing. The cuticle was gently pinned twice on each side (without stretching). The connection of the intestines and trachea to the body at the posterior were cut. Holding the now free ends of the intestines and trachea with a fine forceps, remaining connections were cut moving in an anterior direction (towards the head). The intestines and trachea could then be gently removed without stretching the larva. Finally, the brain was held firmly and slightly raised above the body so that the scissors could be placed underneath to cut the segmental nerves. Care was taken not to touch the underlying muscle and to avoid excessive pulling of the nerves before they were cut. The completed preparation was rinsed 3 times with PhTx-free HL3 (0 mM $CaCl_2$, 10 mM $MgCl_2$). PhTx-free HL3 solution was used in control treatments. Sylgard blocks were kept separate for PhTx and control treatments and all implements were rinsed after each recording.

The Sylgard block and completed larval preparation was placed in the recording chamber which was filled with 2 ml HL3 (0.4 mM $CaCl_2$, 10 mM $MgCl_2$). Recordings were performed at room temperature (~22 °C) in current clamp mode at muscle 6 in segments A2/A3 as previously described[86] using an Axon Digidata 1550 A digitizer, Axoclamp 900 A amplifier with HS-9A x0.1 headstage (Molecular Devices, CA, USA) and on a BX51WI Olympus microscope with a 40X LUMPlanFL/IR water immersion objective. Sharp intracellular recording electrodes were pulled using a Flaming Brown Model P-97 micropipette puller (Sutter Instrument, CA, USA) with a resistance of 20–35 MΩ, back-filled with 3 M KCl. Cells were only considered with a membrane potential less than -60 mV and membrane resistances greater than 4 MΩ. All recordings were acquired using Clampex software (v10.5) and sampled at 10–50 kHz, filtering with a 5 kHz low-pass filter. mEPSPs were recorded for 1 min. eEPSPs were recorded by stimulating the appropriate nerve at 0.1 Hz, five times (8 V, 300 µs pulse) using an ISO-STIM 01D stimulator (NPI Electronic, Germany). Stimulating suction electrodes were pulled on a DMZ-Universal Puller (Zeitz-Instruments GmbH, Germany) and fire polished using a CPM-2 microforge (ALA Scientific, NY, USA). A maximum of two cells were recorded per animal.

Analysis was performed with Clampfit 10.5 and Graphpad Prism 6 software. mEPSPs were further filtered with a 500 Hz Gaussian low-pass filter. Using a single template for all cells, mEPSPs were identified and analyzed, noting the mean mEPSP amplitude per cell. For Fig. 5 and Supplementary Fig. 7, templates were generated for each cell and the first 30 mEPSPs were identified and taken into account for further analysis. An average trace was generated from the 5 eEPSP traces per cell. The amplitude of the average eEPSP trace was divided by the mean mEPSP amplitude, for each respective cell, to determine the quantal content.

Dissection and current clamp recordings of w1118 vs *gluRIIA*$^{\text{Null}}$ were performed as above in male third-instar larvae. Cells with an initial membrane potential greater than −55 mV, resistances less than 5 MΩ or multiple responses to a single stimulus were rejected. eEPSPs were recorded by stimulating the appropriate nerve at 0.2 Hz, 10 times (6 V, 300 µs pulse). An average eEPSP amplitude was calculated from the 10 traces. mEPSPs were analyzed with a genotype specific template. Quantal contents were calculated by dividing the mean eEPSP by mean mEPSP for each cell.

In vivo two-photon live calcium imaging and analysis. Two-photon imaging of odor-evoked calcium responses was conducted in 3–5-day-old mixed-sex flies expressing LexAop-GCaMP6f in VT1211-LexA. For imaging, flies were briefly anesthetized on ice and mounted in a custom made chamber by immobilizing wings, head and proboscis with wax. The head capsule was opened in sugar-free HL3-like extracellular saline[87]. Odor stimulation consisted of a 1.5 s OCT pulse followed by a 30 s break and then a 1.5 s MCH pulse followed again by another 30 s break. This alternating odor pulse protocol was consecutively repeated five times (odor dilution in mineral oil 1/1000). Odors were delivered on a clean air carrier stream and image acquisition and odor stimulation was synchronized temporally using a custom-designed system. Fluorescence was centered on 910 nm generated by a Ti-Sapphire laser (Chameleon Ultra II, Coherent, CA, USA). Images with a pixel size of 0.3 × 0.3 µm were acquired at 70 Hz using two-photon microscopy (Femto2D-Resonant by Femtonics Ltd., Hungary) with a 20×, 1.0 NA water-immersion objective, controlled by MESc v3.5 software (Femtonics Ltd., Hungary). For each animal, a single hemisphere was analyzed. All OCT and MCH responses of a fly were averaged respectively and resulting traces were averaged between flies. Mean intensity values of two-photon fluorescence were calculated, while F0 was defined as the mean F from 0 to 1.5 s at the beginning of a recording (MESc v 3.5 software). Image processing for single frames were manually performed using ImageJ (images did not require registration).

Odor avoidance conditioning. All flies were 3 to 5 days old, raised in 12 h:12 h, light:dark cycle and at 65% relative humidity. One day before the experiment, the flies were transferred to fresh food vials. One hour prior to the experiment, flies were pre-conditioned to experimental conditions (dim red light, 25 °C, humidity of 80%). The aversive odors 3-Octanol (OCT) and Methylcyclohexanol (MCH) were diluted 1:100 in paraffin oil and presented in 14 mm cups. A current of 120 V AC was used as a behavioral reinforcer. The associative training was performed as previously described[88]. In a single-cycle training, nearly 100 flies were presented with one odor (CS^+) paired with electrical shock (US; 12 times for 1 min). After one minute of pure air-flow, the second odor was presented without the shock (CS^-) for another minute. The flies were then immediately tested for short-term memory performance by presenting them the two odors together. A performance index (PI) was calculated as the number of flies choosing the odor without shock (CS^-), minus the number of flies choosing the odor paired with shock (CS^+), divided by the total number of flies, multiplied by 100. The values of PI ranges from 0 to 100 where 0 means no learning (50:50 distribution of flies) and a value of 100 means complete learning (all flies avoided the conditioned odor). The final learning index was calculated as the average of both reciprocal indices for the two odors. Odor Avoidance experiments were used to test innate behavior where each odor was presented to the flies without conditioning. The PIs were calculated as stated above.

Quantification and statistical analysis. Data were analyzed using Prism (GraphPad Software, CA, USA). Per default Student's T test was performed to compare the means of two groups unless the data were either non-normally distributed (as assessed by D'Agostino-Pearson omnibus normality test) or if variances were unequal (assessed by F test) in which case they were compared by a Mann–Whitney U Test. However, in the Source Data file both tests are provided for all relevant cases. For comparison of more than two groups, one-way analysis of variance (ANOVA) tests were used, followed by a Tukey's multiple comparison test. P values and N values are

given in the Source Data file. Means are annotated ± s.e.m. Asterisks are used to denote significance: *$P < 0.05$; **$P < 0.01$; ***$P < 0.001$; n.s. (not significant), $P > 0.05$.

Reporting summary. Further information on experimental design is available in the Nature Research Reporting Summary linked to this article.

Data availability

The data that support the findings of this study, additional information and requests for resources and reagents as well as MATLAB and ImageJ codes used in this study are available from Alexander M. Walter (awalter@fmp-berlin.de) upon request.

Received: 10 August 2018 Accepted: 7 February 2019
Published online: 06 March 2019

References

1. Citri, A. & Malenka, R. C. Synaptic plasticity: multiple forms, functions, and mechanisms. *Neuropsychopharmacology*. **33**, 18–41 (2008).
2. Nicoll, R. A. & Roche, K. W. Long-term potentiation: peeling the onion. *Neuropharmacology* **74**, 18–22 (2013).
3. Acuna, C., Liu, X. & Sudhof, T. C. How to make an active zone: unexpected universal functional redundancy between RIMs and RIM-BPs. *Neuron* **91**, 792–807 (2016).
4. Bohme, M. A. et al. Active zone scaffolds differentially accumulate Unc13 isoforms to tune Ca(2+) channel-vesicle coupling. *Nat. Neurosci.* **19**, 1311–1320 (2016).
5. Kittel, R. J. et al. Bruchpilot promotes active zone assembly, Ca2+ channel clustering, and vesicle release. *Science* **312**, 1051–1054 (2006).
6. Liu, K. S. et al. RIM-binding protein, a central part of the active zone, is essential for neurotransmitter release. *Science* **334**, 1565–1569 (2011).
7. Reddy-Alla, S. et al. Stable positioning of Unc13 restricts synaptic vesicle fusion to defined release sites to promote synchronous neurotransmission. *Neuron* **95**, 1350–1364 e1312. (2017).
8. Sakamoto, H. et al. Synaptic weight set by Munc13-1 supramolecular assemblies. *Nat. Neurosci.* **21**, 41–49 (2018).
9. Sudhof, T. C. The presynaptic active zone. *Neuron* **75**, 11–25 (2012).
10. Tang, A. H. et al. A trans-synaptic nanocolumn aligns neurotransmitter release to receptors. *Nature* **536**, 210–214 (2016).
11. Walter, A. M., Bohme, M. A. & Sigrist, S. J. Vesicle release site organization at synaptic active zones. *Neurosci. Res.* **127**, 3–13 (2018).
12. Wang, S. S. et al. Fusion competent synaptic vesicles persist upon active zone disruption and loss of vesicle docking. *Neuron* **91**, 777–791 (2016).
13. Davis, G. W. & Muller, M. Homeostatic control of presynaptic neurotransmitter release. *Annu. Rev. Physiol.* **77**, 251–270 (2015).
14. Frank, C. A. Homeostatic plasticity at the Drosophila neuromuscular junction. *Neuropharmacology* **78**, 63–74 (2014).
15. Bruckner, J. J. et al. Fife organizes synaptic vesicles and calcium channels for high-probability neurotransmitter release. *J. Cell. Biol.* **216**, 231–246 (2017).
16. Muller, M., Genc, O. & Davis, G. W. RIM-binding protein links synaptic homeostasis to the stabilization and replenishment of high release probability vesicles. *Neuron* **85**, 1056–1069 (2015).
17. Muller, M., Liu, K. S., Sigrist, S. J. & Davis, G. W. RIM controls homeostatic plasticity through modulation of the readily-releasable vesicle pool. *J. Neurosci.* **32**, 16574–16585 (2012).
18. Weyhersmuller, A., Hallermann, S., Wagner, N. & Eilers, J. Rapid active zone remodeling during synaptic plasticity. *J. Neurosci.* **31**, 6041–6052 (2011).
19. Frank, C. A., Kennedy, M. J., Goold, C. P., Marek, K. W. & Davis, G. W. Mechanisms underlying the rapid induction and sustained expression of synaptic homeostasis. *Neuron* **52**, 663–677 (2006).
20. Goel, P., Li, X. & Dickman, D. Disparate postsynaptic induction mechanisms ultimately converge to drive the retrograde enhancement of presynaptic efficacy. *Cell Rep.* **21**, 2339–2347 (2017).
21. Ortega, J. M., Genc, O. & Davis, G. W. Molecular mechanisms that stabilize short term synaptic plasticity during presynaptic homeostatic plasticity. *Elife* **7**, e40385 (2018).
22. DiAntonio, A., Petersen, S. A., Heckmann, M. & Goodman, C. S. Glutamate receptor expression regulates quantal size and quantal content at the Drosophila neuromuscular junction. *J. Neurosci.* **19**, 3023–3032 (1999).
23. Petersen, S. A., Fetter, R. D., Noordermeer, J. N., Goodman, C. S. & DiAntonio, A. Genetic analysis of glutamate receptors in Drosophila reveals a retrograde signal regulating presynaptic transmitter release. *Neuron* **19**, 1237–1248 (1997).
24. Ehmann, N. et al. Quantitative super-resolution imaging of Bruchpilot distinguishes active zone states. *Nat. Commun.* **5**, 4650 (2014).
25. Wilhelm, B. G. et al. Composition of isolated synaptic boutons reveals the amounts of vesicle trafficking proteins. *Science* **344**, 1023–1028 (2014).
26. Akins, M. R., Berk-Rauch, H. E. & Fallon, J. R. Presynaptic translation: stepping out of the postsynaptic shadow. *Front. Neural Circuits* **3**, 17 (2009).
27. Tsurudome, K. et al. The Drosophila miR-310 cluster negatively regulates synaptic strength at the neuromuscular junction. *Neuron* **68**, 879–893 (2010).
28. Wairkar, Y. P. et al. Unc-51 controls active zone density and protein composition by downregulating ERK signaling. *J. Neurosci.* **29**, 517–528 (2009).
29. Johnson, E. L. 3rd, Fetter, R. D. & Davis, G. W. Negative regulation of active zone assembly by a newly identified SR protein kinase. *PLoS Biol.* **7**, e1000193 (2009).
30. Nieratschker, V. et al. Bruchpilot in ribbon-like axonal agglomerates, behavioral defects, and early death in SRPK79D kinase mutants of Drosophila. *PLoS Genet.* **5**, e1000700 (2009).
31. Siebert, M. et al. A high affinity RIM-binding protein/Aplip1 interaction prevents the formation of ectopic axonal active zones. *Elife* **4**, e06935 (2015).
32. Klinedinst, S., Wang, X., Xiong, X., Haenfler, J. M. & Collins, C. A. Independent pathways downstream of the Wnd/DLK MAPKKK regulate synaptic structure, axonal transport, and injury signaling. *J. Neurosci.* **33**, 12764–12778 (2013).
33. Horiuchi, D., Barkus, R. V., Pilling, A. D., Gassman, A. & Saxton, W. M. APLIP1, a kinesin binding JIP-1/JNK scaffold protein, influences the axonal transport of both vesicles and mitochondria in Drosophila. *Curr. Biol.* **15**, 2137–2141 (2005).
34. Bruckner, J. J. et al. Fife, a Drosophila Piccolo-RIM homolog, promotes active zone organization and neurotransmitter release. *J. Neurosci.* **32**, 17048–17058 (2012).
35. Dai, Y. et al. SYD-2 Liprin-alpha organizes presynaptic active zone formation through ELKS. *Nat. Neurosci.* **9**, 1479–1487 (2006).
36. Fouquet, W. et al. Maturation of active zone assembly by Drosophila Bruchpilot. *J. Cell. Biol.* **186**, 129–145 (2009).
37. Hallam, S. J., Goncharov, A., McEwen, J., Baran, R. & Jin, Y. SYD-1, a presynaptic protein with PDZ, C2 and rhoGAP-like domains, specifies axon identity in C. elegans. *Nat. Neurosci.* **5**, 1137–1146 (2002).
38. Kaufmann, N., DeProto, J., Ranjan, R., Wan, H. & Van Vactor, D. Drosophila liprin-alpha and the receptor phosphatase Dlar control synapse morphogenesis. *Neuron* **34**, 27–38 (2002).
39. Owald, D. et al. A Syd-1 homologue regulates pre- and postsynaptic maturation in Drosophila. *J. Cell. Biol.* **188**, 565–579 (2010).
40. Akbergenova, Y., Cunningham, K. L., Zhang, Y. V., Weiss, S. & Littleton, J. T. Characterization of developmental and molecular factors underlying release heterogeneity at Drosophila synapses. *Elife* **7**, e38268 (2018).
41. Holderith, N. et al. Release probability of hippocampal glutamatergic terminals scales with the size of the active zone. *Nat. Neurosci.* **15**, 988–997 (2012).
42. Muhammad, K. et al. Presynaptic spinophilin tunes neurexin signalling to control active zone architecture and function. *Nat. Commun.* **6**, 8362 (2015).
43. Peled, E. S. & Isacoff, E. Y. Optical quantal analysis of synaptic transmission in wild-type and rab3-mutant Drosophila motor axons. *Nat. Neurosci.* **14**, 519–526 (2011).
44. Muller, M. & Davis, G. W. Transsynaptic control of presynaptic Ca(2)(+) influx achieves homeostatic potentiation of neurotransmitter release. *Curr. Biol.* **22**, 1102–1108 (2012).
45. Gratz, S. J. et al. Endogenous tagging reveals differential regulation of Ca2+ channels at single AZs during presynaptic homeostatic potentiation and depression. *J. Neurosci.* Preprint at: https://doi.org/10.1523/JNEUROSCI.3068-18.2019 (2019).
46. Camacho, M. et al. Heterodimerization of Munc13 C2A domain with RIM regulates synaptic vesicle docking and priming. *Nat. Commun.* **8**, 15293 (2017).
47. Deng, L., Kaeser, P. S., Xu, W. & Sudhof, T. C. RIM proteins activate vesicle priming by reversing autoinhibitory homodimerization of Munc13. *Neuron* **69**, 317–331 (2011).
48. Dulubova, I. et al. A Munc13/RIM/Rab3 tripartite complex: from priming to plasticity? *EMBO J.* **24**, 2839–2850 (2005).
49. Hu, Z., Tong, X. J. & Kaplan, J. M. UNC-13L, UNC-13S, and Tomosyn form a protein code for fast and slow neurotransmitter release in Caenorhabditis elegans. *eLife* **2**, e00967 (2013).
50. Zhou, K., Stawicki, T. M., Goncharov, A. & Jin, Y. Position of UNC-13 in the active zone regulates synaptic vesicle release probability and release kinetics. *eLife* **2**, e01180 (2013).
51. Kandel, E. R., Dudai, Y. & Mayford, M. R. The molecular and systems biology of memory. *Cell* **157**, 163–186 (2014).
52. Krashes, M. J., Keene, A. C., Leung, B., Armstrong, J. D. & Waddell, S. Sequential use of mushroom body neuron subsets during drosophila odor memory processing. *Neuron* **53**, 103–115 (2007).
53. Aso, Y. et al. The neuronal architecture of the mushroom body provides a logic for associative learning. *eLife* **3**, e04577 (2014).

54. Owald, D. et al. Activity of defined mushroom body output neurons underlies learned olfactory behavior in Drosophila. *Neuron* **86**, 417–427 (2015).
55. Quinn, W. G. & Dudai, Y. Memory phases in Drosophila. *Nature* **262**, 576–577 (1976).
56. Takeuchi, T., Duszkiewicz, A. J. & Morris, R. G. The synaptic plasticity and memory hypothesis: encoding, storage and persistence. *Philos. Trans. R. Soc. Lond. B. Biol. Sci.* **369**, 20130288 (2014).
57. Castillo, P. E. Presynaptic LTP and LTD of excitatory and inhibitory synapses. *Cold Spring Harb. Perspect. Biol.* **4**, a005728 (2012).
58. Newman, Z. L. et al. Input-Specific Plasticity and Homeostasis at the Drosophila Larval Neuromuscular Junction. *Neuron* **93**, 1388–1404 e1310 (2017).
59. Orr, B. O., Fetter, R. D. & Davis, G. W. Retrograde semaphorin-plexin signalling drives homeostatic synaptic plasticity. *Nature* **550**, 109–113 (2017).
60. Wentzel, C., Delvendahl, I., Sydlik, S., Georgiev, O. & Muller, M. Dysbindin links presynaptic proteasome function to homeostatic recruitment of low release probability vesicles. *Nat. Commun.* **9**, 267 (2018).
61. Li, X. et al. Synapse-specific and compartmentalized expression of presynaptic homeostatic potentiation. *Elife* **7**, e34338 (2018).
62. Hruska, M., Henderson, N., Le Marchand, S. J., Jafri, H. & Dalva, M. B. Synaptic nanomodules underlie the organization and plasticity of spine synapses. *Nat. Neurosci.* **21**, 671–682 (2018).
63. Bademosi, A. T. et al. In vivo single-molecule imaging of syntaxin1A reveals polyphosphoinositide- and activity-dependent trapping in presynaptic nanoclusters. *Nat. Commun.* **8**, 13660 (2017).
64. Sutton, M. A. & Schuman, E. M. Dendritic protein synthesis, synaptic plasticity, and memory. *Cell* **127**, 49–58 (2006).
65. Ziv, N. E. Maintaining the active zone: Demand, supply and disposal of core active zone proteins. *Neurosci. Res.* **127**, 70–77 (2018).
66. Puthanveettil, S. V. et al. A new component in synaptic plasticity: upregulation of kinesin in the neurons of the gill-withdrawal reflex. *Cell* **135**, 960–973 (2008).
67. Sugie, A. et al. Molecular Remodeling of the Presynaptic Active Zone of Drosophila Photoreceptors via Activity-Dependent Feedback. *Neuron* **86**, 711–725 (2015).
68. Wang, Z. et al. Myosin Vb mobilizes recycling endosomes and AMPA receptors for postsynaptic plasticity. *Cell* **135**, 535–548 (2008).
69. Lu, J. et al. Structural basis for a Munc13-1 homodimer to Munc13-1/RIM heterodimer switch. *PLoS Biol.* **4**, e192 (2006).
70. Michelassi, F., Liu, H., Hu, Z. & Dittman, J. S. A C1-C2 Module in Munc13 Inhibits Calcium-Dependent Neurotransmitter Release. *Neuron* **95**, 577–590 (2017). e575.
71. Sigrist, S. J., Reiff, D. F., Thiel, P. R., Steinert, J. R. & Schuster, C. M. Experience-dependent strengthening of Drosophila neuromuscular junctions. *J. Neurosci.* **23**, 6546–6556 (2003).
72. Schmid, A. et al. Activity-dependent site-specific changes of glutamate receptor composition in vivo. *Nat. Neurosci.* **11**, 659–666 (2008).
73. Aberle, H. et al. wishful thinking encodes a BMP type II receptor that regulates synaptic growth in Drosophila. *Neuron* **33**, 545–558 (2002).
74. Kawasaki, F., Zou, B., Xu, X. & Ordway, R. W. Active zone localization of presynaptic calcium channels encoded by the cacophony locus of Drosophila. *J. Neurosci.* **24**, 282–285 (2004).
75. Lin, D. M. & Goodman, C. S. Ectopic and increased expression of Fasciclin II alters motoneuron growth cone guidance. *Neuron* **13**, 507–523 (1994).
76. Connolly, J. B. et al. Associative learning disrupted by impaired Gs signaling in Drosophila mushroom bodies. *Science* **274**, 2104–2107 (1996).
77. Zars, T., Fischer, M., Schulz, R. & Heisenberg, M. Localization of a short-term memory in Drosophila. *Science* **288**, 672–675 (2000).
78. Ullrich, A. et al. Dynamical Organization of Syntaxin-1A at the Presynaptic Active Zone. *PLoS Comput. Biol.* **11**, e1004407 (2015).
79. Chen, X. et al. The BLOC-1 subunit pallidin facilitates activity-dependent synaptic vesicle recycling. *eNeuro* **4**, ENEURO.0335-16.2017 (2017).
80. Tully, T., Preat, T., Boynton, S. C. & Del Vecchio, M. Genetic dissection of consolidated memory in Drosophila. *Cell* **79**, 35–47 (1994).
81. Huang, Y. et al. The glycosphingolipid MacCer promotes synaptic bouton formation in Drosophila by interacting with Wnt. *Elife* **7**, e38183 (2018).
82. Andlauer, T. F. & Sigrist, S. J. Quantitative analysis of Drosophila larval neuromuscular junction morphology. *Cold Spring Harb. Protoc.* **2012**, 490–493 (2012).
83. Gottfert, F. et al. Strong signal increase in STED fluorescence microscopy by imaging regions of subdiffraction extent. *Proc. Natl. Acad. Sci. USA* **114**, 2125–2130 (2017).
84. Gottfert, F. et al. Coaligned dual-channel STED nanoscopy and molecular diffusion analysis at 20 nm resolution. *Biophys. J.* **105**, L01–L03 (2013).
85. Fuger, P., Behrends, L. B., Mertel, S., Sigrist, S. J. & Rasse, T. M. Live imaging of synapse development and measuring protein dynamics using two-color fluorescence recovery after photo-bleaching at Drosophila synapses. *Nat. Protoc.* **2**, 3285–3298 (2007).
86. Zhang, B. & Stewart, B. Electrophysiological recording from Drosophila larval body-wall muscles. *Cold Spring Harb. Protoc.* **2010**, pdb prot5487 (2010).
87. Yoshihara, M. Simultaneous recording of calcium signals from identified neurons and feeding behavior of Drosophila melanogaster. *J. Vis. Exp.* 3625 (2012).
88. Tully, T. & Quinn, W. G. Classical conditioning and retention in normal and mutant Drosophila melanogaster. *J. Comp. Physiol. A* **157**, 263–277 (1985).
89. Barnstedt, O. et al. Memory-relevant mushroom body output synapses are cholinergic. *Neuron* **89**, 1237–1247 (2016).

Acknowledgements

We thank S. Waddell and Y. Huang for the VT1211-LexA fly line. M.A.B. was supported by the SFB 740. A.T.G. was supported by a NeuroCure Ph.D. fellowship funded by the Deutsche Forschungsgemeinschaft (Exc 257) within the International Graduate Program Medical Neurosciences. M. Jusyte was supported by an Einstein Center for Neurosciences Ph.D. fellowship. U.R. was supported by a fellowship of the International Max Planck Research School by the Max-Planck-Gesellschaft. This work was supported by grants from the Deutsche Forschungsgemeinschaft to S.J.S. (Exc 257, TP A3 and A6 SFB 958, TP B9/SFB665; TP09/SFB740; TRR 186) and A.M.W. (Emmy Noether programme, TRR 186), D.O. (Emmy Noether programme) and from the National Institutes of Health to D. D. (NS091546).

Author contributions

M.A.B., S.J.S. and A.M.W. conceived the project. M.A.B., A.W.M., C.B.B., P.G. and A.G. P. performed fly husbandry and maintenance. M.A.B., M.J., M.L. and P.G. performed confocal and/or STED imaging experiments and M.A.B., P.G. and A.T.G. analyzed the data. A.W.M., M.J. and P.G. performed electrophysiological experiments and analyzed the data. U.R. performed live-imaging experiments and analysis. P.H. provided reagents and suggested additional experiments. A.T.G and A.M.W. developed software codes for image alignment and averaging and A.T.G analyzed the data. P.G. and D.D. conceived and performed translation block experiments. C.B.B. performed adult *Drosophila* brain antibody staining and imaging. C.B.B. and S.H. performed behavioral experiments and data analysis. S.H. performed Western blots. D.L. and D.O. planned and performed in vivo two-photon live calcium imaging. F.G. and S.W.H. developed and built the STED microscope. M.A.B., S.J.S., and A.M.W. wrote the paper with input from all co-authors.

Additional information

Supplementary Information accompanies this paper at https://doi.org/10.1038/s41467-019-08977-6.

Competing interests: All authors declare no competing intersets.

Reprints and permission information is available online at http://npg.nature.com/reprintsandpermissions/

Journal Peer Review Information: *Nature Communications* thanks Frederic Meunier and other anonymous reviewer(s) for their contribution to the peer review of this work. Peer reviewer reports are available.

Publisher's note: Springer Nature remains neutral with regard to jurisdictional claims in published maps and institutional affiliations.

page intentionally left blank

2.7 Publication V: Kobbersmed et al., eLife 2020

Full bibliographical reference

Kobbersmed JRL, Grasskamp AT, Jusyte M, Böhme MA, Ditlevsen S, Sørensen JB, Walter AM (2020) - *Rapid regulation of vesicle priming explains synaptic facilitation despite heterogeneous vesicle:Ca^{2+} channel distances*, eLife 9. doi:10.7554/ELIFE.51032.

Permalink: https://doi.org/10.7554/eLife.51032

Author contributions

M.J. performed electrophysiological recordings and analyzed the data. M.A.B. performed STED microscopy, and **A.T.G. analyzed the data with custom-written code.** **A.T.G. conducted presynaptic Calcium live-imaging and analyzed the data**. J.R.-L.K. and **A.T.G. wrote the code used for calcium dynamics and SV release simulations, and parameter optimization**, and J.R.-L.K. performed optimization procedures and devised stochastic simulations. S.D., J.B.S. and A.M.W. conceptualized the study and wrote the manuscript with input from all coauthors.

Contribution details

In this mainly computational study, we investigated how synapses are able to maintain short-term facilitation despite an expected depletion of releasable vesicles upon repetitive release stimulation. We could show that SV release sites follow a specific broad distribution in relation to the AZ center and therefore the SVs remaining after a stimulus should generally exhibit decreased release probabilities. We determined this broad distribution using EM and STED imaging, and compared our stochastic simulations of SV release with experimental data from electrophysiological recordings. In doing so, we found that a calcium dependent mechanism that increases the number of releasable SVs by inhibiting their unpriming explains how synaptic short-term facilitation at this synapse is achieved.

My role in this study covered two aspects:
(1) Building on the computational *Drosophila* AZ model devised for our earlier publication (Böhme et al., 2016), I (together with the first author of the study) helped to prove through simulations and optimizations that neither a single sensor with or without replenishment, nor a second facilitation sensor could produce enough facilitation at low extracellular Ca^{2+} concentrations to match experimental data.

(2) To help understand how Ca^{2+} influx through the central VGCC cluster behaves over a range of extracellular Ca^{2+} concentrations, I conducted live-imaging experiments with larvae presynaptically expressing the fluorescent Ca^{2+} sensor GCaMP6. This helped constrain the computational model by determining parameters of the Michaelis-Menten kinetics of Ca^{2+} influx into the presynaptic terminal.

Rapid regulation of vesicle priming explains synaptic facilitation despite heterogeneous vesicle:Ca^{2+} channel distances

Janus R. L. Kobbersmed[1,4], Andreas T. Grasskamp[2], Meida Jusyte[2,3], Mathias A. Böhme[2], Susanne Ditlevsen[1], Jakob B. Sørensen[4,*] & Alexander M. Walter[2,3,*]

[1]Department of Mathematical Sciences, University of Copenhagen, Universitetsparken 5, 2100 København Ø, Denmark.
[2]Molecular and Theoretical Neuroscience, Leibniz-Forschungsinstitut für Molekulare Pharmakologie, FMP im CharitéCrossOver, Charitéplatz 1, 10117 Berlin, Germany
[3]Einstein Center for Neuroscience, Charitéplatz 1 / Hufelandweg 14, 10117 Berlin, Germany
[4]Department of Neuroscience, University of Copenhagen, Blegdamsvej 3B, 2200 København N, Denmark.
*Correspondence: jakobbs@sund.ku.dk (J.B.S.), awalter@fmp-berlin.de (A.M.W.)

Published: February 20, 2020 in eLife 2020;9:e51032
Full online version and supplementary material
available at https://doi.org/10.7554/eLife.51032

Abstract

Chemical synaptic transmission relies on the Ca^{2+}-induced fusion of transmitter-laden vesicles whose coupling distance to Ca^{2+}-channels determines synaptic release probability and short-term plasticity, the facilitation or depression of repetitive responses. Here, using electron- and super-resolution microscopy at the *Drosophila* neuromuscular junction we quantitatively map vesicle:Ca^{2+} channel coupling distances. These are very heterogeneous, resulting in a broad spectrum of vesicular release probabilities within synapses. Stochastic simulations of transmitter release from vesicles placed according to this distribution revealed strong constraints on short-term plasticity; particularly facilitation was difficult to achieve. We show that postulated facilitation mechanisms operating via activity-dependent changes of vesicular release probability (e.g. by a facilitation fusion sensor) generate too little facilitation and too much variance. In contrast, Ca^{2+}-dependent mechanisms rapidly increasing the number of releasable vesicles reliably reproduce short-term plasticity and variance of synaptic responses. We propose activity-dependent inhibition of vesicle un-priming or release site activation as novel facilitation mechanisms.

Drosophila, synapse, short-term plasticity, (M)Unc13, mathematical modeling, super-resolution microscopy

Impact

Heterogeneous distances between vesicles and Ca^{2+} channels make synapses prone to short-term depression; however, Ca^{2+}-dependent increases in the number of release-ready vesicles supports facilitation even with broadly distributed vesicle:Ca^{2+} channel distances.

Introduction

At chemical synapses, neurotransmitters (NTs) are released from presynaptic neurons and subsequently activate postsynaptic receptors to transfer information. At the presynapse, incoming action potentials (APs) trigger the opening of voltage gated Ca^{2+} channels, leading to Ca^{2+} influx. This local Ca^{2+}-signal induces the rapid fusion of NT-containing synaptic vesicles (SVs) at active zones (AZs) (Sudhof, 2012). In preparation for fusion, SVs localize (dock) to the AZ plasma membrane and undergo functional maturation (priming) into a readily releasable pool (RRP) (Kaeser and Regehr, 2017; Verhage and Sorensen, 2008). These reactions are mediated by an evolutionarily highly conserved machinery. The SV protein VAMP2/Synaptobrevin and the plasma membrane proteins Syntaxin-1 and SNAP25 are essential for docking and priming and the assembly of these proteins into the ternary SNARE complex provides the energy for SV fusion (Jahn and Fasshauer, 2012). The SNARE interacting proteins (M)Unc18s and (M)Unc13s (where "M" indicates mammalian) are also essential for SV docking, priming and NT release (Rizo and Sudhof, 2012; Sudhof and Rothman, 2009), while Ca^{2+} triggering of SV fusion depends on vesicular Ca^{2+}-sensors of the Synaptotagmin family (Littleton and Bellen, 1995; Sudhof, 2013; Walter et al., 2011; Yoshihara et al., 2003). Cooperative binding of multiple Ca^{2+} ions to the SV fusion machinery increases the probability of SV fusion (pV_r) in a non-linear manner (Bollmann et al., 2000; Dodge and Rahamimoff, 1967; Schneggenburger and Neher, 2000).

A distinguishing feature of synapses is their activity profile upon repeated AP activation, where responses deviate between successive stimuli, resulting in either short-term facilitation (STF) or short-term depression (STD). This short-term plasticity (STP) fulfils

essential temporal computational tasks (Abbott and Regehr, 2004). Postsynaptic STP mechanisms can involve altered responsiveness of receptors to NT binding, while presynaptic mechanisms can involve alterations in Ca^{2+} signalling and –sensitivity of SV fusion (von Gersdorff and Borst, 2002; Zucker and Regehr, 2002). Presynaptic STD is often attributed to high pV_r synapses, where a single AP causes significant depletion of the RRP. In contrast, presynaptic STF has often been attributed to synapses with low initial pV_r and a rapid pV_r increase during successive APs. This was often linked to changes in Ca^{2+} signalling, for instance by rapid regulation of Ca^{2+} channels (Borst and Sakmann, 1998; Nanou and Catterall, 2018), saturation of local Ca^{2+} buffers (Eggermann et al., 2012; Felmy et al., 2003; Matveev et al., 2004), or the accumulation of intracellular Ca^{2+} which may increase pV_r either directly or via "facilitation sensors" (Jackman and Regehr, 2017; Katz and Miledi, 1968). Alternatively, fast mechanisms increasing the RRP were proposed (Fioravante and Regehr, 2011; Gustafsson et al., 2019; Pan and Zucker, 2009; Pulido and Marty, 2017).

The coupling distance between Ca^{2+} channels and primed SVs is an important factor governing pV_r (Bohme et al., 2018; Eggermann et al., 2012; Stanley, 2016). Previous mathematical models describing SV fusion rates from simulated intracellular Ca^{2+} transients have in many cases relied on the assumption of uniform (or near uniform) distances between SV release sites surrounding a cluster of Ca^{2+} channels and such conditions were shown to generate STF (Bohme et al., 2016; Meinrenken et al., 2002; Nakamura et al., 2015; Vyleta and Jonas, 2014). However, alternative SV-release site:Ca^{2+} channel topologies have been proposed, including two distinct perimeter distances, tight, one-to-one connections of SVs and channels, or random placement of either the channels, the SVs, or both (Bohme et al., 2016; Chen et al., 2015; Guerrier and Holcman, 2018; Keller et al., 2015; Shahrezaei et al., 2006; Stanley, 2016; Wong et al., 2014). So far, the precise relationship between SV release sites and voltage gated Ca^{2+} channels on the nanometre scale is unknown for most synapses, primarily owing to technical difficulties to reliably map their precise spatial distribution. However, (M) Unc13 proteins were recently identified as a molecular marker of SV release sites (Reddy-Alla et al., 2017; Sakamoto et al., 2018) and super-resolution (STED) microscopy revealed that these sites surround a cluster of voltage gated Ca^{2+} channels in the centre of AZs of the glutamatergic *Drosophila melanogaster* neuromuscular junction (NMJ)(Bohme et al., 2016; Bohme et al., 2019).

Here, by relying on the unique advantage of being able to precisely map Ca^{2+} channel:SV-release site topology we study its consequence for short-term plasticity at the *Drosophila* NMJ. Topologies were measured using electron microscopy (EM) following high pressure freeze fixation (HPF) or STED microscopy of Unc13 which both revealed a broad distribution of Ca^{2+} channel coupling distances. Stochastic simulations were key to identify facilitation mechanisms in the light of heterogenous vesicle:Ca^{2+} channel distances. Contrasting these simulations to physiological data revealed that models explaining STF through gradual increase in pVr (from now on called "pVr-based models") are inconsistent with the experiment while models of activity-dependent regulation of the RRP account for STP profiles and synaptic variance.

Results

Distances between docked SVs and Ca^{2+} channels are broadly distributed

We first set out to quantify the Ca^{2+} channel:SV-release site topology. For this we analysed EM micrographs of AZ cross-sections and quantified the distance between docked SVs (i.e. SVs touching the plasma membrane) and the centre of electron dense "T-bars" (where the voltage gated Ca^{2+} channels are located (Fouquet et al., 2009; Kawasaki et al., 2004)) (Fig. 1A). In wildtype animals, this leads to a broad distribution of distances ("EM dataset wildtype", Fig. 1 – figure supplement 1A) (Bohme et al., 2016; Bruckner et al., 2017). At the *Drosophila* NMJ, the two isoforms Unc13A and –B confer SV docking and priming, but the vast majority (~95 %) of neurotransmitter release and docking of SVs with short coupling distances is mediated by Unc13A (Bohme et al., 2016). We therefore investigated the docked SV distribution in flies expressing only the dominant Unc13A isoform (Unc13A rescue, see methods for exact genotypes) which showed a very similar, broad distribution of distances as wildtype animals ("EM-dataset Unc13A rescue") (Reddy-Alla et al., 2017) (Fig. 1A,B). In both cases, distance distributions were well described by a Rayleigh distribution (Fig. 1B, Fig. 1 – figure supplement 1A, solid green lines). The EM micrographs studied here are a cut cross-section of a three-dimensional synapse. To derive the relevant coupling distance distribution for all release sites (including the ones outside the cross-section), the Rayleigh distribution was integrated around a circle (Fig. 1C), resulting in the following probability density function (pdf, see Methods for derivation):

$$g(x) = \frac{\sqrt{2}}{\sqrt{\pi} \cdot \sigma^3} \cdot x^2 \cdot e^{-x^2/(2\sigma^2)}$$

These pdfs were more symmetrical than the one from the cross-sections and peaked at larger distances (as expected from the increase in AZ area with increasing radius) (Fig. 1D). The estimation of this pdf was very robust, resulting in near identical curves for the two EM datasets (Fig. 1 – figure supplement 1B).

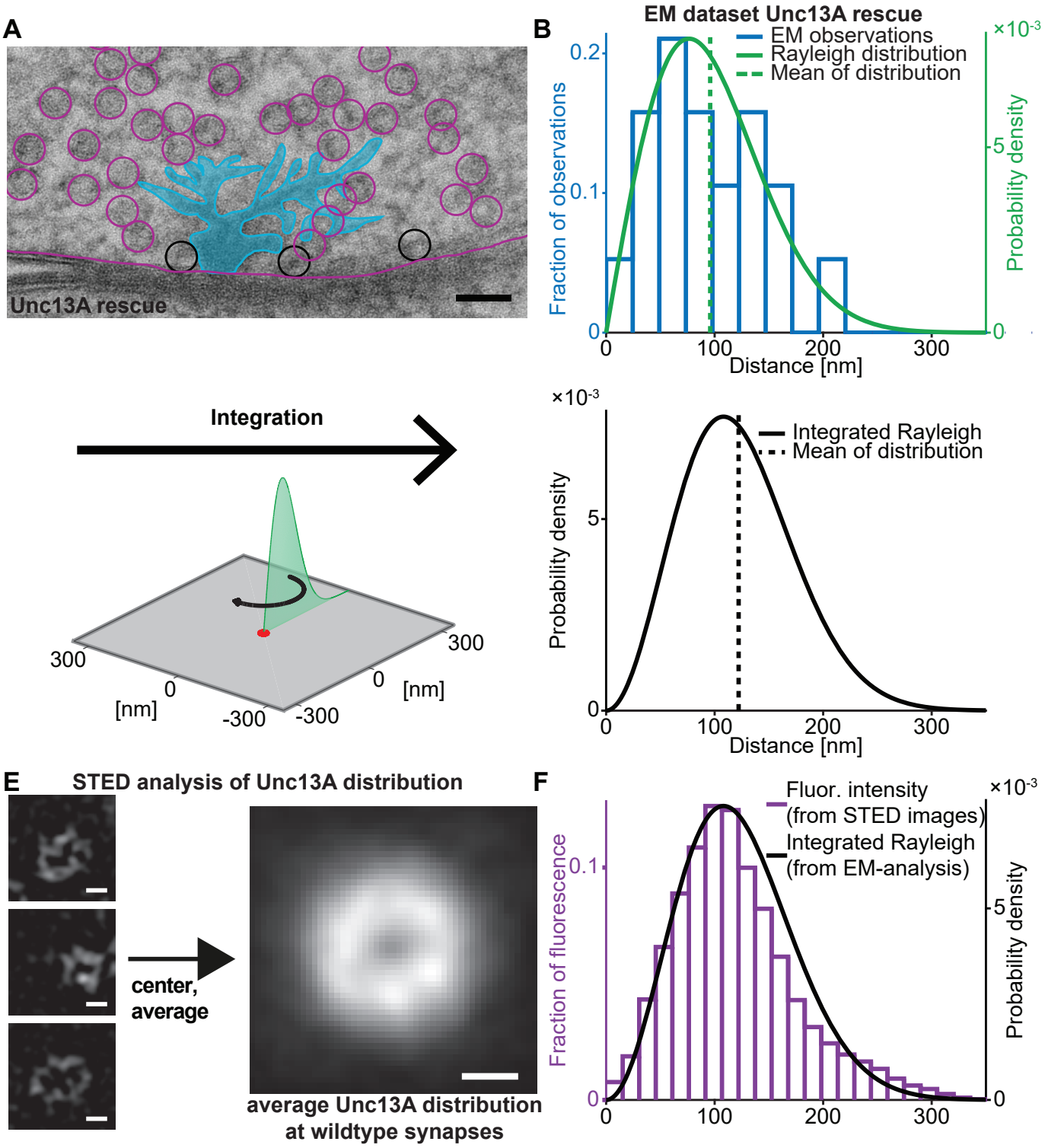

Figure 1. Deriving the spatial docked SV distribution. **(A)** Example EM image of an NMJ active zone (AZ) obtained from a 3rd instar *Drosophila* larva expressing the dominant Unc13A isoform after high pressure freeze fixation. The image captures a T-bar cross section. For clarity, the T-bar is colored in light blue, SVs are indicated with circles, the outline of the presynaptic plasma membrane is shown. Docked SVs are marked with black circles. Black scale bar: 50 nm. **(B)** Histogram of the distances of docked SVs to the T-bar center obtained from EM micrographs (19 SVs observed in n = 10 EM cross-sections/cells from at least two animals, the same distance measurements had previously been used for the analysis depicted in Fig. 5 of (Reddy-Alla et al., 2017)). The solid green line is the fitted Rayleigh distribution (σ = 76.5154 nm, mean is 95.9 nm, standard deviation, SD is 50.1 nm). **(C)** The one-dimensional Rayleigh distribution (green line) is integrated in order to estimate the docked SV distance distribution in the whole presynapse. **(D)** The integrated Rayleigh distribution is more symmetric, and the mean increases to 122.1 nm. SD is 51.5 nm. **(E)** The three left example images show AZs stained against Unc13A and imaged on a STED microscope. The right hand image shows the average fluorescence signal for 524 individual centered AZ images from 16 different NMJs and more than 3 different animals (see Methods for details). White scale bars: 100 nm. **(F)** Histogram of fluorescence intensities against distance from the AZ center, as derived from the average STED image plotted together with the integrated Rayleigh distribution derived from the EM analysis (replotted from panel D), showing a close agreement between the two approaches. Additional EM analysis of wildtype flies and the analysis of an independent STED experiment are compared to the data depicted here in Fig.1 - figure supplement 1. Used genotype: Unc13A rescue (panel A, B), *w[1118]* (panel E, F). Methods section "Fly husbandry, genotypes and handling" lists all genotypes**.** Raw data corresponding to the depicted histograms can be found in the accompanying source data file (Figure 1 – Source Data 1). Scripts used for analysis of average STED image and plotting of histograms in 1B and 1F can be found in accompanying source data zip file (Figure 1 – Source Data 2).

We also used an independent approach to investigate the distribution of docked vesicle:Ca^{2+} channel coupling distances without relying on the integration of docked SV observations from cross-sections: since (M)Unc13 was recently described as a molecular marker of SV release sites (Reddy-Alla et al., 2017; Sakamoto et al., 2018) we investigated AZ images of wildtype NMJs stained against Unc13A (Bohme et al., 2019). Hundreds of individual AZ STED images (lateral resolution of approx. 40 nm) were aligned and averaged to obtain an average image of the AZ (Fig. 1E), which revealed a ring-like distribution of the Unc13A fluorescence. In previous works we had established that the voltage gated Ca^{2+} channels reside in the center of this ring (Bohme et al., 2016). As this average image already reflects the distribution throughout the AZ area (unlike for the EM data above where an integration was necessary) the distribution of coupling distances can directly be computed based on pixel intensities and their distance to the AZ centre. Two independent datasets where analysed, resulting in very similar average images and distance distributions ("wildtype STED dataset 1&2", Fig. 1 – figure supplement 1).

Remarkably, although the two approaches (EM and STED microscopy) were completely independent, the distributions of coupling distances quantified by either method coincided very well (Fig. 1F, Fig. 1 – figure supplement 1D; note that the integrated Rayleigh distributions were determined from EM micrographs and integration; they were not fit to the Unc13A distribution), supporting the accuracy of this realistic release site topology. The compliance between SV docking positions and Unc13A distribution further indicates that SVs dock to the plasma membrane where priming proteins are available, and therefore the entire distribution of docked SVs is potentially available for synaptic release (Imig et al., 2014).

Physiological assessment of short-term facilitation and depression at the *Drosophila* NMJ

Having identified the high degree of heterogeneity in the docked SV:Ca^{2+}-channel coupling distances, we became interested in how this affected synaptic function. We therefore characterized synaptic transmission at control NMJs (*Ok6-GAL4* crossed to *w[1118]*) in two electrode voltage clamp experiments. A common method to quantitatively evaluate synaptic responses and their STP behaviour is to vary the Ca^{2+} concentration of the extracellular solution which affects AP-induced Ca^{2+} influx (see below). We used this approach and investigated responses evoked by repetitive (paired-pulse) AP stimulations (10 ms interval). In line with classical studies (Dodge and Rahamimoff, 1967), our results display an increase of the evoked Excitatory Junctional Current (eEJC) responses to the first AP

Figure 2. Electrophysiological characterization of synaptic transmission in muscle 6 NMJs. Left panel (**A**, **C**, **E**) shows example traces from one cell. Right panel (**B**, **D**, **F**) shows quantification across cells. **(A)** Representative eEJC traces from a single cell measured at different Ca^{2+} concentrations (0.75 – 10 mM). **(B)** Average $eEJC_1$ amplitudes and SD from 6 animals as a function of extracellular Ca^{2+} concentration. **(C)** Representative eEJC traces of paired pulse paradigm (10 ms inter-stimulus interval, normalized to $eEJC_1$) from single cell measured at different Ca^{2+} concentrations (0.75 – 10 mM). While STF can be seen at the two lowest extracellular Ca^{2+} concentrations (0.75 and 1.5 mM), the cell exhibits STD for extracellular Ca^{2+} concentrations of 3 mM or more. Insert (gray background) shows calculation of $eEJC_2$. An exponential function was fitted to the decay to estimate the baseline for the second response (see Methods for details). **(D)** Mean and SD of PPR values (6 cells from 6 animals) at different Ca^{2+} concentrations. **(E)** Experiment to assess variance of repeated synaptic responses in a single cell. $eEJC_1$ traces in response to nine consecutive AP stimulations (10 s interval) are shown (orange lines) together with the mean $eEJC_1$ response (black line) at different extracellular Ca^{2+} concentrations (0.75 – 10 mM, see methods). **(F)** Plot of mean $eEJC_1$ variance as a function of the mean $eEJC_1$ amplitude across 6 cells from 6 animals for each indicated Ca^{2+} concentration. The curve shows best fitted parabola with intercept forced at (0,0)($Var=-0.0061*<eEJC_1>^2+0.6375*<eEJC_1>$, corresponding to $n_{sites}=164$ and $q=0.64$ when assuming a classical binomial model (Clements and Silver, 2000), see Methods). For the variance-mean relationship of the single cell depicted in Fig. 2F, please refer to Fig. 2 – figure supplement 2. Experiments were performed in *Ok6-Gal4/+* 3rd instar larvae, often used as a control genotype for experiments using cell-specific driver lines. Separate experiments were performed to ensure that this genotype showed similar synaptic responses and STP behavior as wildtype animals (Figure 2 – figure supplement 3). Used genotype: *Ok6-Gal4/II* crossed to *w[1118]*. Methods section "Fly husbandry, genotypes and handling" lists all exact genotypes. Data points depict means, error bars are SDs across cells except in (F), where error bars show SEM. Raw data corresponding to the depicted graphs can be found in the accompanying source data file (Figure 2 – Source Data 1). Scripts for analysis of recorded traces are found in accompanying source data zip file (Figure 2 – Source Data 2). Raw traces from paired-pulse experiments summarized in Fig.2 and Fig. 2 figure supplements 2 and 3 can be found in Fig.1 – source data 3, 4, and 5. Estimation of $eEJC_2$ amplitudes and fitting of a smooth mEJC function (used in simulations, see Methods) are illustrated in Figure 2 – figure supplement 1.

($eEJC_1$ amplitudes) with increasing extracellular Ca^{2+} (Fig. 2A,B). STP was assessed by determining the paired-pulse ratio (PPR): The amplitude of the second response divided by first. The $eEJC_2$-amplitude was determined taking the decay of $eEJC_1$ into account (see insert in Fig. 2C, Fig. 2 – figure supplement 1A). At low extracellular Ca^{2+} (0.75 mM), we observed strong STF (with an average PPR value of 1.80), which shifted towards depression (PPR<1) with increasing Ca^{2+}-concentrations (Fig. 2C,D). Thus, the same NMJ displays both facilitation and depression depending on the extracellular Ca^{2+} concentration, making this a suitable model synapse to investigate STP behaviour.

In panels B and D the mean $eEJC_1$ amplitudes and PPRs from 6 animals are shown and the error bars indicate standard deviation, SD (across all animals). We also examined the variation of repeated AP-evoked responses at the same NMJ between trials (10 seconds apart) at different extracellular Ca^{2+}-concentrations (Fig. 2E,F). At low concentrations (0.75 mM), the probability of transmitter release is low, resulting in a low mean $eEJC_1$ amplitude with little variation (Fig. 2E,F, Fig. 2 – supporting data figure 2). With increasing extracellular Ca^{2+}, the likelihood of SV fusion increased and initially so did the variance (e.g. at 1.5 mM extracellular Ca^{2+}). However, further increase in extracellular Ca^{2+} (3 mM, 6 mM, 10 mM) led to a drop in variance (Fig. 2E, Fig. 2 – figure supplement 2). Figure 2F depicts this average

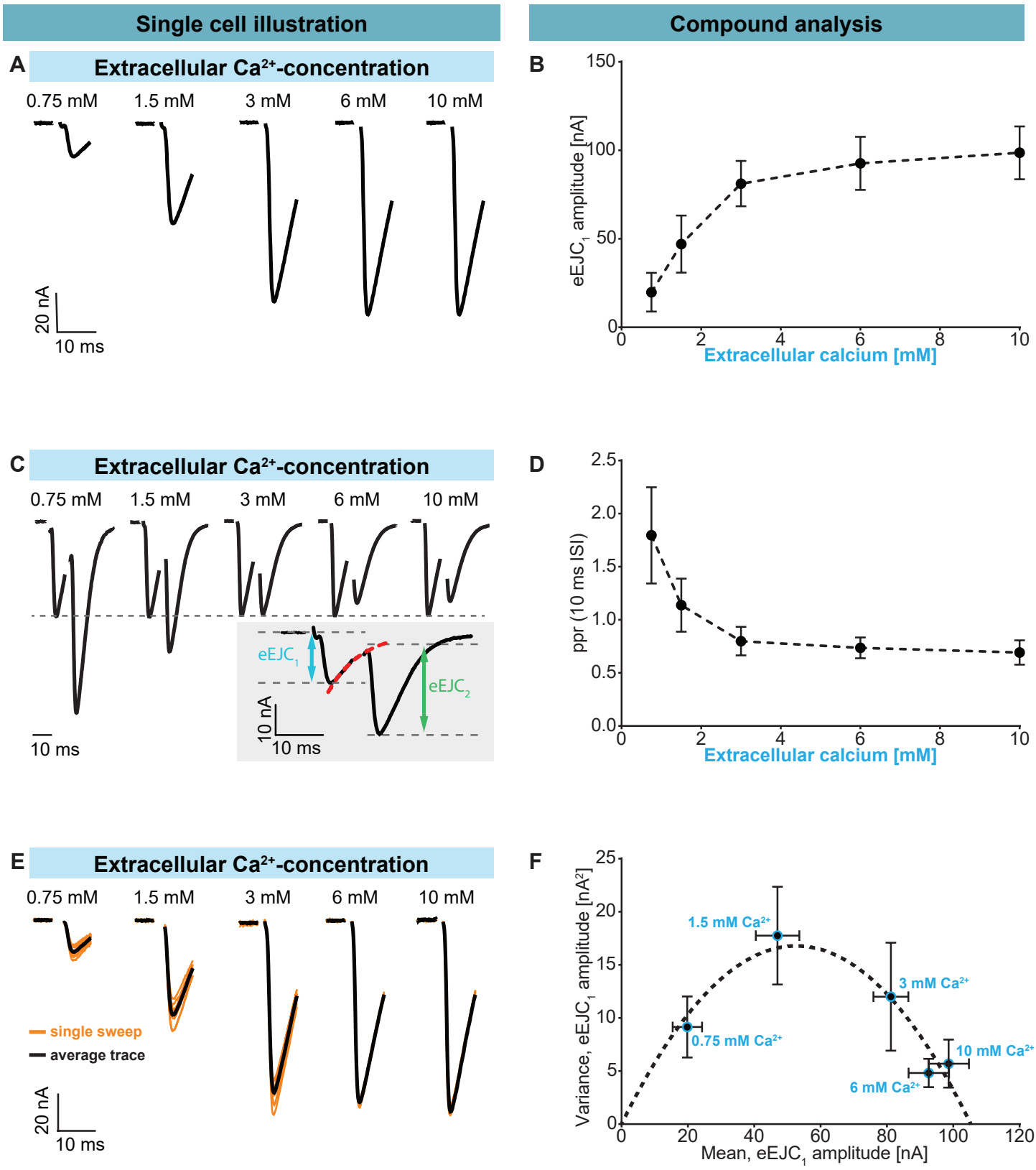

"variance-mean" relationship from 6 cells (means of cell means and means of cell variances, error bars indicate SEM). When assuming a binomial model, this approach has often been used to estimate the number of release sites n_{sites} and the size of the postsynaptic response elicited by a single SV (q)(Clements and Silver, 2000). In agreement with previous studies of the NMJ this relationship was well described by a parabola with forced intercept at y=0 and n_{sites}=164 and q=0.64 (Fig. 2F, Fig. 2 – figure supplement 2)(Matkovic et al., 2013; Muller et al., 2012; Weyhersmuller et al., 2011).

Simulation of AP-induced Ca^{2+} signals

Having determined the distribution of coupling distances (Fig. 1) and the physiological properties of the NMJ synapse (Fig. 2), we next sought to compare how the one affected the other. There are two things two consider here. First of all, the SV release probability steeply depends on the 4th to 5th power of the local Ca^{2+} concentration (Neher and Sakaba, 2008). Secondly, because of the strong buffering of Ca^{2+} signals at the synapse, the magnitude of the AP-evoked Ca^{2+} transients dramatically declines with distance from the Ca^{2+} channel (Bohme et al., 2018; Eggermann et al., 2012). These two phenomena together make the vesicular release probability extremely sensitive to the coupling distance to the Ca^{2+} channels. Because we find that this distance is highly heterogeneous among SVs within the same NMJ, the question arises how these two properties (heterogeneity of distances combined with a strong distance dependence of pV_r) functionally impact on synaptic transmission. Indeed, approaches by several labs to map the activity of individual NMJ AZs revealed highly heterogeneous activity profiles (Akbergenova et al., 2018; Gratz et al., 2019; Muhammad et al., 2015; Peled and Isacoff, 2011).

To quantitatively investigate the functional impact of heterogeneous SV placement, we wanted to use mathematical modeling to predict AP-induced fusion events of docked SVs placed according to the found distribution. A prerequisite for this is to first faithfully simulate local, AP-induced Ca^{2+} signals throughout the AZ (such that the local transients at each docking site are known). We first determined the relevant AZ dimensions at the *Drosophila* NMJ, which, similarly to the murine Calyx of Held, is characterized by many AZs operating in parallel. We therefore followed previous suggestions from the Calyx using a box with reflective boundaries containing a cluster of Ca^{2+} channels in the base center (Meinrenken et al., 2002). The base dimensions (length=width) were determined as the mean inter-AZ distance of all AZs to their four closest neighbours (because of the 4-fold symmetry) from NMJs stained against the AZ-marker BRP (Kittel et al., 2006; Wagh et al., 2006)(Fig. 3A). To save computation time, we further simplified to a cylindrical simulation (where the distance to the Ca^{2+} channel is the only relevant parameter) covering the same AZ area (Fig. 3B, Table 1).

To simulate the electrophysiological experiments above, where the extracellular Ca^{2+} concentration was varied (Fig. 2), it was important to establish how the extracellular Ca^{2+} concentration influenced AP-induced Ca^{2+} influx. In particular, it is known that Ca^{2+} currents saturate at high extracellular Ca^{2+} concentrations (Church and Stanley, 1996). Unlike other systems, the presynaptic NMJ terminals are not accessible to electrophysiological recordings, so we could not measure the currents directly. We therefore used a fluorescence-based approach as a proxy. AP-evoked Ca^{2+} influx was assessed in flies presynaptically expressing the Ca^{2+}-dependent fluorescence reporter GCaMP6m (*;P{y[+t7.7] w[+mC]=20XUAS-IVS-GCaMP6m}attP40/Ok6-GAL4)*. Fluorescence increase was monitored upon stimulation with 20 APs (at 20 Hz) while varying the extracellular Ca^{2+} concentration and showed saturation behaviour for high concentrations (Fig. 3 – figure supplement 1). This is consistent with a previously described Michaelis-Menten type saturation of fluorescence responses of a Ca^{2+} sensitive dye upon single AP stimulation at varying extracellular Ca^{2+} concentrations at the Calyx of Held, where half-maximal Ca^{2+} influx was observed at 2.6 mM extracellular Ca^{2+} (Schneggenburger et al., 1999). This relationship was successfully used in the past to predict Ca^{2+} influx in modeling approaches (Trommershauser et al., 2003). In our measurements, we determined a half maximal fluorescence response at a very similar concentration of 2.68 mM extracellular Ca^{2+} and therefore used this value in a Michaelis-Menten equation (Materials and Methods, equation 5) to calculate AP-induced presynaptic Ca^{2+} influx. The second parameter of the Michaelis-Menten equation, (the maximal Ca^{2+} current charge, Q_{max}) was optimized for each model (Fig. 3 – figure supplement 2, for best fit parameters see table 3). We furthermore assumed that basal, intracellular Ca^{2+} concentrations at rest were also slightly dependent on the extracellular Ca^{2+} levels in a Michaelis-Menten relationship with the same $K_{M,current}$ and a maximal resting Ca^{2+} concentration of 190 nM (resulting in 68 nM presynaptic basal Ca^{2+} concentration at 1.5 mM external Ca^{2+}). With these and further parameters taken from the literature on Ca^{2+} diffusion and buffering (see Table 1) the temporal profile of Ca^{2+} signals in response to paired AP stimulation (10 ms interval) could be calculated at all AZ locations using the software CalC (Matveev et al., 2002)(Fig. 3C, Fig.3 – figure supplement 2). This enabled us to perform simulations of NT release from vesicles placed according to the distribution described above.

Stochastic simulations and fitting of release models

In the past, we and others have often relied on deterministic simulations based on numerical integration of kinetic reaction schemes (ordinary differential equations, ODEs). These are computationally effective and fully reproducible, making them well-behaved and ideal for the optimisation of parameters (a property that was also used here for initial parameter searches, see Methods). However, NT release is quantal and relies on only a few (hundred) SVs, indicating that stochasticity plays a large role (Gillespie, 2007). Moreover, deterministic simulations always predict identical output making it impossible to analyse the synaptic variance between successive stimulations, which is a fundamental hallmark of synaptic transmission and an important physiological

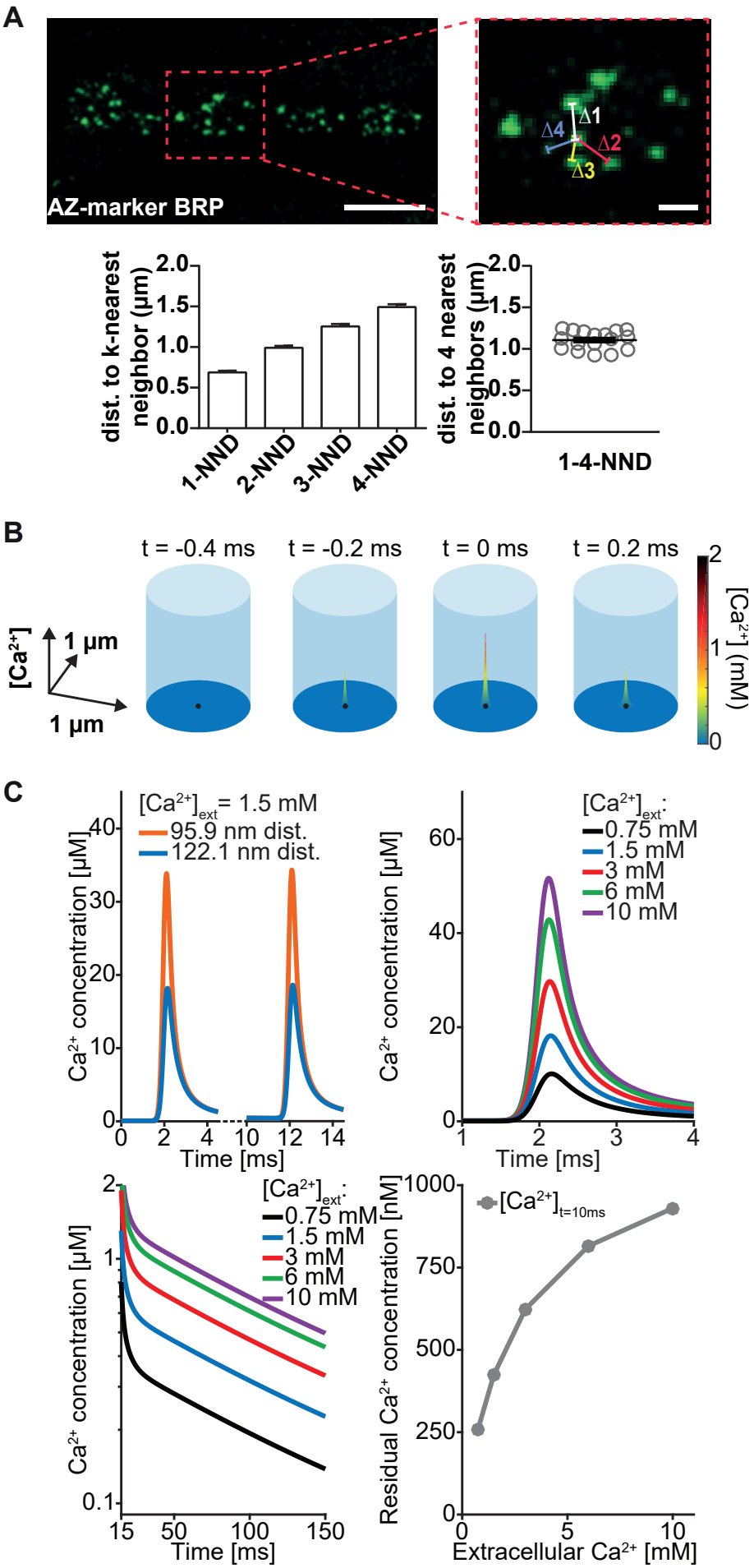

Figure 3. Estimation of the simulation volume and Ca^{2+} simulations. **(A)** The left hand image shows a confocal scan of a 3rd instar larval NMJ stained against the AZ marker Bruchpilot (BRP). The right hand image shows a higher magnification of the indicated region. To determine the dimensions of the simulation volume, the average distance of each AZ to its closest four neighboring AZs (*k*-NND = k^{th} nearest neighbor distance) was determined. The average inter-AZ distance to each of the closest four neighboring AZs (1- through 4-NND) is depicted on the left. Average and SEM of inter-AZ distances (1-4-NND) are depicted on the right. White scale bars: Left: 5 µm; right: 1 µm. **(B)** Example illustration of the Ca^{2+} simulation. The simulation volume is a cylinder whose base area is the same as a square with side length of the mean 1-4-NND. The local Ca^{2+} concentration is shown at different time points following an AP-induced Gaussian Ca^{2+} current (the area/height is a free parameter, see Table 3, the FWHM is 0.36 ms), t = 0 ms is the time of the peak current. The Ca^{2+} (point) source is located in the AZ center (black dot) and the Ca^{2+} concentration is determined at 10 nm height from the plasma membrane. **(C)** Example simulation of the local Ca^{2+} concentration profile in response to stimulation with a pair of APs (current peak at 2 and 12 ms,). Simulations were performed using the best fit parameters of the single sensor model described below (see Fig. 4, Table 3). Top left: Ca^{2+} transients in response to the first AP at two distances: 95.9 nm and 122.1 nm (the mean of Rayleigh/integrated Rayleigh). Top right: AP-induced Ca^{2+} transient at 122.1 nm for all experimental extracellular Ca^{2+} concentrations. Bottom left: Semi-logarithmic plot of Ca^{2+} decays toward baseline after the 2nd transient (residual Ca^{2+}) at different extracellular Ca^{2+} concentrations ($[Ca^{2+}]_{ext}$). Time constant of decay is τ = 111 ms. Bottom right: Residual Ca^{2+} levels at 122.1 nm 10 ms after the first stimulus as a function of extracellular Ca^{2+} concentrations. Data depicted in panel A were collected from 17 different animals. Used genotype: *w[1118]; P{w[+mC]=Mhc-SynapGCaMP6f}3-5* (Bloomington Stock No. 67739, panel A). Methods section "Fly husbandry, genotypes and handling" lists all exact genotypes. Values used for graphs can be found in the accompanying source data file (Figure 3 – Source Data 1). GCaMP6m experiment is summarized in Figure 3 – figure supplement 1. Ca^{2+} signals for all optimised models (below) are summarised in Figure 3 – figure supplement 2.

parameter (Fig. 2F) (Scheuss and Neher, 2001; Vere-Jones, 1966; Zucker, 1973). Stochastic simulations allow a prediction of variance which can help identify adequate models that will not only capture the mean of the data, but also its variance. To compare this, data points are now shown with error bars indicating the square root of the average variance between stimulations within a cell (Figs. 4C,E, 6E,G, 7E,G). This is the relevant parameter since the model is designed to resemble an 'average' NMJ' and therefore cannot predict inter-animal variance. Finally, as we show here (full proof in Methods) deterministic simulations cannot be compared

to experimentally determined PPR values because of Jensen's inequality (full proof in Methods, see Fig. 4 - figure supplement 1). Thus, stochastic simulations are necessary to account for SV pool sizes, realistic release site distributions, synaptic variance and STP. We thus implemented stochastic models of SV positions (drawn randomly from the distribution above) and SV Ca^{2+} binding states based on inhomogeneous, continuous time Markov models with transition rates governing reaction probabilities (see Methods for details).

We also needed to consider where new SVs would (re)dock once SVs had fused and implemented the simplest scenario of re-docking in the same positions. This ensures a stable distribution over time and agrees with the notion that vesicles prime into pre-defined release sites, which are stable over much longer time than a single priming/unpriming event (Reddy-Alla et al., 2017).

A single-sensor model fails to induce sufficient facilitation and produces excessive variance

The first model we tested was the single-sensor model proposed by Lou et al. (Lou et al., 2005), where an SV binds up to 5 Ca^{2+} ions, with each ion increasing its fusion rate or probability (Fig. 4A). Release sites were placed according to the distance distribution in Fig. 1D and all sites were occupied by a primed SV prior to stimulation (i.e. the number of release sites equals the number of vesicles in the RRP). Sites becoming available following SV fusion were replenished from an unlimited pool, making the model identical to the one described by Wölfel et al (Wolfel et al., 2007). Ca^{2+}-(un)binding kinetics were taken from Wölfel et al. (Wolfel et al., 2007), the values of the maximal Ca^{2+} current charge (Q_{max}), the SV replenishment rate (k_{rep}) and the number of release sites (n_{sites}) were free parameters optimized to match the experimental data (see Methods for details, best fit parameters in Table 3).

To be able to compare the output of this and all subsequent models to experimental data as depicted in Fig. 2 (postsynaptic eEJC measurements), the predicted fusion events were convolved with a typical postsynaptic response to the fusion of a single SV (mEJC, Fig. 2 – figure supplement 1B, see methods for more details). From the stochastic simulations (1000 runs each), we calculated the mean and variance

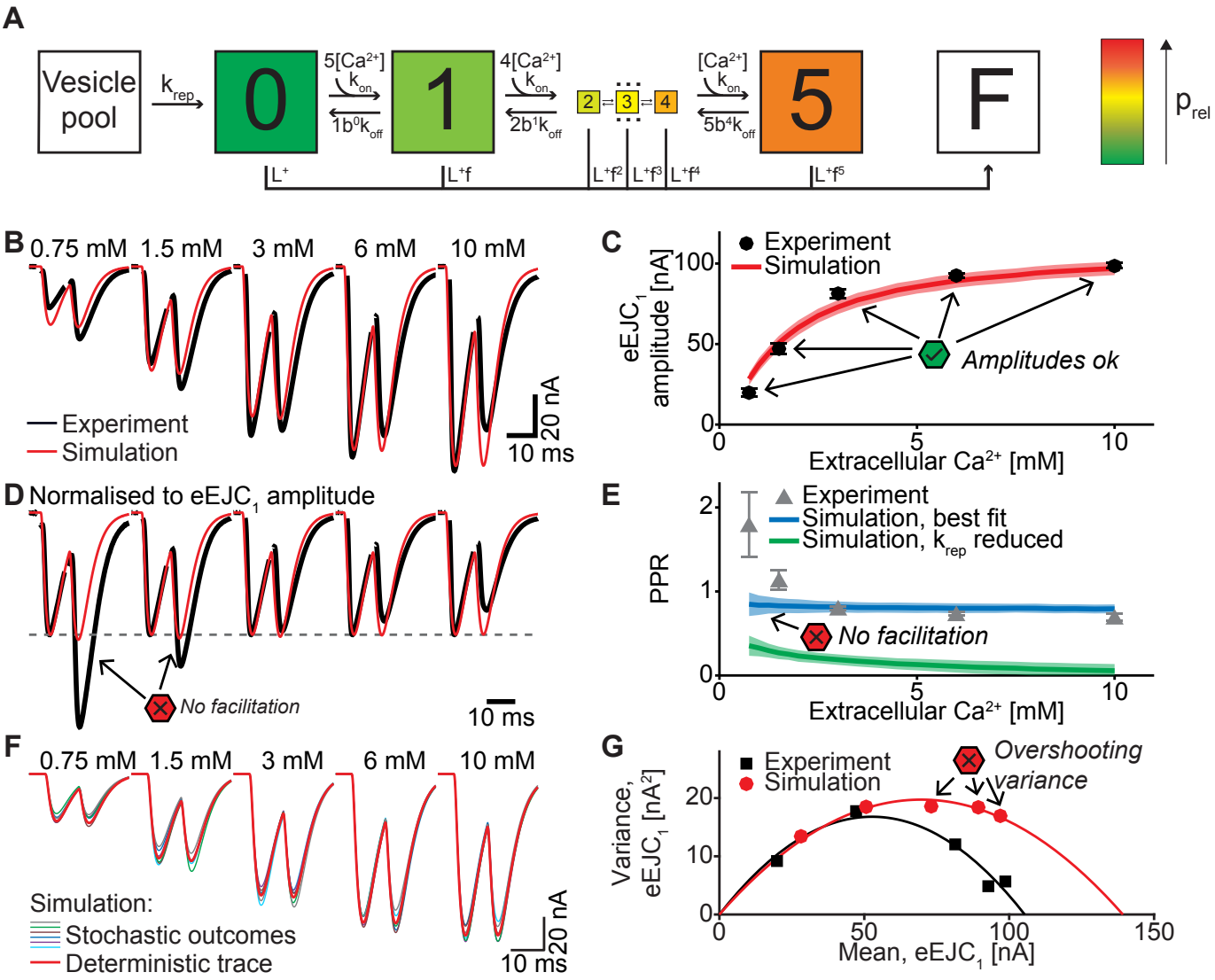

of $eEJC_1$ amplitudes, and the mean and variance of PPRs at various extracellular Ca^{2+} concentrations and contrasted these with the experimental data.

This single-sensor model was able to reproduce the $eEJC_1$ values (Fig. 4B,C). Moreover, the model accounted for the STD typically observed at high extracellular Ca^{2+} concentrations in the presence of rapid replenishment (Hallermann et al., 2010; Miki et al., 2016)(our best fit yielded $\tau \approx 6.0$ ms and reducing this rate led to unnaturally strong depression, Fig. 4E, green curve+area). However, even despite rapid replenishment this model failed to reproduce the STF observed at low extracellular Ca^{2+} (Fig. 4D,E) and the variances predicted by this model were much larger than found experimentally (Fig. 4F,G). The observation that $eEJC_1$ amplitudes were well accounted for, but STPs were not, may relate to the fact that this model was originally constructed to account for a single Ca^{2+}-triggered release event (Lou et al., 2005). As this model lacks a specialized mechanism to induce facilitation, residual Ca^{2+} binding to the Ca^{2+}-sensor is the only facilitation method which appears to be insufficient (Jackman and Regehr, 2017; Ma et al., 2015; Matveev et al., 2002). This result differs from our previous study using this model where we had placed all SVs at the same distance to Ca^{2+} channels which reliably produced STF (Bohme et al., 2016). So why does the same model fail to produce STF with this broad distribution of distances? To understand this we investigated the spatial distribution of SV release in simulations of the paired-pulse experiment at 0.75 mM extracellular Ca^{2+} (Fig. 5).

Figure 4. A single-sensor model reproduces the magnitude of transmission to single APs, but cannot account for STF and variances. **(A)** Diagram of the single-sensor model. Consecutive binding of up to 5 Ca^{2+} ions to a vesicular Ca^{2+} sensor increases the probability of SV fusion (transition to state F) indicated by the color of the state. Primed SVs can be replenished from an infinite pool. **(B)** Experimental eEJC traces averaged over all cells (black) together with average simulated traces (red). **(C)** $eEJC_1$ amplitudes of experiment (black) and simulation (red). Error bars and colored bands show the standard deviations of data (see text) and simulations, respectively. Simulations reproduce $eEJC_1$ amplitudes well. **(D)** Average (over all cells), normalized eEJC traces of experiment (black) and simulation (red). Simulations obtained with this model lack facilitation, as indicated by the red symbols. **(E)** PPR values of experiment (gray) and best fit simulation (blue). Green curve show simulations with replenishment 100x slower than the fitted value illustrating the effect of replenishment on the PPR. Error bars and colored bands show standard deviation. Best fit simulations do not reproduce the facilitation observed in the experiment at low extracellular Ca^{2+} concentrations. **(F)** Average simulated traces (black) and examples of different outcomes of the stochastic simulation (colors). **(G)** Plot of the mean synaptic variance vs. the mean $eEJC_1$ amplitudes, both from the experiment (black) and the simulations (red). The curves show the best fitted parabolas with forced intercept at (0,0)(simulation: $Var=-0.0041*<eEJC_1>^2+0.5669*<eEJC_1>$, corresponding to $n_{sites}=244$ and $q=0.57$ when assuming a classical binomial model (Clements and Silver, 2000), see Methods). Simulations reveal too much variance in this model. Experimental data (example traces and means) depicted in panels B-E,G are replotted from Fig. 2A-D,F. All parameters used for simulation can be found in tables 1,2,3. Simulation scripts can be found in the source code file. Results from simulations (means and SDs) can be found in the accompanying source data file (Figure 4 – Source Data 1). Exploration of the difference between PPR estimations in deterministic and stochastic simulations are illustrated in Figure 4 – figure supplement 1.

In the absence of a facilitation mechanism, only part of the SV distribution is utilized

Fig. 5A depicts two examples of synapses – seen from above – with SVs randomly placed according to the distance distribution in Figs. 1D/5B. The synapse is shown immediately before AP_1, immediately after AP_1, immediately before AP_2 (i.e. after refilling) and immediately after AP_2 (the external Ca^{2+} concentration was 0.75 mM). From this analysis it becomes clear that the pV_r1 caused by AP_1 essentially falls to zero around the middle of the SV distribution (Fig. 5B, top panel). This means that only SVs close to the synapse center fuse, and these high-pV_r SVs are depleted by AP_1. SV replenishment refills the majority (but not all) of those sites and thus AP_2/pV_r2 essentially draws on the same part of the distribution (Fig. 5B, bottom panel). Because of this, and because the refilling is incomplete, this causes STD. Even with faster replenishment (which would be incompatible with the low PPR values at high extracellular Ca^{2+}, Fig. 4E) this scenario would only lead to a modest increase of the PPR to values around 1. Therefore, our analysis reveals that large variation in Ca^{2+} channel distances results in a specific problem to generate STF. Our analysis further indicates that with the best fit parameters of the single sensor model, the majority of SVs (those further away) is not utilized at all.

A dual fusion-sensor model improves PPR values, but generates too little facilitation and suffers from asynchronous release and too much variance

The single-sensor model failed to reproduce the experimentally observed STF at low extracellular Ca^{2+} concentrations because of the dominating depletion of SVs close to Ca^{2+} channels, and the inability to draw on SVs further away. However, this situation may be improved by a second Ca^{2+} sensor optimized to enhance the pV_r2 in response to AP_2 . Indeed, in the absence of the primary Ca^{2+} sensor for fusion, Ca^{2+} sensitivity of synaptic transmission persists, which was explained by a dual sensor model (Sun et al., 2007). It was recently suggested that syt-7 functions alongside syt-1 as a Ca^{2+} sensor for release (Jackman et al., 2016), and a deterministic mathematical dual fusion-sensor model assuming homogeneous release probabilities (which implies homogeneous vesicle:Ca^{2+} channel distances) was shown to generate facilitation (Jackman and Regehr, 2017). Similarly, stochastic modeling of NT release at the frog NMJ also showed a beneficial effect of a second fusion sensor for STF (Ma et al., 2015). We therefore explored whether a dual fusion sensor model could account for synaptic facilitation from realistic release site topologies.

The central idea of this dual fusion-sensor model is that while syt-1 is optimized to detect the rapid, AP-induced Ca^{2+} transients (because of its fast Ca^{2+} (un)binding rates, but fairly low Ca^{2+} affinity), the

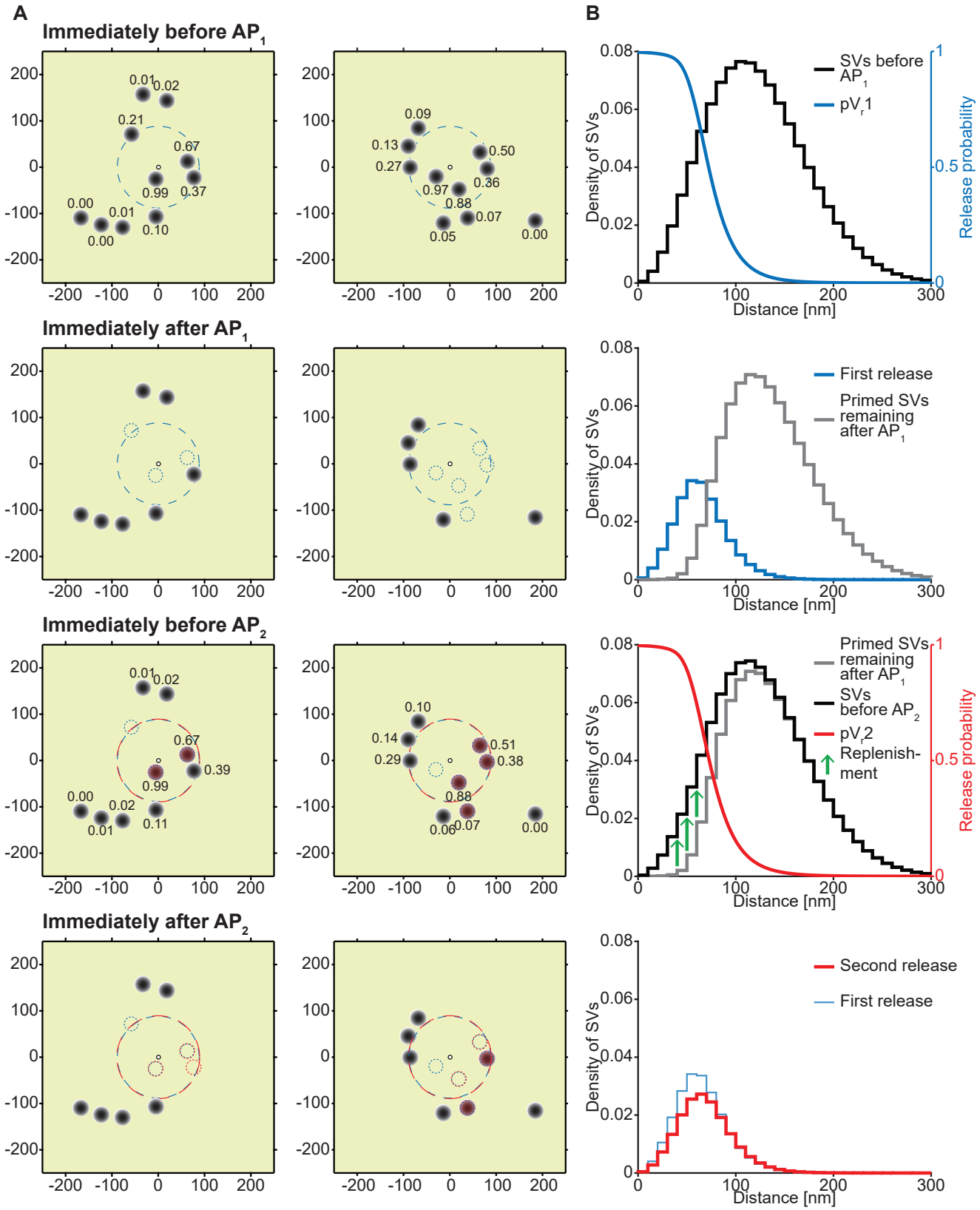

Figure 5. Analysis of the spatial dependence of SV fusion in the single-sensor model reveals a near-identical use of release sites during the two APs, thereby favoring STD. **(A)** Two examples of docked SVs stochastically placed according to the distribution described in Fig. 1D and their behavior in the PPR simulation at 0.75 mM extracellular Ca^{2+}. For clarity, 10 SVs are shown per AZ (the actual number is likely lower) and only a central part of the AZ is shown. Top row: Prior to AP_1 SVs are primed (dark gray circles) and pV_r1 is indicated as numbers. The larger dashed, blue circle in the AZ center indicates $pV_r1 = 0.25$. Second row: After AP_1 some of the SVs have fused (dashed blue circles). Third row: Right before AP_2 some of the SVs that had fused in response to AP_1 have been replenished (orange shading), and pV_r2 is indicated as a number. The larger dashed, red circle indicates $pV_r2 = 0.25$. Bottom row: After AP_2 the second release has taken place. Small dashed circles indicate release from AP_1 and AP_2 (blue and red, respectively). The small increase in pV_r caused by Ca^{2+} accumulation cannot produce facilitation because of depletion of SVs. **(B)** The average simulation at the same time points as in (A). Histograms represent primed SVs (black and gray) as well as first and second release (blue and red) illustrating how release from AP_1 and AP_2 draw on the same subpopulation of SVs. The blue and red curves indicate the vesicular release probability as a function of distance during AP_1 (blue) and AP_2 (red). The green arrows show the repopulation of previously used sites via replenishment. AP_2 draws on the same portion of the SV distribution as AP_1 causing depression despite the fast replenishment mechanism. Parameters used for simulations can be found in tables 1,2,3.

cooperating Ca^{2+} sensor is optimized to sense the residual Ca^{2+} after this rapid transient (Fig. 3C) (with slow Ca^{2+} (un)binding, but high Ca^{2+}-affinity). The activation of this second sensor after (but not during) AP_1 could then enhance the release probability of the remaining SVs for AP_2 (Fig. 6A,B). This is illustrated in Fig. 6B, where k_2 (the on-rate of Ca^{2+} binding to the slow sensor) is varied resulting in different time courses and amounts of Ca^{2+} binding to the second sensor. Increasing the release probability is equivalent to lowering the energy barrier for SV fusion (Schotten et al., 2015). In this model both sensors regulate pV_r and therefore additively lower the fusion barrier with each associated Ca^{2+} ion (Fig. 6A), resulting in multiplicative effects on the SV fusion rate. While the fast fusion reaction appears to have a 5-fold Ca^{2+} cooperativity (Bollmann et al., 2000; Burgalossi et al., 2010; Schneggenburger and Neher, 2000), it is less clear what the Ca^{2+} cooperativity of a second Ca^{2+} sensor may be, although the fact that the cooperativity is reduced in the absence of the fast sensor (Burgalossi et al., 2010; Kochubey and Schneggenburger, 2011; Sun et al., 2007) could be taken as evidence for a Ca^{2+} cooperativity <5. We explored cooperativities 2, 3, 4, and 5 (cooperativities 2 and 5 are displayed in Fig. 6 and Fig. 6 – figure supplement 1). It is furthermore not clear whether such a sensor would be targeted to the SV (like syt-1/-2), or whether it is present at the plasma membrane. Both scenarios are functionally possible and it was indeed reported that syt-7 is predominantly or partly localized to the plasma membrane (Sugita et al., 2001; Weber et al., 2014). A facilitation sensor on the plasma membrane would be more effective, which our simulations confirmed (not shown), because it would not be consumed by SV fusion, allowing the sensor to remain activated. We therefore present this version of the model here. We used a second sensor with a Ca^{2+} affinity of K_D = 1.5 µM (Brandt et al., 2012; Jackman and Regehr, 2017).

Like for the single-sensor model, all release sites were occupied with releasable vesicles (n_{sites} equals the number of RRP vesicles) and their locations determined by drawing random numbers from the pdf. When fitting this model five parameters were varied: Q_{max}, k_{rep}, and n_{sites} (like in the single-sensor model) together with k_2 (Ca^{2+} association rate constant to the second sensor) and s (the factor describing the effect of the slow sensor on the energy barrier for fusion)(see table 3 for best fit parameters). The choice of k_2 had an effect on the PPR in simulations, confirming that the second sensor was able to improve the release following AP_2 (Fig. 6C). Figures 6D-I show that the dual fusion-sensor model could fit the $eEJC_1$ amplitudes and the model slightly improved the higher PPR values at the low- and the lower PPR values at high extracellular Ca^{2+} concentrations compared to the single sensor model (compare Figs. 4E and 6G). However, the model failed to produce the STF observed experimentally (the PPR values at 0.75 mM Ca^{2+} were ~1.08 in the simulation compared to ~1.80 in the experiments). Another problem of the dual fusion-sensor model was that release became more asynchronous than observed experimentally (Fig. 6D), which was due to the triggering of SV fusion in-between APs. Finally, predicted variances were much larger than the experimental values (Fig. 6I).

In addition to the optimization, we systematically investigated a large region of the parameter space (Fig. 6J,K), but found no combination of parameters that would be able to generate the experimentally observed STF. Lowering the Ca^{2+} influx (by decreasing Q_{max}) yielded a modest increase in PPR values (Fig. 6J), but required a large number of release sites (n_{sites}) to match the $eEJC_1$ amplitudes (Fig. 6K). Changing s had the largest effect when k_2 was close to the best fit value and moving away from this value decreased the PPRs, either by increasing the effect of the second sensor on AP_1 (when increasing k_2) or by decreasing the effect on AP_2 (when decreasing k_2), which both counteracts STF (Fig. 6B,J).

Fitting the dual fusion-sensor model with a Ca^{2+} cooperativity of 5 did not improve the situation (Fig. 6 – figure supplementary 1, best fit parameters in Table 3): Although slightly more facilitation was observed, this model suffered from even larger variance overshoots (Fig. 6 – figure supplementary 1E) and excessive asynchronous release (Fig. 6 – figure supplementary 1A,C). We explored different K_D values between 0.5 and 2 µM at cooperativities 2-5 in separate simulations, but found no satisfactory fit of the data (results not shown). Thus, a dual fusion-sensor model is unlikely to account for STF observed from the realistic SV release site topology at the *Drosophila* NMJ. Note that this finding does not rule out that syt-7 functions in STF, but argues against a role in cooperating alongside syt-1 in a pV_r-based facilitation mechanism.

Rapidly regulating the number of RRP vesicles accounts for $eEJC_1$ amplitudes, STF, temporal transmission profiles and variances

Since dual fusion-sensor models and other models depending on changes in pV_r (see Discussion) are likely insufficient, we next investigated mechanisms involving an activity-dependent regulation of the number of participating release sites. For this we extended the single sensor model by a single unpriming reaction (compare Fig. 4A and 7A). The consequence of reversible priming is that the initial release site occupation can be less than 100% (in which cases n_{sites} does not equal the number of RRP vesicles). This enables an increase ('overfilling') of the RRP (increase in site occupancy) during the inter-stimulus interval (consistent with reports in other systems (Dinkelacker et al., 2000; Gustafsson et al., 2019; Pulido et al., 2015; Smith et al., 1998; Trigo et al., 2012)). We assumed that Ca^{2+} would stabilize the RRP/release site occupation by slowing down unpriming (Fig. 7A). This made the steady-state RRP size dependent on the resting Ca^{2+} concentration and the modest dependence of this on the extracellular Ca^{2+} resulted in RRP enlargement

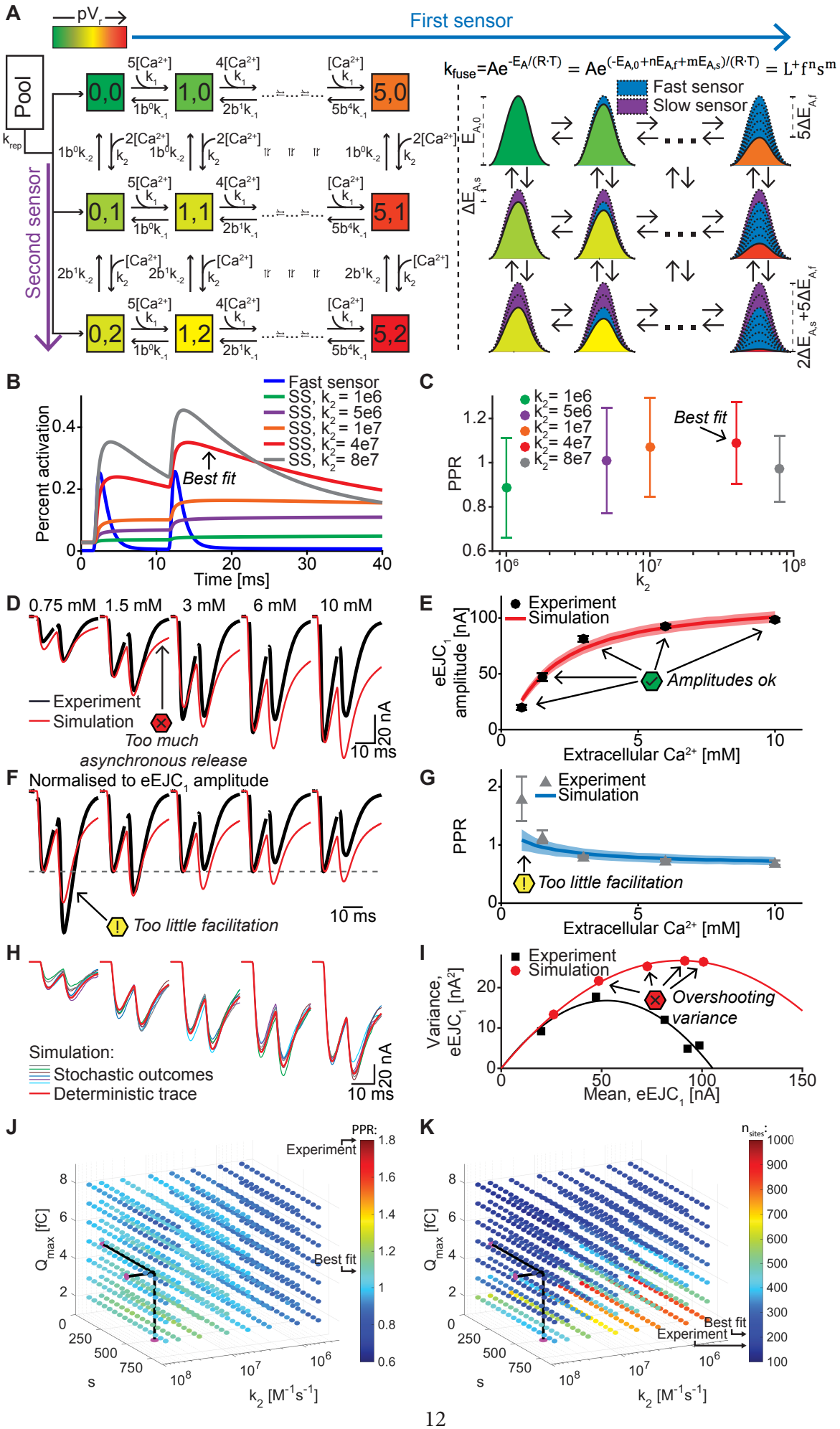
A
First sensor
Second sensor
Pool
Fast sensor
Slow sensor
B
Fast sensor
SS, k2 = 1e6
SS, k2 = 5e6
SS, k2 = 1e7
SS, k2 = 4e7
SS, k2 = 8e7
Best fit
Percent activation
Time [ms]
C
Best fit
PPR
k2
D
0.75 mM
1.5 mM
3 mM
6 mM
10 mM
Experiment
Simulation
Too much
asynchronous release
20 nA
10 ms
E
Experiment
Simulation
Amplitudes ok
eEJC1 amplitude [nA]
Extracellular Ca2+ [mM]
F
Normalised to eEJC1 amplitude
Too little facilitation
10 ms
G
Experiment
Simulation
Too little facilitation
PPR
Extracellular Ca2+ [mM]
H
Simulation:
Stochastic outcomes
Deterministic trace
20 nA
10 ms
I
Experiment
Simulation
Overshooting
variance
Variance, eEJC1 [nA2]
Mean, eEJC1 [nA]
J
PPR:
Experiment
Best fit
Qmax [fC]
s
k2 [M-1s-1]
K
nsites:
Best fit
Experiment
Qmax [fC]
s
k2 [M-1s-1]

Figure 6. A dual fusion-sensor model of Ca^{2+} sensors cooperating for SV fusion improves STP behavior, but suffers from too little STF, asynchronous release and too much variance. **(A)** Diagram of the dual fusion-sensor model (left). A second Ca^{2+} sensor for fusion with slower kinetics can increase pV_r (indicated by color of each Ca^{2+} binding state). The second fusion sensor is assumed to act on the energy barrier in a similar way as the first sensor (right). The top right equation shows the relation between the fusion constant, k_{fuse}, and energy barrier modulation with n and m being the number of Ca^{2+} bound to the first and second Ca^{2+} sensor, respectively. Ca^{2+} binding to the second sensor is described by similar equations as for the first sensor, but with different rate constants and impact on the energy barrier. **(B)** Simulation of Ca^{2+} binding to the fast (blue) and slow (other colors) Ca^{2+} sensor in simulations at 0.75 mM extracellular Ca^{2+} with different k_2 values but with constant affinity (i.e. fixed ratio of k_{-2}/k_2). The binding is normalized to the maximal number of bound Ca^{2+} to each sensor (5 and 2, respectively). For illustration purposes in this graph the fusion rate was set to 0 (because otherwise the fast sensor (blue line) would be consumed by SV fusion). k_2=4e7 (red trace) illustrates the situation for the optimal performance of the model (approximately best fit value). **(C)** PPR values in stochastic simulations with the same parameter choices as in (B) but allowing fusion. **(D)** Experimental eEJC traces (black) together with average simulated traces (red). Simulations show too much asynchronous release compared to experiments. **(E)** $eEJC_1$ amplitudes of experiment (black) and simulation (red). Error bars and colored bands show standard deviations of data and simulations, respectively. Simulations reproduce $eEJC_1$ amplitudes well. **(F)** Average, normalized eEJC traces of experiment (black) and simulation (red). Simulations show too little facilitation compared to the experiment. **(G)** PPR values of experiment (gray) and simulation (blue). Error bars and colored bands show standard deviation. Simulations show too little facilitation compared to the experiment. **(H)** Average simulated traces (black) and examples of different outcomes of the stochastic simulation (colors). **(I)** Plot of the mean synaptic variance vs. the mean $eEJC_1$ values, both from the experiment (black) and the simulations (red). Curves are the best fitted parabolas with forced intercept at (0,0)(simulation: $Var=-0.0034*\langle eEJC_1\rangle^2+0.5992*\langle eEJC_1\rangle$, corresponding to n_{sites}=294 and q=0.60 when assuming a classical binomial model (Clements and Silver, 2000), see Methods). Simulations lead to too much variance at the highest Ca^{2+} concentrations. **(J)** Parameter exploration of the second sensor varying the parameters Q_{max}, k_2, and s. Each ball represents a choice of parameters and the color indicates the average PPR value in stochastic simulations with 0.75 mM extracellular Ca^{2+}. None of the PPR values match the experiment (indicated by the black arrow). Black lines show the best fit parameters. **(K)** Same parameter choices as in (I). The colors indicate the number of RRP SVs in order to fit the $eEJC_1$ amplitudes at the 5 different experimental Ca^{2+} concentrations. Black lines show the best fit parameters, and arrows show the experimental and best fit simulation values. Note that the best fit predicted more release sites than fluctuation analysis revealed in the experiment. Experimental data (example traces and means) depicted in panels D-G,I are replotted from Fig. 2A-D,F. Parameters used for simulations can be found in tables 1,2,3. Simulation scripts can be found in the source code file. Results from simulations (means and SDs) can be found in the accompanying source data file (Figure 6 – Source Data 1). Simulations of the dual fusion-sensor model with cooperativity 5 are summarized in Figure 6 – figure supplement 1.

with increasing extracellular Ca^{2+} (Fig. 7B). This model (like the dual fusion-sensor models depicted in Fig. 6 and Fig. 6 – figure supplement 1) includes two different Ca^{2+}-sensors, but the major difference is that these Ca^{2+} sensors operate to regulate two separate sequential steps (priming and fusion). Indeed, this scenario aligns with reports of a syt-7 function upstream of SV fusion (Liu et al., 2014; Schonn et al., 2008). Fig. 7C shows how the number of RRP vesicles develops over time in this model during a paired-pulse experiment for low and high extracellular Ca^{2+} concentrations. In all cases, SV priming was in equilibrium prior to the first stimulus, indicated by the horizontal lines (0-2 ms, Fig. 7C). Note that prior to AP_1 priming is submaximal (~41 %) for 0.75 mM extracellular Ca^{2+}, but near complete (~99 %) at 10 mM extracellular Ca^{2+}. At low extracellular Ca^{2+} the elevation of Ca^{2+} caused by AP_1 results in a sizable inhibition of unpriming, leading to an increase ('overfilling') of the RRP during the inter-stimulus interval. With this, more primed SVs are available for AP_2, causing facilitation (green line in Fig. 7C). In contrast, at high extracellular Ca^{2+} concentrations, the rate of unpriming is already low at steady state and the RRP close to maximal capacity (grey line in Fig. 7C). At this high extracellular Ca^{2+} concentration, AP_1 induces a larger Ca^{2+} current (higher pV_r), resulting in strong RRP depletion, of which only a fraction recovers between APs (as in the other models, replenishment commences with a Ca^{2+} independent rate k_{rep}). Because Ca^{2+} acts in RRP stabilization, not in stimulating forward priming, this model (unlike the dual fusion-sensor models in Fig. 6 and Fig. 6 – figure supplement 1) did not yield asynchronous release in-between APs (Fig. 7D). Thus, the two most important features of this model are the submaximal site occupation and an inhibition of unpriming by intracellular Ca^{2+}.

In this model we assumed a Ca^{2+} cooperativity of n = 5 for the unpriming mechanism (we also explored n = 2, see Fig. 7 – figure supplement 1). The following parameters were optimized: Q_{max}, n_{sites} and k_{rep} (like in the single- and dual fusion-sensor models), together with $K_{M,prim}$, the Ca^{2+} affinity of the priming sensor and u, its Ca^{2+}-cooperativity. These values together define the Ca^{2+}-dependent unpriming rate (see Table 3 for best fit parameters). The total number of fitted parameters (5) was the same as for the dual fusion-sensor models (Fig. 6 and Fig. 6 – figure supplement 1). Fig. 7D-I present the results. It is clear that both $eEJC_1$ amplitudes and PPR values were described very well with this model at all extracellular Ca^{2+} concentrations. We also explored the time-dependence of the facilitation by simulating PPR values for various inter-stimulus intervals at different extracellular Ca^{2+} concentrations which could be investigated experimentally in the future to further refine parameters (Fig. 7 – figure supplement 3). In addition, the variance-mean relationship of the $eEJC_1$ was reproduced satisfactorily, except for a small variance overshoot for the highest extracellular Ca^{2+} concentrations (Fig. 7I, see Discussion). Fitting of the unpriming model with a Ca^{2+} cooperativity of 2 also led to a good fit (Fig. 7 – figure supplement 1), although the variance overshoot was somewhat larger.

Different facilitating synapses exhibit a large range of PPR values, some larger than observed at the *Drosophila* NMJ (Jackman et al., 2016). Therefore, if this were a general mechanism to produce facilitation, we would expect it to be flexible enough to increase the PPR much more than observed here. To investigate the model's flexibility we systematically explored the parameter space by varying Q_{max}, $K_{M,prim}$, and u (Fig. 7J,K). Similar to figure 6J,K, the colors of the points represent the PPR value and the number of release sites needed to fit the $eEJC_1$ amplitudes. Consistent with a very large dynamic range of this mechanism, PPR values ranged from 0.85 to 3.90 (Fig. 7J,K) and unlike the dual fusion-sensor model, PPR values were fairly robust to changes in Ca^{2+} influx

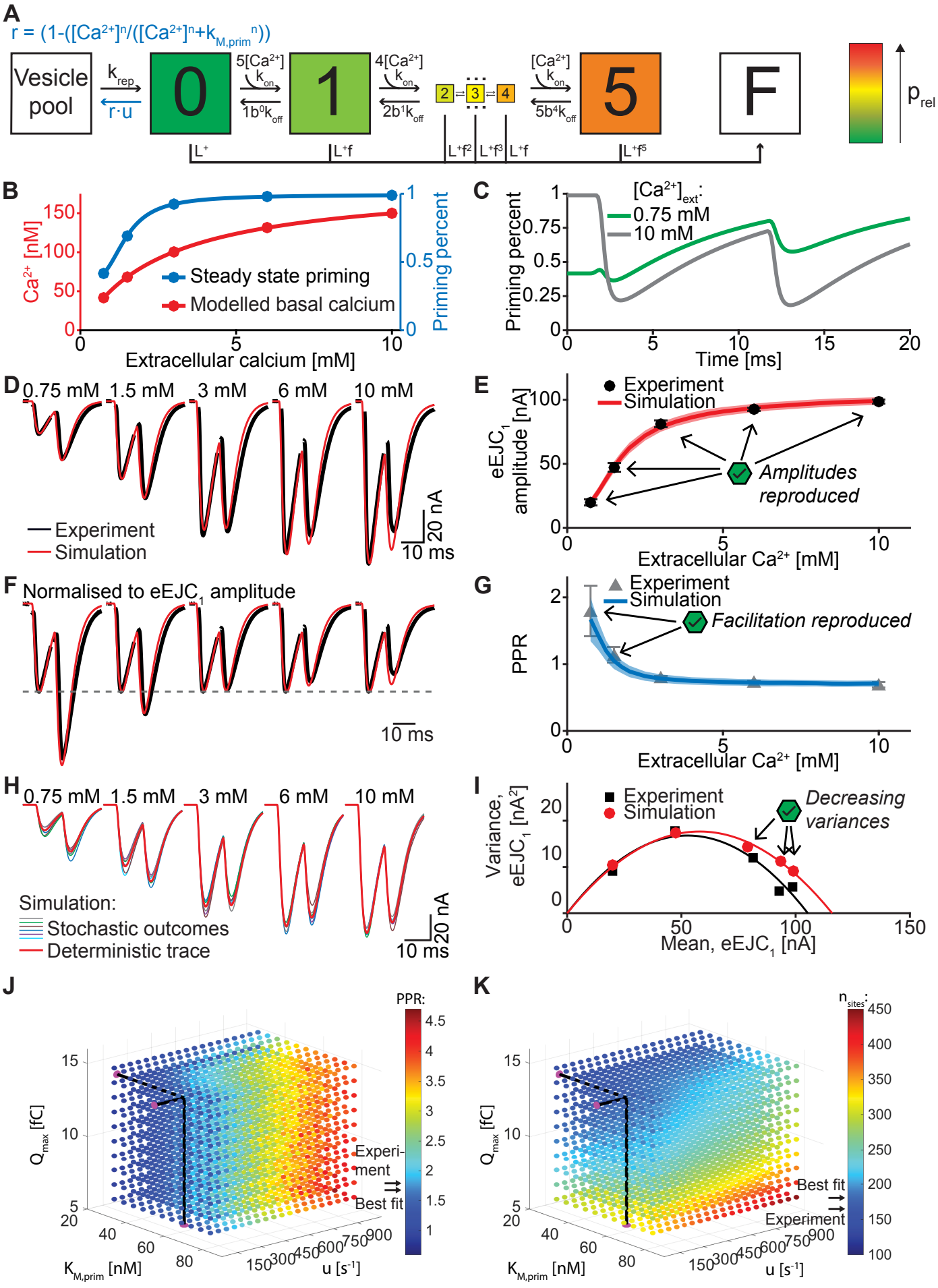
A
r = (1-([Ca2+]n/([Ca2+]n+kM,primn))
Vesicle pool
krep
r·u
0
5[Ca2+]
kon
1b0koff
1
4[Ca2+]
kon
2b1koff
2
3
4
[Ca2+]
kon
5b4koff
5
F
prel
L+
L+f
L+f2
L+f3
L+f
L+f5
B
Ca2+ [nM]
Priming percent
Steady state priming
Modelled basal calcium
Extracellular calcium [mM]
C
[Ca2+]ext:
0.75 mM
10 mM
Priming percent
Time [ms]
D
0.75 mM
1.5 mM
3 mM
6 mM
10 mM
Experiment
Simulation
20 nA
10 ms
E
Experiment
Simulation
eEJC1 amplitude [nA]
Amplitudes reproduced
Extracellular Ca2+ [mM]
F
Normalised to eEJC1 amplitude
10 ms
G
Experiment
Simulation
Facilitation reproduced
PPR
Extracellular Ca2+ [mM]
H
0.75 mM
1.5 mM
3 mM
6 mM
10 mM
Simulation:
Stochastic outcomes
Deterministic trace
20 nA
10 ms
I
Experiment
Simulation
Decreasing variances
Variance, eEJC1 [nA2]
Mean, eEJC1 [nA]
J
PPR:
Qmax [fC]
KM,prim [nM]
u [s-1]
Experi-ment
Best fit
K
nsites:
Qmax [fC]
KM,prim [nM]
u [s-1]
Best fit
Experiment

Figure 7. An unpriming model with Ca^{2+}-dependent regulation of the RRP accounts for experimentally observed Ca^{2+} dependent eEJCs, STP and variances. **(A)** Diagram of the unpriming model. The rate of unpriming decreases with the Ca^{2+} concentration. All other reactions are identical to the one-sensor model (Fig. 4A). **(B)** Assumed basal Ca^{2+} concentration at different extracellular Ca^{2+} concentrations (red curve) together with the steady-state amount of priming (blue). Increasing basal Ca^{2+} concentration increases priming. **(C)** The average fraction of occupied release sites as a function of time in simulations with 0.75 mM (green) and 10 mM (gray) extracellular Ca^{2+} concentration. Release reduced the number of primed SVs. At 0.75 mM Ca^{2+}, the Ca^{2+}-dependent reduction of unpriming leads to 'overfilling' of the RRP between AP_1 and AP_2, thereby inducing facilitation. **(D)** Average experimental eEJC traces (black) together with average simulated traces (red). **(E)** $eEJC_1$ amplitudes of experiment (black) and simulation (red). Error bars and colored bands show standard deviation. **(F)** Average, normalized eEJC traces of experiment (black) and simulation (red). **(G)** PPR values of experiment (gray) and simulation (blue). Error bars and colored bands show standard deviation. Simulations reproduce the experimentally observed facilitation. **(H)** Average simulated traces (black) and examples of different outcomes of the stochastic simulation (colors). **(I)** Plot of the mean synaptic variance vs. the mean $eEJC_1$ values, both from the experiment (black) and the simulations (red). The curves show the best fitted parabolas with forced intercept at (0,0)(simulation: $Var=-0.0053*<eEJC_1>^2+0.6090*<eEJC_1>$, corresponding to $n_{sites}=189$ and $q=0.61$ when assuming a classical binomial model (Clements and Silver, 2000), see Methods). **(J)** Similar to Fig. 6J. Parameter exploration of the unpriming model varying Q_{max}, $k_{M,prim}$, and u (unpriming rate constant). Each ball represents a choice of parameters and the color indicates the PPR value. Black lines show the best fit parameters, and arrows show the experimental and best fit simulation values. **(K)** Same parameter choices as in (J). The colors indicate the optimal maximal number of SVs (i.e. number of release sites, n_{sites}) in order to fit the $eEJC_1$ amplitude at the 5 different Ca^{2+} concentrations. A large span of PPR values (shown in (J)) can be fitted with a reasonable number of release sites (shown in (K)). Experimental data depicted in panels E,G,I are replotted from Fig. 2 B,D,F. Experimental data (example traces and means) depicted in panels D-G,I are replotted from Fig. 2A-D,F. Parameters used for simulation can be found in tables 1,2,3. Simulation scripts can be found in the source code file. Results from simulations (means and SDs) can be found in the accompanying source data file (Figure 7 – Source Data 1). Simulations of the unpriming model with cooperativity 2 are summarized in Figure 7 – figure supplement 1. The site activation model (described later) is introduced and results are summarized in Figure 7 - figure supplement 2. Simulations of the unpriming model with various inter-stimulus intervals are summarized in Fig. 7 – figure supplement 3.

(note the different scales on Fig. 7J,K and Fig. 6J,K). Moreover, because this mechanism does not affect the Ca^{2+} sensitivity of SV fusion, facilitation was achieved without inducing asynchronous release (Fig. 7D).

We also investigated an alternative model based on Ca^{2+}-dependent release site activation. In this model, all sites are occupied by a vesicle, but some sites are inactive and fusion is only possible from activated sites. We assumed that site activation was Ca^{2+}-dependent. In order to avoid site activation during AP_1, which would again hinder STF and could contribute to asynchronous release, we implemented an intermediate delay state (Fig. 7 – figure supplement 2A-B) from which sites were activated in a Ca^{2+}-independent reaction. This could mean that priming occurs in two-steps, with the first step being Ca^{2+}-dependent. Similar to the unpriming model presented above, the modest increase of intracellular Ca^{2+} with extracellular Ca^{2+} yielded an RRP increase (increase in active sites) (Fig. 7 – figure supplement 2I). This model agreed similarly well with the data as the unpriming model (Fig. 7 – figure supplement 2C-H). Thus, both mechanisms which modulate the RRP rather than pV_r are fully capable of reproducing the experimentally observed Ca^{2+}-dependent $eEJC_1$ amplitudes, STF, release synchrony and variance. The unpriming model was preferred since it had fewer parameters and performed slightly better in optimisations than the site activation model.

A release site facilitation mechanism utilizes a larger part of the SV distribution

Why do n_{site}/priming-based mechanisms (Fig. 7, Fig. 7 – figure supplement 1, Fig. 7 – figure supplement 2) account for STF from the broad distribution of SV:Ca^{2+} channel coupling distances, while the pV_r-based models (Figs. 4, 6, Fig. 6 – figure supplement 1) cannot? To gain insight into this, we analysed the spatial dependence of transmitter release in the unpriming model during the paired-pulse experiment (0.75 mM extracellular Ca^{2+}) in greater detail (Fig. 8). Panel 8A, similarly to Fig. 5A, shows example stochastic simulations (at external Ca^{2+} concentration 0.75 mM, to illustrate facilitation). The best fit parameters of the unpriming model predicted a larger Ca^{2+} influx (1.64-fold and 3.05-fold larger Q_{max} value) than the single- and dual fusion-sensor models (Table 3). The larger Ca^{2+} influx compensated for the submaximal priming of SVs (reduced release site occupancy) prior to the first stimulus by expanding the region where SVs are fused (Fig. 8B). Comparing to Fig. 5B, a much larger part of the SV distribution is utilized during the first stimulus. Following AP_1, vesicles prime into empty sites across the entire distribution, allowing AP_2 to draw again from the entire distribution. During this time, the increased residual Ca^{2+} causes overfilling of the RRP, i.e. more release sites are now occupied, giving rise to more release during AP_2. Notably, the AP_2-induced release again draws from the entire distribution. Thus, the unpriming model not only reproduces STF and synaptic variance, but also utilizes docked SVs more efficiently from the entire distribution compared to the single- and dual fusion-sensor model.

Discussion

We here described a broad distribution of vesicle:Ca^{2+}-channel coupling distances in the *Drosophila* NMJ and compared physiological measurements with stochastic simulations of four different release models (single-sensor, dual fusion-sensor, Ca^{2+}-dependent unpriming and site activation model). We showed that the two first models (single-sensor and dual fusion-sensor), where residual Ca^{2+} acts on the energy barrier for fusion and results in an increase in pV_r, failed to reproduce facilitation. The two latter models involve a Ca^{2+}-dependent regulation of participating release sites and reproduced release amplitudes, variances and PPRs. Therefore, the Ca^{2+}-dependent accumulation of releasable SVs is a plausible mechanism for paired-pulse facilitation at the *Drosophila* NMJ, and possibly in central synapses as well. In more detail, our insights are as follows:

1. The SV distribution was described by the single-peaked integrated Rayleigh distribution with a fitted

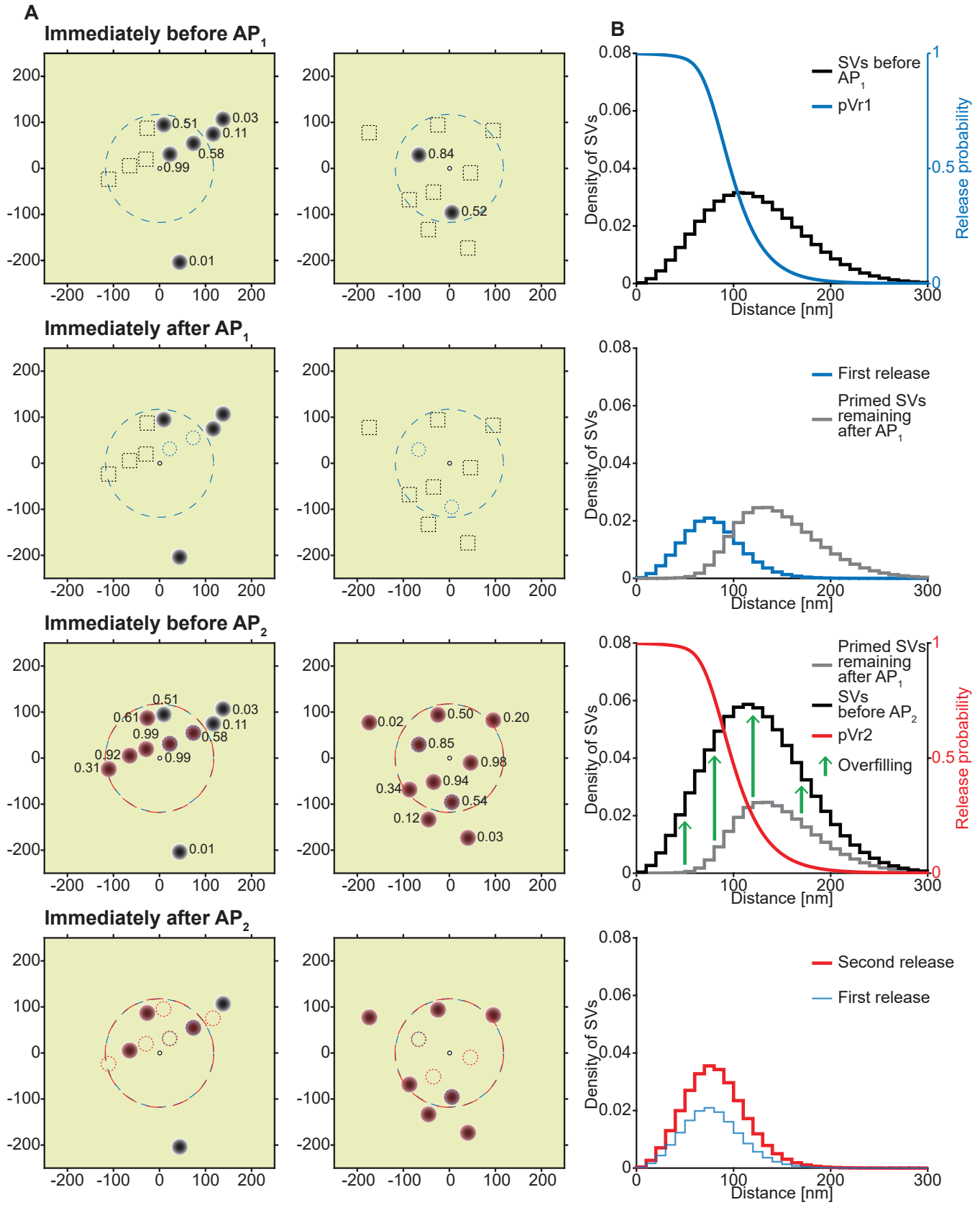

Figure 8. Analysis of the spatial dependence of SV fusion in the unpriming model. **(A)** Two examples of docked SVs stochastically placed according to the distribution described in Fig. 1D and their behavior in the PPR simulation at 0.75 mM extracellular Ca^{2+} concentration. For clarity, 10 SVs are shown per AZ and only a central part of the AZ is shown. Top row: Prior to AP_1, only some release sites contain a primed SV (dark gray circles) and pV_r1 is indicated as a number. Initially empty release sites are indicated by dashed black squares. The larger dashed, blue circle in the AZ center indicates pV_r1 = 0.25. Second row: After AP_1 some of the SVs have fused (dashed blue circles). Third row: Right before AP_2 the initially empty sites as well as the sites with SV fusion in response to AP_1 have been (re)populated (orange shading). pV_r2 is indicated as a number. The larger dashed, red circle indicates pV_r2 = 0.25. Bottom row: After AP_2 the second release has taken place. Dashed circles indicate release from AP_1 and AP_2 (blue and red resp.). **(B)** The average simulation at the same time points as in (A). Histograms represent primed SVs (black and gray) as well as first and second release (blue and red) illustrating how release from AP_1 and AP_2 draw on a larger part of the SV distribution (comp. to Fig. 5) and how the increase in RRP size can induce facilitation. The blue and red curves indicate the vesicular release probability as a function of distance during AP_1 (blue) and AP_2 (red). Parameters used for simulations can be found in tables 1,2,3.

mean of 122 nm. The distribution has a low probability for positioning of SVs very close to Ca^{2+}-channels (less than 1.5% within 30 nm) and is therefore reasonably consistent with suggestions of a SV exclusion zone of ~30 nm around Ca^{2+}-channels (Keller et al., 2015). Strikingly, almost exactly the same distribution was identified for the essential priming protein Unc13 (Fig. 1F, Fig. 1 – figure supplement 1D), indicating that docked SVs are likely primed (Imig et al., 2014).

2. The broad distribution of release-site:Ca^{2+} channel distances particularly impedes pV_r-based facilitation mechanisms. Indeed, previous models that reproduced facilitation using pV_r-mechanisms typically placed SVs at an identical distance to Ca^{2+} channels, resulting in intermediate (and identical) pV_r for all SVs (Bohme et al., 2016; Bohme et al., 2018; Bollmann and Sakmann, 2005; Fogelson and Zucker, 1985; Jackman and Regehr, 2017; Matveev et al., 2006; Matveev et al., 2004; Tang et al., 2000; Vyleta and Jonas, 2014; Yamada and Zucker, 1992). Here, having mapped the precise AZ topology, we show that the broad SV distribution together with the steep dependence of release rates on [Ca^{2+}] creates a situation where pV_r falls to almost zero for SVs further away than the mean of the distribution (Fig. 5). As a result, most SVs either fuse during AP_1, or have pV_r values close to zero, leaving little room for modulation of pV_r to create facilitation. Such mechanisms (including buffer saturation, and Ca^{2+}-binding to a second fusion sensor) will act to multiply release rates with a number >1. However, since SVs with pV_r close to 1 have already fused during AP_1, and most of the remaining vesicles have pV_r close to zero such a mechanism will be ineffective in creating facilitation. Thus, the broad distribution of SV:Ca^{2+} channel distances makes it unlikely that pV_r-based mechanisms can cause facilitation.

3. The dual fusion-sensor model was explored as an example of a pV_r-based model. Two problems were encountered: The first problem was that the second sensor, due to its high affinity for Ca^{2+}, was partly activated in the steady state prior to the stimulus (Fig. 6B). Therefore, it could not increase pV_r2 without also increasing pV_r1. This makes it inefficient in boosting the PPR. The second problem was kinetic: the second sensor should be fast enough to activate between two APs, but slow enough not to activate during AP_1. This is illustrated in Fig. 6B-C, which shows the time course of activation of the two sensors and the corresponding PPR values for varying Ca^{2+} binding rates of the second sensor. Since the sensor is Ca^{2+}-dependent, the rate inevitably increases during the Ca^{2+} transient, leading to too much asynchronous release. In principle, the first problem could be alleviated by increasing the Ca^{2+}-cooperativity of the second sensor, which would make it easier to find parameters where the sensor would activate after but not before AP_1. We therefore tried to optimize the model with cooperativities of 3, 4, and 5 (Fig. 6 – figure supplement 1 shows cooperativity 5), and indeed, the higher cooperativity made it possible to obtain slightly more facilitation. However, activation during the AP (the second problem) was exacerbated and caused massive and unphysiological asynchronous release. Thus, a secondary Ca^{2+} sensor acting on the energy barrier for fusion is unlikely to account for facilitation in synapses with a broad distribution of SV:Ca^{2+} channel distances.

4. We included stochasticity at the level of the SV distribution (release sites were randomly drawn from the distribution) and at the level of SV Ca^{2+} (un)binding and fusion. This was essential since deterministic and stochastic simulations do not agree on PPR-values due to Jensen's inequality (for a stochastic process the mean of a ratio is not the same as the ratio of the means) (see Methods and Fig. 4 – figure supplement 1). The effect is largest when the evoked release amplitude is smallest. Since small amplitudes are often associated with high facilitation, this effect is important and needs to be taken into account. Stochastic Ca^{2+}-channel gating on the other hand was not included, as this would increase simulation time dramatically. At the NMJ, the Ca^{2+} channels are clustered (Gratz et al., 2019; Kawasaki et al., 2004), and most SVs are relatively far away from the cluster, a situation that was described to make the contribution of Ca^{2+}-channel gating to stochasticity small (Meinrenken et al., 2002). However, the situation will be different in synapses where individual SVs co-localize with individual Ca^{2+}-channels (Stanley, 2016).

5. Stochastic simulations made it possible to not only determine the mean $eEJC_1$ and PPR values, but also the standard deviation around these values upon repeated activation of the NMJ (indicated as lightly colored bands on the simulations in Fig. 4C,E, Fig. 6E,G, and Fig. 7E,G), which can be compared to measurements (shown as black error bars in the same figure panels). This also enabled us to compare our model to experimental variance-mean data (Fig. 4G, 6I, 7I), which we found was key to identify valid models. All models tested resulted in variance-mean dependences that were well approximated by a parabola with intercept 0. Note that such parabola agrees with the mean-variance relationship in a binomial distribution. However these simulations show that the assumption of heterogeneous release probability (and changing RRP size) can also lead to the experimentally observed parabolic variance-mean relationship.

The single-sensor and dual fusion-sensor models resulted in overshooting variances (Fig. 4G, 6I), which became even worse in the case of higher cooperativity of the second fusion sensor (Fig. 6 – figure supplement 1). The right-hand intercept of the variance-mean relationship with the abscissa is interpreted as the product of the number of release sites (n_{sites}) and q (the single SV quantum) and the tendency of these models to overshoot the variance is due to the fitting procedure increasing n_{sites}, while at the same time reducing pV_r (by reducing Q_{max}, the maximal AP-induced Ca^{2+}-influx). The lower pV_r increases the PPR by reducing the effect

of depletion, but results in unrealistically high $n_{sites.}$ Therefore, it was essential to contrast the models to experimental variance-mean data, which restrict n_{sites}. This revealed that pV_r-based facilitation mechanisms produced unrealistic variance-mean behavior.

In this context, models involving a Ca^{2+}-dependent accumulation of releasable SVs fare much better, because only those can cause facilitation in the presence of realistic n_{sites}, resulting in very similar variance-mean behaviour to the experiment (Fig. 7I, Fig. 7 – figure supplement 1E). The remaining slight overshoot for variances at high extracellular Ca^{2+} concentrations could have technical/experimental reasons, because these experiments are of long duration, which might lead to run-down over time (which is not present in the model simulations) that causes a compression of the parabolic relationship along the abscissa (experiments were performed by increasing Ca^{2+} concentrations).

6. We arrived at two models that can explain paired-pulse facilitation and variance-mean behaviour at the *Drosophila* NMJ. Both models include a Ca^{2+}-dependent increase in the number of participating (occupied/activated) release sites. In the Ca^{2+}-dependent unpriming model, forward priming happens at a constant rate, but unpriming is inversely Ca^{2+}-dependent, such that increases in residual Ca^{2+} lead to inhibition of unpriming, thereby increasing release site occupation between stimuli (Fig. 7). Ca^{2+}-dependent replenishment has been observed in multiple systems (Dinkelacker et al., 2000; Smith et al., 1998; Stevens and Wesseling, 1998; Wang and Kaczmarek, 1998). This has traditionally been implemented in various release models as a Ca^{2+} dependent forward priming rate (Man et al., 2015; Pan and Zucker, 2009; Voets, 2000; Weis et al., 1999). In a previous secretion model in chromaffin cells, we had proposed a catalytic function of Ca^{2+} upstream of vesicle fusion (Walter et al., 2013). However, in the context of STF such models would favour accelerated priming during the AP, which would counteract this facilitation mechanism and might cause asynchronous release, similar to the problem with the dual fusion-sensor model (Fig. 6). In the model presented here this is prevented by including the Ca^{2+} dependency on the unpriming rate. Consistent with this idea, recent data in cells and in biochemical experiments showed that the Ca^{2+}-dependent priming protein (M)Unc13 reduces unpriming (He et al., 2017; Prinslow et al., 2019). Another model that reproduced the electrophysiological data was the site activation model, where sites are activated Ca^{2+}-dependently under docked (but initially unprimed) SVs (Fig. 7 – figure supplement 2). In this case, we had to prevent rapid activation-and-fusion during the AP by including an extra, Ca^{2+}-independent transition, which introduces a delay before sites are activated (Fig. 7 – figure supplement 2). The two models are conceptually similar in that they either recruit new SVs to (always active) sites, or activate sites underneath dormant SVs. Those two possibilities are almost equivalent when measuring with electrophysiology, but they might be distinguished in the future using flash-and-freeze electron microscopy (Chang et al., 2018; Watanabe et al., 2013). Interestingly, Unc13 has recently been shown to form release sites at the *Drosophila* NMJ (Reddy-Alla et al., 2017). Therefore, the two models also correspond to two alternative interpretations of Unc13 action (to prevent unpriming, or form release sites).

In our model, all primed vesicles have identical properties, and only deviate in their distance to the Ca^{2+}-channel cluster (positional priming, (Neher and Brose, 2018)). Alternatively, several vesicle pools with different properties (molecular priming) could be considered, which might involve either vesicles with alternative priming machineries, or vesicles being in different transient states along the same (slow) priming pathway (Walter et al., 2013). In principle, if different primed SV states are distributed heterogenously such that more distant vesicles are more primed/releasable, such an arrangement might counteract the effects of a broad distance distribution, although this is speculative. Without such a peripheral distribution, the existence of vesicles in a highly primed/releasable state (such as the "super-primed" vesicles reported at the Calyx of Held synapse), would result in pronounced STD, and counteract STF, which indeed has been observed (Lee et al., 2013; Taschenberger et al., 2016).

In this study, electrophysiological recordings were performed on muscle 6 of the *Drosophila* larva which receives input from morphologically distinct NMJs containing big (Ib) and small (Is) synaptic boutons, which were shown to differ in their physiological properties (Atwood et al., 1993; He et al., 2009; Newman et al., 2017). This could add another layer of functional heterogeneity in the postsynaptic responses analysed here (the EM and STED analyses shown here were focused on Ib inputs). Because our model does not distinguish between Is and Ib inputs, the estimated parameters represent a compound behaviour of all types of synaptic input to this muscle. Future investigations to isolate the contribution of the different input types (e.g. by genetically targeting Is/Ib-specific motoneurons using recently described GAL4 lines; Perez-Moreno and O'Kane, 2019) could help distinguish between inputs and possibly further refine the model to identify parameter differences between these input types.

Fig. 9 summarizes the results for the single-sensor, dual fusion-sensor and unpriming models. Facilitation in single and dual fusion-sensor models depend on the increase in release probability from the first AP to the next (compare colored rings representing 25% release probability between row 2 and 4). However, the increase is very small, even for the dual fusion-sensor model, and to nevertheless produce some facilitation, optimisation finds a small Ca^{2+}-influx, which leads to an ineffective use of the broad vesicle distribution (and a too-high estimate of n_{sites}). In the unpriming model a higher

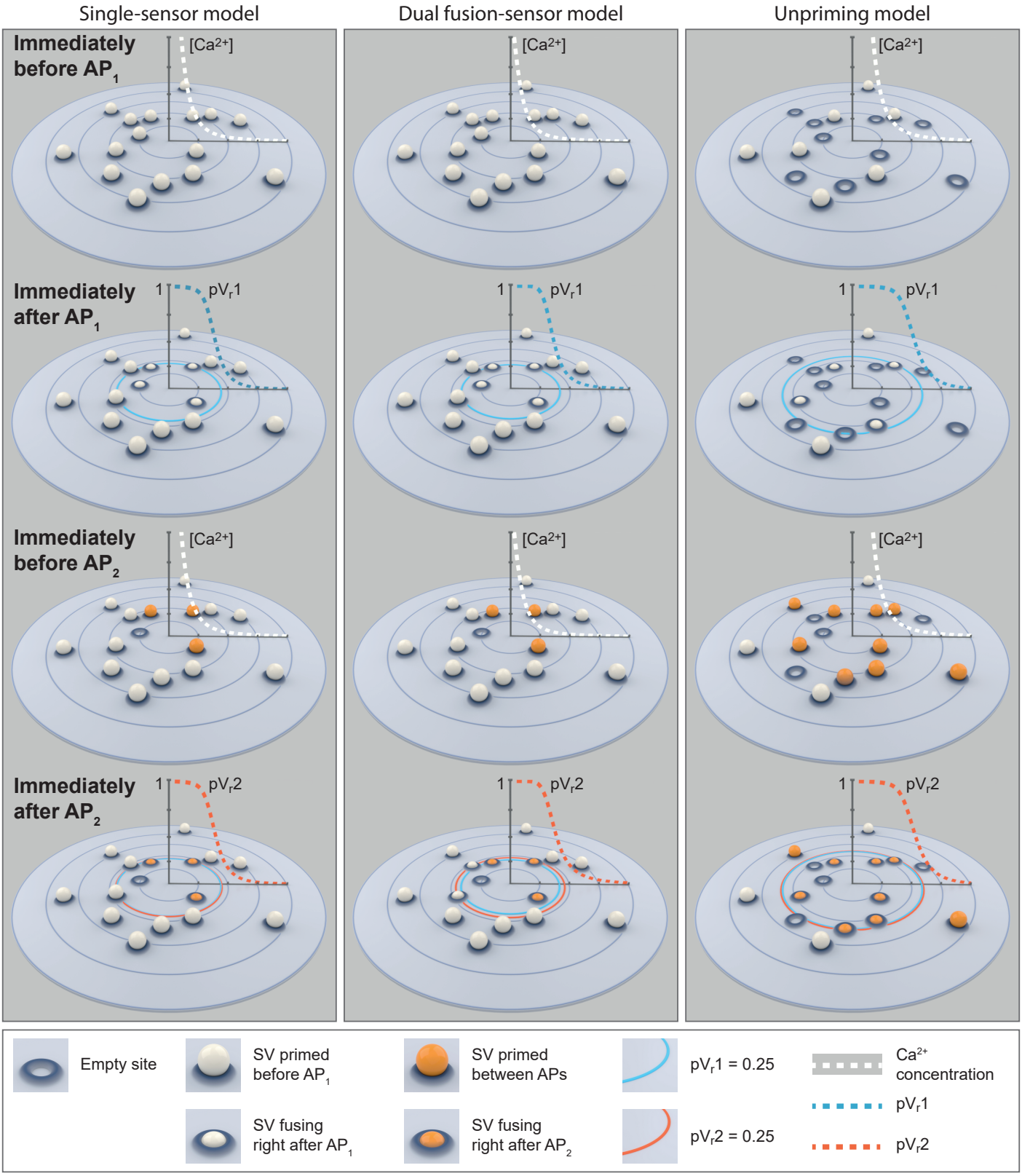

Figure 9: Cartoon illustrations of the single-sensor, the dual fusion-sensor, and the unpriming models during a paired-pulse simulation at 0.75 mM. Top row: SVs primed (white ball) prior to AP_1. In the single- and dual fusion-sensor models all release sites are occupied. In the unpriming model priming is in an equilibrium with unpriming and some release sites are empty. The dashed white graphs show the peak Ca^{2+} concentration (simulation of optimal fits for each model) during the first transient as a function of distance to the Ca^{2+} source. Second row: Some of the SVs fuse in response to AP_1. The dashed blue graphs show the pV_r1 as a function of distance. The large blue circles indicate $pV_r1 = 0.25$. In the unpriming model the larger Ca^{2+} influx (according to the optimal fit) increases the area from which SVs fuse. Third row: Right before AP_2 some of the empty release sites have been repopulated or newly filled by priming (orange balls). The shift in the (un)priming equilibrium in the unpriming model makes the increase in the number of primed SVs substantially larger than in the other models. The dashed white graphs show the peak Ca^{2+} concentration during the second transient as a function of distance to the Ca^{2+} source. Bottom row: SV fusion in response to AP_2. The large dashed red graphs show pV_r2 as a function of distance to the Ca^{2+} source. The blue and red circles indicate pV_r1 and pV_r2 of 0.25. In the dual fusion-sensor model, the second sensor increases pV_r between stimuli, but the effect is small, even in the best fit of the model. These cartoons illustrate the mechanisms underlying our fitting results of the different models: The dual fusion-sensor model shows a small increase in second release compared to the single-sensor model, but only the unpriming model reproduces the experimentally observed facilitation. Parameters used for simulations can be found in tables 1,2,3.

fitted Ca^{2+} influx (Q_{Max}) leads to a more effective use of the entire SV distribution, and facilitation results from the combination of incomplete occupancy of release sites before the first AP (row 1), combined with 'overshooting' priming into empty sites between APs (row 3).

Molecularly, syt-7 was linked to STF behaviour (Jackman et al., 2016), and our data does not rule out that syt-7 is essential for STF at the *Drosophila* NMJ. However, we show clearly that a pV_r-based facilitation mechanism (dual fusion-sensor model) cannot account for STF in synapses with heterogeneous distances between release sites and Ca^{2+} channels. Interestingly, syt-7 was also reported to function in vesicle priming and RRP replenishment (Liu et al., 2014; Schonn et al., 2008). Thus, future work will be necessary to investigate whether the function of syt-7 in STF might take place by Ca^{2+}-dependent inhibition of vesicle unpriming or release site activation.

Similar suggestions that facilitation results from a build-up of primed SVs during stimulus trains were made for the crayfish NMJ and mammalian synapses (Gustafsson et al., 2019; Pan and Zucker, 2009; Pulido and Marty, 2018). This is in line with our results, with facilitation arising from modulation of the number of primed SVs rather than pV_r. Our models are conceptually simple (e.g. all SVs are equally primed and distinguished only by distance to Ca^{2+}-channels, sometimes referred to as 'positional priming'; Neher and Sakaba, 2008), and we improved conceptually on previous work by using estimated SV:Ca^{2+}-channel distributions, stochastic simulations and comparison to variance-mean relationships and we performed a systematic comparison of pV_r- and priming-based models. It has not been clear whether increases in primed SVs are also required for paired-pulse facilitation, or only become relevant in the case of 'tonic' synapses that build up release during longer stimulus trains (frequency facilitation; Neher and Brose, 2018). Paired-pulse facilitation is a more wide-spread phenomenon in synapses than frequency facilitation, and we show here for the case of *Drosophila* NMJ that it also seems to require priming-based mechanisms. Thus, Ca^{2+}-dependent increases of the RRP during STP might be a general feature of chemical synapses.

Author contributions

M.J. performed electrophysiological recordings and analyzed the data. M.A.B. performed STED microscopy, and A.T.G. analyzed the data with custom-written code. A.T.G. conducted presynaptic Calcium live-imaging and analyzed the data. J.R.-L.K. and A.T.G. wrote the code used for calcium dynamics and SV release simulations, and parameter optimization, and J.R.-L.K. performed optimization procedures. S.D., J.B.S. and A.M.W. conceptualized the study and wrote the manuscript with input from all coauthors.

Acknowledgments

J.R.L. Kobbersmed was supported by a pregraduate Scholarship in the Medical Sciences from the Independent Research Fund Denmark (application by J.B. Sørensen) and by the Data Science Laboratory, Faculty of Science, University of Copenhagen. A.T. Grasskamp was supported by a NeuroCure Ph.D. fellowship within the International Graduate Program Medical Neurosciences (Charité Universitätsmedizin Berlin, Germany). M. Jusyte was supported by an Einstein Center for Neurosciences Ph.D. fellowship. This work was supported by grants from the Deutsche Forschungsgemeinschaft to A.M. Walter (Emmy Noether program project number 261020751, TRR 186 project number 278001972). We thank Matthijs Verhage and Niels Cornelisse for helpful comments on our manuscript. We would like to thank Victor Matveev for helpful comments on the use of his Ca^{2+} simulator software. We thank Barth van Rossum, Leibniz-Forschungsinstitut für Molekulare Pharmakologie (FMP), for the illustrations in Figure 9. We also thank The Bioinformatics Centre, University of Copenhagen, for the use of their servers for heavy computations. Stocks obtained from the Bloomington *Drosophila* Stock Center (NIH P40OD018537) and from the Kyoto Stock Center were used in this study.

Competing Interests

The authors declare no conflicting financial and non-financial interest.

References

► Abbott, L.F., and Regehr, W.G. (2004). Synaptic computation. Nature 431, 796-803.

► Aberle, H., Haghighi, A.P., Fetter, R.D., McCabe, B.D., Magalhaes, T.R., and Goodman, C.S. (2002). wishful thinking encodes a BMP type II receptor that regulates synaptic growth in Drosophila. Neuron 33, 545-558.

► Akbergenova, Y., Cunningham, K.L., Zhang, Y.V., Weiss, S., and Littleton, J.T. (2018). Characterization of developmental and molecular factors underlying release heterogeneity at Drosophila synapses. Elife 7.

► Allbritton, N.L., Meyer, T., and Stryer, L. (1992). Range of messenger action of calcium ion and inositol 1,4,5-trisphosphate. Science 258, 1812-1815.

► Atwood, H.L., Govind, C.K., and Wu, C.F. (1993). Differential ultrastructure of synaptic terminals on ventral longitudinal abdominal muscles in Drosophila larvae. J Neurobiol 24, 1008-1024.

► Barnett, L.M., Hughes, T.E., and Drobizhev, M. (2017). Deciphering the molecular mechanism responsible for GCaMP6m's Ca2+-dependent change in fluorescence. PLoS One 12, e0170934.

► Bohme, M.A., Beis, C., Reddy-Alla, S., Reynolds, E., Mampell, M.M., Grasskamp, A.T., Lutzkendorf, J., Bergeron, D.D., Driller, J.H., Babikir, H., *et al.* (2016). Active zone scaffolds differentially accumulate Unc13 isoforms to tune Ca(2+) channel-vesicle coupling. Nat Neurosci 19, 1311-1320.

► Bohme, M.A., Grasskamp, A.T., and Walter, A.M. (2018). Regulation of synaptic release-site Ca(2+) channel coupling as a mechanism to control release probability and short-term plasticity. FEBS Lett, 3516-3531.

► Bohme, M.A., McCarthy, A.W., Grasskamp, A.T., Beuschel, C.B., Goel, P., Jusyte, M., Laber, D., Huang, S., Rey, U., Petzoldt, A.G., *et al.* (2019). Rapid active zone remodeling consolidates presynaptic potentiation. Nat Commun 10, 1085.

► Bollmann, J.H., and Sakmann, B. (2005). Control of synaptic strength and timing by the release-site Ca2+ signal. Nature neuroscience 8, 426-434.

► Bollmann, J.H., Sakmann, B., and Borst, J.G. (2000). Calcium sensitivity of glutamate release in a calyx-type terminal. Science 289, 953-957.

► Borst, J.G., and Sakmann, B. (1998). Facilitation of presynaptic calcium currents in the rat brainstem. J Physiol 513 (Pt 1), 149-155.

► Brandt, D.S., Coffman, M.D., Falke, J.J., and Knight, J.D. (2012). Hydrophobic contributions to the membrane docking of synaptotagmin 7 C2A domain: mechanistic contrast between isoforms 1 and 7. Biochemistry 51, 7654-7664.

► Bruckner, J.J., Zhan, H., Gratz, S.J., Rao, M., Ukken, F., Zilberg, G., and O'Connor-Giles, K.M. (2017). Fife organizes synaptic vesicles and calcium channels for high-probability neurotransmitter release. J Cell Biol 216, 231-246.

► Burgalossi, A., Jung, S., Meyer, G., Jockusch, W.J., Jahn, O., Taschenberger, H., O'Connor, V.M., Nishiki, T., Takahashi, M., Brose, N., and Rhee, J.S. (2010). SNARE protein recycling by alphaSNAP and betaSNAP supports synaptic vesicle priming. Neuron 68, 473-487.

► Chang, S., Trimbuch, T., and Rosenmund, C. (2018). Synaptotagmin-1 drives synchronous Ca(2+)-triggered fusion by C2B-domain-mediated synaptic-vesicle-membrane attachment. Nat Neurosci 21, 33-40.

► Chen,Z.,Das,B.,Nakamura,Y.,DiGregorio,D.A.,andYoung,S.M.,Jr.(2015). Ca2+ channel to synaptic vesicle distance accounts for the readily releasable pool kinetics at a functionally mature auditory synapse. J Neurosci 35, 2083-2100.

► Church, P.J., and Stanley, E.F. (1996). Single L-type calcium channel conductance with physiological levels of calcium in chick ciliary ganglion neurons. J Physiol 496 (Pt 1), 59-68.

► Clements, J.D., and Silver, R.A. (2000). Unveiling synaptic plasticity: a new graphical and analytical approach. Trends Neurosci 23, 105-113.

► Dinkelacker, V., Voets, T., Neher, E., and Moser, T. (2000). The readily releasable pool of vesicles in chromaffin cells is replenished in a temperature-dependent manner and transiently overfills at 37 degrees C. The Journal of neuroscience : the official journal of the Society for Neuroscience 20, 8377-8383.

► Dodge, F.A., Jr., and Rahamimoff, R. (1967). Co-operative action of calcium ions in transmitter release at the neuromuscular junction. J Physiol 193, 419-432.

► Eggermann, E., Bucurenciu, I., Goswami, S.P., and Jonas, P. (2012). Nanodomain coupling between Ca(2)(+) channels and sensors of exocytosis at fast mammalian synapses. Nat Rev Neurosci 13, 7-21.

► Felmy, F., Neher, E., and Schneggenburger, R. (2003). Probing the intracellular calcium sensitivity of transmitter release during synaptic facilitation. Neuron 37, 801-811.

► Fioravante, D., and Regehr, W.G. (2011). Short-term forms of presynaptic plasticity. Curr Opin Neurobiol 21, 269-274.

► Fogelson, A.L., and Zucker, R.S. (1985). Presynaptic calcium diffusion from various arrays of single channels. Implications for transmitter release and synaptic facilitation. Biophysical journal 48, 1003-1017.

► Fouquet, W., Owald, D., Wichmann, C., Mertel, S., Depner, H., Dyba, M., Hallermann, S., Kittel, R.J., Eimer, S., and Sigrist, S.J. (2009). Maturation of active zone assembly by Drosophila Bruchpilot. J Cell Biol 186, 129-145.

► Gillespie, D.T. (2007). Stochastic Simulation of Chemical Kinetics. Annual Review of Physical Chemistry 58, 35-55.

► Gottfert, F., Pleiner, T., Heine, J., Westphal, V., Gorlich, D., Sahl, S.J., and Hell, S.W. (2017). Strong signal increase in STED fluorescence microscopy by imaging regions of subdiffraction extent. Proc Natl Acad Sci U S A 114, 2125-2130.

► Gratz, S.J., Goel, P., Bruckner, J.J., Hernandez, R.X., Khateeb, K., Macleod, G.T., Dickman, D., and O'Connor-Giles, K.M. (2019). Endogenous Tagging Reveals Differential Regulation of Ca(2+) Channels at Single Active Zones during Presynaptic Homeostatic Potentiation and Depression. J Neurosci 39, 2416-2429.

► Guerrier, C., and Holcman, D. (2018). The First 100 nm Inside the Presynaptic Terminal Where Calcium Diffusion Triggers Vesicular Release. Front Synaptic Neurosci 10, 23.

► Gustafsson, B., Ma, R., and Hanse, E. (2019). The Small and Dynamic Pre-primed Pool at the Release Site; A Useful Concept to Understand Release Probability and Short-Term Synaptic Plasticity? Front Synaptic Neurosci 11, 7.

► Hallermann, S., Heckmann, M., and Kittel, R.J. (2010). Mechanisms of short-term plasticity at neuromuscular active zones of Drosophila. HFSP J 4, 72-84.

► He, E., Wierda, K., van Westen, R., Broeke, J.H., Toonen, R.F., Cornelisse, L.N., and Verhage, M. (2017). Munc13-1 and Munc18-1 together prevent NSF-dependent de-priming of synaptic vesicles. Nat Commun 8, 15915.

► He, T., Singh, V., Rumpal, N., and Lnenicka, G.A. (2009). Differences in Ca2+ regulation for high-output Is and low-output Ib motor terminals in Drosophila larvae. Neuroscience 159, 1283-1291.

► Helmchen, F., Borst, J.G., and Sakmann, B. (1997). Calcium dynamics associated with a single action potential in a CNS presynaptic terminal. Biophys J 72, 1458-1471.

► Imig, C., Min, S.W., Krinner, S., Arancillo, M., Rosenmund, C., Sudhof, T.C., Rhee, J., Brose, N., and Cooper, B.H. (2014). The morphological and molecular nature of synaptic vesicle priming at presynaptic active zones. Neuron 84, 416-431.

► Jackman, S.L., and Regehr, W.G. (2017). The Mechanisms and Functions of Synaptic Facilitation. Neuron 94, 447-464.

► Jackman, S.L., Turecek, J., Belinsky, J.E., and Regehr, W.G. (2016). The calcium sensor synaptotagmin 7 is required for synaptic facilitation. Nature 529, 88-91.

► Jahn, R., and Fasshauer, D. (2012). Molecular machines governing exocytosis of synaptic vesicles. Nature 490, 201-207.

► Kaeser, P.S., and Regehr, W.G. (2017). The readily releasable pool of synaptic vesicles. Curr Opin Neurobiol 43, 63-70.

► Katz, B., and Miledi, R. (1968). The role of calcium in neuromuscular facilitation. J Physiol 195, 481-492.

► Kawasaki, F., Zou, B., Xu, X., and Ordway, R.W. (2004). Active zone localization of presynaptic calcium channels encoded by the cacophony locus of Drosophila. J Neurosci 24, 282-285.

► Keller, D., Babai, N., Kochubey, O., Han, Y., Markram, H., Schurmann, F., and Schneggenburger, R. (2015). An Exclusion Zone for Ca2+ Channels around Docked Vesicles Explains Release Control by Multiple Channels at a CNS Synapse. PLoS Comput Biol 11, e1004253.

► Kittel, R.J., Wichmann, C., Rasse, T.M., Fouquet, W., Schmidt, M., Schmid, A., Wagh, D.A., Pawlu, C., Kellner, R.R., Willig, K.I., *et al.* (2006). Bruchpilot promotes active zone assembly, Ca2+ channel clustering, and vesicle release. Science 312, 1051-1054.

► Kochubey, O., and Schneggenburger, R. (2011). Synaptotagmin Increases the Dynamic Range of Synapses by Driving Ca2+-Evoked Release and by Clamping a Near-Linear Remaining Ca2+ Sensor. Neuron 69, 736-748.

► Lee, J.S., Ho, W.K., Neher, E., and Lee, S.H. (2013). Superpriming of synaptic vesicles after their recruitment to the readily releasable pool. Proc Natl Acad Sci U S A 110, 15079-15084.

► Lin, D.M., and Goodman, C.S. (1994). Ectopic and increased expression of Fasciclin II alters motoneuron growth cone guidance. Neuron 13, 507-523.

► Littleton, J.T., and Bellen, H.J. (1995). Synaptotagmin controls and modulates synaptic-vesicle fusion in a Ca(2+)-dependent manner. Trends Neurosci 18, 177-183.

► Liu, H., Bai, H., Hui, E., Yang, L., Evans, C.S., Wang, Z., Kwon, S.E., and Chapman, E.R. (2014). Synaptotagmin 7 functions as a Ca2+-sensor for synaptic vesicle replenishment. Elife 3, e01524.

► Lou, X., Scheuss, V., and Schneggenburger, R. (2005). Allosteric modulation of the presynaptic Ca2+ sensor for vesicle fusion. Nature 435, 497-501.

► Ma, J., Kelly, L., Ingram, J., Price, T.J., Meriney, S.D., and Dittrich, M. (2015). New insights into short-term synaptic facilitation at the frog neuromuscular junction. J Neurophysiol 113, 71-87.

► Man, K.M., Imig, C., Walter, A.M., Pinheiro, P.S., Stevens, D.R., Rettig, J., Sorensen, J.B., Cooper, B.H., Brose, N., and Wojcik, S.M. (2015). Identification of a Munc13-sensitive step in chromaffin cell large dense-core vesicle exocytosis. Elife 4.

► Matkovic, T., Siebert, M., Knoche, E., Depner, H., Mertel, S., Owald, D., Schmidt, M., Thomas, U., Sickmann, A., Kamin, D., *et al.* (2013). The Bruchpilot cytomatrix determines the size of the readily releasable pool of synaptic vesicles. J Cell Biol 202, 667-683.

► Matveev, V., Bertram, R., and Sherman, A. (2006). Residual bound Ca2+ can account for the effects of Ca2+ buffers on synaptic facilitation. J Neurophysiol 96, 3389-3397.

► Matveev, V., Sherman, A., and Zucker, R.S. (2002). New and corrected simulations of synaptic facilitation. Biophys J 83, 1368-1373.

► Matveev, V., Zucker, R.S., and Sherman, A. (2004). Facilitation through buffer saturation: constraints on endogenous buffering properties. Biophysical journal 86, 2691-2709.

► Meinrenken, C.J., Borst, J.G., and Sakmann, B. (2002). Calcium secretion coupling at calyx of Held governed by nonuniform channel-vesicle topography. J Neurosci 22, 1648-1667.

► Miki, T., Malagon, G., Pulido, C., Llano, I., Neher, E., and Marty, A. (2016). Actin- and Myosin-Dependent Vesicle Loading of Presynaptic Docking Sites Prior to Exocytosis. Neuron 91, 808-823.

► Muhammad, K., Reddy-Alla, S., Driller, J.H., Schreiner, D., Rey, U., Bohme, M.A., Hollmann, C., Ramesh, N., Depner, H., Lutzkendorf, J., *et al.* (2015). Presynaptic spinophilin tunes neurexin signalling to control active zone architecture and function. Nat Commun 6, 8362.

► Muller, M., Liu, K.S., Sigrist, S.J., and Davis, G.W. (2012). RIM controls homeostatic plasticity through modulation of the readily-releasable vesicle pool. J Neurosci 32, 16574-16585.

► Nakamura, Y., Harada, H., Kamasawa, N., Matsui, K., Rothman, J.S., Shigemoto, R., Silver, R.A., DiGregorio, D.A., and Takahashi, T. (2015). Nanoscale distribution of presynaptic Ca(2+) channels and its impact on vesicular release during development. Neuron 85, 145-158.

► Nanou, E., and Catterall, W.A. (2018). Calcium Channels, Synaptic Plasticity, and Neuropsychiatric Disease. Neuron 98, 466-481.

► Neher, E., and Brose, N. (2018). Dynamically Primed Synaptic Vesicle States: Key to Understand Synaptic Short-Term Plasticity. Neuron 100, 1283-1291.

► Neher, E., and Sakaba, T. (2008). Multiple roles of calcium ions in the regulation of neurotransmitter release. Neuron 59, 861-872.

► Newman, Z.L., Hoagland, A., Aghi, K., Worden, K., Levy, S.L., Son, J.H., Lee, L.P., and Isacoff, E.Y. (2017). Input-Specific Plasticity and Homeostasis at the Drosophila Larval Neuromuscular Junction. Neuron 93, 1388-1404 e1310.

► Pan, B., and Zucker, R.S. (2009). A general model of synaptic transmission and short-term plasticity. Neuron 62, 539-554.

► Peled, E.S., and Isacoff, E.Y. (2011). Optical quantal analysis of synaptic transmission in wild-type and rab3-mutant Drosophila motor axons. Nat Neurosci 14, 519-526.

► Perez-Moreno, J.J., and O'Kane, C.J. (2019). GAL4 Drivers Specific for Type Ib and Type Is Motor Neurons in Drosophila. G3 (Bethesda) 9, 453-462.

► Prinslow, E.A., Stepien, K.P., Pan, Y.Z., Xu, J., and Rizo, J. (2019). Multiple factors maintain assembled trans-SNARE complexes in the presence of NSF and alphaSNAP. Elife 8.

► Pulido, C., and Marty, A. (2017). Quantal Fluctuations in Central Mammalian Synapses: Functional Role of Vesicular Docking Sites. Physiol Rev 97, 1403-1430.

► Pulido, C., and Marty, A. (2018). A two-step docking site model predicting different short-term synaptic plasticity patterns. The Journal of General Physiology.

► Pulido, C., Trigo, F.F., Llano, I., and Marty, A. (2015). Vesicular release statistics and unitary postsynaptic current at single GABAergic synapses. Neuron 85, 159-172.

► Qin, G., Schwarz, T., Kittel, R.J., Schmid, A., Rasse, T.M., Kappei, D., Ponimaskin, E., Heckmann, M., and Sigrist, S.J. (2005). Four different subunits are essential for expressing the synaptic glutamate receptor at neuromuscular junctions of Drosophila. J Neurosci 25, 3209-3218.

► Reddy-Alla, S., Bohme, M.A., Reynolds, E., Beis, C., Grasskamp, A.T., Mampell, M.M., Maglione, M., Jusyte, M., Rey, U., Babikir, H., *et al.* (2017). Stable Positioning of Unc13 Restricts Synaptic Vesicle Fusion to Defined Release Sites to Promote Synchronous Neurotransmission. Neuron 95, 1350-1364 e1312.

► Rizo, J., and Sudhof, T.C. (2012). The membrane fusion enigma: SNAREs, Sec1/Munc18 proteins, and their accomplices--guilty as charged? Annu Rev Cell Dev Biol 28, 279-308.

► Sakamoto, H., Ariyoshi, T., Kimpara, N., Sugao, K., Taiko, I., Takikawa, K., Asanuma, D., Namiki, S., and Hirose, K. (2018). Synaptic weight set by Munc13-1 supramolecular assemblies. Nat Neurosci 21, 41-49.

► Scheuss, V., and Neher, E. (2001). Estimating synaptic parameters from mean, variance, and covariance in trains of synaptic responses. Biophys J 81, 1970-1989.

► Schneggenburger, R., Meyer, A.C., and Neher, E. (1999). Released fraction and total size of a pool of immediately available transmitter quanta at a calyx synapse. Neuron 23, 399-409.

► Schneggenburger, R., and Neher, E. (2000). Intracellular calcium dependence of transmitter release rates at a fast central synapse. Nature 406, 889-893.

► Schonn, J.S., Maximov, A., Lao, Y., Sudhof, T.C., and Sorensen, J.B. (2008). Synaptotagmin-1 and -7 are functionally overlapping Ca2+ sensors for exocytosis in adrenal chromaffin cells. Proc Natl Acad Sci U S A 105, 3998-4003.

► Schotten, S., Meijer, M., Walter, A.M., Huson, V., Mamer, L., Kalogreades, L., ter Veer, M., Ruiter, M., Brose, N., Rosenmund, C., *et al.* (2015). Additive effects on the energy barrier for synaptic vesicle fusion cause supralinear effects on the vesicle fusion rate. Elife 4, e05531.

► Shahrezaei, V., Cao, A., and Delaney, K.R. (2006). Ca2+ from one or two channels controls fusion of a single vesicle at the frog neuromuscular junction. J Neurosci 26, 13240-13249.

► Sigrist, S.J., Reiff, D.F., Thiel, P.R., Steinert, J.R., and Schuster, C.M. (2003). Experience-dependent strengthening of Drosophila neuromuscular junctions. J Neurosci 23, 6546-6556.

► Smith, C., Moser, T., Xu, T., and Neher, E. (1998). Cytosolic Ca2+ acts by two separate pathways to modulate the supply of release-competent vesicles in chromaffin cells. Neuron 20, 1243-1253.

► Stanley, E.F. (2016). The Nanophysiology of Fast Transmitter Release. Trends in Neurosciences 39, 183-197.

► Stevens, C.F., and Wesseling, J.F. (1998). Activity-dependent modulation of the rate at which synaptic vesicles become available to undergo exocytosis. Neuron 21, 415-424.

► Stewart, B.A., Atwood, H.L., Renger, J.J., Wang, J., and Wu, C.F. (1994). Improved stability of Drosophila larval neuromuscular preparations in haemolymph-like physiological solutions. J Comp Physiol A 175, 179-191.

► Sudhof, T.C. (2012). The presynaptic active zone. Neuron 75, 11-25.

► Sudhof, T.C. (2013). A molecular machine for neurotransmitter release: synaptotagmin and beyond. Nat Med 19, 1227-1231.

► Sudhof, T.C., and Rothman, J.E. (2009). Membrane fusion: grappling with SNARE and SM proteins. Science 323, 474-477.

► Sugita, S., Han, W., Butz, S., Liu, X., Fernandez-Chacon, R., Lao, Y., and Sudhof, T.C. (2001). Synaptotagmin VII as a plasma membrane Ca(2+) sensor in exocytosis. Neuron 30, 459-473.

► Sun, J., Pang, Z.P., Qin, D., Fahim, A.T., Adachi, R., and Sudhof, T.C. (2007). A dual-Ca2+-sensor model for neurotransmitter release in a central synapse. Nature 450, 676-682.

► Tang, Y., Schlumpberger, T., Kim, T., Lueker, M., and Zucker, R.S. (2000). Effects of mobile buffers on facilitation: experimental and computational studies. Biophys J 78, 2735-2751.

► Taschenberger, H., Woehler, A., and Neher, E. (2016). Superpriming of synaptic vesicles as a common basis for intersynapse variability and modulation of synaptic strength. Proc Natl Acad Sci U S A 113, E4548-4557.

► Trigo, F.F., Sakaba, T., Ogden, D., and Marty, A. (2012). Readily releasable pool of synaptic vesicles measured at single synaptic contacts. Proc Natl Acad Sci U S A 109, 18138-18143.

► Trommershauser, J., Schneggenburger, R., Zippelius, A., and Neher, E. (2003). Heterogeneous presynaptic release probabilities: functional relevance for short-term plasticity. Biophys J 84, 1563-1579.

► Vere-Jones, D. (1966). Simple stochastic models for the release of quanta of transmitter from a nerve terminal. The Australian Journal of Statistics 8, 53-63.

► Verhage, M., and Sorensen, J.B. (2008). Vesicle docking in regulated exocytosis. Traffic 9, 1414-1424.

► Voets, T. (2000). Dissection of three Ca2+-dependent steps leading to secretion in chromaffin cells from mouse adrenal slices. Neuron 28, 537-545.

► von Gersdorff, H., and Borst, J.G. (2002). Short-term plasticity at the calyx of Held. Nat Rev Neurosci 3, 53-64.

► Vyleta, N.P., and Jonas, P. (2014). Loose coupling between Ca2+ channels and release sensors at a plastic hippocampal synapse. Science 343, 665-670.

► Wagh, D.A., Rasse, T.M., Asan, E., Hofbauer, A., Schwenkert, I., Durrbeck, H., Buchner, S., Dabauvalle, M.C., Schmidt, M., Qin, G., *et al.* (2006). Bruchpilot, a protein with homology to ELKS/CAST, is required for structural integrity and function of synaptic active zones in Drosophila. Neuron 49, 833-844.

► Walter, A.M., Groffen, A.J., Sorensen, J.B., and Verhage, M. (2011). Multiple Ca2+ sensors in secretion: teammates, competitors or autocrats? Trends Neurosci 34, 487-497.

► Walter, A.M., Pinheiro, P.S., Verhage, M., and Sorensen, J.B. (2013). A sequential vesicle pool model with a single release sensor and a Ca(2+)-dependent priming catalyst effectively explains Ca(2+)-dependent properties of neurosecretion. PLoS Comput Biol 9, e1003362.

► Wang, L.Y., and Kaczmarek, L.K. (1998). High-frequency firing helps replenish the readily releasable pool of synaptic vesicles. Nature 394, 384-388.

► Watanabe, S., Rost, B.R., Camacho-Perez, M., Davis, M.W., Sohl-Kielczynski, B., Rosenmund, C., and Jorgensen, E.M. (2013). Ultrafast endocytosis at mouse hippocampal synapses. Nature 504, 242-247.

► Weber, J.P., Toft-Bertelsen, T.L., Mohrmann, R., Delgado-Martinez, I., and Sorensen, J.B. (2014). Synaptotagmin-7 is an asynchronous calcium sensor for synaptic transmission in neurons expressing SNAP-23. PLoS One 9, e114033.

► Weis, S., Schneggenburger, R., and Neher, E. (1999). Properties of a model of Ca++-dependent vesicle pool dynamics and short term synaptic depression. Biophysical journal 77, 2418-2429.

► Weyhersmuller, A., Hallermann, S., Wagner, N., and Eilers, J. (2011). Rapid active zone remodeling during synaptic plasticity. J Neurosci 31, 6041-6052.

► Wolfel, M., Lou, X., and Schneggenburger, R. (2007). A mechanism intrinsic to the vesicle fusion machinery determines fast and slow transmitter release at a large CNS synapse. J Neurosci 27, 3198-3210.

► Wong, A.B., Rutherford, M.A., Gabrielaitis, M., Pangrsic, T., Gottfert, F., Frank, T., Michanski, S., Hell, S., Wolf, F., Wichmann, C., and Moser, T. (2014). Developmental refinement of hair cell synapses tightens the coupling of Ca2+ influx to exocytosis. EMBO J 33, 247-264.

► Xu, T., Naraghi, M., Kang, H., and Neher, E. (1997). Kinetic studies of Ca2+ binding and Ca2+ clearance in the cytosol of adrenal chromaffin cells. Biophys J 73, 532-545.

► Yamada, W.M., and Zucker, R.S. (1992). Time course of transmitter release calculated from simulations of a calcium diffusion model. Biophysical journal 61, 671-682.

► Yoshihara, M., Adolfsen, B., and Littleton, J.T. (2003). Is synaptotagmin the calcium sensor? Curr Opin Neurobiol 13, 315-323.

► Zucker, R.S. (1973). Changes in the statistics of transmitter release during facilitation. J Physiol 229, 787-810.

► Zucker, R.S., and Regehr, W.G. (2002). Short-term synaptic plasticity. Annu Rev Physiol 64, 355-405.

Materials and Methods

Key Resources Table				
Reagent type (species) or resource	**Designation**	**Source or reference**	**Identifiers**	**Additional information**
strain (*Drosophila melanogaster*)	w[1118]	Bloomington Drosophila Stock Center		
genetic reagent (*D. melanogaster*)	Ok6-GAL4/II	(Aberle et al., 2002)	PMID: 11856529	Ok6-Gal4/II crossed to w[1118]
genetic reagent (*D. melanogaster*)	elav-Gal4/I	(Lin and Goodman, 1994)	PMID: 7917288	Used for elav-GAL4/+;;UAS-Unc13A-GFP/+;P84200/P84200
genetic reagent (*D. melanogaster*)	UAS-Unc13A-GFP/III	(Bohme et al., 2016)	PMID: 27526206	Used for elav-GAL4/+;;UAS-Unc13A-GFP/+;P84200/P84200
genetic reagent (*D. melanogaster*)	ry^{506} ; P{ry11}unc-13^{P84200} / ci^{D}	Kyoto Stock Center	FlyBase: FBst0300878	Used for elav-GAL4/+;;UAS-Unc13A-GFP/+;P84200/P84200
genetic reagent (*D. melanogaster*)	w[1118]; P{w[+mC]=Mhc-SynapGCaMP6f}3-5	(Newman et al., 2017) Bloomington Drosophila Stock Center	PMID: 28285823 Bloomington Stock # 67739	
genetic reagent (*D. melanogaster*)	w[1118]; P{y[+t7.7] w[+mC]=20XUAS-IVS-665GCaMP6m} attP40/Ok6-GAL4	Bloomington Drosophila Stock Center	Bloomington Stock # 42748	
antibody	Anti-Unc13A (guinea pig polyclonal)	(Bohme et al., 2016)	PMID: 27526206	Dilution: 1:500
antibody	Anti guinea pig STAR635 (goat polyclonal)	(Bohme et al., 2016)	PMID: 27526206	Dilution: 1:100
antibody	Anti Nc82 (mouse monoclonal)	Developmental Studies Hybridoma Bank	Antibody Registry ID: AB_2314866	Dilution: 1:1000
antibody	Anti-mouse Cy5 (goat polyclonal)	Jackson ImmunoResearch	SKU: 115-175-072	Dilution: 1:500
software, algorithm	LAS X software	Leica Microsystems	https://www.leica-microsystems.com	

Reagent type (species) or resource	Designation	Source or reference	Identifiers	Additional information
software, algorithm	LCS AF	Leica Microsystems		
software, algorithm	Image J	NIH	Version 1.48q/1.50 g; https://imagej.nih.gov/ij/	
software, algorithm	Imspector Software	Max Planck Innovation	Version 0.10	
software, algorithm	MATLAB	MathWorks	R2010b/R2016b	
software, algorithm	Clampfit	Molecular Devices	Version 10.3	
software, algorithm	GraphPad Prism	GraphPad Software	Version 5.01/6.01	
software, algorithm	pClamp 10	Molecular Devices		
software, algorithm	CalC	(Matveev et al., 2002)	PMID: 12202362 Version 6.8.6	
other	Computer grid	Bioinformatics Center, University of Copenhagen	https://www1.bio.ku.dk/scarb/bioinformatics-centre/	Used for simulations
other	custom-built STED-microscope	(Gottfert et al., 2017)	PMID: 23823248	
other	HPF machine (HPM100)	Leica Microsystems	https://www.leica-microsystems.com	
other	AFS	Leica Microsystems	https://www.leica-microsystems.com	
other	Ultramicrotome (RMC PowerTome XL; Reichert Ultracut S)	Leica Microsystems	https://www.leica-microsystems.com	
other	Electrone microscope (TecnaiSpirit; FEI or Zeiss 900)	FEI; Zeiss	https://www.fei.com,https://www.zeiss.com	

Fly husbandry, genotypes and handling

Flies were kept under standard laboratory conditions as described previously (Sigrist et al., 2003) and reared on semi-defined medium (Bloomington recipe) at 25°C, except for GCaMP6m and synapGCaMP6f flies which were kept at room temperature, and *Ok6-GAL4/+* (Figure 2, Figure 2 – figure supplement 1, Figure 4 panel B-E and G, Figure 6 panel D-G and I, Figure 6 – figure supplement 1, Figure 7 D-G and I, Figure 7 – figure supplement 1, Figure 7 – figure supplement 2 C-F, H) which were kept at 29°C (for detailed genotypes see below). For experiments both male and female 3rd instar larvae were used. The following genotypes were used:

Figure 1: Unc13A rescue: *elav-GAL4/+;;UAS-Unc13A-GFP/+;P84200/P84200* (panel A, B), *w[1118]* (panel E, F). Figure 1- figure supplement 1: *w[1118]* ("EM dataset wildtype", panel A-D), *elav-GAL4/+;;UAS-Unc13A-GFP/+;P84200/P84200* ("EM dataset Unc13A rescue", panel B, D).

Figure 2: *Ok6-GAL4/+* (*Ok6-Gal4/II* crossed to *w[1118]*). Figure 2 - figure supplement 1: *Ok6-GAL4/+* (*Ok6-Gal4/II* crossed to *w[1118]*). Figure 2 - figure supplement 2: *Ok6-GAL4/+* (*Ok6-Gal4/II* crossed to *w[1118]*). Figure 2 - figure supplement 3: *Ok6-GAL4/+* (*Ok6-Gal4/II* crossed to *w[1118]*) and +/+: *w[1118]*.

Figure 3: *w[1118]; P{w[+mC]=Mhc-SynapGCaMP6f}3-5* (Bloomington Stock No. 67739, panel A). Figure 3 - figure supplement 1: *;P{y[+t7.7] w[+mC]=20XUAS-IVS-GCaMP6m}attP40-* (Bloomington Stock No. 42748) crossed to Ok6-GAL4/II.

Figure 4: *Ok6-GAL4/+* (*Ok6-Gal4/II* crossed to *w[1118]*; panel B-E, G).

Figure 6: *Ok6-GAL4/+* (*Ok6-Gal4/II* crossed to *w[1118]*; panel D-G, I). Figure 6 –figure supplement 1: *Ok6-GAL4/+* (*Ok6-Gal4/II* crossed to *w[1118]*).

Figure 7: *Ok6-GAL4/+* (*Ok6-Gal4/II* crossed to *w[1118]*; panel D-G, I). Figure 7 - supplement 1: *Ok6-GAL4/+* (*Ok6-Gal4/II* crossed to *w[1118]*). Figure 7 - supplement 2: *Ok6-GAL4/+* (*Ok6-Gal4/II* crossed to *w[1118]*; panel C-F, H).

The following stocks were used: *Ok6-GAL4/II* (Aberle et al., 2002), *UAS-Unc13A-GFP/III* (Bohme et al., 2016), *elav-Gal4/I* (Lin and Goodman, 1994). The following stock were obtained from the Bloomington *Drosophila* Stock Center: *P{w[+mC]=Mhc-SynapGCaMP6f}3-5/III* (Newman et al., 2017) and *w[1118]; P{y[+t7.7] w[+mC]=20XUAS-IVS-GCaMP6m}attP40*. The following stock was obtained from Kyoto Stock Center: *P84200/IV*.

EM data acquisition and analysis

Sample preparation, EM image acquisition and the quantification of docked SV distances to the AZ center (center of the electron dense "T-bar") are described in (Bohme et al., 2016; Reddy-Alla et al., 2017). The Rayleigh distributions were fit to the distances of docked SVs to the T-bar pedestal center, which had been collected in two EM datasets; analyses of these datasets were published in two previous studies, (Reddy-Alla et al., 2017) for the histogram of distances depicted in Fig. 1A and (Bohme et al., 2016) for the histogram of distances depicted in Fig. 1 – figure supplement 1A.

Derivation of the realistic docked SV distribution from EM measurements

The distances between Ca^{2+} channels and docked SVs in *Drosophila* NMJ obtained by EM was found to follow a Rayleigh distribution with best fit scale parameter σ = 76.51 nm (EM dataset 1) and σ = 74.07 nm (EM dataset 2). As these distances are found by EM of a cross-section of the active zone, we integrate this distribution around a circle to obtain the two-dimensional distribution of SVs in the circular space around the active zone.

The Rayleigh distribution has the following probability density function (pdf):

$$f(x) = \frac{x}{\sigma^2} e^{-x^2/2\sigma^2}, \qquad x > 0$$

The pdf of the SV distribution will then be a scaling of the following function

(1) $$\hat{g}(x) = 2\pi x f(x) = 2\pi x \frac{x}{\sigma^2} e^{-x^2/2\sigma^2}$$

In order to find the pdf of the 2D SV distribution, we integrate $\hat{g}$ to find the normalizing constant. By integration by parts we get:

$$\int_0^\infty \hat{g}(x)\,dx = \int_0^\infty 2\pi x \frac{1}{\sigma^2} x e^{-\frac{x^2}{2\sigma^2}}\,dx$$

$$= 2\pi\left(\left[-xe^{-\frac{x^2}{2\sigma^2}}\right]_0^\infty + \int_0^\infty e^{-\frac{x^2}{2\sigma^2}}\,dx\right)$$

$$= 2\pi\int_0^\infty e^{-\frac{x^2}{2\sigma^2}}\,dx$$

$$= 2\pi\,\frac{1}{2}\sigma\sqrt{2\pi}$$

where the standard normal distribution was used in the last equality. Normalising (1) by this constant, we get the pdf of the distance distribution on a circular area in the active zone:

$$g(x) = \frac{\sqrt{2}}{\sqrt{\pi}\cdot\sigma^3}\cdot x^2\cdot e^{-x^2/2\sigma^2}$$

The SV distribution in simulations

In order to use the above SV distribution in simulations, we need to determine probabilities. *g(x)* is a generalized gamma distribution with $a = \sqrt{2}\cdot\sigma,\ \ p = 2,\ \ d = 3$. The generalized gamma distribution with *a>0, p>0, d>0* has the following pdf:

$$h(x;a,d,p) = \frac{p}{a^d}\cdot\frac{x^{d-1}\cdot e^{-\left(\frac{x}{a}\right)^p}}{\Gamma(d/p)}$$

and cumulative density function (cdf):

$$H(x;a,d,p) = \frac{\gamma(d/p\,,(x/a)^p)}{\Gamma(d/p)}$$

where γ is the lower incomplete gamma function, and Γ is the (regular) gamma function. Both of these functions are implemented in MATLAB (MathWorks, version R2018b), which easily allows us to draw numbers from them.

Thus, the SV distribution has the following cdf:

$$H(x) = \ G(x) = \frac{\gamma(1.5,(x^2/2\sigma^2))}{\Gamma(1.5)}$$

That is, given a uniformly distributed variable $q \in (0,1)$, we can use inbuilt MATLAB functions to sample SV distances, *d*:

(2) $$d = H^{-1}(q) = \sqrt{\gamma^{-1}\big(1.5, q\cdot\Gamma(1.5)\big)\cdot 2\sigma^2}$$

The implementation is as follows:

```
q = rand(1);
d = sqrt( 2 * sigma^2 * gammaincinv(q, 1.5));
```

Note that in MATLAB the inverse incomplete gamma function with parameter *s* is scaled by $\Gamma(s)$, which is why we input *q* and not $q/\Gamma(1.5)$.

STED data acquisition and analysis

Sample preparation, Unc13A antibody staining, STED image acquisition and the isolation of single AZ images are described in (Bohme et al., 2019) and in the following. Third-instar *w[1118]* larvae were put on a dissection plate with both ends fixed by fine pins. Larvae were then covered by 50 µl of ice-cold hemolymph-like saline solution (HL3, pH adjusted to 7.2 (Stewart et al., 1994): 70 mM NaCl, 5 mM KCl, 20 mM $MgCl_2$, 10 mM $NaHCO_3$, 5 mM Trehalose, 115 mM D-Saccharose, 5 mM HEPES). Using dissection scissors a small cut at the dorsal, posterior midline of the larva was made from where on the larvae was cut completely open along the dorsal midline until its anterior end. Subsequently, the epidermis was pinned down and slightly stretched and the internal organs and tissues removed. For the "STED dataset 2" shown in Fig. 1 – figure supplement 1C,D, animals were then incubated in a HL3 solution containing 0.5% DMSO for 10 minutes (this served as a mock control for another experiment not shown in this paper using a pharmacological agent diluted in DMSO). The dissected samples were washed 3x with ice-cold HL3 and then fixed for 5 minutes with ice-cold methanol. After fixation, samples were briefly rinsed with HL3 and then blocked for 1h in 5% native goat serum (NGS; Sigma-Aldrich, MO, USA, S2007) diluted in phosphate buffered saline with 0.05% Triton-X100 (PBT). Subsequently dissected samples were incubated with primary antibodies (guinea-pig Unc13A (1:500;(Bohme et al., 2016)) diluted in 5% NGS in PBT overnight. Afterwards samples were washed 5x for 30 min with PBT and then incubated for 4h with fluorescence-labeled secondary antibodies (goat anti-guinea pig STAR635 (1:100) diluted in 5% NGS in PBT. For secondary antibody production STAR635 fluorophore (Abberior, Germany) was coupled to respective IgGs (Dianova, Germany). Samples were then washed overnight in PBT and subsequently mounted in Mowiol (Max-Planck Institute for Biophysical Chemistry, Group of Stefan Hell) on high-precision glass coverslips (Roth, Germany, LH24.1). Two-color STED images were recorded on a custom-built STED-microscope (Gottfert et al., 2017), which combined two pairs of excitation laser beams of 595 nm and 635 nm with one STED fiber laser beam at 775 nm. All STED images were acquired using Imspector Software (Max Planck Innovation GmbH, Germany). STED images were processed using a linear deconvolution function integrated into Imspector Software (Max Planck Innovation GmbH, Germany). Regularization parameters were 1e−e−11. The point spread function (PSF for deconvolution was generated using a 2D Lorentz function with its half-width and half-length fitted to the half-width and half-length of each individual image. Single AZ images of "STED dataset 1" (Fig. 1 E,F, Fig. 1 –figure supplement 1C,D) had previously been used for a different type of analysis (defining AZ Unc13A cluster numbers; Wild-type in supplementary Figure 2a of (Bohme et al., 2019)) . In this study here, we wanted to obtain the mean Unc13A distribution from all AZs (no distinction of AZ types). To get an average image of the Unc13A AZ distribution, we used a set of hundreds of 51x51 pixel images with a pixel size of 10x10 nm. We identified Unc13A clusters in each image using the fluorescence peak detection procedure described in (Bohme et al., 2019) using MATLAB (version 2016b). Peak detection was performed as follows: In each deconvolved 51x51 pixel image of an Unc13A-stained AZ, a threshold of 25 gray values was applied below which no pixels were considered. Then, local maxima values were found by finding slope changes corresponding to peaks along pixel columns using the function *diff*. The same was done along rows for all column positions where peaks were found. The function *intersect* was then used to determine all pixel positions common in both columns and rows. A minimum distance of 50 nm between neighboring peaks was used to exclude the repeated detection of the same peak, and an edge of 10 nm around the image was excluded to prevent the detection of neighboring AZs. The center of mass of all peak *x,y*-coordinates found in a single image was then calculated as follows:

$$P_x = n^{-1} * \sum_{1}^{n} x_{obs}(n)$$

$$P_y = n^{-1} * \sum_{1}^{n} y_{obs}(n)$$

Here, n is the number of detected peaks, (P_x, P_y) represents the center of mass (*x,y*)-coordinate, and $x_{obs}(n)$ and $y_{obs}(n)$ are the coordinates of the *n*-th detected peak. The image was then shifted such that this position (P_x,P_y) would fall into the center pixel of the 51x51 AZ image. For this, we calculated the required shift (d_x and d_y):

$$d_x = \frac{imgsize(x)}{2} - P_x$$

$$d_y = \frac{imgsize(y)}{2} - P_y$$

Here, imgsize(*x,y*) refers to the pixel dimensions of the image in both *x* and *y* dimensions. The required shift $d_{x,y}$ was then applied to the image using *imtranslate*, which directly takes these shift values as an input. All shifted images were then averaged into a single compound average image of all AZs by taking the mean of each individual pixel and linearly scaling the result in a range between 0 and 255. This resulted in a circular cloudy structure depicted in Fig. 1E, Fig. 1 – figure supplement 1C. To obtain the distribution of fluorescence as a function of distance to the AZ center in the average picture, we determined the distance between the center of the image and the center of the pixel together with the fluorescence intensity in each pixel. The fluorescence intensity in each pixel was obtained by using the inbuilt MATLAB function 'imread', which outputs the intensities in a matrix with indexes corresponding to the pixel location in the picture. From the indexes (x_p,y_p) of each pixel (of size 10 nm), the distance to the center was calculated by the following formula:

$$d(p) = \sqrt{(x_p - 26)^2 + (y_p - 26)^2}$$

We subtract 26 from the pixel number, since the center pixel is the 26th pixel in x- and y-direction. This provided the data for the histograms in Fig. 1F and Fig. 1 – figure supplement 1D.

Calculation of mean distance to four nearest neighbors (1-4-NND)

Stage L3 larvae (n = 17; genotype: w[1118]; P{w[+mC]=Mhc-SynapGCaMP6f}3-5, Bloomington #67739) were fixed in ice-cold Methanol for 7 min and IHC-stained for BRP (mouse anti-Nc82, 1:1000; secondary AB: goat anti-mouse Cy5 1:500). Confocal images of the preparations were taken and processed as described in (Reddy-Alla et al., 2017) for a different set of experiments not shown in this paper. Subsequently, the BRP channel was used to identify local fluorescence intensity maxima using the ImageJ-function "Find Maxima" with a threshold setting between 10 and 20. The locations of maxima for each cell were then loaded into MATLAB (version 2016b) and the distances of each x,y-coordinate to all others were determined using the MATLAB function *pdist2*, resulting in a square matrix containing all possible inter-AZ distances. Each column of this matrix was then sorted in ascending order, and (as the distance of one AZ to itself is always 0) the mean of the 2nd to 5th smallest values across all AZs was determined and depicted as 1-NND through 4-NND in Fig. 3A. The mean distance of the 4 nearest neighbouring AZs (1-4-NND) was calculated in each AZ (gray circles in Fig. 3A bottom right) and the mean across AZs was used for quantification of the simulation volume (see below).

Electrophysiological data acquisition and analysis

For both eEJC and mEJC (spontaneous release events, "miniature Excitatory Junctional Currents") recordings, two electrode voltage clamp (TEVC) recordings were performed from muscle 6 NMJs of abdominal segments A2 and A3 as reported previously (Qin et al., 2005). Prior to recordings, the larvae were dissected in haemolymph-like solution without Ca^{2+} (HL3, pH adjusted to 7.2 (Stewart et al., 1994): 70 mM NaCl, 5 mM KCl, 20 mM $MgCl_2$, 10 mM $NaHCO_3$, 5 mM Trehalose, 115 mM D-Saccharose, 5 mM HEPES) on Sylgard (184, Dow Corning, Midland, MI, USA) and transferred into the recording chamber containing 2 ml of HL3 with $CaCl_2$ (concentrations used in individual experiments described below). TEVC recordings were conducted at 21°C using sharp electrodes (borosilicate glass with filament, 0.86x1.5x80 nm, Science Products, Hofheim, Germany) with pipette resistances between 20-30 MΩ, which were pulled with a P-97 micropipette puller (Sutter Instrument, CA, USA) and filled with 3 mM KCl. Signals were low-pass filtered at 5 KHz and sampled at 20 KHz. Data was obtained using a Digidata 1440A digitizer (Molecular devices, Sunnyvale, CA, USA), Clampex software (v10.6) and an Axoclamp 900A amplifier (Axon instruments, Union City, CA, USA) using Axoclamp software. Only cells with a resting membrane potential V_m below -50mV, membrane resistances R_m above 4 MΩ and a leak currents of less than 10 nA were included in the dataset.

eEJC recordings

eEJC recordings were conducted at a membrane holding potential of -70 mV in TEVC mode. APs were evoked by giving 300 µs short depolarizing pulses (8 V) to respective innervating motoneuron axons using a suction electrode (pulled with DMZ-Universal Puller (Zeitz-Instruments GmbH, Germany) polished with the CPM-2 microforge (ALA Scientific, NY, USA)) and a stimulator (S48, Grass Technologies, USA).

For experiments shown in Fig. 2, individual cells were recorded at an initial extracellular $CaCl_2$ concentration of 0.75 mM which was subsequently increased to 1.5 mM, 3 mM, 6 mM and 10 mM by exchanging and carefully mixing 1 ml of the bath solution with 1 ml HL3 of a higher $CaCl_2$ concentration (total concentrations of exchange solutions: 2.25 mM, 4.5 mM, 9 mM, 14 mM), ultimately adding up to the desired $CaCl_2$ concentration in the bath. At each titration step, cells were acclimated in the bath solution for 60s and 10 repetitions of paired stimulating pulses (0.1 Hz, 10 ms interstimulus interval) were given.

eEJC data shown in Fig. 2 – figure supplement 4 was obtained by recording *Ok6-Gal /+* and +/+ NMJs at 0.75 mM (Fig. 2 – figure supplement 4A-D) and 1.5 mM (Fig. 2 – figure supplement 4E-H) Ca^{2+}. A single preparation AP was given (followed by a 20 s intermission) and cells were stimulated once by two consecutive APs (10 ms inter-stimulus interval). In panels B, D, E and G, $eEJC_1$ and PPR averages are shown ± the estimated single-cell SD (see below).

eEJC data was analyzed with our own custom-built MATLAB script (provided with the source data file, Figure 2 – Source Data 2). After stimulation artifact removal, the $eEJC_1$ amplitude was determined as the minimum current value within 10 ms from the time of stimulation. To account for the decay only being partial before the second stimulus, we fitted a single exponential function to the eEJC decay from the time point of 90 % of the amplitude to the time point of the second stimulus. The $eEJC_2$ amplitude was determined as the difference between the minimum after the second stimulus and the value of the fitted exponential at the time point of the second minimum (see insert in Fig. 2C and Fig. 2 – figure supplement 1A). For analysis shown in Fig. 2, the first stimulation per Ca^{2+} concentration was excluded, as we noticed that the first trial often gave first eEJC responses that were higher than in the following trials. This may reflect the presence of a slow reaction by which SVs can be primed with an even higher release probability (possibly due to the "super-priming" described at the murine Calyx of Held synapse (Lee et al., 2013)). However, as the var/mean analysis requires the existence of an equilibrium in-between stimuli which appears to have been reached between all of the succeeding stimuli, we decided to use only those for our analysis. For $eEJC_1$ amplitudes the average over all measurements and all cells (6 cells, 9 measurements each) was calculated (Fig. 2B). The PPR was calculated by dividing the second amplitude by the first throughout trials and averaging over all measurements and all cells (Fig. 2D). In each cell, the variance of $eEJC_1$ and PPR was estimated (9 stimulations per Ca^{2+} concentration) and the average variance (averaged across cells) was calculated at each extracellular Ca^{2+} concentration. The error bars in Fig. 2B,D are the SD (across all animals) at each extracellular Ca^{2+} concentration. In Fig. 2F the $eEJC_1$ averages and variances are ± SEM. A parabola with intersect y=0 was fitted using the function *polyfitZero* (version 1.3.0.0 from MathWorks file exchange) in MATLAB. ($Var = q*I-I^2/N$, q being the quantal size, I the mean $eEJC_1$ amplitude and N number of release sites)(Clements and Silver, 2000).

mEJC recordings

mEJC data was obtained from a separate set of experiments where mEJCs were recorded for 60s in TEVC mode at 1.5 mM extracellular Ca^{2+} and a holding potential of -80 mV for easier identification of miniature events. Because different holding potentials (-80 mV here compared to -70 mV for the data shown in Fig. 2) it must be pointed out that these recordings were only used to determine the shape of the response for later convolution with SV fusion events predicted by the model (see below). For this, the average mEJC traces from 5 different cells were aligned to 50 % of the rise and averaged. We then fitted the following formula to the data:

$$I_{mini}(t) = A \cdot \left(1 - e^{-\frac{(t-t_0)}{\tau_r}}\right) \cdot \left(B \cdot e^{-\frac{(t-t_0)}{\tau_{df}}} + (1-B) \cdot e^{-\frac{(t-t_0)}{\tau_{ds}}}\right)$$

t_0 is the onset, A is the full amplitude (if there was no decay), B is the fraction of the fast decay, and $\tau_r, \tau_{df}, \tau_{ds}$ are the time constants of the rise, fast decay, and slow decay respectively.

The best fit was

$$t_0 \approx 3.0\ ms, A \approx 7.21\ \mu A, B \approx 2.7e-9, \tau_r \approx 10.6928\ s, \tau_{df} \approx 1.5\ ms, \tau_{ds} \approx 2.8\ ms$$

and is plotted together with the average experimental mini trace in Fig. 2 – figure supplement 1B. Note that t_0 is a time delay when this mEJC is implemented in the simulation and is therefore arbitrary. B is very small making the decay close to a single exponential. The maximum of this function is ~0.7 nA. However, as mentioned above, this function was rescaled to a value of 0.6 nA to match the mEJC amplitudes of the experiments conducted with a holding potential of -70 mV to match the size of a single quantal event, q=0.6 nA, estimated from the variance-mean analysis (see fig. 2F).

Presynaptic GCaMP recordings & analysis

Because the presynaptic terminals of the *Drosophila* larval NMJ are not readily accessible to electrical recordings of Ca^{2+} currents, the saturation behaviour of Ca^{2+} influx as a function of extracellular Ca^{2+} concentrations was measured. We did so by engaging the fluorescent Ca^{2+} indicator GCaMP6m (Genotype: w[1118]; P{y[+t7.7] w[+mC]=20XUAS-IVS-GCaMP6m}attP40, Flybase ID: FBti0151346), which we expressed presynaptically using OK6-Gal4 as a motoneuron-specific driver. Third instar larvae heterozygously expressing the indicator were used in experiments as follows. Dissection took place in Ca^{2+}-free, standard hemolymph-like solution HL-3 (in mM: NaCl 70, KCl 5, $MgCl_2$ 20, $NaHCO_3$ 10, Trehalose 5, Sucrose 115, HEPES 5, pH adjusted to 7.2) (Stewart et al., 1994). After dissection on a

Sylgard-184 (Dow-Corning) block, larvae were transferred to the recording chamber containing HL-3 at varying $CaCl_2$ concentrations (see below). The efferent motoneuron axons were sucked into a polished glass electrode containing a chlorided silver-wire, which could be controlled via a mechanical micromanipulator (Narishige NMN25) and was connected to a pipette holder (PPH-1P-BNC, NPI electronics) via a patch electrode holder (NPI electronics), and connected to an S48 stimulator (Grass Technologies). Larvae were then recorded using a white-light source (Sutter DG-4, Sutter Instruments) and a GFP filter set with a Hamamatsu OrcaFlash 4.0v2 sCMOS (Hahamatsu Photonics) with a framerate of 20 Hz (50 ms exposure) controlled by µManager software (version 1.4.20, https://micro-manager.org) on an upright microscope (Olympus BX51WI) with a 60x water-immersion objective (Olympus LUMFL 60x 1.10w). Muscle 4 1b NMJs in abdominal segments 2 to 4 were used for imaging. Imaging was conducted over 10 s, and at 5 s, 20 stimuli were applied to the nerve at 20 Hz in 300µs 7V depolarization steps. This procedure was begun in the lowest Ca^{2+} concentration (0.75 mM) and then repeated in the same larva at increasing Ca^{2+} concentrations (in mM 1.5, 3, 6) by exchanging the extracellular solution. To achieve a situation with no Ca^{2+} influx, a final recording was conducted where the bath contained HL-3 without $CaCl_2$ and instead 8.3 mM EGTA (this solution was made by diluting 2.5 ml of a 50 mM stock solution in H_2O in 12.5 ml of HL3, resulting in a pH of 8.0). Because this results in a slight dilution (16%) of the components in the HL3, the same dilution was performed for the above described Ca^{2+} containing solutions by adding 2.5 ml H_2O to 12.5 ml of HL3 before $CaCl_2$ was added at above mentioned concentrations.

Analysis of 5 *Drosophila* 3rd instar larvae was done after automated stabilization of *x,y*-movement in the recordings (8-bit multipage .TIF-stacks, converted from 16-bit) as described previously (Reddy-Alla et al., 2017), manually selecting a ROI around the basal fluorescent GCaMP signal, and reading out the integrated density (the sum of all pixel grey values) of the whole region over time. Background fluorescence was measured in a region of the same size and shape outside of the NMJ and subtracted from the signal, separately for each single recording. The quantification was then performed individually for each Ca^{2+}-concentration, by subtracting the fluorescence 250 ms before the stimulation ($F_{t=4.75s}$) from the maximum fluorescence of the trace (F_{max}), yielding the change in fluorescence dF:

$$dF(Ca^{2+}) = F_{max} - F_{t=4,75s}$$

This was repeated for each cell and a Hill fit was performed on the individual values using Prism (version 6.07, GraphPad Software Inc.):

$$F([Ca^{2+}]_{ext}) = \frac{F_{end} * [Ca^{2+}]_{ext}^{m}}{(K_{M,fluo})^{m} + [Ca^{2+}]_{ext}^{m}} + C \quad (3)$$

In the above equation, F_{end} is the asymptotic plateau of the fluorescence increase. Furthermore, $[Ca^{2+}]_{ext}$ is the extracellular Ca^{2+} concentration. $K_{M,fluo}$ (best fit value: 2.679 mM) is the concentration of extracellular Ca^{2+} at which fluorescence was half of F_{end}. The exponent m indicates a cooperative effect of the extracellular Ca^{2+} concentration on the fluorescence increase, which was constrained to a value of 2.43 (unitless) based on the described Ca^{2+}-cooperativity of GCaMP6m (Barnett et al., 2017). However, constraining this value only had a modest effect on the estimate of $K_{M,fluo}$ as leaving it as a free parameter yielded similar values for $K_{M,fluo}$ (3.054 mM) and m (1.887). The constant C added at the end of equation 3 allowed the baseline fluorescence to be different from zero. Results and best fit are summarized in Fig. 3 – figure supplement 1.

Proof that stochastic simulation of release is needed for PPR estimation

We here prove that stochastic simulations of neurotransmitter release provide a different average PPR value than the PPR value estimated in deterministic simulations. In the following, the stochastic variables A_1 and A_2 represent the amplitudes of the first and second release, respectively, capital 'E' denotes the mean of a stochastic variable (e.g. EA_1), and a_1 and a_2 represent the amplitudes of the first and second release in the deterministic simulations. In all cases of parameter sets that we tried, the average amplitudes from the stochastic simulations with 1000 repetitions differed <0.5 nA from the deterministically determined amplitudes. Thus, we can assume that $EA_1 = a_1$ and likewise for the second release.

In deterministic simulations, the estimate of the PPR is

$$\overline{PPR} = \frac{a_2}{a_1} = \frac{EA_2}{EA_1}$$

On the other hand, stochastic simulations yield a sample of different PPR values, since repetitions of the simulation routine yield release varying from trial to trial. In that case, the estimated PPR is

(4) $$\widetilde{PPR} = \mathrm{E}\left(\frac{A_2}{A_1}\right)$$

This resembles the way the PPR is estimated in experiments.

Using Jensen's Inequality and the fact that the function f(x) = 1/x is strictly convex, we get

$$\frac{1}{\mathrm{E}A_1} < \mathrm{E}\left(\frac{1}{A_1}\right) = \mathrm{E}(A_1^{-1})$$

Applying this to (4) we get

$$\widetilde{PPR} = \mathrm{E}\left(\frac{A_2}{A_1}\right) = \mathrm{E}(A_1^{-1}A_2) = Cov(A_1^{-1}, A_2) + \mathrm{E}(A_1^{-1})\mathrm{E}(A_2) > Cov(A_1^{-1}, A_2) + \frac{\mathrm{E}A_2}{\mathrm{E}A_1}$$

$$= Cov(A_1^{-1}, A_2) + \overline{PPR}$$

Thus, the average stochastically simulated PPR do not necessarily converge to the deterministic estimate with increasing repetitions (note that in general it is true that the mean of a non-linear function of two random variables is not equal to the non-linear function evaluated in the means). An example is shown in Fig. 4 – figure supplement 1, where the single-sensor model was simulated with varying amounts of Ca^{2+} influx (by varying Q_{max}). The most left blue point, for example, is significantly higher than the deterministic estimate (p=4e-16, one-sample t-test). This motivates the use of stochastic simulations for correct estimation of the PPR.

Simulation flow

All MATLAB procedures for simulation of the models can be found in the source code file linked to this paper.

All simulations (deterministic and stochastic, see below) consisted of the same four basic steps, which we describe in detail here.

1. Given a set of parameters, we first ran deterministic Ca^{2+} simulations in space and time in the presynapse at the desired extracellular Ca^{2+}-concentrations.
2. A set of SV distances was drawn from the generalized gamma distribution. The set of SV distances provided the points at which to read the intracellular Ca^{2+}-concentrations for the exocytosis simulation.
3. The simulation of the models for Ca^{2+} binding and exocytosis was performed for each SV position with the Ca^{2+} transients giving rise to the changing reaction rates.
4. The outcome of the exocytosis simulation were convolved with a mEJC which yielded the EJC.

For each new set of parameters, steps 1-4 were repeated. For stochastic simulations, steps 2-4 were repeated 1000 times except for the parameter exploration in Fig. 6J-K and 7J-K, where we ran 200 repetitions per parameter set. The many repetitions allowed a good estimate of both mean and variance of the models. In all cases, the mean amplitudes from the stochastic simulations with 1000 repetitions differed <0.5 nA from the deterministically determined amplitudes.

Ca^{2+} simulation

Simulation of Ca^{2+} signals in the presynapse was performed with the program CalC version 6.8.6 developed and maintained by Victor Matveev (Matveev et al., 2002). After this work was initiated, a bug affecting simulations of multiple Ca^{2+} channels in the same topology was found and a new version of CalC was released. This update had no effect on the simulations used in this study.

Intracellular Ca^{2+} concentrations were simulated in space and time in a cylinder shaped volume. The cylinder allowed us to assume spatial symmetry which reduced simulation time significantly. Borders of the simulation volume were assumed to be reflective to mimic diffusion of Ca^{2+} from adjacent AZs (Meinrenken et al., 2002) and a volume-distributed uptake mechanism was assumed.

From measurements of the distance between an AZ and its four nearest neighbors (Fig. 3A) we estimated the distance between centers of active zones to be 1.106 µm, leading to the assumption that the AZ spans a square on the membrane with area of 1.223 µm^2. In order for the cylindrical simulation volume to cover an area of the same size, the radius was set to 0.624 µm. The height of the simulation volume was set to 1 µm making the simulation volume 1.223 µm^3. Increasing the height further had no effect on the Ca^{2+} transients.

The total amount of charge flowing into the cell was assumed to relate to extracellular Ca^{2+} in a Michaelis-Menten-like way (as previously described by Schneggenburger et al. (1999) and Trommershauser et al. (2003)) such that

(5) $$Q = \frac{Q_{max} \cdot [Ca]_{ext}}{K_{M,current} + [Ca]_{ext}}$$

$K_{M,current}$ was set to the value of 2.679 mM as determined for $K_{M,fluo}$ in the GCaMP6m experiments (see above). Q_{max} was fitted during the optimizations of the models.

We simulated a 10 ms paired pulse stimulus initiated after 0.5 ms of simulation. The Ca^{2+} currents for the two stimuli were simulated for 3 ms each and assumed to be Gaussian with FWHM = 360 µs and peak 1.5 ms after initiation. That is:

$$I_{Ca} = \begin{cases} Q \cdot \frac{1}{\sigma \cdot \sqrt{2\pi}} e^{-\frac{(t-2)^2}{2\sigma^2}}, for\ t \in [0.5, 3.5] \\ Q \cdot \frac{1}{\sigma \cdot \sqrt{2\pi}} e^{-\frac{(t-12)^2}{2\sigma^2}}, for\ t \in [10.5, 13.5] \\ 0 \qquad\qquad\qquad\quad , else \end{cases}$$

with $\sigma = \frac{0.360}{2\sqrt{2 \cdot \ln(2)}} = 0.153$.

The CalC simulation output are data files that contain the spatio-temporal intracellular Ca^{2+} profile at the height of 10 nm from the plasma membrane. In exocytosis simulations, these concentrations were interpolated at the SV distances in the x,y-plane and at time points with MATLAB's built-in interpolate functions when computing the reaction rates of the system at a given time point.

The resting Ca^{2+} concentration was assumed to relate to the extracellular Ca^{2+} concentration in a similar way as during stimulation, such that

(6) $$[Ca^{2+}]_{basal} = [Ca^{2+}]_{max} \cdot \frac{[Ca^{2+}]_{ext}}{K_{M,current} + [Ca^{2+}]_{ext}}$$

with $[Ca^{2+}]_{max} = 190\ nM$.

For designation and value of Ca^{2+} parameters, see Table 1.

SV distribution drawing

In all simulations we had to determine where to place release site. This was done by using the cdf of the SV distance distribution derived above (equation 2).

For deterministic simulations, which were used in the fitting routine of the models (see below), the unit interval was divided into 180 bins of the form

$$\left(\frac{k-1}{180}, \frac{k}{180}\right), \qquad k = 1, 2 \ldots 180.$$

The midpoints were the percentiles giving rise to distances at which we read the Ca^{2+} simulation. This approach provided an approximation of the SV distribution. In accordance with our assumption that the AZs work in parallel the 180 distances gave rise to 180 independent different systems of ODEs with 1/180 of the total amount of SVs in each system. The results were then added together as a good approximation of the mean of the stochastic simulations with random SV distance drawings.

In each run of the stochastic simulations, we drew *n* random numbers from the unit interval, *n* being the number of SVs, and computed the distances based on the above formula.

Rate equations of the simulated models

The models are summarized in Figs. 4A, 6A, 7A, and Fig. 7 – figure supplement 2A,B. In the following equations the single-sensor, dual fusion-sensor, and unpriming models are all described. The site activation model is a combination of the equations for the single-sensor model and the site activation equations described below. The green text denotes terms that are unique to the dual fusion-sensor model, blue text indicates unpriming, which is unique to the unpriming model. Parameters are described below. For designation and value of parameters, see Table 2 and 3.

Rate equations of the single-sensor model, dual fusion-sensor model and unpriming model

$$\frac{d[R(0,0)]}{dt} = k_{rep}[P0] - (r \cdot u + 5[Ca^{2+}]k_1 + 2[Ca^{2+}]k_2 + L^+)[R(0,0)] + k_{-1}[R(1,0)] + k_{-2}[R(0,1)]$$

$$\frac{d[R(1,0)]}{dt} = -(4[Ca^{2+}]k_1 + k_{-1} + 2[Ca^{2+}]k_2 + L^+f)[R(1,0)] + 5[Ca^{2+}]k_1[R(0,0)] + 2b_f k_{-1}[R(2,0)] + k_{-2}[R(1,1)]$$

$$\frac{d[R(2,0)]}{dt} = -\left(3[Ca^{2+}]k_1 + 2b_f k_{-1} + 2[Ca^{2+}]k_2 + L^+f^2\right)[R(2,0)] + 4[Ca^{2+}]k_1[R(1,0)] + 3b_f^2 k_{-1} \cdot [R(3,0)] + k_{-2} \cdot [R(2,1)]$$

$$\frac{d[R(3,0)]}{dt} = -\left(2[Ca^{2+}]k_1 + 3b_f^2\, k_{-1} + 2[Ca^{2+}]k_2 + L^+f^3\right)[R(3,0)] + 3[Ca^{2+}]k_1[R(2,0)] + 4b_f^3 k_{-1} \cdot [R(4,0)] + k_{-2} \cdot [R(3,1)]$$

$$\frac{dR[(4,0)]}{dt} = -\left([Ca^{2+}]k_1 + 4b_f^3 k_{-1} + 2[Ca^{2+}]k_2 + L^+f^4\right)[R(4,0)] + 2[Ca^{2+}]k_1[R(3,0)] + 5b_f^4 k_{-1} \cdot [R(5,0)] + k_{-2} \cdot [R(4,1)]$$

$$\frac{d[R(5,0)]}{dt} = -\left(2[Ca^{2+}]k_2 + 5b_f^4 k_{-1} + L^+f^5\right)[R(5,0)] + [Ca^{2+}]k_1[R(4,0)] + k_{-2} \cdot [R(4,1)]$$

$$\frac{d[R(0,1)]}{dt} = k_{rep}[P1] - (5[Ca^{2+}]k_1 + [Ca^{2+}]k_2 + k_{-2} + L^+s)[R(0,1)] + k_{-1} \cdot [R(1,1)] + 2[Ca^{2+}]k_2[R(0,0)] + 2b_s k_{-2} \cdot [R(0,2)]$$

$$\frac{d[R(1,1)]}{dt} = -(4[Ca^{2+}]k_1 + k_{-1} + [Ca^{2+}]k_2 + k_{-2} + L^+fs)[R(1,1)] + 5[Ca^{2+}]k_1[R(0,1)] + 2b_f k_{-1} \cdot [R(2,0)] + 2[Ca^{2+}]k_2[R(1,0)] + 2b_s k_{-2} \cdot [R(1,2)]$$

$$\frac{d[R(2,1)]}{dt} = -\left(3[Ca^{2+}]k_1 + 2b_f k_{-1} + [Ca^{2+}]k_2 + k_{-2} + L^+f^2s\right)[R(2,1)] + 4[Ca^{2+}]k_1[R(1,1)] + 3 \cdot b_f^2 \cdot k_{-1}[R(3,1)] + 2[Ca^{2+}]k_2[R(2,0)] + 2b_s k_{-2} \cdot [R(2,2)]$$

$$\frac{d[R(3,1)]}{dt} = -\left(2[Ca^{2+}]k_1 + 3b_f^2\, k_{-1} + [Ca^{2+}]k_2 + k_{-2} + L^+f^3s\right)[R(3,1)] + 3[Ca^{2+}]k_1[R(2,1)] + 4b_f^3 k_{-1} \cdot [R(4,1)] + 2[Ca^{2+}]k_2[R(3,0)] + 2b_s k_{-2} \cdot [R(3,2)]$$

$$\frac{d[R(4,1)]}{dt} = -\left([Ca^{2+}]k_1 + 4b_f^3k_{-1} + [Ca^{2+}]k_2 + k_{-2} + L^+f^4s\right)[R(4,1)] + 2[Ca^{2+}]k_1[R(3,1)]$$
$$+ 5b_f^3k_{-1}\cdot[R(5,1)] + 2[Ca^{2+}]k_2[R(4,0)] + 2b_sk_{-2}[R(4,2)]$$

$$\frac{d[R(5,1)]}{dt} = -\left(5b_f^4k_{-1} + [Ca^{2+}]k_2 + k_{-2} + L^+f^5s\right)[R(5,1)] + [Ca^{2+}]k_1[R(4,1)]$$
$$+ 2[Ca^{2+}]k_2[R(5,0)] + 2b_sk_{-2}\cdot[R(5,2)]$$

$$\frac{d[R(0,2)]}{dt} = k_{rep}[P2] - (5[Ca^{2+}]k_1 + 2b_sk_{-2} + L^+s^2)[R(0,2)] + k_{-1}[R(1,2)]$$
$$+ [Ca^{2+}]k_2[R(0,1)]$$

$$\frac{d[R(1,2)]}{dt} = -(4[Ca^{2+}]k_1 + k_{-1} + 2b_sk_{-2} + L^+fs^2)[R(1,2)] + 5[Ca^{2+}]k_1[R(0,2)]$$
$$+ 2b_fk_{-1}[R(2,2)] + [Ca^{2+}]k_2[R(1,1)]$$

$$\frac{d[R(2,2)]}{dt} = -\left(3[Ca^{2+}]k_1 + 2b_fk_{-1} + 2b_sk_{-2} + L^+f^2s^2\right)[R(2,0)] + 4[Ca^{2+}]k_1[R(1,2)]$$
$$+ 3b_f^2k_{-1}[R(3,0)] + [Ca^{2+}]k_2[R(2,1)]$$

$$\frac{d[R(3,2)]}{dt} = -\left(2[Ca^{2+}]k_1 + 3b_f^2\,k_{-1} + 2b_sk_{-2} + [Ca^{2+}]k_2 + L^+f^3s^2\right)[R(3,2)]$$
$$+ 3[Ca^{2+}]k_1[R(2,2)] + 4b_f^3k_{-1}\cdot[R(4,2)] + [Ca^{2+}]k_2[R(3,1)]$$

$$\frac{d[R(4,2)]}{dt} = -\left([Ca^{2+}]k_1 + 4b_f^3k_{-1} + 2b_sk_{-2} + [Ca^{2+}]k_2 + L^+f^4s^2\right)[R(4,2)]$$
$$+ 2[Ca^{2+}]k_1[R(3,2)] + 5b_f^3k_{-1}\cdot[R(5,2)] + [Ca^{2+}]k_2[R(4,1)]$$

$$\frac{d[R(5,2)]}{dt} = -\left(5b_f^4k_{-1} + 2b_sk_{-2} + L^+f^5s^2\right)[R(5,2)] + [Ca^{2+}]k_1[R(4,2)] + [Ca^{2+}]k_2[R(5,1)]$$

$$\frac{d[F]}{dt} = L^+([R(0,0)] + f[R(1,0)] + f^2[R(2,0)] + f^3[R(3,0)] + f^4[R(4,0)] + f^5[R(5,0)]$$
$$+ [sR(0,1)] + fs[R(1,1)] + f^2s[R(2,1)] + f^3s[R(3,1)] + f^4s[R(4,1)]$$
$$+ f^5s[R(5,1)] + [s^2R(0,2)] + fs^2[R(1,1)] + f^2s^2[R(2,1)] + f^3s^2[R(3,1)]$$
$$+ f^4s^2[R(4,1)] + f^5s^2[R(5,1)])$$

$$\frac{d[P0]}{dt} = L^+([R(0,0)] + f[R(1,0)] + f^2[R(2,0)] + f^3[R(3,0)] + f^4[R(4,0)] + f^5[R(5,0)])$$
$$+ k_{-2}[P1] - 2k_2[Ca^{2+}][P0] - k_{rep}[R(0,0)] + \mathrm{r}\cdot\mathrm{u[R(0,0)]}$$

$$\frac{d[P1]}{dt} = L^+([sR(0,1)] + fs[R(1,1)] + f^2s[R(2,1)] + f^3s[R(3,1)] + f^4s[R(4,1)]$$
$$+ f^5s[R(5,1)]) - k_{-2}[P1] + 2k_2[Ca^{2+}][P0] + 2b_sk_{-2}\cdot[P2] - k_{rep}[R(0,1)]$$

$$\frac{d[P2]}{dt} = L^{+}([R(0,0)] + f[R(1,0)] + f^2[R(2,0)] + f^3[R(3,0)] + f^4[R(4,0)] + f^5[R(5,0)]$$
$$+ [sR(0,1)] + fs[R(1,1)] + f^2s[R(2,1)] + f^3s[R(3,1)] + f^4s[R(4,1)]$$
$$+ f^5s[R(5,1)] + [s^2R(0,2)] + fs^2[R(1,1)] + f^2s^2[R(2,1)] + f^3s^2[R(3,1)]$$
$$+ f^4s^2[R(4,1)] + f^5s^2[R(5,1)]) + 2k_2[P1] - 2b_sk_{-2}[Ca^{2+}][P2] - k_{rep}[R(0,2)]$$

$$r = 1 - \frac{[Ca^{2+}]^n}{[Ca^{2+}]^n + K_{M,unprim}^n}$$

In the single-sensor and site activation models, k_2=k_{-2}=u=0, and s=1. This excludes all reactions exclusive for the dual fusion-sensor and unpriming models. Similarly, u=0 in the dual fusion-sensor model and k_2=k_{-2}=0 and s=1 in the unpriming model.

[*R(n,m)*] denotes the Ca^{2+} binding state of a SV with n Ca^{2+} ions bound to the first sensor and m Ca^{2+} ions bound to the second fusion sensor. Note that in the single-sensor, site activation and unpriming models, m is always zero (since there is no second fusion sensor), and the states are denoted [*R(n)*] in Figs. 4A, 6A, and Fig. 7 – figure supplement 2. [*F*] counts the cumulative number of fused SVs. [*P0*] is not shown in the figures, but are part of the equations denoting the number of empty sites. That is, in the single-sensor and unpriming models $\frac{d[P0]}{dt}$ has a positive part equal to $\frac{d[F]}{dt}$ and a negative part equal to the rate of replenishment. In the dual fusion-sensor model, there are three states of empty sites, [P0], [P1], [P2]. These corresponded to the different states of Ca^{2+} binding to the second fusion sensor of the empty sites since we assumed the second sensor to be located on the plasma membrane. Note that these equations describe the second sensor with cooperativity 2, which is described in Results. We also optimized cooperativities 3, 4, and 5. The equations can easily be extended to these cases, since the rate equations of the second fusion sensor are of the same form as for the first sensor. In the unpriming model (Fig. 7A) we assumed unpriming to take place from state *[R(0)]* with a Ca^{2+}-dependent rate.

For the individual reactions, we can express the rates of Ca^{2+} (un)binding, fusion, and replenishment of a single SV in a more general form. This is useful in the stochastic simulation method introduced later. In the following, we denote the general form of the rate for each possible reaction in the models described above. The expressions in brackets denote the states involved in the reaction.

$$[R(n,m)] \rightarrow [R(n-1,m)]: nk_{-1}b^{n-1}$$
$$[R(n,m)] \rightarrow [R(n+1,m)]: (n_{max}-n)[Ca^{2+}]k_1$$
$$[R(n,m)] \rightarrow [R(n,m-1)]: mk_{-2}b^{m-1} \quad (7)$$
$$[R(n,m)] \rightarrow [R(n,m+1)]: (m_{max}-m)[Ca^{2+}]k_2$$
$$[R(n,m)] \rightarrow [F]: L^{+}s^m f^n$$
$$[P0] \rightarrow [R(0,0)]: k_{rep}$$

with n_{max} and m_{max} denoting the cooperativity of the first and second fusion sensors, respectively. Equations in line 3 and 4 in (7) were only non-zero in the dual fusion-sensor model.

Rate equation of the site activation model

In the site activation model (Fig. 7 – figure supplement 2), all reactions regarding Ca^{2+} (un)binding and replenishment was as in the one-sensor model. In addition we assumed a mechanism acting on the release sites independently of the Ca^{2+} binding of the SV. All sites regardless of the SV status were either activated (A state) or not (D or I states). This

mechanism is proposed as a facilitation mechanism, which necessitates its primary effect to be on the second stimulus rather than the first. We were therefore forced to implement the D state, which is a temporary "delay" state making sure the mechanism does not increase first release. The changing of [A] and [I] states at 0.75 and 10 mM extracellular Ca^{2+} are shown in (Fig. 7 – figure supplement 2I).

The site activation mechanism has the following rate equations:

$$\frac{d[A]}{dt} = -\delta[A] + \gamma[D]$$

$$\frac{d[D]}{dt} = -(\beta + \gamma)[D] + \alpha[Ca^{2+}]^n[I] + \delta[A]$$

$$\frac{d[I]}{dt} = -\alpha[Ca^{2+}]^n[I] + \beta[D]$$

where $\alpha, \beta, \delta, \gamma > 0$ are rate parameters.

The deterministic implementation of the site activation model included 3 sets of ODEs, one for each state in the site activation model. Each set consisted of the equations of the one-sensor model as well as transitions between states of equal Ca^{2+} binding in the 3 sets of ODEs (e.g. from R(0,D) to R(0,A))(Fig. 7 – figure supplement 2B).

In the stochastic simulations the site activation rates were included in the propensity vector like any other reaction. Whenever a site activation reaction occurred, a release site vector consisting of n_{sites} elements was updated. For each site, the fusion rate was multiplied by 0, when the site state was I or D.

Steady-state estimation

Prior to simulation, the Ca^{2+} binding states of all SVs were assumed to be in equilibrium. We can determine the steady state iteratively by setting

$$[R(0,0)]_{init} = 1$$

$$[R(n+1,m)]_{init} = \frac{(n_{max} - n)[Ca^{2+}]k_1}{(n+1)k_{-1}b^n}[R(n,m)]_{init}$$

$$[R(n,m+1)]_{init} = \frac{(m_{max} - m)[Ca^{2+}]k_2}{(m+1)k_{-2}b^m}[R(n,m)]_{init}$$

This can be reduced to the non-iterative expression:

$$[R(n,m)]_{init} = \frac{(\prod_{i=1}^{n}(n_{max}+1-i)) \cdot [Ca^{2+}]^n \cdot k_1^n}{n! \cdot b^{\sum_{j=1}^{n}(j-1)} \cdot k_{-1}^n} \cdot \frac{(\prod_{i=1}^{m}(m_{max}+1-i)) \cdot [Ca^{2+}]^m \cdot k_2^m}{m! \cdot b^{\sum_{j=1}^{m}(j-1)} \cdot k_{-2}^m}$$

$$= \left(\frac{\frac{n_{max}!}{(n_{max}-n)!} \cdot [Ca^{2+}]^n k_1^n}{n! \cdot b^{\frac{n(n-1)}{2}} \cdot k_{-1}^n}\right) \cdot \left(\frac{\frac{m_{max}!}{(m_{max}-m)!} \cdot [Ca^{2+}]^m k_2^m}{m! \cdot b^{\frac{m(m-1)}{2}} \cdot k_{-2}^m}\right)$$

Note that for n = 0, the first parenthesis is 1, while m = 0 implies that the second parenthesis is 1, making this solution valid also in the absence of a second fusion-sensor. We ignored the very small fusion rate. In the steady-state of the unpriming model, the number of SVs in *[R(0,0)]* must furthermore be in equilibrium with the number of empty states:

$$[P] = \frac{r \cdot u}{k_{rep} + r \cdot u} \cdot [R(0,0)]$$

After finding this steady-state, the solution is scaled to match the desired number of SVs, by multiplying all states with a constant, such that the sum of all *[R(n,m)]* and *[P]* equals the number of SVs. The steady-state of the site activation was determined before simulation by calculating the fraction of states being in [A], [D], or [I]. This was done by calculating

$$[D] = 1, \quad [A] = \frac{\delta}{\gamma}[D] = \frac{\delta}{\gamma}, \quad [I] = \frac{\beta}{[Ca^{2+}]^n\alpha}[D] = \frac{\beta}{[Ca^{2+}]^n\alpha}$$

and normalizing to sum to 1. This determined the steady state fraction of activation of sites. In the stochastic simulations, the SVs were randomly assigned initial states according to the probabilities of the different states in the steady-state.

Deterministic exocytosis simulation

All deterministic exocytosis simulations of the above equations were carried out with the inbuilt MATLAB ODE solver *ode15s*.

Stochastic exocytosis simulation

All stochastic exocytosis simulations as well as simulation data handling were carried out in MATLAB with custom-written scripts (included in the accompanying source code file). For the simulation itself we used a modified version of the Gillespie Algorithm (Gillespie, 2007), which included a minimal time step since reaction rates change quickly with the changing intracellular Ca^{2+} concentration. The minimal step was μ=1e-6 s. In the algorithm, the time from the current simulation time point, *t*, until the next reaction,τ, is determined, the reaction is carried out and the new simulation time point is set to t+τ. Whenever the simulation yielded τ>μ, the simulation time point was set to t+μ, no reaction was carried out and the propensities of the model were updated at the new time point. This is a valid method of obtaining a better estimate because the waiting time until next reaction is exponentially distributed.

The implementation of the algorithm takes advantage of the general form of the rate equations in (7). Instead of calculating matrices of states and reaction rates, we have a vector, *V*, of length n_{sites}, where each element represents the status of one SV/site. The SV state of a docked SV on the *kth* site in state [R(n,m)] is denoted by the two-digit number

$$V_k = m \cdot 10 + n$$

If the site is empty (due to initial submaximal priming or SV fusion) we assigned $V_k = 100$.

Using equation 7, the rates of any primed SV are

$$r_k = \begin{pmatrix} m \cdot k_{-2} \cdot b^{m-1} \\ n \cdot k_{-1} \cdot b^{n-1} \\ L^+ f^n s^m \\ (n_{max} - n) \cdot [Ca^{2+}] \cdot k_1 \\ (m_{max} - m) \cdot [Ca^{2+}] \cdot k\_2 \\ r \cdot b \end{pmatrix}$$

The sum of these rates of all SVs yield the summed propensities of the system, a_0, which is the basis of the calculation of τ, whereas the cumulative sum is used for determination of which SV undergoes a reaction (Gillespie, 2007). When a SV undergoes a reaction, we find the index of the reaction occurring, *j*, by using the cumulative sum of r_i in the same way as in the standard implementation of the Gillespie Algorithm (Gillespie, 2007). Putting $\hat{\jmath} = j - 3$ allows us to easily update the status of the SV, since

$$V_k = V_k + \mathbf{1}_{(\hat{\jmath}\neq 3)} \cdot sign(\hat{\jmath}) \cdot 10^{|\hat{\jmath}|-1} + \mathbf{1}_{(\hat{\jmath}=0)\vee(\hat{\jmath}=3)} \cdot (100 - V_k)$$

In parallel with this a vector of fusions is updated, such that at every time point, the next element in the fusion vector is set to $\mathbf{1}_{(\hat{\jmath}=0)}$.

Parallel computing

Many repetitions of time consuming stochastic simulations had to be performed, and many sets of ODEs were solved for each choice of parameters. Therefore, simulations were carried out on the computer grid on The Bioinformatics Center, University of Copenhagen. This allowed running repetitions in parallel with MATLAB's *Parallel Computing toolbox* using between 5 and 100 cores depending on the simulation job.

Calculating the postsynaptic response

In order to calculate the eEJC, we needed a vector of the SV fusions at different time points. Both deterministic and stochastic simulations yielded the vectors *time_outcome* and *fuse_outcome*, which is a pair of vectors of the same

length but with changing time steps. For the sampling we generated a time vector, *time_sample,* with a fixed time step of 1 µs. From here, the determining of the SV fusion times differ between deterministic and stochastic simulations.

In the deterministic simulations, we simulated a sample of distances, *bins*, as described earlier. Each bin gave rise to a set of ODEs, which could be simulated independently, and the *fuse_outcome* is continuously changing based on the rates. In MATLAB the interpolation for bin *k* was done as follows:

$fuse\_interp_k = interp1(time\_outcome, fuse\_outcome, time\_sample)$

$fuse\_interp_k$ contained the cumulative fused SVs over time in a single bin sampled at the time points of the vector *time_sample*. These were summed to find the total number of fused SVs:

$$fuse\_interp = \sum_{k=1}^{n_{bins}} fuse\_interp_k$$

Therefore the SVs fused per time step were be the difference between neighboring values in the *fuse_interp* vector:

$fusion\_vec = [0, diff(fuse\_interp)]$

This vector was the basis for the computation of the eEJC d.

In the stochastic simulations, the *fuse_outcome* vector contains discrete SV fusions at certain time points. We therefore sample the SV fusions by assigning them to the nearest time points on the *time_sample* vector. That is, each fusion time was rounded to the nearest microsecond, thereby giving rise to the *fusion_vec*, which in the stochastic case contained whole numbers of SV fusions at different time points.

In both deterministic and stochastic simulations the mEJC was generated as a vector, *mEJC_vec,* with the same time step as the *time_sample* and *fuse_vec*. This allows us to calculate the eEJC with MATLAB's convolve function, *conv*, such that

$$eEJC = conv(fuse\_vec, mEPSC\_vec)$$

where *fusion_vec* is a vector with the same time step, each element being the number of SV fusions at each time point.

Analysis of simulated eEJCs

The $eEJC_1$ amplitude was determined as the minimum current of the eEJC within the time interval (0,10) ms. Similar to the analysis of experimental eEJC data, we fitted an exponential function to the decay for estimation of the base value for the second response (Fig. 2 – figure supplement 1A). The $eEJC_2$ amplitude was the difference between the second local minimum and the fitted exponential function extrapolated to the time point of the second local minimum (as described for the analysis of electrophysiology experiments).

Fitting routine

Because deterministic simulations cannot predict PPR-values (due to Jensen's inequality, see above), but stochastic simulations cannot be fitted to data, we first ran deterministic simulations comparing the simulated first and second absolute eEJC amplitudes to the experimental amplitudes (not the PPR, see Methods). Afterwards we ran stochastic simulations with the optimised parameters in order to compare PPRs and variances to experimental results. To determine the optimal parameters for the deterministic simulations at the five experimental extracellular Ca^{2+} concentrations, the models were fitted to the two peak amplitudes, $eEJC_1$ and $eEJC_2$, by minimizing the following cost value:

$$cost(eEJC_{1,sim}, eEJC_{2,sim}) = \sum_{k=1}^{5} \left(\frac{\left(eEJC_{1,sim,k} - eEJC_{1,exp,k}\right)^2}{eEJC_{1,exp,k}} + \frac{\left(eEJC_{2,sim,k} - eEJC_{2,exp,k}\right)^2}{eEJC_{2,exp,k}} \right)$$

where we sum over the five different experimental Ca^{2+} concentrations. Note that in deterministic simulations, $eEJC_1$ and $eEJC_2$ amplitudes are precise estimates of average amplitudes in stochastic simulations allowing us to do deterministic optimizations.

When fitting the models, we used the inbuilt MATLAB function *fminsearch,* which uses the Nelder-Mead Simplex Search, to minimize the above cost function. The cost calculation in each iteration was a two-step process

taking advantage of the fact that the total number of SVs scales the $eEJC_1$ and $eEJC_2$ values in the deterministic simulations. For each choice of parameters the simulation was run with 180 sites (the initial number of sites is arbitrary, but matched the number of bins), and the optimal number of sites were determined afterwards. Thus, a given set of parameters gave rise to amplitudes $eEJC_{1,init}$ and $eEJC_{2,init}$ from simulations with 180 sites. After that we determined $c_{sites} \in \mathbb{R}^+$ such that $cost(c_{sites}\mathrm{eEJC}_{1,\mathrm{init}}, c_{sites}eEJC_{2,init})$ was minimized. The number of sites in the given iteration was therefore $180 \cdot c_{sites}$ and the cost of that particular iteration was

$$cost\left(eEJC_{1,sim}, eEJC_{2,sim}\right) = cost(c_{sites}\mathrm{eEJC}_{1,\mathrm{init}}, c_{sites}eEJC_{2,init})$$

In this way the optimization algorithm did not have to include n_{sites} in the parameter search algorithm, which reduced the number of iterations significantly. In the stochastic simulations, the number of SVs was set to $180 \cdot c_{sites}$ rounded to nearest integer.

Table 1: Parameters of Ca^{2+} and buffer dynamics

Simulation volume		
r	Radius of cylindric simulation volume	623.99 nm
h	Height of cylindric simulation volume	1 µm
n_{grid}	Spatial grid points in CalC simulation	71x101 (radius x height)
Ca^{2+}		
Q_{max}	Scaling of the total amount of Ca^{2+} charge influx	Fitted (all models), see Table 3
D_{Ca}	Diffusion coefficient of Ca^{2+} (Allbritton et al., 1992)	0.223 $\mu m^2/ms$
$[Ca]_{bgr}$	Background Ca^{2+}	$190\ nm \cdot \frac{[Ca^{2+}]_{ext}}{[Ca^{2+}]_{ext} + K_M}$
$K_{M,current}$	Set to the same value as $K_{M,fluo}$ determined in GCaMP6 experiments	2.679 mM
Uptake	Volume-distributed uptake (Helmchen et al., 1997)	0.4 ms^{-1}
Buffer Bm ("fixed" buffer)		
D_{Bm}	Diffusion coefficient	0.001 $\mu m^2/ms$
K_D	Equilibrium dissociation constant (Xu et al., 1997)	100 µM
K_+	Ca^{2+} binding rate (Xu et al., 1997)	0.1 $(\mu M \cdot ms)^{-1}$
K_-	Ca^{2+} unbinding rate: $K_D \cdot K_+$	1 ms^{-1}
Total Bm	Total concentration (bound+unbound) (Xu et al., 1997)	4000 µM
Buffer ATP		
D_{ATP}	Diffusion coefficient (Chen et al., 2015)	0.22 $\mu m^2/ms$
K_D	Equilibrium dissociation constant (Chen et al., 2015)	200 µM
K_+	Ca^{2+} binding rate (Chen et al., 2015)	0.5 $(\mu M \cdot ms)^{-1}$
K_-	Ca^{2+} unbinding rate: $K_D \cdot K_+$	100 ms^{-1}
Total ATP	Total concentration (bound+unbound) (Chen et al., 2015)	650 µM
Resting Ca^{2+}		
$K_{M,current}$	Michaelis Menten-constant of resting Ca^{2+} (same as $K_{M,current}$ of Ca^{2+} influx)	2.679 mM
$[Ca^{2+}]_{max}$	Asymptotic max value of resting Ca^{2+}	190 nM

Table 2: Parameters of exocytosis simulation

Parameter	Explanation and reference	Value
Common parameters		
n_{sites}	Number of sites (=maximal number of SVs)	Fitted (all models), see Table 3
L^+	Basal fusion rate constant (Kochubey and Schneggenburger, 2011)	$3.5 \cdot 10^{-4}$ s^{-1}
q	Amplitude of the mEJC. Estimated from variance-mean of data (see Fig. 2F)	0.6 nA
Fast sensor (all models)		
n_{max}	Cooperativity, fast sensor (Lou et al., 2005; Schneggenburger and Neher, 2000; Wolfel et al., 2007)	5
k_1	Ca^{2+} binding rate, first sensor (Wolfel et al., 2007)	$1.4 \cdot 10^8$ $M^{-1}s^{-1}$
k_{-1}	Ca^{2+} unbinding rate, first sensor (Wolfel et al., 2007)	4000 s^{-1}
b_f	Cooperativity factor, first sensor (Lou et al., 2005; Wolfel et al., 2007)	0.5
k_f	Fusion rate constant of R(5,0) (fast sensor fully activated). (Lou et al., 2005; Schneggenburger and Neher, 2000; Wolfel et al., 2007)	6000 s^{-1}
f	$\sqrt[5]{\frac{k_f}{L^+}}$	27.978
Replenishment (all models)		
k_{rep}	Replenishment rate constant	Fitted (all models), see Table 3
Slow sensor (dual fusion-sensor model)		
m_{max}	Cooperativity, second fusion sensor	2 (5 in figure supplement)
k_D	Dissociation constant, second fusion sensor (Brandt et al., 2012)	1.5 µM
k_2	Ca^{2+} binding rate, second fusion sensor	Fitted (dual fusion-sensor model), see Table 3
k_{-2}	Ca^{2+} unbinding rate, second fusion sensor	$k_D \cdot k_2$
b_s	Cooperativity factor, second fusion sensor (=b_f)	0.5
s	Second fusion sensor analogue of f: Factor on the fusion rate	Fitted (dual fusion-sensor model), see Table 3
Unpriming (unpriming model)		
n	Cooperativity (exponent in unpriming rate equation)	5 (2 in figure supplement)

u	Rate constant of unpriming	Fitted (unpriming model), see Table 3
$K_{M,prim}$	Michaelis-Menten constant in expression of r	
Site activation (site activation model)		
n	Cooperativity (exponent on $[Ca^{2+}]$	5
α	Rate constant [I] to [D]	1e6
β	Rate constant [D] to [I]	Fitted (site activation model), see Table 3
γ	Rate constant [D] to [A]	
δ	Rate constant [A] to [D]	

Table 3: Best fit parameters of all models

Models presented in main figures			
	Single sensor model (Fig. 4)	**Dual fusion-sensor model, cooperativity 2 (Fig. 6)**	**Unpriming model, cooperativity 5 (Fig. 7)**
Q_{max}	8.42 fC	4.51 fC	13.77 fC
k_{rep}	165.53 s^{-1}	159.30 s^{-1}	134.85 s^{-1}
n_{sites}	216	211	180
k_2		4.10e7 $M^{-1}s^{-1}$	
s		510.26	
u			236.82 s^{-1}
$k_{M,prim}$			55.21 nM^{-1}
Cost value (see Methods)	9.689	4.129	0.340
Models presented in figure supplements			
	Dual fusion-sensor model, cooperativity 5 Fig. 6 – figure supplement 1)	**Unpriming model, cooperativity 2 (Fig. 7 – figure supplement 1)**	**Site activation model (Fig. 7 – figure supplement 2)**
Q_{max}	8.10 fC	13.49 fC	12.59 fC
k_{rep}	492.56 s^{-1}	106.59 s^{-1}	141.20 s^{-1}
n_{sites}	112	203	189
k_2	5.41e6 $M^{-1}s^{-1}$		
s	261.07		
u		5207.70 s^{-1}	
$k_{M,prim}$		7.61 nM^{-1}	
β			0.09 s^{-1}
γ			194.77 s^{-1}
δ			10.70 s^{-1}
Cost value (see Methods)	2.941	0.642	1.57

Supplementary Figures

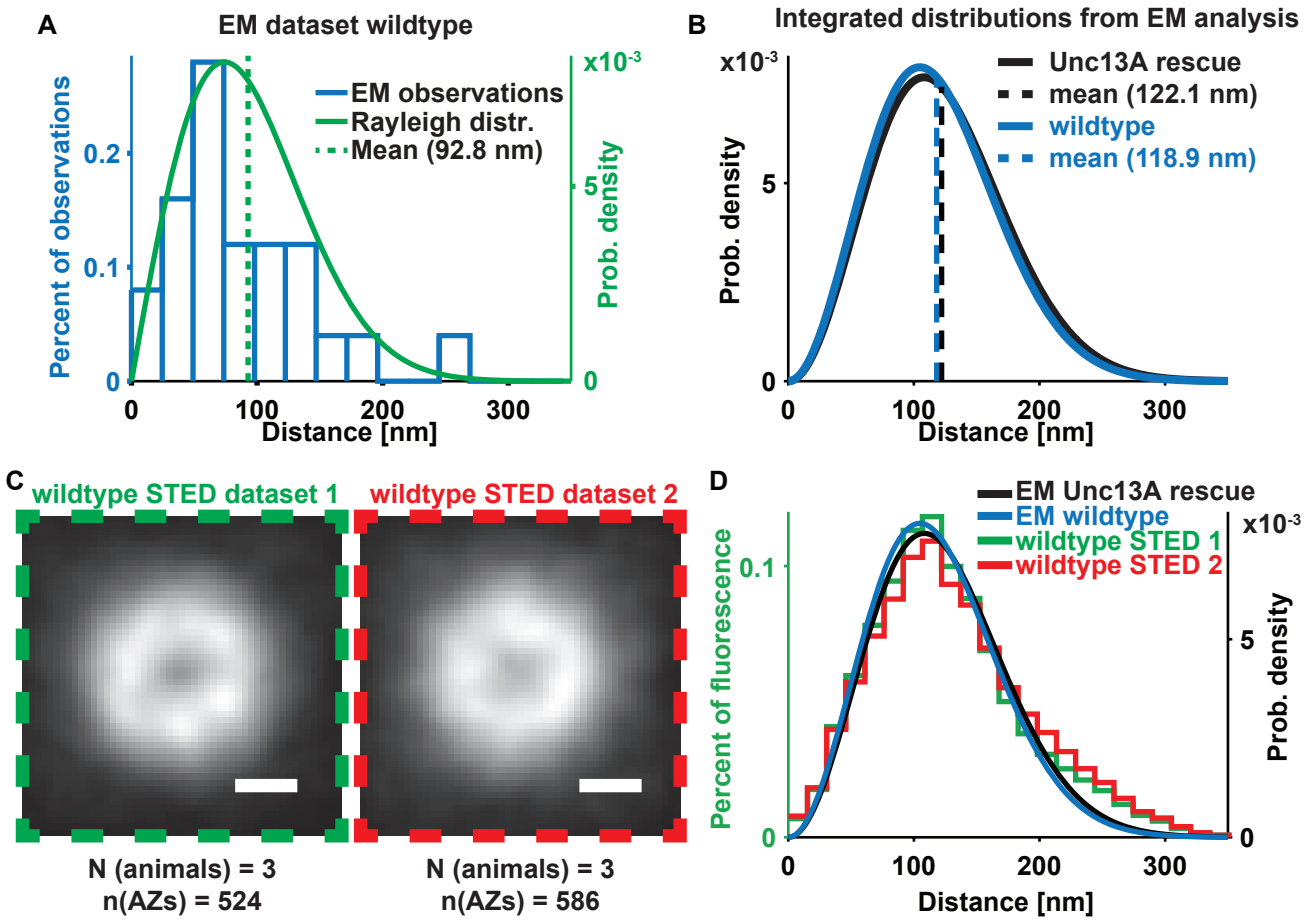

Figure 1 – figure supplement 1. EM + STED vesicle positions are consistent between independent datasets and overlapping with each other. **(A)** Histogram (blue) of the distances of docked SVs to the T-bar center obtained from EM micrographs of Wild-type animals ("EM dataset 1") plotted with a fitted Rayleigh distribution (green, N = 5 animals, n = 11 AZs, mean of Rayleigh distibution = 92.83 nm, SD is 48.5 nm; the same distance measurements had been used for the analysis depicted in Fig. 6 of (Bohme et al., 2016)). **(B)** Integrated distributions of "EM dataset 2" (Fig. 1B, black) with a mean of 122.1 nm and SD of 51.5 nm and of "EM dataset 1" with a mean of 118.9 nm (blue) and SD of 49.9 nm. **(C)** Average images of "STED dataset 1" (replotted from Fig. 1E, green box) (N = 3 animals, n = 524 AZs) and "STED dataset 2" (red box) (N = 3 animals, n = 586 AZs). **(D)** Overlay of the distance distributions derived from all four (two EM and two STED) datasets. Used genotypes: *w[1118]* ("EM dataset 2", panel A-D), Unc13A rescue ("EM dataset 1", panel B, D). Methods section "Fly husbandry, genotypes and handling" lists all exact genotypes.

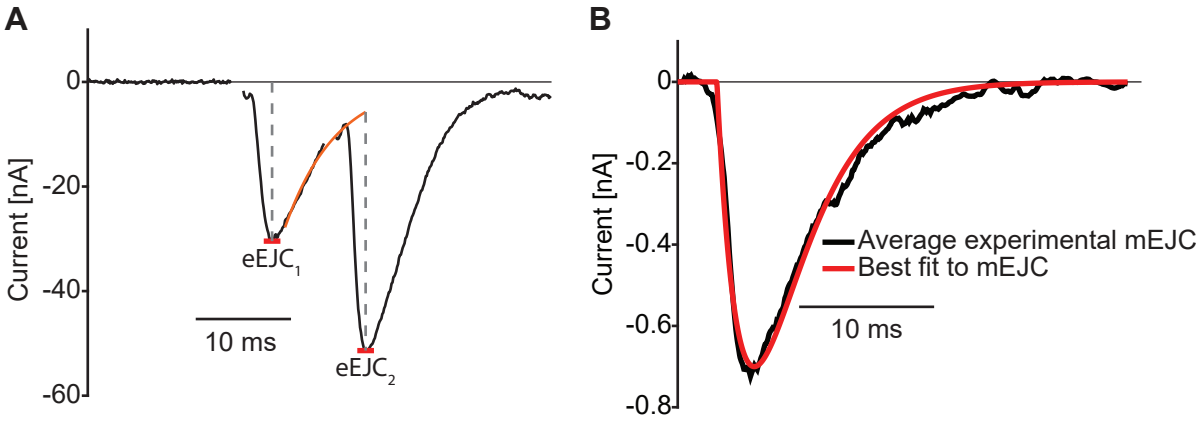

Figure 2 – figure supplement 1. Illustration of analysis of experimental data. **(A)** Analysis of eEJCs. The $eEJC_1$ amplitude is determined as the first minimum within 10 ms of the stimulus. The $eEJC_2$ amplitude is determined from the baseline found by exponential extrapolation of the $eEJC_1$ decay. **(B)** The mean mEJC from experimental recordings and the best fit used for convolution (see Methods). Used genotype: *Ok6-Gal4/II* crossed to *w[1118]*. Methods section "Fly husbandry, genotypes and handling" lists all exact genotypes.

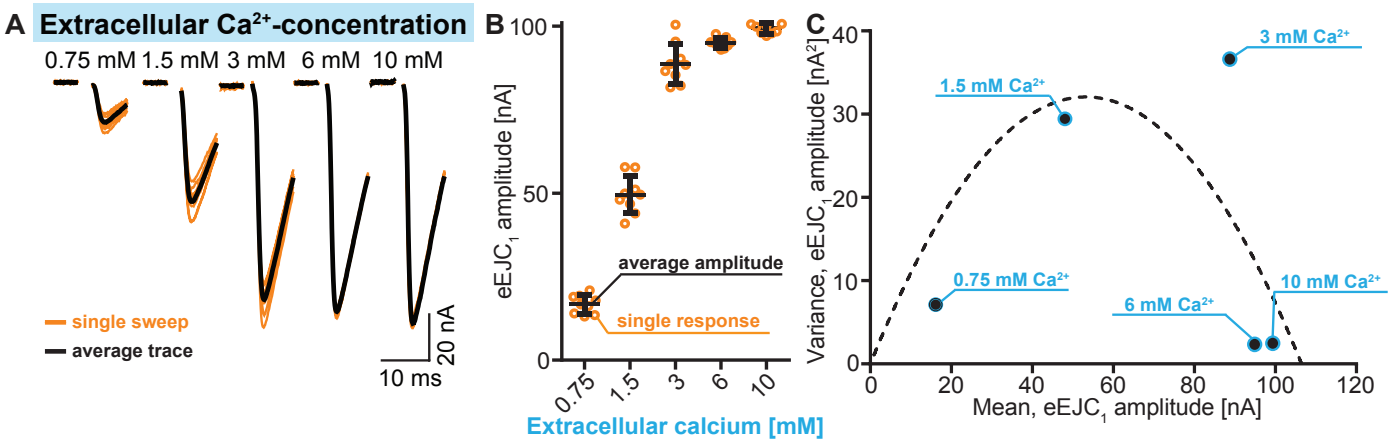

Figure 2 - figure supplement 2. Illustration of fluctuation analysis (quantification across cells shown in Fig. 2F) in a single representative cell. **(A)** Example traces showing 9 individual stimulation sweeps (orange) per Ca^{2+} concentration (0.75 – 10 mM). Averages of single sweeps are shown in black. **(B)** Quantification of eEJC amplitudes of single sweeps (orange) at different Ca^{2+} concentrations. Scattering of these values illustrates the variance of eEJC amplitudes between individual sweeps. Average eEJC amplitudes per Ca^{2+} concentration are indicated in black, error bars show SDs. Average amplitudes (and their variance) shown here were used in **C**. **(C)** Variances of eEJC amplitudes (from 9 repetitions per Ca^{2+} concentration, indicated in blue) plotted as a function of the mean eEJC amplitude. A parabola can be fitted to the data points (forced through (0,0) intercept, see methods for futher information and exact genoytpes). Used genotype: *Ok6-Gal4/II* crossed to *w[1118]*. Methods section "Fly husbandry, genotypes and handling" lists all exact genotypes.

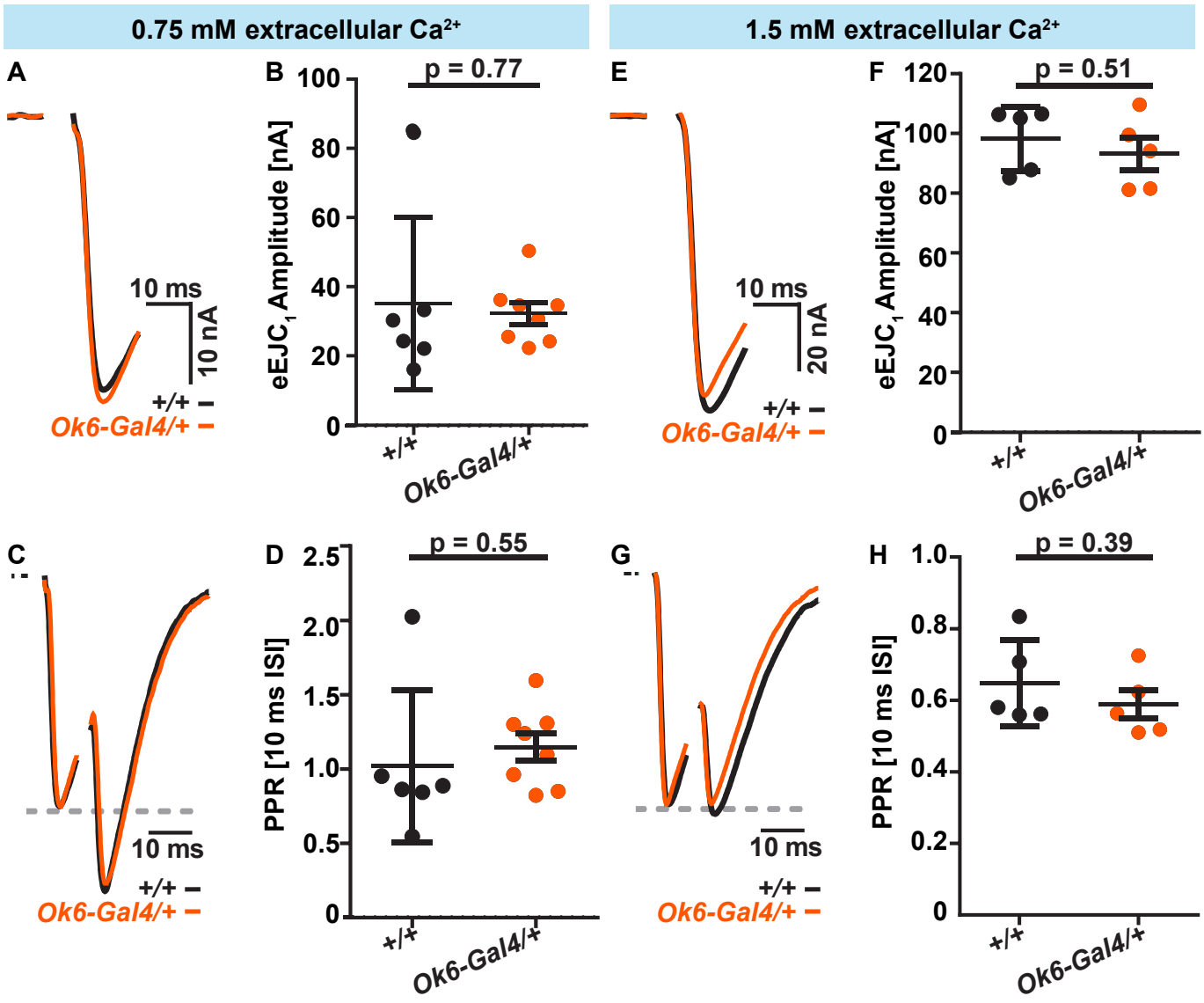

Figure 2 - figure supplement 3. Electrophysiological recordings from wildtype *w[1118]* (+/+) (black) and *Ok6-Gal4/+* (orange) muscle 6 NMJs upon a single paired-pulse stimulation (10 ms inter-stimulus interval) at 0.75 mM **(A-D)** and 1.5 mM Ca^{2+} **(E-H)**. **(A)** Representative example traces for $eEJC_1$ from single cells in +/+ or *Ok6-Gal4/+*. **(B)** Quantification of $eEJC_1$ amplitudes in +/+ (n = 6 cells from 3 animals) and *Ok6-Gal4/+* (n = 8 cells from 4 animals), averages and SDs across cells are indicated. **(C)** Representative normalized eEJC example traces of paired pulse (10 ms inter-stimulus interval) responses in representative cells of +/+ and *Ok6-Gal4/+* animals. **(D)** Quantification of paired pulse ratios (PPRs) in +/+ (n = 6 cells from 3 animals) and *Ok6-Gal4/+* (n = 8 cells from 4 animals), averages across cells and SDs are indicated. **(E)** Representative example traces for $eEJC_1$ from single cells of +/+ or *Ok6-Gal4/+* animals. **(F)** Quantification of $eEJC_1$ amplitudes in +/+ (n = 5 cells from 3 animals) and *Ok6-Gal4/+* (n = 5 cells from 3 animals), averages and SDs across cells are indicated. **(G)** Normalized eEJC example traces of paired pulse (10 ms inter-stimulus interval) from single cells in +/+ and *Ok6-Gal4/+* animals. **(G)** Quantification of PPRs in +/+ (n = 5 cells from 3 animals) and *Ok6-Gal4/+* (n = 5 cells from 3 animals), averages across cells and STDs are indicated. Used genotypes: *Ok6-GAL4/+* (*Ok6-Gal4/II* crossed to *w[1118]*) and +/+: *w[1118]*. Methods section "Fly husbandry, genotypes and handling" lists all exact genotypes.

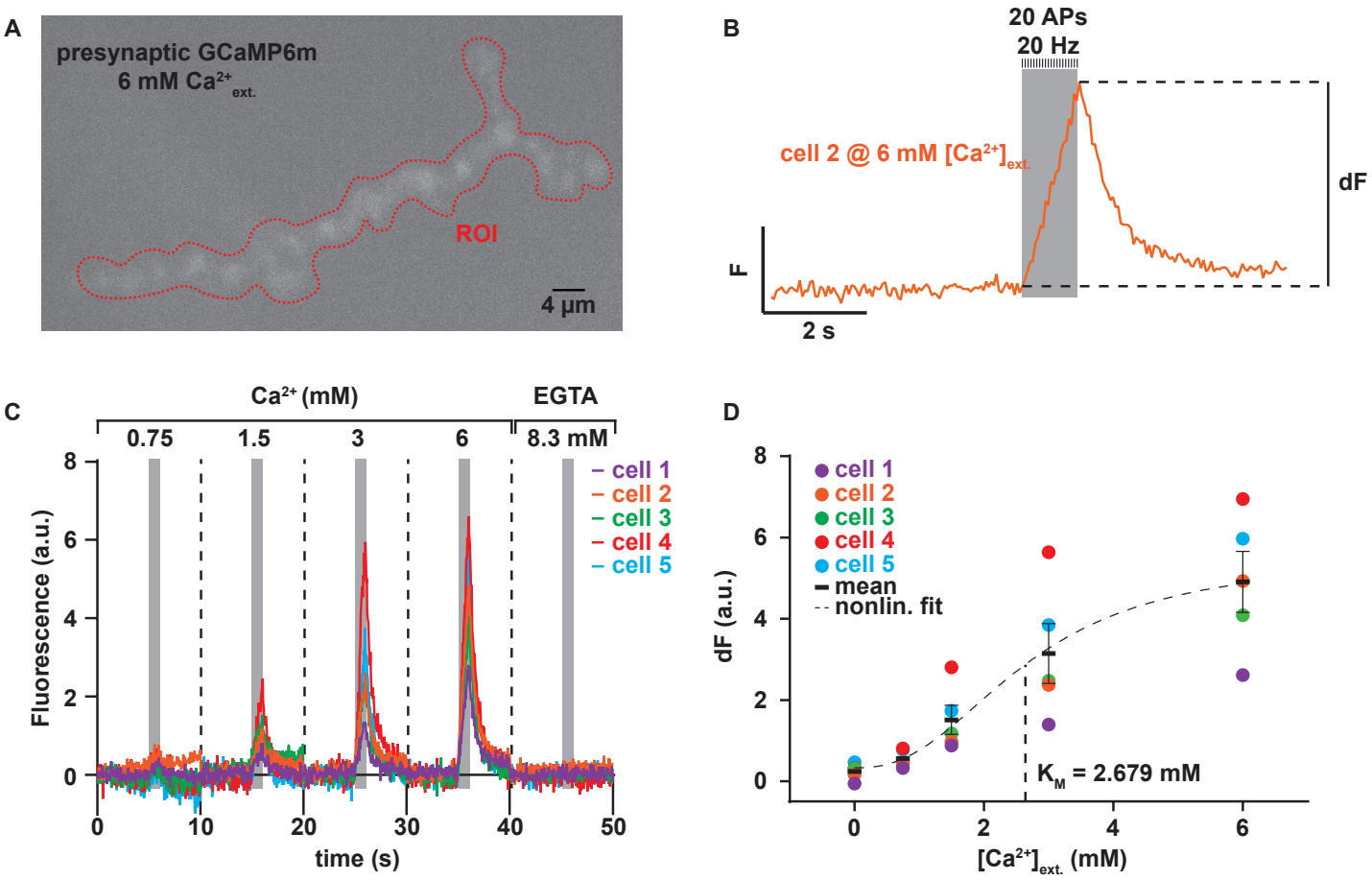

Figure 3 – figure supplement 1. Experiment to determine the dependence of AP-induced Ca^{2+} influx on the extracellular Ca^{2+} concentration. **(A)** Example frame of maximum fluorescence during recording of presynaptic GCaMP6m at 6 mM extracellular Ca^{2+}. Red dotted line indicates the ROI used for read-out of the fluorescence signal. **(B)** 10 s fluorescence trace of experiment shown in A. At the 5 s mark, 20 APs are given over 1 s. Subtracting the fluorescence at 4.75 s from the maximum fluorescence gives the value dF plotted in panel D. **(C)** Baseline-subtracted fluorescence (see Methods for details) traces of 5 different animals over the whole range of extracellular Ca^{2+} concentrations. 8.3 mM EGTA was added at the end to quench Ca^{2+} influx. **(D)** Quantification of dF (see panel B) per cell and Ca^{2+} concentration. The nonlinear fit with hill coefficient, m, of 2.43 (as previously determined for GCaMP6m (Barnett et al., 2017)) is indicated as a dashed black line, see methods for details. Mean is shown as black bars ± SEM. Used genotype: *w[1118]; P{y[+t7.7] w[+mC]=20XUAS-IVS-GCaMP6m}attP40 crossed to Ok6-GAL4*. Methods section "Fly husbandry, genotypes and handling" lists all exact genotypes. Data summary as well as best fit Hill curve corresponding to the depicted graph can be found in the accompanying source data file (Figure 2 – Source Data 1).

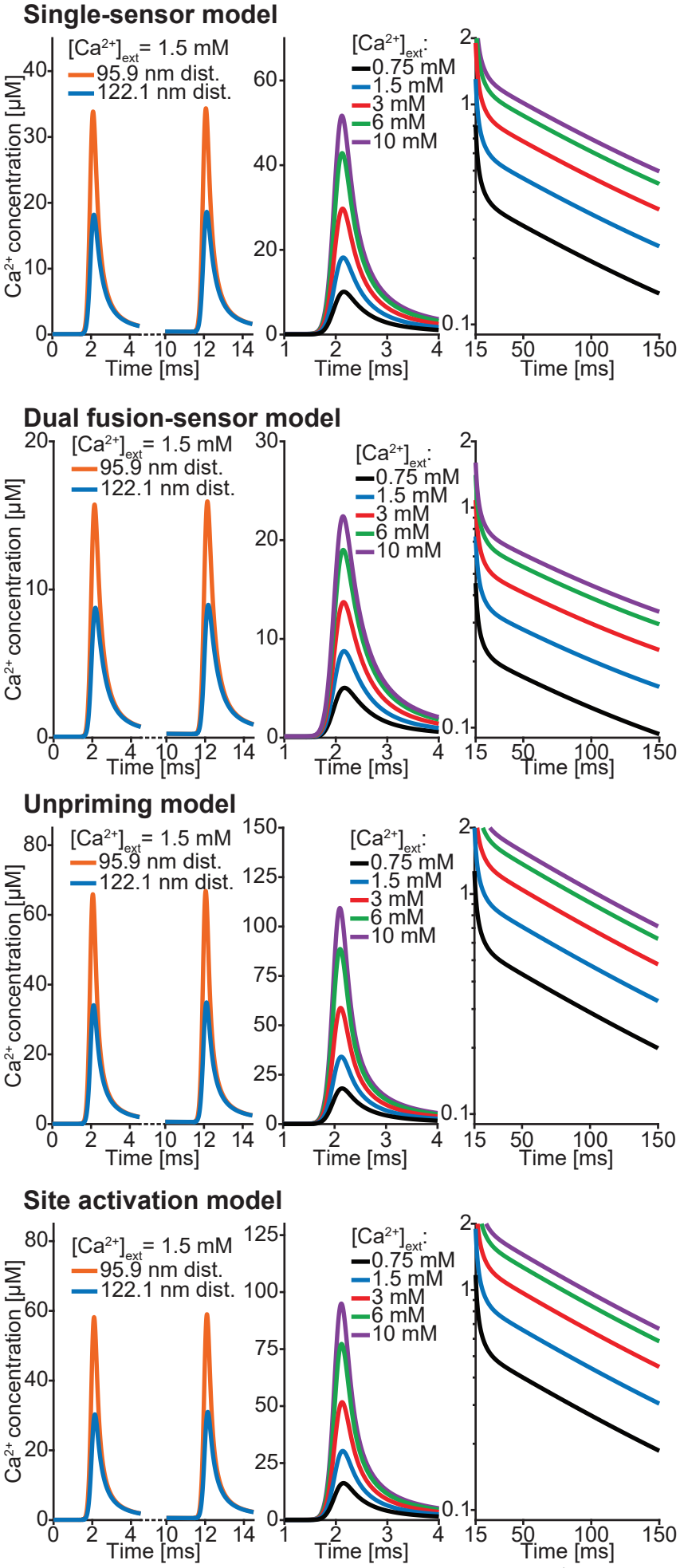

Figure 3 – figure supplement 2. Ca^{2+} profiles of all models using best fit parameters (reported in tables S2-5). Left: Both transients at 1.5 mM extracellular Ca^{2+} concentration at 95.9 nm and 122.1 nm. Middle: For all experimental extracellular Ca^{2+} concentrations an AP induced Ca^{2+} transient at a distance of 122.1 nm distance from the Ca^{2+} source is shown. Right: Semilogarithmic plot of Ca^{2+} decays at the different extracellular Ca^{2+} concentration. Time constant of decay is τ = 111 ms in all models. Plots of Ca^{2+} in the single-sensor model are the same as Fig. 3C. Parameters can be found in Tables 2,3.

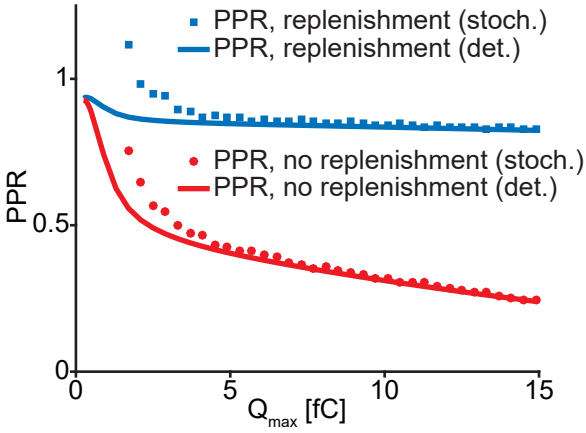

Figure 4 – figure supplement 1. Stochastic and deterministic simulations yield different PPR values**. (A)** PPR values from stochastic (bullets) and deterministic (curves) simulations of the single-sensor model (Fig. 4) at varying amounts of Ca^{2+} influx. Simulations are performed with (blue) and without (red) replenishment. Decreasing Ca^{2+} influx increases the PPR values due to less SV depletion. Stochastic simulations generally yield higher PPR estimations than the deterministic simulations. The effect is most significant at the lower Ca^{2+} influx. Parameters used for simulation can be found in tables 1,2,3. Simulation scripts can be found in the source code file. Results from simulations (means) can be found in the accompanying source data file (Figure 4 – Source Data 1).

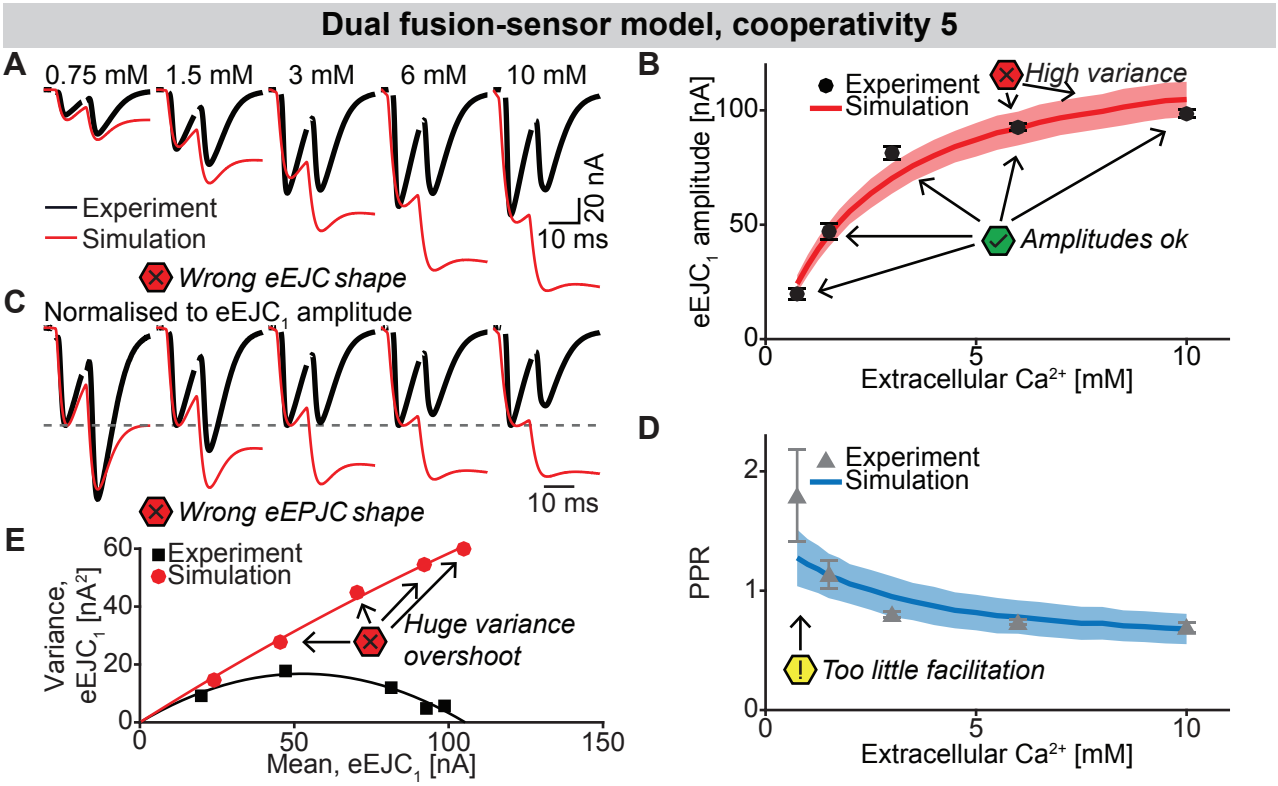

Figure 6 – figures supplement 1. The dual fusion-sensor sensor model with cooperativity 5 (allowing the binding of 5 Ca^{2+} to the second fusion sensor). **(A)** Average, experimental $eEJC_1$ traces (black) together with average simulated traces (red). The higher cooperativity increases the PPR compared to cooperativity 2 (Fig. 6), but introduces massive asynchronous release resulting in distorted eEJC shapes. **(B)** $eEJC_1$ amplitudes of experiment (black) and simulation (red). Error bars and colored bands show standard deviation. Like with the three models described in the main text, simulations of this model reproduces $eEJC_1$ amplitudes well, but the variance at the higher extracellular Ca^{2+} concentrations is too large. **(C)** Average, normalized eEJC traces of experiment (black) and simulation (red). Like in (A) the wrong shape of the eEJC is evident. **(D)** PPR values of experiment (gray) and simulation (blue). Error bars and colored bands show standard deviation. Despite the increase in PPR compared to the dual fusion-sensor model with cooperativity 2, the PPR is still too low. **(E)** Plot of the mean synaptic variance vs. the mean $eEJC_1$ values, both from the experiment (black) and the simulation (red). The curves show the best fitted parabolas with forced intercept at (0,0)(simulation: $Var=-0.00089<eEJC_1>^2+0.6728<eEJC_1>$, corresponding to $n_{sites}=1124$ and $q=0.67$ when assuming a classical binomial model (Clements and Silver, 2000), see Methods). This model leads to an even larger overshoot of the variance than the dual fusion-sensor model with cooperativity 2 (Fig. 6). Experimental data (example traces and means) depicted in panels A-E are replotted from Fig. 2A-D,F. Parameter values used for simulations can be found in tables 1,2,3. Simulation scripts can be found in the source code file. Results from simulations (means and SDs) can be found in the accompanying source data file (Figure 6 – Source Data 1).

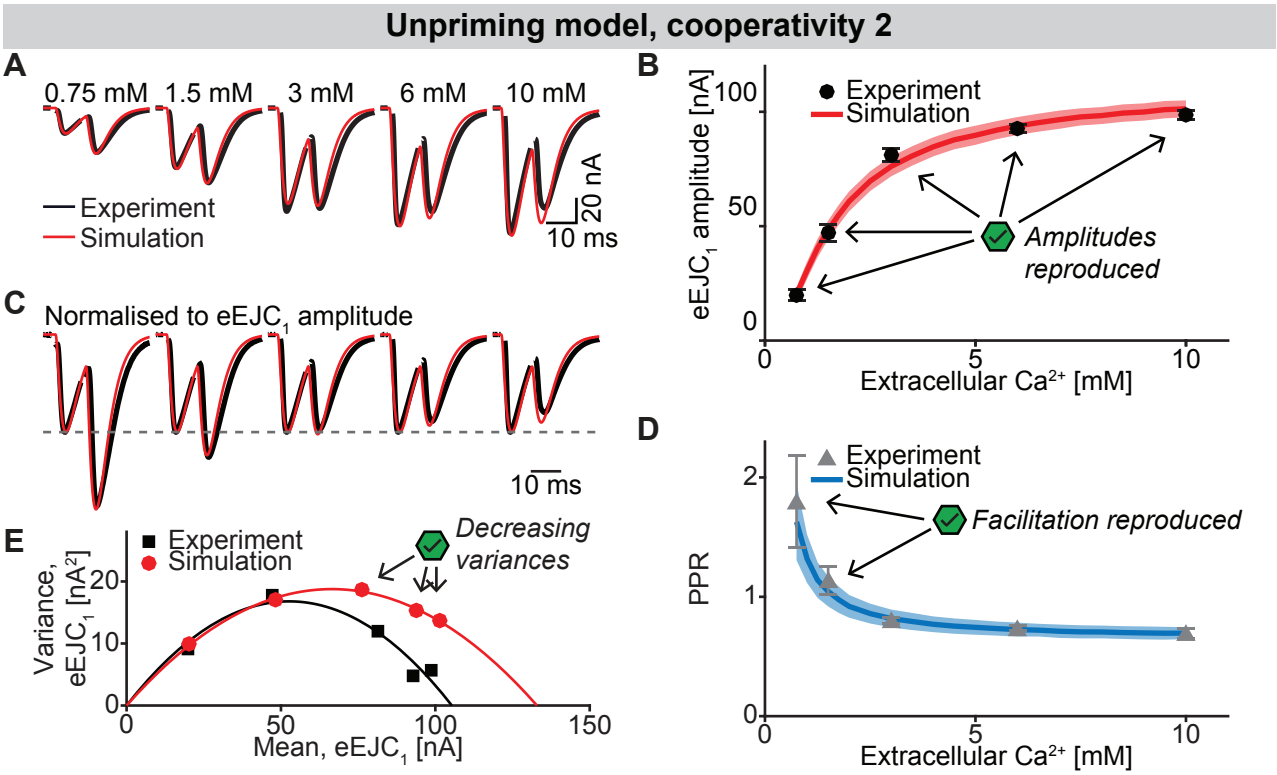

Figure 7 – figure supplement 1. The unpriming model with cooperativity 2. **(A)** Average, experimental eEJC traces (black) together with average simulated traces (red). **(B)** $eEJC_1$ amplitudes of experiment (black) and simulation (red). Error bars and colored bands show standard deviation. Like with the three models described in the main text, simulations of this model reproduce $eEJC_1$ amplitudes well. **(C)** Average, normalized eEJC traces of experiment (black) and simulation (red). **(D)** PPR values of experiment (gray) and simulation (blue). Error bars and colored bands show standard deviation. Like the unpriming model with cooperativity 5 (Fig. 7), this model reproduces the short-term facilitation observed in experiments. **(E)** Plot of the mean synaptic variance vs. the mean $eEJC_1$ values, both from the experiment (black) and the simulation (red). The curves show the best fitted parabolas with forced intercept at (0,0)) (simulation: $Var=-0.0042< eEJC_1>^2+0.5648< eEJC_1>$, corresponding to $n_{sites}=238$ and $q=0.56$ when assuming a classical binomial model (Clements and Silver, 2000), see Methods). Like the unpriming model with cooperativity 5, variances decrease with increasing extracellular Ca^{2+} concentration, although the variances are slightly higher. Experimental data (example traces and means) depicted in panels A-E are replotted from Fig. 2A-D,F. Parameter values used for simulations can be found in tables 1,2,3. Simulation scripts can be found in the source code file. Results from simulations (means and SDs) can be found in the accompanying source data file (Figure 7 – Source Data 1).

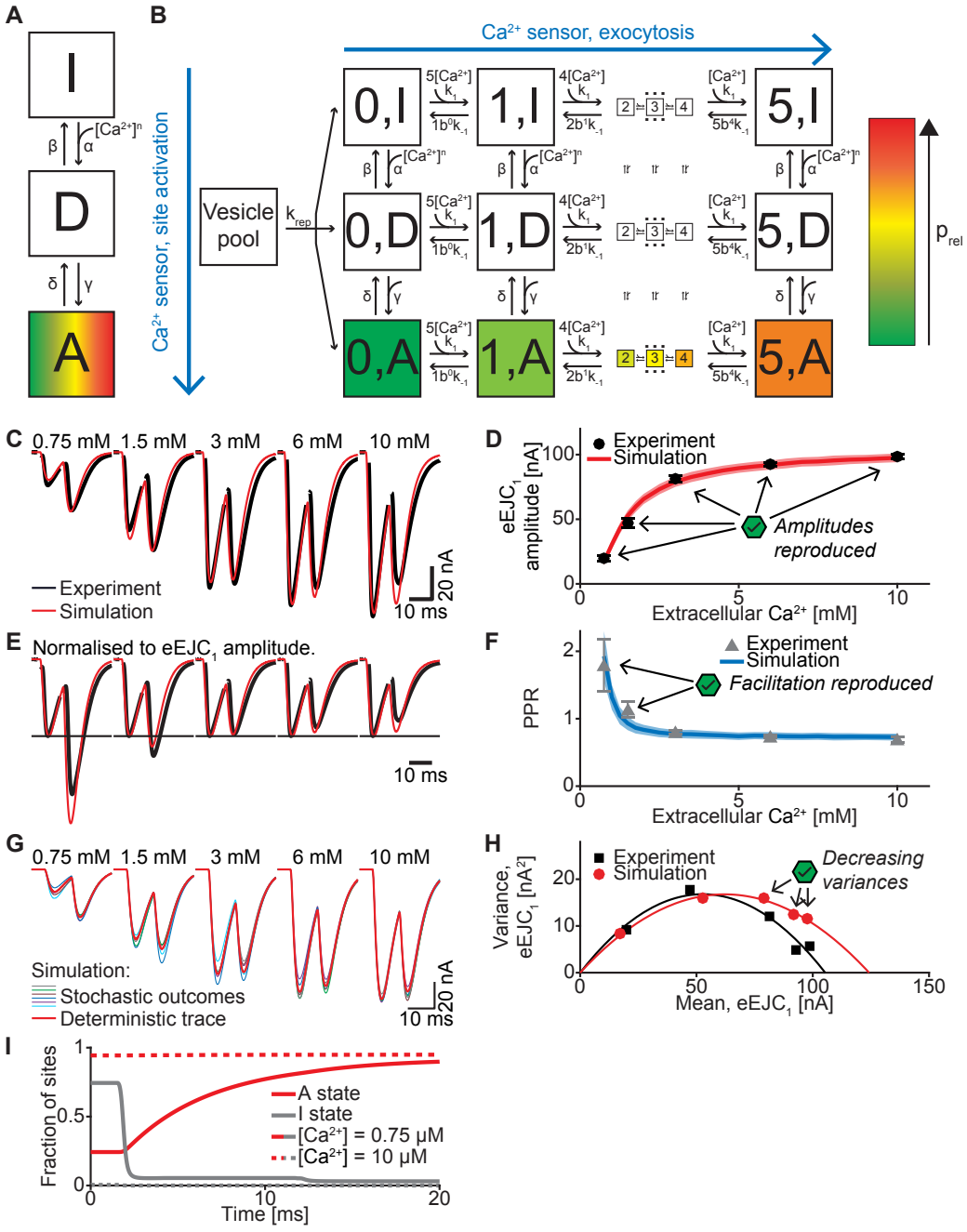

Figure 7 – figure supplement 3. Simulation based time course predictions of paired-pulse STF recovery for different interstimulus intervals across different Ca^{2+} concentrations (0.75 - 10 mM). **(A)** Estimated PPRs for 0.75, 1.5, 3, 6 and 10 mM extracellular Ca^{2+} (from top to bottom) as a function of interstimulus interval (5, 10, 25, 50, 100, 250, 500 and 1000 ms). STF can be detected at low (0.75 mM) and physiological (1.5 mM) Ca^{2+} concentrations and decays after approximately 100 ms, no STF can be detected at high (3 – 10 mM) Ca^{2+} concentrations (starting with PPR values below 0.5 at 5 ms and increasing to PPR values around one for intervals above 25 ms). Regions of interest indicated by dashed red square are shown as a close-up in next panel. **(B)** Estimated paired-pulse ratio values (PPR) for Ca^{2+} concentrations (0.75 - 10 mM) 0.75, 1.5, 3, 6 and 10 mM extracellular Ca^{2+} (from top to bottom) as a function of their interstimulus interval (5, 10, 25, 50 ms). **(C)** Examples of average traces from paired-pulse simulations at different (0.75 - 10 mM) extracellular Ca^{2+} (from top to bottom) for 5 ms (blue), 10 ms (red), 25 ms (yellow) and 50 ms (purple) interstimulus intervals. Results from simulations (means and SDs) can be found in the accompanying source data file (Fig. 7 - source data 1).

Figure 7 – figure supplement 2. Site activation model. **(A)** Diagram of the site activation mechanism. Three states are introduced: [I], inactive, [D], delay, and [A], activated. SV fusion is only allowed from sites in state [A]. The rate from [I] to [D] is increased by Ca^{2+}, whereas the rate from [D] to [A] is slower and independent of Ca^{2+}, thereby introducing a delay. All (in)activation reactions are assumed to be reversible. **(B)** Full site activation model. The Ca^{2+} (un)binding of the SVs follow the same equations as in the single-sensor model and occurs independently of the site (in)activation. Replenishment is allowed into empty release sites regardless of activation status. **(C)** Average, experimental eEJC traces (black) together with average simulated traces (red). **(D)** $eEJC_1$ amplitudes of experiment (black) and simulation (red). Error bars and colored bands show standard deviation. Like with the three models described in the main text, simulations reproduce $eEJC_1$ amplitudes well. **(E)** Average, normalized eEJC traces of experiment (black) and simulation (red). **(F)** PPR values of experiment (gray) and simulation (blue). Error bars and colored bands show standard deviation. Like the unpriming model, simulations reproduce the experimentally observed facilitation. **(G)** Average simulated traces (black) and examples of different outcomes of the stochastic simulation (colors). **(H)** Plot of the mean synaptic variance vs. the mean $eEJC_1$ values, both from the experiment (black) and the simulation (red). The curves show the best fitted parabolas with forced intercept at (0,0) (simulation: $Var=-0.0043<eEJC_1>^2+0.5398<eEJC_1>$, corresponding to $n_{sites}=233$ and $q=0.54$ when assuming a classical binomial model (Clements and Silver, 2000), see Methods). Like in experiments, simulations lead to decreasing variance at the highest Ca^{2+} concentrations. **(I)** The number of sites in state [I] and [A] (gray and red resp.) in simulations with extracellular Ca^{2+} concentrations of 0.75 mM and 10 mM (solid and dashed resp.). The varying basal Ca^{2+} concentration yield different initial amounts of site activation. The activation of sites mainly occurs between APs because of the delay state. Experimental data (example traces and means) depicted in panels C-F,H are replotted from Fig. 2A-D,F. Parameter values used for simulations can be found in tables 1,2,3. Simulation scripts can be found in the source code file. Results from simulations (means and SDs) can be found in the accompanying source data file (Figure 7 – Source Data 1).

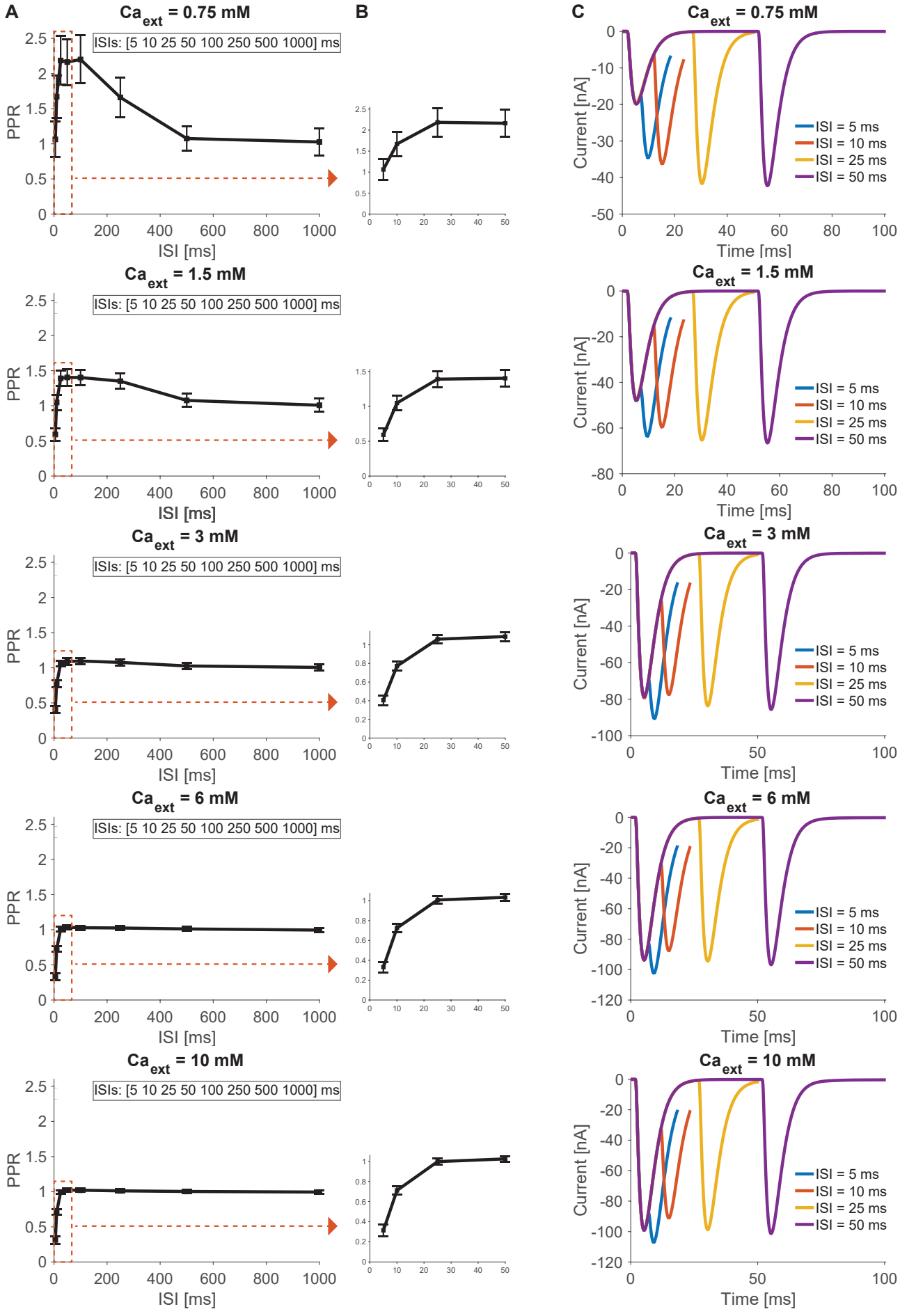
A
B
C
Ca ext = 0.75 mM
ISIs: [5 10 25 50 100 250 500 1000] ms
PPR
ISI [ms]
Current [nA]
Time [ms]
ISI = 5 ms
ISI = 10 ms
ISI = 25 ms
ISI = 50 ms
Ca ext = 1.5 mM
Ca ext = 3 mM
Ca ext = 6 mM
Ca ext = 10 mM

2.8 Publication VI: Schuhmacher et al., PNAS 2020

Full bibliographical reference

Schuhmacher M, Grasskamp AT, Barahtjan P, Wagner N, Lombardot B, Schuhmacher JS, Sala P, Lohmann A, Henry I, Shevchenko A, Coskun Ü, Walter AM, Nadler A (2020) - *Live-cell lipid biochemistry reveals a role of diacylglycerol side-chain composition for cellular lipid dynamics and protein affinities*, Proceedings of the National Academy of Sciences:201912684. doi:10.1073/PNAS.1912684117.

Permalink: https://doi.org/10.1073/pnas.1912684117

Author contributions

M.S. and A.N. conceived the project and performed all life-cell experiments. M.S. synthesized and characterized cgDAGs, developed lipid biosensors, performed GUV experiments, and analyzed data. P.B. performed ATP addition experiments together with A. N. and M.S. and analyzed data. N.W. optimized synthesis. B.L. and I.H. developed image analysis tools. **A.T.G.** and A.M.W. **analyzed data, developed the kinetic model, performed *in silico* experiments, and performed statistical data analysis**. J.S.S. purified recombinant proteins. A.L. optimized transfection conditions. P.S. acquired and analyzed mass spectrometry data. Ü.C. and A.S. contributed to the analysis of mass spectrometry data. M.S., **A.T.G.**, A.M.W. and A.N. **wrote the manuscript**. All authors critically read and corrected the manuscript.

Contribution details

For this work in quantitative lipid biochemistry and computational simulations, I contributed a mathematical model that we based on a relatively simple kinetic model of lipid dynamics and turnover. The caged DAG species generated for this only differed in their acyl chain structures, but exhibited vastly different PKC-C1 recruitment profiles, speaking for a structurally imposed difference in trans-bilayer movement rates, metabolism and lipid-protein interactions. Once uncaged at the outer leaflet of the cellular lipid bilayer membrane by a UV uncaging laser flash, the different DAGs were assumed to translocate to the inner leaflet and back, reversibly bind an intracellular, genetically encoded fluorescent sensor harboring a PKC-C1 domain, or get metabolized. By comparing our simulations based on this kinetic model with experimental data acquired at different uncaging laser powers to achieve a range of DAG concentrations, we could show that the acyl chain structure differences indeed resulted in vastly different DAG dynamics and protein affinities. I further performed statistical analysis of data shown in Figure 2 and wrote parts of the manuscript.

Live-cell lipid biochemistry reveals a role of diacylglycerol side-chain composition for cellular lipid dynamics and protein affinities

Milena Schuhmacher[a], Andreas T. Grasskamp[b], Pavel Barahtjan[a], Nicolai Wagner[a], Benoit Lombardot[a], Jan S. Schuhmacher[a], Pia Sala[c,d], Annett Lohmann[a], Ian Henry[a], Andrej Shevchenko[a], Ünal Coskun[c,d], Alexander M. Walter[b,1], and André Nadler[a,1]

[a]Max Planck Institute of Molecular Cell Biology and Genetics, 01307 Dresden, Germany; [b]Leibniz-Forschungsinstitut für Molekulare Pharmakologie, 13125 Berlin, Germany; [c]Paul Langerhans Institute Dresden, Helmholtz Zentrum München, University Hospital and Faculty of Medicine Carl Gustav Carus, Technische Universität Dresden, 01307 Dresden, Germany; and [d]German Center for Diabetes Research, 85764 Neuherberg, Germany

Edited by Satyajit Mayor, National Centre for Biological Sciences, Bangalore, India, and approved February 24, 2020 (received for review July 24, 2019)

Every cell produces thousands of distinct lipid species, but insight into how lipid chemical diversity contributes to biological signaling is lacking, particularly because of a scarcity of methods for quantitatively studying lipid function in living cells. Using the example of diacylglycerols, prominent second messengers, we here investigate whether lipid chemical diversity can provide a basis for cellular signal specification. We generated photo-caged lipid probes, which allow acute manipulation of distinct diacylglycerol species in the plasma membrane. Combining uncaging experiments with mathematical modeling, we were able to determine binding constants for diacylglycerol–protein interactions, and kinetic parameters for diacylglycerol transbilayer movement and turnover in quantitative live-cell experiments. Strikingly, we find that affinities and kinetics vary by orders of magnitude due to diacylglycerol side-chain composition. These differences are sufficient to explain differential recruitment of diacylglycerol binding proteins and, thus, differing downstream phosphorylation patterns. Our approach represents a generally applicable method for elucidating the biological function of single lipid species on subcellular scales in quantitative live-cell experiments.

signaling lipids | diacylglycerol | protein kinase C | mathematical modeling | caged lipid probes

Membrane lipids play a central role in cellular signal transduction. As receptor ligands, enzyme cofactors, and allosteric modulators, they control cellular excitability (1), immune responses (2), cell migration (3, 4), and stem cell differentiation (5, 6). In line with their fundamental importance, dysregulation of signaling lipids has been firmly established as a hallmark of severe diseases such as cancer (7) and diabetes (8). Lipids are grouped into classes characterized by common chemical features, such as their headgroup. Each of these classes comprises many molecularly distinct lipid species that differ in subtle chemical details, e.g., number of double bonds, ether or ester linkages, as well as fatty acid chain length and positioning, ultimately suggesting the presence of thousands of individual lipid species in mammalian cells (9, 10). While the heterogeneity of the cellular lipidome in general and of signaling lipids in particular is well established, it is much less clear whether this heterogeneity has causal relations to cellular function (11, 12).

Intriguingly, a growing body of evidence suggests that changes in the levels of individual lipid species rather than entire lipid classes determine cellular signaling outcome. For instance, early studies reported that activation of individual cell surface receptors leads to the formation and degradation of distinct patterns of diacylglycerol (DAG) species during signal transduction (13–15) on minute timescales. This suggests that crucial information could be encoded in the molecular spectrum of generated signaling lipids. Supporting this notion, drastically altered levels of distinct lipid species were correlated with cellular processes, e.g., the increase of a phosphatidic acid ether lipid during cytokinesis (16) or the reciprocal regulation of ceramide species during Toll-like receptor signaling in innate immunity (17). DAGs appear to be prime targets to study the importance of lipid heterogeneity in cell signaling, as they act as second messengers at the plasma membrane and function in many cellular processes, including insulin signaling, ion channel regulation, and neurotransmitter release (18, 19). Many of these processes involve effector proteins such as protein kinase C (PKC) isoforms, which are recruited to cellular membranes by DAG binding to their C1 domains (20). Faithful process initiation thus requires the activation of a subset of DAG effector proteins in the presence of others as observed during the formation of the immunological synapse (21). However, the molecular mechanisms of such specific recruitment events are not well understood. Here, specificity could be provided by differential activation of effectors by structurally distinct DAG species, which recruit specific DAG binding proteins due to differences in lipid-protein affinities, local lipid densities, and lifetimes. Determining

Significance

Every cell produces thousands of lipid species, but studying the function of individual lipids in living cells is almost impossible with existing methodologies. Addressing this experimental bottleneck, we developed a strategy to quantify dissociation constants for lipid–protein interactions and transmembrane flip-flop rates of native lipids in live-cell experiments. Using a combination of plasma membrane-specific photochemical probes and mathematical modeling, we demonstrate that, for diacylglycerols as a model lipid class, the inherent lipid structural diversity caused by variations in acyl chain composition determines lipid protein affinities and transbilayer kinetics. In fact, subtle chemical differences change these values by orders of magnitude. Our approach represents a generally applicable method for elucidating the biological function of single lipid species on subcellular scales.

Author contributions: M.S., A.M.W., and A.N. designed research; M.S., A.T.G., P.B., N.W., J.S.S., P.S., A.L., A.M.W., and A.N. performed research; M.S., A.T.G., B.L., I.H., and A.M.W. contributed new reagents/analytic tools; M.S., A.T.G., P.B., A.S., Ü.C., and A.N. analyzed data; and M.S., A.T.G., A.M.W., and A.N. wrote the paper.

The authors declare no competing interest.

This article is a PNAS Direct Submission.

Data deposition: All software codes used for analysis have been deposited on the Max Planck Institute of Molecular Cell Biology and Genetics repository, https://dx.doi.org/21.11101/0000-0007-DF4A-C.

[1]To whom correspondence may be addressed. Email: awalter@fmp-berlin.de or nadler@mpi-cbg.de.

This article contains supporting information online at https://www.pnas.org/lookup/suppl/doi:10.1073/pnas.1912684117/-/DCSupplemental.

these parameters requires quantitative experimental strategies that allow perturbing and monitoring levels of native lipid species and lipid–protein complexes in specific membranes of living cells. However, such methods are not yet available (22).

Closing this methodological gap, we developed chemical probes for rapid, leaflet-specific ultraviolet (UV) uncaging of individual DAG species at the plasma membrane of living cells. This allowed temporally well-defined increases of native DAG species in a quantitative and dose-dependent fashion as a prerequisite for kinetic analysis. By combining DAG uncaging and live-cell fluorescence imaging of DAG-binding proteins with mathematical modeling, we demonstrate that 1) structural differences between DAG species are sufficient to trigger different recruitment patterns of various PKC isoforms and lead to differential phosphorylation of downstream signaling targets; 2) K_d values of DAG–C1–domain interactions as well as transbilayer movement and turnover rates differ by orders of magnitude between DAG species; 3) the affinity of the lipid–protein interaction primarily influences the magnitude of DAG signaling events (recruitment of a specific effector protein); whereas 4) the kinetics of DAG signaling events are largely determined by lipid transbilayer movement and turnover rates. Overall, our data demonstrate that subtle differences in DAG structure affect lipid-protein affinities and the kinetics of transbilayer movement and lipid turnover. This results in preferential recruitment of DAG-binding proteins, which may serve as a mechanism to encode information during cellular signaling events.

Results

Photoactivation Allows Acute DAG Density Increases at the Plasma Membrane. Photoliberation of native lipid species from caged lipids constitutes the most straightforward experimental approach to induce well-defined, temporally controlled density increases of a single lipid species in individual membrane leaflets (23–25), which is essential for kinetic analysis (Fig. 1*A*). In order to study the influence of DAG chemical heterogeneity on cellular signaling, we prepared four caged DAGs: One variant with short acyl chains (dioctanoylglycerol, cgDOG) and two typical, naturally occurring DAGs with long acyl chains, featuring one and four double bonds, respectively (stearoyl-arachidonylglycerol, cgSAG and stearoyl-oleoylglycerol, cgSOG) (Fig. 1 *B* and *C*). As a negative control, we prepared a caged regioisomer of the native species, 1,3-dioleoylglycerol (cg1,3DOG), which does not recruit DAG effector proteins to cellular membranes (26). To ensure plasma membrane-specific DAG photorelease, we used a sulfonated coumarin photo-caging group (27), which allows lipid side chains to incorporate selectively into the outer plasma membrane leaflet but completely blocks transbilayer movement (flip-flop) due to two negative charges (Fig. 1*A*). The absorption and emission spectra of coumarin derivatives cgDOG, cgSAG, cgSOG, and cg1,3DOG were very similar (*SI Appendix*, Fig. S1-1 *B* and *C*).

Brief loading followed by extensive washing ensured sufficient and comparable plasma membrane incorporation of all caged DAGs into HeLa Kyoto cells (Fig. 1*D* and *SI Appendix*, *Extended Experimental Procedures*) and membrane localization was confirmed by confocal microscopy using the intrinsic fluorescence of the coumarin caging group (Fig. 1*D*). Endocytosis of caged DAGs was slow (*SI Appendix*, Fig. S1-2*A*), resulting in a period of 40–60 min suitable for uncaging experiments. The uncaging reaction was confirmed in vitro in solution by NMR spectroscopy, found to be similarly efficient for all probes (Fig. 1*E* and *SI Appendix*, Fig. S1-1*C*) and comparable to previously reported probes bearing traditional caging groups (*SI Appendix*, Fig. S1-1*D*) (26).

To assess the uncaging efficiency in living cells, whole-field-of-view UV irradiation was combined with monitoring coumarin fluorescence at low intensity illumination. The coumarin fluorescence decreased at the plasma membrane, consistent with uncaging and subsequent dissipation of the cleaved coumarin alcohol, whereas the fluorescence signal remained unchanged in endosomes (where the coumarin alcohol is trapped in the lumen) (Fig. 1*F* and Movie S1). By quantifying the observed fluorescence decreases at the plasma membrane and correcting for baseline fluorescence levels, we found very similar (on average 66 ± 4%) uncaging efficiencies for all caged DAGs (Fig. 1*G* and *SI Appendix*, Fig. S1-2 *B–D* and *Extended Experimental Procedures*). Since these experiments were done with a laser scanning microscope in a single plane, we also assessed whether the uncaging changed throughout the cell in the *z* direction. To test this, we acquired *z*-stacks of coumarin fluorescence before and after uncaging at low laser intensity and found that the observed uncaging fluorescence loss was very similar throughout the *z*-stack suggesting that out of plane uncaging and/or rapid lateral diffusion of caged DAGs contribute to near-homogenous DAG photo release (*SI Appendix*, Fig. S1-3). These settings were used for all uncaging experiments in this study unless stated otherwise (*SI Appendix*, *Extended Experimental Procedures*). Taken together, our approach enables acute DAG density increases of different DAG species at the outer leaflet of the plasma membrane.

DAG Fatty Acid Composition Determines Selective Recruitment of PKC Isoforms. Varying DAG species patterns generated after receptor activation (13–15) can only encode information during signal transduction if chemically distinct DAG species differentially recruit DAG-binding proteins and, ultimately, cause different phosphorylation patterns of downstream effectors. We thus first tested whether uncaging of molecularly distinct DAG species resulted in specific recruitment patterns of individual EGFP-tagged PKC isoforms (Fig. 2*A*) in HeLa Kyoto cells. The extent of PKC recruitment was measured as "translocation efficiency," the ratio between normalized fluorescence intensities (FI) at the plasma membrane and in the cytosol (28, 29) (Fig. 2*B*). Simultaneously, we monitored accompanying Ca^{2+} signaling events using RGECO, a red fluorescent, intensiometric Ca^{2+} indicator (30), as elevated DAG levels can directly induce Ca^{2+} signaling via activation of transient-receptor potential (TRP) channels (31).

Upon uncaging of DAGs, we observed a unique temporal recruitment profile in response to the photorelease of individual 1,2-DAG species, while no recruitment was observed for the negative control 1,3-DOG. (Fig. 2 *C* and *D* and *SI Appendix*, Figs. S2-3 *B–K* and S2-4 *B–F*). The PKC isoforms (PKCδ and PKCε) were recruited to the plasma membrane in a staggered manner after uncaging of all three active 1,2-DAGs (Fig. 2*D*, PKCδ and PKCε), with SAG typically eliciting the strongest responses and DOG the weakest. PKCε recruitment was more pronounced than PKCδ recruitment for all DAGs, suggesting a higher affinity of PKCε for DAG. All PKCε translocation events observed after DAG uncaging were less intense than endogenous DAG production after ionomycin treatment, which should trigger a maximal, PLC-mediated response (*SI Appendix*, Fig. S2-1), indicating that the DAG concentration increases caused by DAG uncaging are within the concentration range of endogenous DAG generation events.

Both long-chain DAGs elicited Ca^{2+} transients, both in the presence and absence of PKC expression (Fig. 2*E* and *SI Appendix*, Fig. S2-2*A*), whereas no Ca^{2+} transients were observed for uncaging of the short-chain variant 1,2-DOG or the negative control lipid 1,3-DOG. We also found that the SAG- and SOG-induced Ca^{2+} transients appeared rather variable between cells and experiments (and in some cases were even absent). This could potentially be due to varying expression levels of DAG-sensitive Ca^{2+} channels (e.g., TRPC3/6). Thus, we drew comparative conclusions only from uncaging datasets acquired strictly in parallel under identical conditions. To assess whether the uncaging-triggered DAG signaling events could be obscured

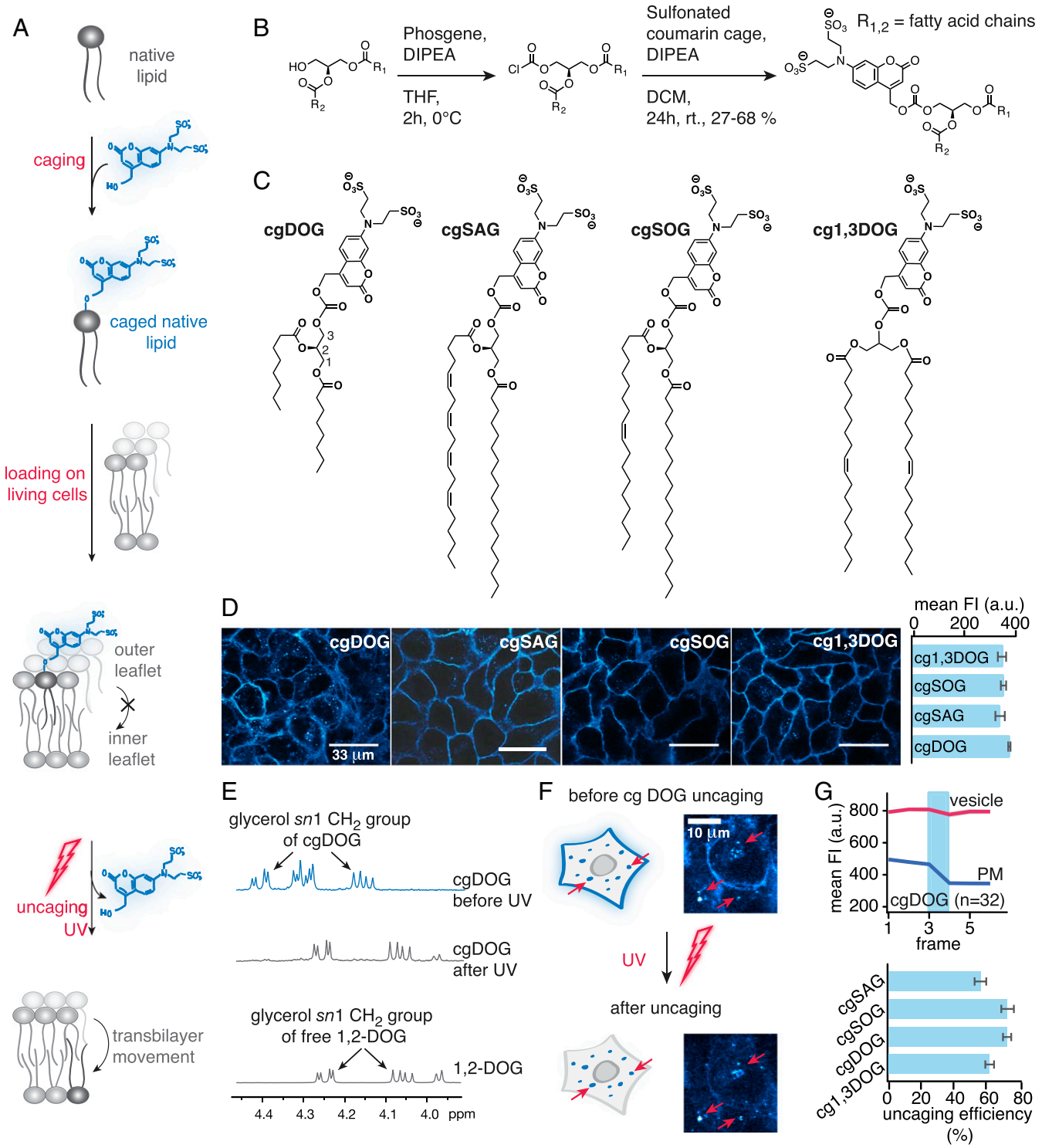

Fig. 1. Caged diacylglycerols for acute lipid density increases at the outer plasma membrane leaflet. (*A*) Schematic description of the experimental approach. (*B*) Synthesis of the cgDAGs. (*C*) Structures of synthesized cgDAGs. (*D*, *Left*) Cellular localization of cgDAGs visualized by coumarin fluorescence. (Scale bars, 33 µm.) (*D*, *Right*) Quantification of FI after cellular uptake. (*E*–*G*) Quantification of cgDAG incorporation and photoreaction efficiency in vitro in solution and in living cells. (*E*) NMR spectra of cgDOG before and after irradiation using a 345-nm high-pass filter and DOG as reference compound. Photocleavage was monitored by the distinct shift of *sn*1 glycerol protons signal from 4.39 ppm (cgDAG) to 4.24 ppm (free DAG). (*F*) Whole field of view uncaging of cgDAGs after allowing for membrane turnover causes loss of fluorescence at the plasma membrane but not in endosomes (red arrows), in line with exclusive initial localization of the caged lipid at the outer plasma membrane leaflet. Both images are displayed at the same magnification. (*G*, *Upper*) Quantification of fluorescence intensity changes at the plasma membrane and in endosomes upon photoactivation. The blue bar indicates the uncaging event. (*G*, *Lower*) Uncaging efficiency for the different DAG species at 40% laser power calculated from FI loss at the plasma membrane. All live-cell experiments were carried out in HeLa Kyoto cells, n, numbers represent cell numbers, in a typical experiment 5 to 10 cells were imaged simultaneously. Data are mean; error bars represent SEM.

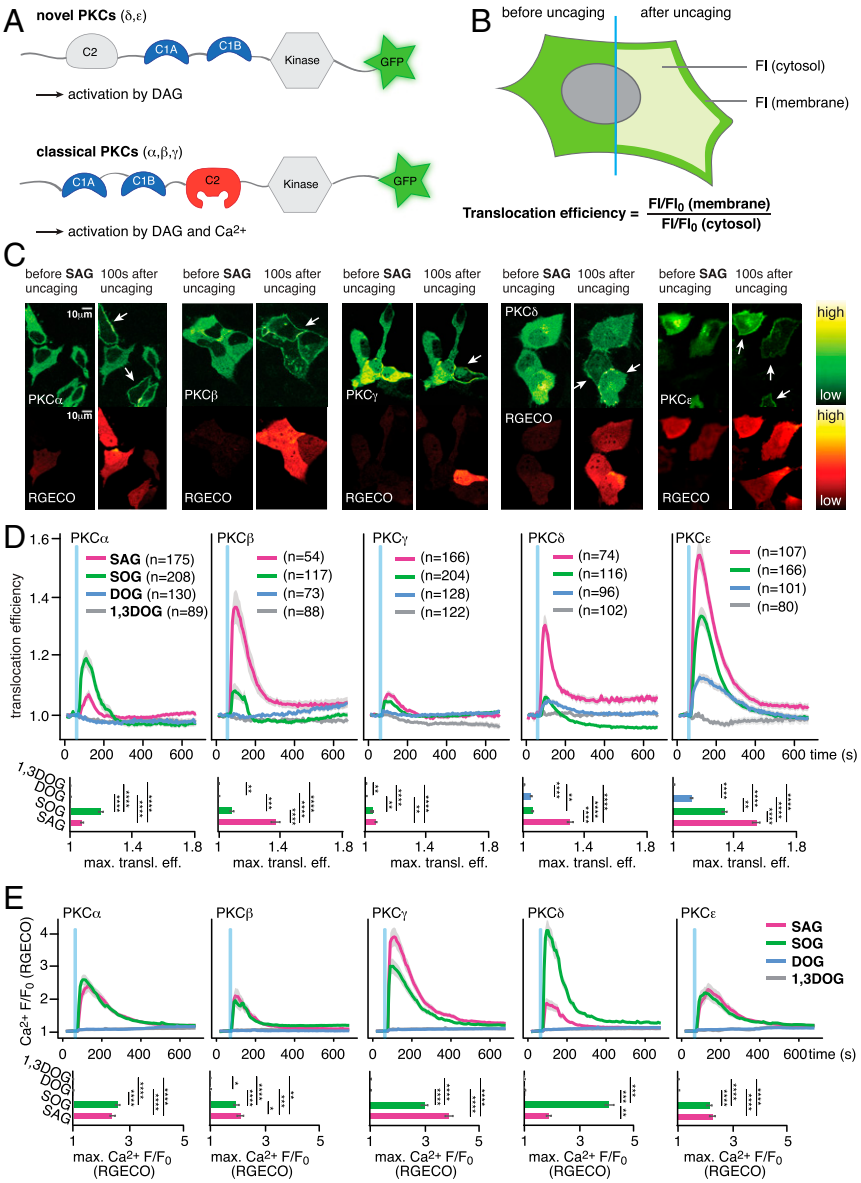

Fig. 2. Cellular responses after DAG uncaging. (*A*) Domain architecture of novel and classical PKCs. (*B*) Schematic illustration of the image analysis approach FI/FI_0 are normalized fluorescence intensities at each time point in the time series. (*C*) Time-lapse montage of representative PKC (*Upper*) and RGECO (*Lower*) responses to uncaging of SAG. (*D*) Quantification of the recruitment of PKC isoforms PKCα, PKCβ, PKCγ, PKCδ, and PKCε to uncaging of different DAG species. The blue bar indicates the uncaging event. (*Upper*) Mean translocation efficiency traces. (*Lower*) Bar graphs show maximal translocation efficiency. Significance was tested using ANOVA followed by Dunn's post hoc test and is represented by * (multiplicity adjusted *P* value, $^{**}P < 0.01$; $^{***}P < 0.001$; $^{****}P < 0.0001$). Error bars represent SEM, data are mean. n, numbers represent cell numbers. (*E*) Quantification of Ca^{2+}-signaling events in response to DAG uncaging. (*Upper*) Mean normalized fluorescence intensity traces for RGECO. (*Lower*) Bar graphs show maximal normalized fluorescence intensity. Significance was tested using the Dunn's post hoc test and is represented by * (multiplicity adjusted *P* value, $^{*}P < 0.05$; $^{**}P < 0.01$; $^{***}P < 0.001$; $^{****}P < 0.0001$). Shaded areas indicate SEM; blue bars indicate the uncaging event.

by Ca^{2+}-induced production of endogenous DAG (via Ca^{2+}-induced, PLC-mediated cleavage of PIP_2), we performed an analysis of single-cell traces of PKCε translocation events. This isoform should only react to DAG levels, irrespective of the DAG source. We used the inherent variability of the Ca^{2+} transients to sort these cells into ones with large Ca^{2+} transients (larger than 50% RGECO fluorescence increase) and ones with lower Ca^{2+} transients and compared whether strong Ca^{2+} transients affected the observed PKC translocation events. This was not the case, and the resulting PKC recruitment profiles were very similar, even in cases where Ca^{2+} transients were not visible (*SI Appendix*, Fig. S2-2 *B* and *C*). Furthermore, analysis of the peak fluorescence ratios in the PKC and RGECO responses revealed no correlation between the two observables (*SI Appendix*, Fig. S2-2 *B* and *C*). Consequently, Ca^{2+}-induced production of endogenous DAG in the uncaging experiments had no major effects on the observed PKC recruitment patterns.

The three classical, Ca^{2+}-dependent PKC isoforms (PKCα, PKCβ, PKCγ) were only recruited by the long-chain DAGs (SAG and SOG) and did not respond to photoactivation of the short-chain probe cgDOG (Fig. 2*D* and *SI Appendix*, Figs. S2-3 *B–K* and S2-4 *B–F*). This is likely due to the fact that DOG never triggered elevated cytosolic Ca^{2+} levels (Fig. 2*E*), consistent with the requirement on coincident DAG and Ca^{2+} binding of these classical PKCs. The average PKCα translocation event was larger and longer-lasting for SOG uncaging than for SAG uncaging,

whereas the opposite effect was observed for PKCβ (Fig. 2*D*). This particular difference appeared to depend exclusively on PKC–DAG interactions and not on Ca^{2+} levels, as similar Ca^{2+} transients were observed for both species (Fig. 2*E*). PKCγ was the only isoform similarly recruited by both native DAGs (SAG and SOG) (Fig. 2*D*). Interestingly, uniform elevation of plasma membrane DAG levels by photoactivation often led to the formation of localized patches of PKC recruitment or triggered global responses, which transformed into localized patches over time. Both effects were most pronounced for cgSAG (Fig. 2*C* and *SI Appendix*, Figs. S2-3 *B–K* and S2-4 *B–F* and *H* and Movies S2–S6), suggesting a varying capacity of individual DAG species to stabilize or form lipid gradients in the plasma membrane.

To compare PKC recruitment patterns after DAG uncaging with responses to a physiological stimulus, we monitored Ca^{2+} transients and PKC recruitment after ATP addition at different concentrations (1 and 5 mM), which should lead to the generation of endogenous DAG by PLCβ-mediated cleavage of PIP_2, as well as IP_3-induced Ca^{2+} transients. We observed that PKCε was recruited to the plasma membrane after ATP addition for both concentrations, featuring uniform, strong translocation events, whereas PKCδ-expressing cells exhibited less pronounced events when treated with 5 mM ATP (Fig. 3), in line with the pattern observed for all DAGs (compare Fig. 2). In contrast to the treatment with 5 mM ATP, PKCδ translocation events after adding 1 mM ATP were seldom observed (*SI Appendix*, Fig. S3). Moreover, translocation of the classical PKC isoforms was almost never observed when adding 1 mM ATP (*SI Appendix*, Fig. S3) despite the fact that pronounced Ca^{2+} transients were observed in these cases (*SI Appendix*, Fig. S3). The most likely explanation is that the necessary combined thresholds for DAG and Ca^{2+} concentrations were not reached. When adding 5 mM ATP, we observed pronounced translocation of PKCβ, whereas translocation was rare in cells expressing either PKCα or PKCγ. Importantly, the relative recruitment patterns for the five analyzed PKC isoforms after adding 5 mM ATP matched the ones observed for SAG uncaging (Fig. 2 *C* and *D*). Since PLC-mediated cleavage of PIP_2 typically results in the generation of highly unsaturated DAG species such as SAG (32), this finding suggests that physiological DAG signaling events can be faithfully replicated by DAG uncaging with regard to effector protein recruitment patterns.

Next, we investigated whether uncaging of distinct DAGs gave rise to different phosphorylation patterns of bona fide PKC targets (C-Raf and GSK3β) and key players in cellular signaling cascades (MAPK, MEK1/2, and HDAC7). Cells were loaded with the caged DAGs (cgDAGs), and uncaging was performed on the whole dish. Cells were then collected, the cell lysate captured, and phosphorylation levels monitored with Western blot analysis (*SI Appendix*, Fig. S2-4 *G* and *Extended Experimental Procedures*). As expected, the negative control 1,3DOG did not significantly increase phosphorylation of any of the proteins studied. Significantly increased phosphorylation was observed in C-Raf at S298/296 after stimulation with SAG and in MEK1/2 and MAPK both after SAG and SOG uncaging, while DOG uncaging only significantly increased the phosphorylation of p-MAPK. This analysis confirmed that distinct phosphorylation profiles were triggered by the respective DAGs. Taken together, our data indicate that chemical differences between individual DAG species are sufficient to modulate DAG effector protein recruitment as well as downstream phosphorylation patterns.

Live-Cell Quantification of DAG Dynamics and DAG-Protein Affinities. While our data suggest that DAG chemical diversity may provide a basis for specific recruitment of effector proteins, it is unclear how the chemical differences between individual lipid species are

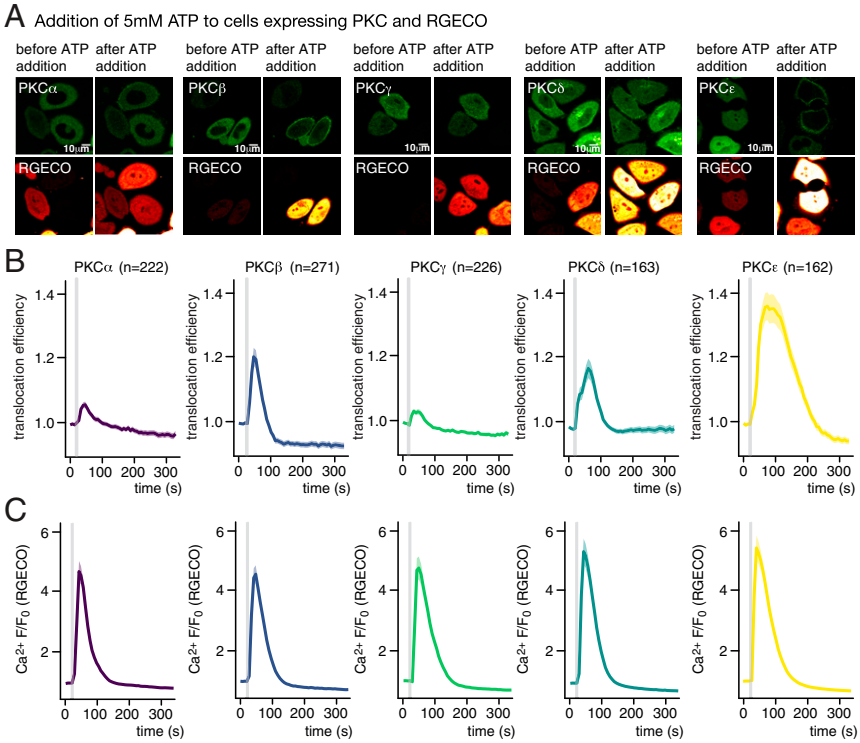

Fig. 3. Cellular responses after ATP addition. (*A*) Time-lapse montage of representative PKC (*Upper*) and RGECO (*Lower*) responses following addition of 5 mM ATP. (Scale bars, 10 μM.) (*B*) Quantification of the recruitment of PKC isoforms PKCα, PKCβ, PKCγ, PKCδ, and PKCε to addition of 5 mM ATP. The gray bar indicates the ATP addition. (*C*) Quantification of Ca^{2+} signaling events in response to addition of 5 mM ATP as mean normalized fluorescence intensity traces for RGECO. Shaded areas represent SEM.

mechanistically translated into the different recruitment profiles. We decided to address this question using a minimal DAG-binding protein to isolate and quantify the lipid-driven protein recruitment process (Fig. 4*A*). We chose to use the known GFP fusion protein of the C1a domain of PKCγ, which is commonly used as a DAG biosensor (33) rather than screening for the most responsive C1 domains as this rendered our data as comparable as possible to our published data (26, 28) and the dynamic range of this sensor was assumed to be sufficient for kinetic analysis. However, we noticed that a significant part of the protein was retained in the nucleus and only exported when the cytosolic fraction was recruited to the plasma membrane upon DAG uncaging (Fig. 4*B* and Movie S7). This leads to an intrinsic delay of the sensor (Fig. 4*D*) and could hinder a kinetic analysis of the actual recruitment process. To avoid this, we equipped the protein with a nuclear export sequence (NES) to have the protein expressed solely in the cytosol (Fig. 4*C* and Movie S8). This suppressed the distortion of translocation kinetics by nuclear export compared to the original C1-EGFP construct (Fig. 4*D*).

Uncaging of cgDOG, cgSAG, and cgSOG using the above described conditions triggered C1-EGFP-NES translocation to the plasma membrane, whereas neither cg1,3DOG uncaging nor illumination of unloaded cells caused translocation (Fig. 4*E* and *SI Appendix*, Fig. S4 *A–D*). A thorough characterization of C1-EGFP-NES in comparison with the C1-EGFP construct revealed no significant differences regarding the response rates to cgDAG uncaging (*SI Appendix*, Fig. S4 *E–G*). Importantly, striking differences between the individual lipid species were again observed (Fig. 4*E*): C1-EGFP-NES was recruited much faster to the plasma membrane after cgDOG uncaging compared to cgSOG or cgSAG uncaging (Fig. 4 *E*, *Right*), whereas the subsequent release of the sensor from the plasma membrane appeared to be fastest for SAG (Fig. 4 *E*, *Left*).

Quantitative Live-Cell Imaging Combined with Mathematical Modeling Reveals Specific Differences in Kinetics and Protein Affinities Among DAG Species. We hypothesized that the observed differences in protein recruitment between DAGs might be caused by distinct temporal DAG density profiles in the inner leaflet and, therefore,

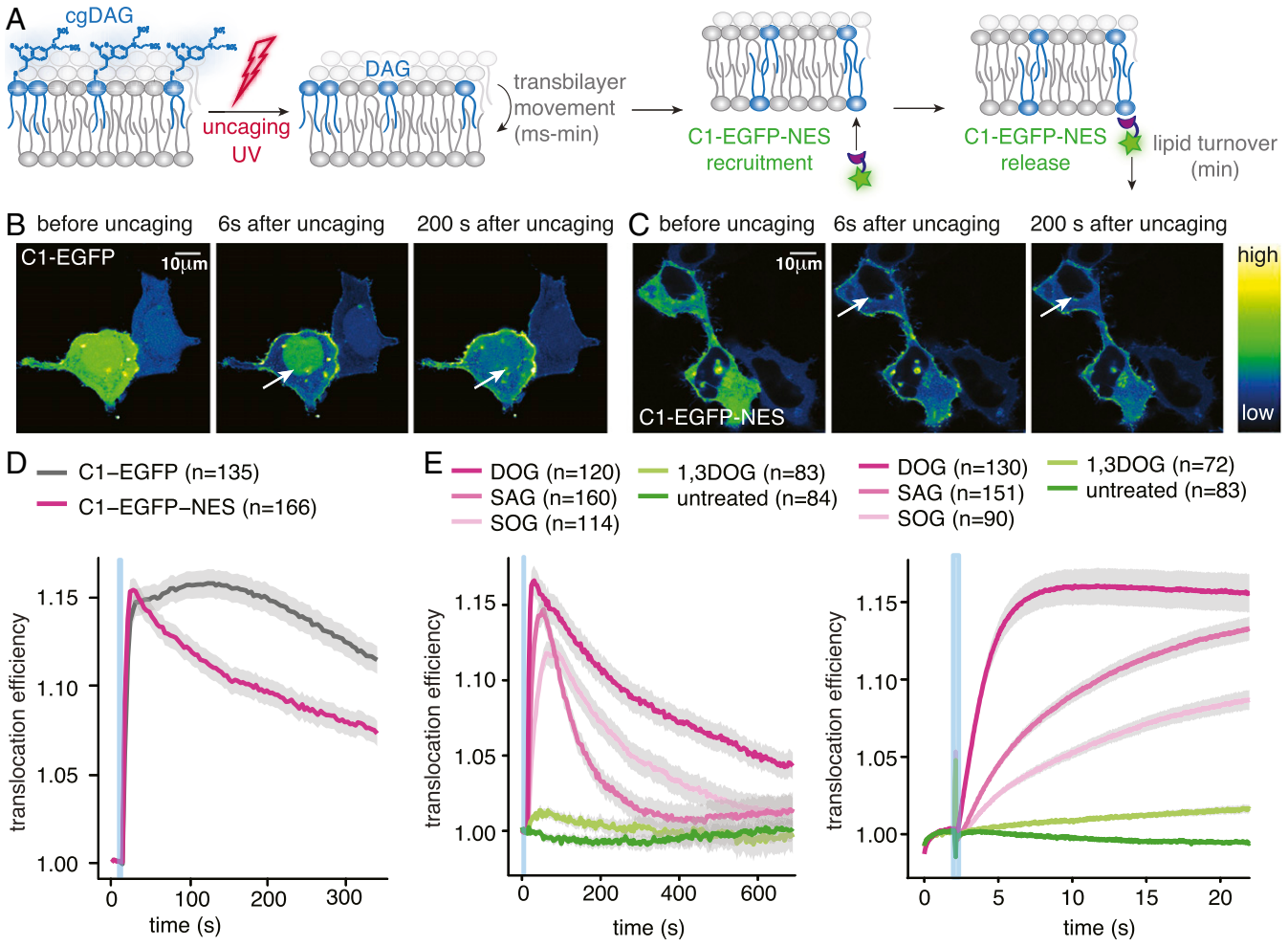

Fig. 4. An improved DAG biosensor allows precise analysis of membrane association kinetics and reveals differences between DAG species. (*A*) Schematic representation of the uncaging experiment. (*B*) Time-lapse montage of the C1-EGFP response to cgDOG uncaging in HeLa Kyoto cells. Note the presence of a nuclear protein pool indicated by the white arrows. (*C*) Time-lapse montage of the C1-EGFP-NES response to cgDOG uncaging in HeLa Kyoto cells. Note the absence of a nuclear protein pool indicated by the white arrows. (*D*) Translocation efficiency traces of C1-EGFP and C1-EGFP-NES after cgDOG uncaging. (*E*, *Left*) C1-EGFP-NES release kinetics after DAG uncaging in HeLa Kyoto cells. (*E*, *Right*) C1-EGFP-NES recruitment kinetics after DAG uncaging in HeLa Kyoto cells shown in more detail during the initial response. Uncaging experiments were carried out on a spinning disk microscope (*SI Appendix*, *Additional Experimental Procedures*). In all images, the blue bar indicates the uncaging event. n, numbers represent cell numbers; in a typical experiment, 5–10 cells were imaged simultaneously. Shaded regions surrounding mean traces in *D* and *E* represent SEM.

sought to characterize the kinetics of lipid transbilayer movement, lipid turnover, and lipid-protein affinities. For this, we developed a minimal kinetic model that could then be compared to the experimentally obtained temporal C1-EGFP-NES fluorescence profiles (Fig. 5*A*). This required quantitative knowledge of the number of C1-EGFP-NES protein copies and of the number of photoliberated DAG molecules. The number of free C1-EGFP-NES molecules of the resting cell was calculated from the cytosolic fluorescence intensity using a calibration curve generated from recombinantly produced C1-EGFP-NES at known concentrations (Fig. 5 *B* and *C*) and by estimating the cellular volume (*SI Appendix*, *Extended Experimental Procedures*). We determined the number of cgDAG in the outer leaflet of the plasma membrane before UV uncaging and the number of liberated DAG upon uncaging using the coumarin fluorescence. For this, the intensity of giant plasma membrane unilamellar vesicles (GPMVs) derived from cgDAG-loaded cells was quantified and compared to a calibration curve obtained from giant unilamellar vesicles (GUVs) containing defined mole percentages of caged DAG (Fig. 5*D*) (quantitative incorporation into GUVs was confirmed by mass spectrometry [*SI Appendix*, *Extended Experimental Procedures* and Table S1]). The uncaging efficiencies were determined for different laser powers, and this number was multiplied with the total amount of caged DAG to obtain the absolute number of liberated DAG molecules (Fig. 5 *E*–*G*). We found that uncaging of merely $1–2 \times 10^{-3}$ mol% of an individual DAG species sufficed to induce the recruitment of C1-EGFP-NES to the plasma membrane, resulting in a sizable reduction of free C1-EGFP-NES in the cytosol (Fig. 5 *H*–*J* and *SI Appendix*, *Extended Experimental Procedures*). This observation allows the conclusion that the molecular composition of plasma membrane appears to be tuned in a way that enables the efficient recruitment of DAG-binding proteins in response to remarkably small elevations of DAG levels.

To study how varying the amount of liberated DAG affected the translocation of C1-EGFP-NES, we used different laser powers for uncaging. This revealed an unexpected saturation of responses even when sizable fluorescence was still onserved in the cytosol (Fig. 5 *H*–*M*). This was accounted for in the model (which cannot by itself produce such a behavior due to its minimal design) by subtracting the experimentally observed nonresponsive fraction (determined from the experiment, not a model parameter). There are a few possible explanations for this phenomenon. Most likely, not all fluorescence in the cytosol corresponds to C1-EGFP-NES or the number of binding sites at the plasma membrane might be limiting.

Our minimal kinetic model was designed to describe the observed C1-EGFP-NES responses to DAG uncaging and featured DAG transbilayer movement, metabolism, and association to C1-EGFP-NES in equilibrium (Fig. 5*A* and *SI Appendix*, Fig. S5-1). Although the model only contained four free parameters, parameter optimization to all 510 experimental data points led to a very good agreement between model and experiment over the full range of laser powers (0–40%) used to liberate increasing amounts of DAG (compare experimental traces, faint lines, with model predictions, solid lines in Fig. 5 *H*–*J*). Specifically, the rate constant for outside-in movement across the plasma membrane (k_{in}), the rate constant for inside-out movement (k_{out}), and the rate constant for DAG turnover (k_{met}), and the affinity for binding C1-EGFP-NES (K_d) could be estimated by a parameter optimization sampling a large region of the parameter space (see *SI Appendix*, *Extended Experimental Procedures* for details). To investigate how variability in the experimental data might affect parameter estimates, we performed a bootstrapping analysis where the model parameters were repeatedly estimated from random subsets of the experimental traces (see *SI Appendix*, *Extended Experimental Procedures* for details). This lead to largely similar parameter estimates close to the ones obtained from the full dataset, in line with reliable and reproducible parameter estimates. We also performed a sensitivity analysis by investigating the agreement between model and data for various parameter combinations (*SI Appendix*, Fig. S5-2). This revealed a global minimum for SAG and for SOG, but the situation was less clear for DOG where multiple solutions for k_{in} and k_{out} produced similarly good agreement of the model with the data (*SI Appendix*, Fig. S5-2 *C* and *F*). This aligns with the experimental observation, where the recruitment of C1-EGFP-NES is already maximal with the first acquired data point (Fig. 5*J*), meaning that the sampling rate in the experiment is too low to define the speed of outside-in movement and only the ratio between k_{in} and k_{out} should be considered (the estimate of k_{met} was not affected by this, Fig. 5*P*). This was different for SAG and SOG, where multiple measurement points were acquired before the maximal C1-EGFP-NES recruitment was reached, which allowed for a robust estimate of k_{in}, which was much lower (SAG: 0.065 s^{-1}, SOG: 0.036 s^{-1}, DOG: 17.02 s^{-1}; for all parameters, see *SI Appendix*, Table S5). The estimated rate constant for inside-out transbilayer movement (k_{out}) was much larger for SAG than for SOG (Fig. 5*O*). In fact, k_{out} was essentially zero in the case of SOG and, indeed, a model without any inside-out transbilayer movement was preferred for SOG according to Akaike's information criterion (34) (while the full model was preferred for SAG and DOG, although the major species-specific differences were overt in both models, see *SI Appendix*, *Extended Experimental Procedures* and Fig. S5-3). While the DAG turnover rate constant k_{met} was very similar for SAG and SOG, its value was much lower in the case of DOG (Fig. 5*P*), indicating that this nonnatural variant cannot be metabolized via the same pathways. Importantly, the DAG:C1-EGFP-NES affinities ($1/K_d$) of the two natural lipids SAG and SOG differed by one order of magnitude (in both models, Fig. 5*Q* and *SI Appendix*, Fig. S5-3*L*), indicating a clear side-chain specificity of the DAG-binding domain. This finding demonstrates that species-specific lipid–protein interactions can occur within biological membranes, a hypothesis that has been frequently put forward (12), but only rarely experimentally tested (35).

Simulating DAG Signaling Highlights the Importance of Lipid Dynamics. Knowledge of the species-specific kinetic parameters and affinities allowed us to simulate the relevant lipid and protein pools during physiological signaling events, where DAG is generated at the inner leaflet by PLC-mediated PIP_2 cleavage (36) (Fig. 6*A*). We investigated how the temporal profile of DAG-mediated C1-EGFP-NES recruitment would deviate assuming (in theory) that either SAG, SOG, or DOG would exclusively be generated. Although we assumed that either species would be generated at the same rate, the resulting temporal profiles deviated significantly, owing to the species-specific properties: The model predicted much higher levels of DOG in the inner leaflet as compared to both SAG and SOG (Fig. 6*B*). Conversely, the respective maximal amounts of DAG-bound C1-EGFP-NES were much more similar (Fig. 6 *C* and *D*). The differences between DOG and SOG are a consequence of deviating lipid-protein affinities and turnover rates (Fig. 5 *P* and *Q*). However, lower SAG levels on the inner leaflet were also caused by differences in transbilayer movement (Fig. 5*O*), as SAG was the only species that accumulated to a significant amount on the outer leaflet of the plasma membrane (Fig. 6*E*). Physiologically, this would constitute a nonmetabolizable SAG buffer on the outer plasma membrane leaflet, prolonging the duration of SAG-mediated signaling events at the cost of an attenuated amplitude.

Discussion

Quantitative Lipid Biochemistry in Living Cells. In this study, we report a conceptual strategy to analyze the dynamics and molecular interactions of native lipid species in quantitative live-cell experiments. As biological membranes—unlike model membranes—feature an asymmetric lipid distribution (37) and highly complex lipid composition (12), such experiments are needed

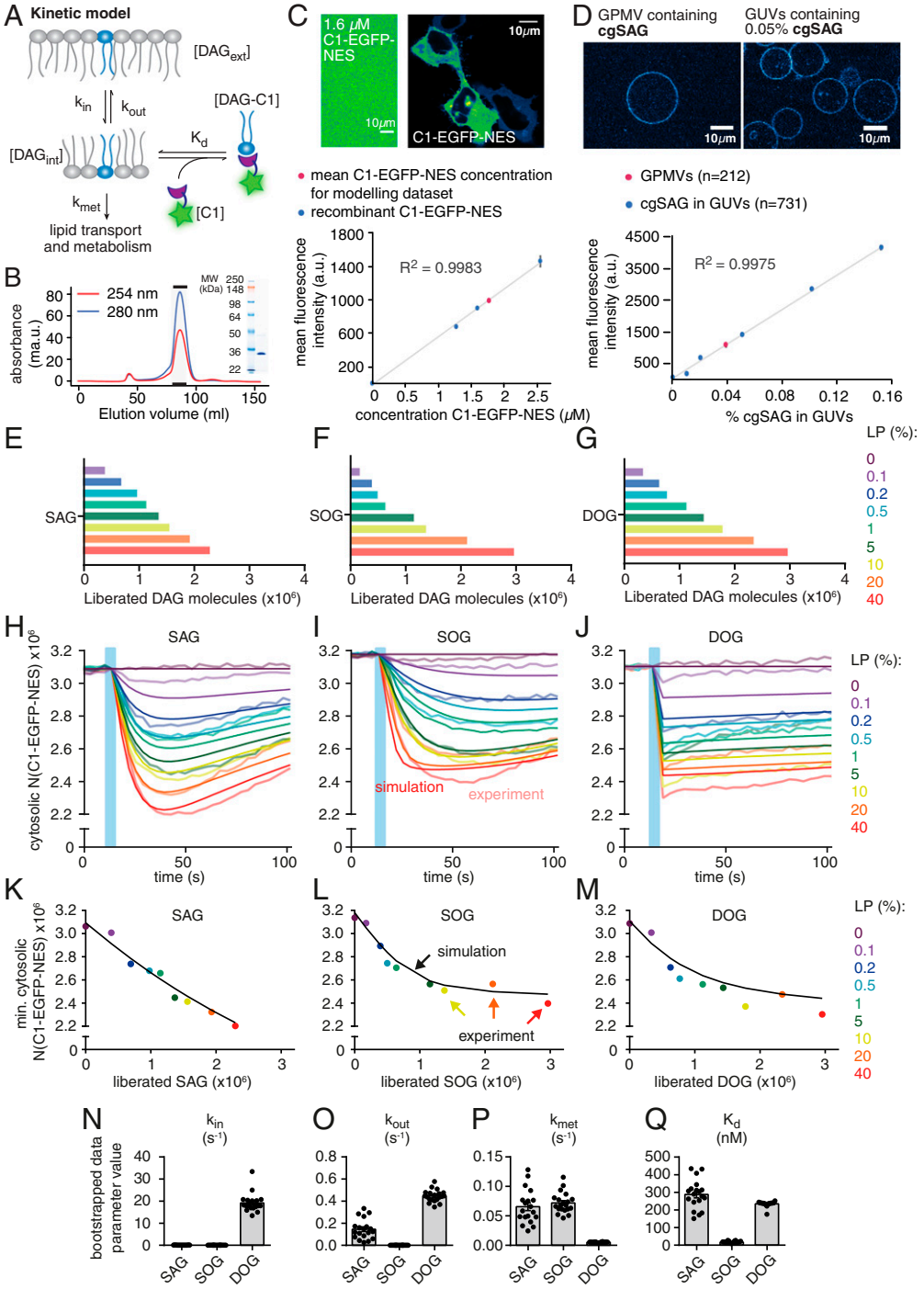

Fig. 5. Kinetic model and determination of kinetic rate constants and K_d values for DAGs. (*A*) Kinetic scheme of relevant processes for DAG-induced plasma membrane recruitment of C1-EGFP-NES. (*B*) Size exclusion chromatography profile and corresponding SDS/PAGE analysis for purified C1-EGFP-NES. (*C*) Quantification of C1-EGFP-NES concentration in HeLa Kyoto cells. (*Upper*) Comparison of C1-EGFP-NES fluorescence intensity in HeLa Kyoto cells with a C1-EGFP-NES solution with a defined concentration of 1.6 μM. (*Lower*) Calibration curve with purified C1-EGFP-NES and comparison to average intracellular protein concentration. (*D*) Quantification of cgDAG density in HeLa Kyoto cells. (*Upper*) Comparison of GPMVs (giant plasma membrane vesicles) derived from cgSAG loaded cells with GUVs containing 0.05% cgSAG. (*Lower*) Quantification of fluorescence intensity of GPMVs (red) and GUVs featuring varying cgSAG content (blue). Error bars represent SEM. (*E*–*G*) Number of liberated DAG molecules for the different laser powers used to titrate C1-EGFP-NES responses. (*H*–*J*) Experimentally determined number of free C1-EGFP-NES proteins (mean number shown by faint lines) in the cytosol as a function of time for the three DAG species. Upon UV uncaging using the indicated nine different laser powers (0–40%, time of uncaging indicated by blue bar), the number of free proteins drops due to the recruitment of C1-EGFP-NES molecules to the plasma membrane upon DAG binding there. The measured/calculated mean amount of the free C1-EGFP-NES in the cytosol (faint lines) is shown together with predictions of this behavior by the model with its best fit parameters (solid lines). (*K*–*M*) For each of the nine laser powers, the minimal number of free C1-EGFP molecules in the cytosol that were observed upon uncaging (i.e., at the time point of maximal recruitment of the sensor to the plasma membrane) is plotted as a function of the amount of liberated DAG for the three DAG species. Colored dots represent experimental mean values, black lines show simulated results. (*N*–*Q*) Estimation of kinetic parameters and their respective variability by bootstrapping (one extreme outlier of SAG is not shown for scaling reasons and because it likely represents a nonfeasible local minimum). Data are shown as mean ± SEM and respective n numbers are given in *SI Appendix*, Fig. S5-1*K*.

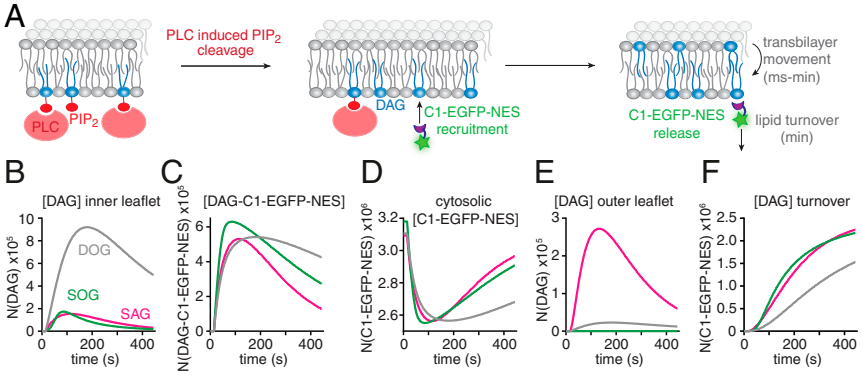

Fig. 6. Simulation of physiological DAG signaling events. (*A*) Scheme depicting the in silico experiment of DAG generation in the inner leaflet of the plasma membrane by stimulation of PLC-mediated cleavage of 2.5×10^6 PIP_2 molecules generating different DAG species with a time constant of $\tau = 100$ s, in line with observations made in ATP stimulation experiments (*SI Appendix*, Fig. S3). (*B–F*) Temporal development of SAG (magenta), SOG (green), and DOG (gray) molecule numbers on the inner leaflet (*B*), the number of membranous DAG–C1–EGFP–NES complexes (*C*), the number of cytosolic C1-EGFP-NES molecules (*D*), the number of DAG molecule on the outer leaflet (*E*), the number of DAG molecule removed from the plasma membrane due to lipid turnover (*F*). Note that SAG is the only species exhibiting a sizable outer-leaflet pool.

to understand the biological function of distinct lipid species. We developed a generation of caged DAG probes equipped with a sulfonated caging group designed for triggering rapid and temporally defined, quantitative increases of DAG levels specifically at the outer plasma membrane leaflet. Our experimental strategy enables quantitative kinetic analysis of DAG signaling events as it provides a defined starting point for both the amount of liberated DAG and signal initiation, which is not possible for receptor-induced DAG production, where the exact amount and time course of DAG production is experimentally not accessible.

Importantly, the induced changes appear to be comparable with alterations of DAG levels observed during physiological signaling events, as PKC recruitment patterns after stimulation of endogenous DAG production by ATP were replicated by SAG uncaging-induced recruitment (Figs. 2 and 3). While our approach does not capture effects during physiological signaling events that might be caused by localized DAG production in preorganized signaling clusters below the diffraction limit, it allows testing the hypothesis that lipid diversity provides a mechanistic basis for lipid function (12, 22). Importantly, a recent report suggests a high degree of species selectivity for a major family of DAG metabolizing enzymes, diacylglycerol kinases (38). The authors report distinct specificities for individual isoforms, a pattern that is reminiscent of the differences in recruitment patterns that we observe for PKC isoforms. Both findings strongly suggest that individual DAG species play distinct roles in lipid signaling networks.

Species-Specific DAG Dynamics and DAG–Protein Interactions Regulate Signaling. We show that comparable increases of individual DAG species result in strikingly different PKC recruitment and downstream phosphorylation patterns, consistent with a functional role of DAG fatty acid composition in cellular signaling events. To understand the mechanistic basis for the observed differences, we devised a minimal mathematical model and optimized its parameters to fit the temporal recruitment profiles of the DAG sensor C1-EGFP-NES. We determined K_d values for DAG–C1–domain interactions as well as rate constants for transbilayer movement and turnover of individual DAG species using dose-dependent DAG photorelease.

We found that subtle variations in DAG acyl chain length and unsaturation degree result in markedly different parameter values. For instance, although structurally very similar, SAG and SOG deviate by an order of magnitude in their affinity for binding DAG sensing proteins (Fig. 5*Q*). Moreover, while our parameter estimates implied no movement of SOG from the inner to the outer leaflet of the plasma membrane, SAG was predicted to accumulate on the outer leaflet of the plasma membrane during physiological signaling, which could markedly affect the temporal signaling profile, because SAG on the outer leaflet would constitute a nonmetabolizable buffer, thus resulting in attenuated but temporally extended elevation of SAG levels.

We show that combining quantitative live imaging with mathematical modeling enables a quantitative comparison of specific molecular properties related to the chemical structure of diverse DAG species, which are not directly experimentally accessible. As with all modeling approaches, these parameter values can only be judged in the context of the model itself, which will always be an approximation of reality. Yet, such approximations are particularly useful to make predictions and to generate key hypotheses in membrane biology, which can then be addressed experimentally. Future work will identify the limitations and further requirements of the model and, together with experimental refinements, iteratively lead to improvements of the model's predictive value.

Taken together, the combination of quantitative lipid biochemistry in living cells and mathematical modeling allowed us to study the mechanistic basis of cellular lipid signaling events in unprecedented molecular detail down to the elementary reactions that govern the behavior of distinct lipid species. We anticipate that the described experimental strategy could be expanded to other lipid classes, as the fundamental design principle of the utilized caged lipids is universal, and recently developed screening approaches have streamlined the discovery and characterization of lipid-binding domains (39). As more and more individual lipid species are linked to specific cellular processes by lipidomic screens, the need for experimental strategies to validate their involvement in live-cell assays and to investigate the underlying mechanisms will only increase.

Materials and Methods

The materials and methods used in this study are described in detail in *SI Appendix, Additional Experimental Procedures*. Information includes general synthetic procedures, photophysical characterization of compounds, description of plasmids and cloning, virus production, protein production and purification, Western blot analysis, preparation of giant unilamellar vesicles, mass spectrometric analysis of vesicle lipid content, cell culture and cDNA transfection protocols, life cell imaging, loading procedures for caged lipids, uncaging experiments, quantification of uncaging reactions, image analysis and data processing, and the kinetic model and fitting procedures. Data availability statement: All relevant datasets are included as figure items in the main text or *SI Appendix*. All software codes used for analysis will be made available to readers via the institute repository of the Max Planck Institute of

Molecular Cell Biology and Genetics (MPI-CBG) (https://dx.doi.org/21.11101/0000-0007-DF4A-C) and upon request from the corresponding authors.

ACKNOWLEDGMENTS. We thank the following services and facilities at MPI-CBG Dresden for their support: Protein Expression Facility, Mass Spectrometry Facility, and the Light Microscopy Facility. We thank Jan Peychl, Britta Schroth-Diez, and Sebastian Bundschuh for the outstanding support and expert advice. A.N. acknowledges funding by the European Research Council under the European Union's Horizon 2020 research and innovation program Grant Agreement GA758334 ASYMMEM, the Max Planck Lipid Research Center, and the Deutsche Forschungsgemeinschaft (DFG) as a member of the TRR83 consortium. A.M.W. was funded by the DFG from Emmy Noether Grant and TRR186, Project 278001972, and A.T.G. was further part of the international program Medical Neurosciences. Ü.C. acknowledges financial support from the DFG as a member of the TRR83 and FOR2682 consortia and the German Federal Ministry of Education and Research (BMBF) grant to the German Center for Diabetes Research. A.S. acknowledges financial support from the DFG as a member of the TRR83 and FOR2682 consortia and BMBF Grant "Lipidomics for Life Sciences."

1. T. Baukrowitz, B. Fakler, K(ATP) channels: Linker between phospholipid metabolism and excitability. *Biochem. Pharmacol.* **60**, 735–740 (2000).
2. A. R. Tall, L. Yvan-Charvet, Cholesterol, inflammation and innate immunity. *Nat. Rev. Immunol.* **15**, 104–116 (2015).
3. F.-C. Tsai *et al*., A polarized Ca2+, diacylglycerol and STIM1 signalling system regulates directed cell migration. *Nat. Cell Biol.* **16**, 133–144 (2014).
4. M. Krause, A. Gautreau, Steering cell migration: Lamellipodium dynamics and the regulation of directional persistence. *Nat. Rev. Mol. Cell Biol.* **15**, 577–590 (2014).
5. R. Mancini *et al*., Metabolic features of cancer stem cells: The emerging role of lipid metabolism. *Oncogene* **37**, 2367–2378 (2018).
6. B. Wang *et al*., Phospholipid remodeling and cholesterol availability regulate intestinal stemness and tumorigenesis. *Cell Stem Cell* **22**, 206–220.e4 (2018).
7. S. Beloribi-Djefaflia, S. Vasseur, F. Guillaumond, Lipid metabolic reprogramming in cancer cells. *Oncogenesis* **5**, e189 (2016).
8. R. J. Perry, V. T. Samuel, K. F. Petersen, G. I. Shulman, The role of hepatic lipids in hepatic insulin resistance and type 2 diabetes. *Nature* **510**, 84–91 (2014).
9. U. Coskun, K. Simons, Cell membranes: The lipid perspective. *Structure* **19**, 1543–1548 (2011).
10. M. R. Wenk, Lipidomics: New tools and applications. *Cell* **143**, 888–895 (2010).
11. A. Shevchenko, K. Simons, Lipidomics: Coming to grips with lipid diversity. *Nat. Rev. Mol. Cell Biol.* **11**, 593–598 (2010).
12. T. Harayama, H. Riezman, Understanding the diversity of membrane lipid composition. *Nat. Rev. Mol. Cell Biol.* **19**, 281–296 (2018).
13. C. Lee, S. K. Fisher, B. W. Agranoff, A. K. Hajra, Quantitative analysis of molecular species of diacylglycerol and phosphatidate formed upon muscarinic receptor activation of human SK-N-SH neuroblastoma cells. *J. Biol. Chem.* **266**, 22837–22846 (1991).
14. M. S. Pessin, J. J. Baldassare, D. M. Raben, Molecular species analysis of mitogen-stimulated 1,2-diglycerides in fibroblasts. Comparison of alpha-thrombin, epidermal growth factor, and platelet-derived growth factor. *J. Biol. Chem.* **265**, 7959–7966 (1990).
15. B. Peter-Riesch, M. Fathi, W. Schlegel, C. B. Wollheim, Glucose and carbachol generate 1,2-diacylglycerols by different mechanisms in pancreatic islets. *J. Clin. Invest.* **81**, 1154–1161 (1988).
16. G. E. Atilla-Gokcumen *et al*., Dividing cells regulate their lipid composition and localization. *Cell* **156**, 428–439 (2014).
17. M. S. Köberlin *et al*., A conserved circular network of coregulated lipids modulates innate immune responses. *Cell* **162**, 170–183 (2015).
18. C. Ma, L. Su, A. B. Seven, Y. Xu, J. Rizo, Reconstitution of the vital functions of Munc18 and Munc13 in neurotransmitter release. *Science* **339**, 421–425 (2013).
19. G. C. Yaney, B. E. Corkey, Fatty acid metabolism and insulin secretion in pancreatic beta cells. *Diabetologia* **46**, 1297–1312 (2003).
20. A. C. Newton, Protein kinase C: Poised to signal. *Am. J. Physiol. Endocrinol. Metab.* **298**, E395–E402 (2010).
21. E. J. Quann, X. Liu, G. Altan-Bonnet, M. Huse, A cascade of protein kinase C isozymes promotes cytoskeletal polarization in T cells. *Nat. Immunol.* **12**, 647–654 (2011).
22. E. Muro, G. E. Atilla-Gokcumen, U. S. Eggert, Lipids in cell biology: How can we understand them better? *Mol. Biol. Cell* **25**, 1819–1823 (2014).
23. A. Honigmann, A. Nadler, The next frontier: Quantitative Biochemistry in living cells. *Biochemistry* **57**, 47–55 (2018).
24. N. Wagner, M. Stephan, D. Höglinger, A. Nadler, A click cage: Organelle-specific uncaging of lipid messengers. *Angew. Chem. Int. Ed. Engl.* **57**, 13339–13343 (2018).
25. S. Feng *et al*., Mitochondria-specific photoactivation to monitor local sphingosine metabolism and function. *eLife* **7**, e34555 (2018).
26. A. Nadler *et al*., The fatty acid composition of diacylglycerols determines local signaling patterns. *Angew. Chem. Int. Ed. Engl.* **52**, 6330–6334 (2013).
27. A. Nadler *et al*., Exclusive photorelease of signalling lipids at the plasma membrane. *Nat. Commun.* **6**, 10056 (2015).
28. D. Höglinger *et al*., Trifunctional lipid probes for comprehensive studies of single lipid species in living cells. *Proc. Natl. Acad. Sci. U.S.A.* **114**, 1566–1571 (2017).
29. F. Stein, M. Kress, S. Reither, A. Piljić, C. Schultz, FluoQ: A tool for rapid analysis of multiparameter fluorescence imaging data applied to oscillatory events. *ACS Chem. Biol.* **8**, 1862–1868 (2013).
30. Y. Zhao *et al*., An expanded palette of genetically encoded Ca^{2+} indicators. *Science* **333**, 1888–1891 (2011).
31. T. Hofmann *et al*., Direct activation of human TRPC6 and TRPC3 channels by diacylglycerol. *Nature* **397**, 259–263 (1999).
32. J. C. Bozelli, Jr, R. M. Epand, Specificity of acyl chain composition of phosphatidylinositols. *Proteomics* **19**, e1900138 (2019).
33. E. Oancea, M. N. Teruel, A. F. Quest, T. Meyer, Green fluorescent protein (GFP)-tagged cysteine-rich domains from protein kinase C as fluorescent indicators for diacylglycerol signaling in living cells. *J. Cell Biol.* **140**, 485–498 (1998).
34. H. Akaike, A new look at the statistical model identification. *IEEE Trans. Automat. Contr.* **19**, 716–723 (1974).
35. P. Björkholm *et al*., Identification of novel sphingolipid-binding motifs in mammalian membrane proteins. *Biochim. Biophys. Acta* **1838**, 2066–2070 (2014).
36. S. Carrasco, I. Mérida, Diacylglycerol, when simplicity becomes complex. *Trends Biochem. Sci.* **32**, 27–36 (2007).
37. T. Kobayashi, A. K. Menon, Transbilayer lipid asymmetry. *Curr. Biol.* **28**, R386–R391 (2018).
38. T. B. Ware *et al*., Reprogramming fatty acyl specificity of lipid kinases via C1 domain engineering. *Nat. Chem. Biol.* **16**, 170–178 (2020).
39. A.-E. Saliba *et al*., A quantitative liposome microarray to systematically characterize protein-lipid interactions. *Nat. Methods* **11**, 47–50 (2014).

page intentionally left blank

2.9 Manuscript in preparation: Grasskamp et al.

Manuscript Title

Molecular and functional interdependence of spontaneous and action potential evoked neurotransmission at individual synapses

Authors

Andreas T. Grasskamp, Meida Jusyte, Anthony W. McCarthy, Alexander M. Walter

Author contributions

A.T.G. and A.M.W. conceived the project, and wrote algorithms for data analysis. A.T.G. and M.J. performed GCaMP experiments, pharmacology, and immunohistochemistry, and analyzed the data. M.J. and A.W.M. performed electrophysiological recordings and pharmacology, and analyzed the data. A.T.G. and A.M.W. wrote the manuscript with input from all co-authors.

Contribution details

For this manuscript in preparation, we again made use of the genetically encoded fluorescent calcium indicator GCaMP as well as pharmacological and electrophysiological methodologies. This project spanned the whole duration of my doctoral work and encompasses most of my experimental work. Parts of it have been published in Reddy-Alla et al. (2017), notably the fact that spontaneous SV release scales with presynaptic AZ protein levels which had not been shown before. Here, we elaborate on the role of presynaptic AZ molecules in both AP-evoked and spontaneous SV release. My experiments showed the differential dependence of spontaneous and evoked release on several AZ proteins (BRP, Unc13A, Unc13B, Unc18, Syx-1A). I performed TTX- and Cd^{2+}-experiments together with Meida Jusyte, and analyzed all GCaMP imaging data using preexisting and self-developed algorithms. Together with my colleague Anthony McCarthy (who performed electrophysiological PhTx-experiments), we found that postsynaptic receptors are shared in detecting NT from both release modes. Lastly, I found that spontaneous and evoked release generally scale with each other at individual AZs, implying shared SV pools and mechanisms. Furthermore, as the first author I wrote the manuscript (with help and input from all co-authors) and integrated all data that my colleagues had gathered and analyzed for this project into comprehensible figures. At the time of thesis submission, the manuscript had not been submitted to any scientific journal.

Molecular and functional interdependence of spontaneous and action potential evoked neurotransmission at individual synapses

Andreas T. Grasskamp[1], Meida Jusyte[1,2], Anthony W. McCarthy[1], Alexander M. Walter[1,2,*]

[1] Leibniz-Forschungsinstitut für Molekulare Pharmakologie, Robert-Rössle-Straße 10, 13125 Berlin, Germany
[2] Einstein Center for Neurosciences, Charité Universitätsmedizin Berlin, Charitéplatz 1, 10117 Berlin, Germany

* Corresponding author: awalter@fmp-berlin.de (A.M.W.)

Summary

Communication between nerve cells relies on highly regulated neurotransmitter (NT) release from synaptic vesicles (SVs) at presynaptic active zones (AZs) and on postsynaptic NT receptors that respond and propagate the signal. NT release is triggered by local Ca^{2+} elevations when action potentials (AP) open presynaptic voltage-gated Ca^{2+}-channels (VGCCs) (Südhof, 2013), but it also happens spontaneously, without corresponding AP stimuli (Kaeser and Regehr, 2014). Whether or how spontaneous neurotransmission is regulated, or if it serves a specific function, has recently been of interest (Ramirez and Kavalali, 2011; Walter et al., 2014; Kavalali, 2015). We used pharmacology, electrophysiological recordings, and live imaging of AZ activity at the *Drosophila melanogaster* glutamatergic neuromuscular junction (NMJ) to study interdependences between spontaneous and AP-evoked neurotransmission. We found that the levels of proteins contributing to AP-evoked NT release, including ones forming the AZ cytomatrix, neuronal SNARE proteins, and SV docking/priming factors also predicted spontaneous activity at the same AZs. Blocking voltage-gated Na^{+} channels only eliminated AP-evoked, but not spontaneous transmission. In contrast, blocking VGCCs inhibited both transmission modes, indicating that spontaneous transmission is induced by spontaneous Ca^{2+} influx. Use-dependent inhibition of NT receptors by AP-evoked transmission decreased spontaneous transmission, demonstrating that both transmission modes activate overlapping postsynaptic receptors. Furthermore, spontaneous and AP-evoked events were correlated, indicating that most AZs contribute to both transmission modes with similar strength. Finally, cross-depletion of NT release was observed at single AZs, indicating that the same SVs mediate both activity modes. Our results thus argue that at the vast majority of AZs, both transmission modes coexist, depend on the same molecular machinery, activate overlapping NT receptors, and draw on the same SV pool.

Results & Discussion

Presynaptic active zone protein levels predict NT release modes

It has been debated whether spontaneous and AP-evoked SV release modes use overlapping or distinct molecular machinery (Groemer and Klingauf, 2007; Pang et al., 2011; Cornelisse et al., 2012; Kavalali, 2015). We therefore investigated the molecular determinants of AP-evoked and spontaneous neurotransmission with single-AZ resolution. To do so, we used a live-imaging approach in 3rd instar *Drosophila melanogaster* larvae postsynaptically expressing the fluorescent Ca^{2+}-reporter GCaMP (Peled and Isacoff, 2011; Melom et al., 2013; Peled et al., 2014; Muhammad et al., 2015; Reddy-Alla et al., 2017; Newman et al., 2017). Presynaptic exocytosis of SVs containing glutamate leads to an opening of postsynaptic ionotropic receptors permeable for Na^{+}, K^{+} and Ca^{2+} (Chang et al., 1994), and to a temporally and spatially confined postsynaptic increase in GCaMP fluorescence, enabling the mapping of single SV release events (**Figure 1 C**).

We imaged synaptic activity profiles at type 1b boutons on muscle 4 NMJs (**Figure 1 A**) which were subsequently fixated and immunohistochemically stained to visualize presynaptic proteins. Developing synapses in this model show varying composition, cytomatrix size, and function (Guerrero et al., 2005; Melom et al., 2013; Peled et al., 2014; Reddy-Alla et al., 2017), which allows the investigation of heterogeneous AZs in parallel. This approach enabled the assignment of spontaneous and AP-evoked neurotransmission events (100 s of imaging without stimulation followed by 36 AP stimuli at 0.2 Hz) to single AZs which we

Keywords:
Drosophila, neuromuscular junction, calcium imaging, active zone, neurotransmission, spontaneous release, release probability, synaptic mechanisms

Abbreviations:
(M)Unc13/18 – (mammalian) uncoordinated 13/18; BRP – bruchpilot; Syx – syntaxin; SNARE – soluble N-ethylmaleimide sensitive factor attachment protein receptor; Syt-1 – synaptotagmin-1; AZ – active zone; NT – neurotransmitter; SV – synaptic vesicle; AP – action potential; mEJP/mEJC – miniature Excitatory Junction Potential/Current; NMJ – neuromuscular junction; VGCC/VGSC – voltage-gated calcium/sodium channel; TTX – Tetrodotoxin; PhTx – philanthotoxin

identified by immunohistochemically visualizing the AZ scaffolding protein bruchpilot (BRP; Kittel et al., 2006) (**Figure 1 B-E** and **Supplementary Figure S1-1 A&B**). Electrophysiological recordings obtained simultaneously confirmed that these events reported on synaptic transmission (**Supplementary Figure S1-3**). Fluorescence signals in response to NT release were similar in both release modes (**Figure 1 E**) and non-saturating at 1.5 mM $[Ca^{2+}]_{ext.}$ (**Supplementary Figure S1-1 C**), confirming the quantal resolution of this assay (see methods and **Supplementary Figure S1-2** for further details). The number of events was counted at each AZ (events were assigned to single AZs) and only events within 1 s of the AP were considered as AP-evoked. Based on this, release maps for either transmission mode were generated (shown for BRP in **Figure 1 F**). Furthermore, AZs were binned into 4 equally sized groups based on their fluorescence intensity and the mean number of events plotted as a function of the mean AZ levels of several proteins of interest to determine whether and how their levels related to the number of spontaneous and AP-evoked events (**Figure 1 F-P**).

For BRP, this analysis showed a positive relation between its levels and both spontaneous and AP-evoked activity (**Figure 1 G**), consistent with previous findings (Reddy-Alla et al., 2017). The scaling of AP-evoked activity with BRP levels had been noted before (Peled et al., 2014) and fits the observation that BRP colocalizes with the *Drosophila* VGCC Cac, whose levels also predict AP-evoked activity (Gratz et al., 2019). In contrast to previous reports of a negative correlation between BRP levels and spontaneous activity levels (investigated in animals lacking the small GTPase Rab3; Peled et al., 2014) we found a clear positive correlation with BRP (as noted before in Reddy-Alla et al., 2017). The quantification in **Figure 1 G, bottom panel** shows a cell-wise analysis of linear fits to average spontaneous and AP-evoked activity levels vs. BRP, revealing a positive scaling in both cases. BRP was used to identify AZ positions in all following analysis where we investigated how the levels of other, evolutionarily conserved presynaptic proteins (co-stained with BRP) related to the two transmission modes (**Figure 1 H-P**).

The AZ protein Unc13, originally discovered because mutation of its gene led to paralysis in *C. elegans* (uncoordinated-13; Brenner, 1974), is essential for SVs to localize (dock) to the presynaptic plasma membrane and to gain fusion competence (prime) in several species, including nematodes, insects and mammals (reviewed in Brose et al., 2000; Rizo and Rosenmund, 2008; Rizo, 2018; Böhme et al., 2018;

Figure 1. Quantal single AZ Ca^{2+}-imaging shows influence of protein abundance on release modes. (A) BRP (light green) is situated at the presynaptic active zone, positioned around a voltage-gated Ca^{2+}-channel cluster (cyan). Release of glutamate (black dots) from SVs leads to the opening of ligand-gated ion channels (purple) in the postsynaptic membrane, making them inwardly permeable to Na^{+} and Ca^{2+} (blue dots). Postsynaptic influx of Ca^{2+} elicits fluorescence increases in GCaMP molecules (dark green) tethered to the postsynaptic membrane. (B) Overlay of a 100 s GCaMP video (maximal projection, grey) with confocal image of larval tissue anti-BRP IHC (green). (C) Detail from (B): 500 ms sequence (16-color LUT, contrast adjusted) of a single spontaneous SV fusion event, attributed to a single AZ (white circle) distinct from the surrounding AZs (yellow asterisks). (D) Fluorescence traces (corrected for bleaching) from individual AZs in (B) for either spontaneous (orange) or evoked (blue) SV release events. (E) Cell-wise averaged (N = 15 animals) fluorescence traces of 670 spontaneous and 2849 evoked events show no difference in fluorescence amplitude, indicating quantal quality. (F) Top: 90° CCW rotated detail from (B); Confocal image of IHC against BRP (BW inverted and contrast adjusted). Middle: image from top overlaid with positions of maximal BRP intensity values (yellow asterisks) and circles of different sizes corresponding to spontaneous activity levels. Bottom: same as middle, but overlaid with evoked activity. (G) Top: Binned normalized BRP fluorescence levels plotted against average number of spontaneous (orange) or evoked (blue) events at AZs in these bins. Bottom: Cell-wise quantification of slopes (N = 15 animals); ev: $p < 0.0001$; sp: $p = 0.0008$. (H-O) Same as (F&G), for Unc13A (N = 15 animals) ev: $p < 0.0001$; sp: $p = 0.0002$, Unc13B (N = 19) ev: $p = 0.1349$; sp: $p = 0.2493$, Syntaxin/Syx-1A (N = 10 animals) ev: $p = 0.0004$; sp: $p = 00025$. and Unc-18/ROP (N = 8 animals) ev: $p = 0.4200$; sp: $p = 0.0133$; all asterisks correspond to AZ locations defined by α-BRP IHC. (P) Summary of all slope quantifications. All data shown is represented as mean±SEM. All statistical tests on slopes are one-sample t-tests against a hypothetical value of 0. n.s. not significant; * $p<0.05$; ** $p<0.01$; *** $p<0.001$; **** $p<0.0001$. All scale bars represent 5 µm. Evoked measurements combined with IHC for Syx-1A and Unc-18 have been reanalyzed from Reddy-Alla et al., 2017. Refer to statistics table for details on mean values and testing.

Dittman, 2019). It is a major contributing factor in the generation of SV release sites in invertebrates and mammals (Reddy-Alla et al., 2017; Sakamoto et al., 2018). Of the two major isoforms in *Drosophila*, Unc13A mainly contributes to synaptic transmission at the NMJ, while Unc13B plays a minor role (Böhme et al., 2016). In congruence with this, single AZ Unc13A levels predicted evoked and spontaneous release similarly to BRP (**Figure 1 H+I**), but neither release mode scaled with Unc13B levels (**Figure 1 J+K**).

We next investigated whether we could find a comparable influence on either release mode for other essential synaptic proteins: the tSNARE-protein (membrane-localized target soluble N-ethylmaleimide sensitive factor attachment protein receptor; SNAREs are essential to fuse docked and primed SVs to release NT; Rizo and Rosenmund, 2008) Syntaxin-1

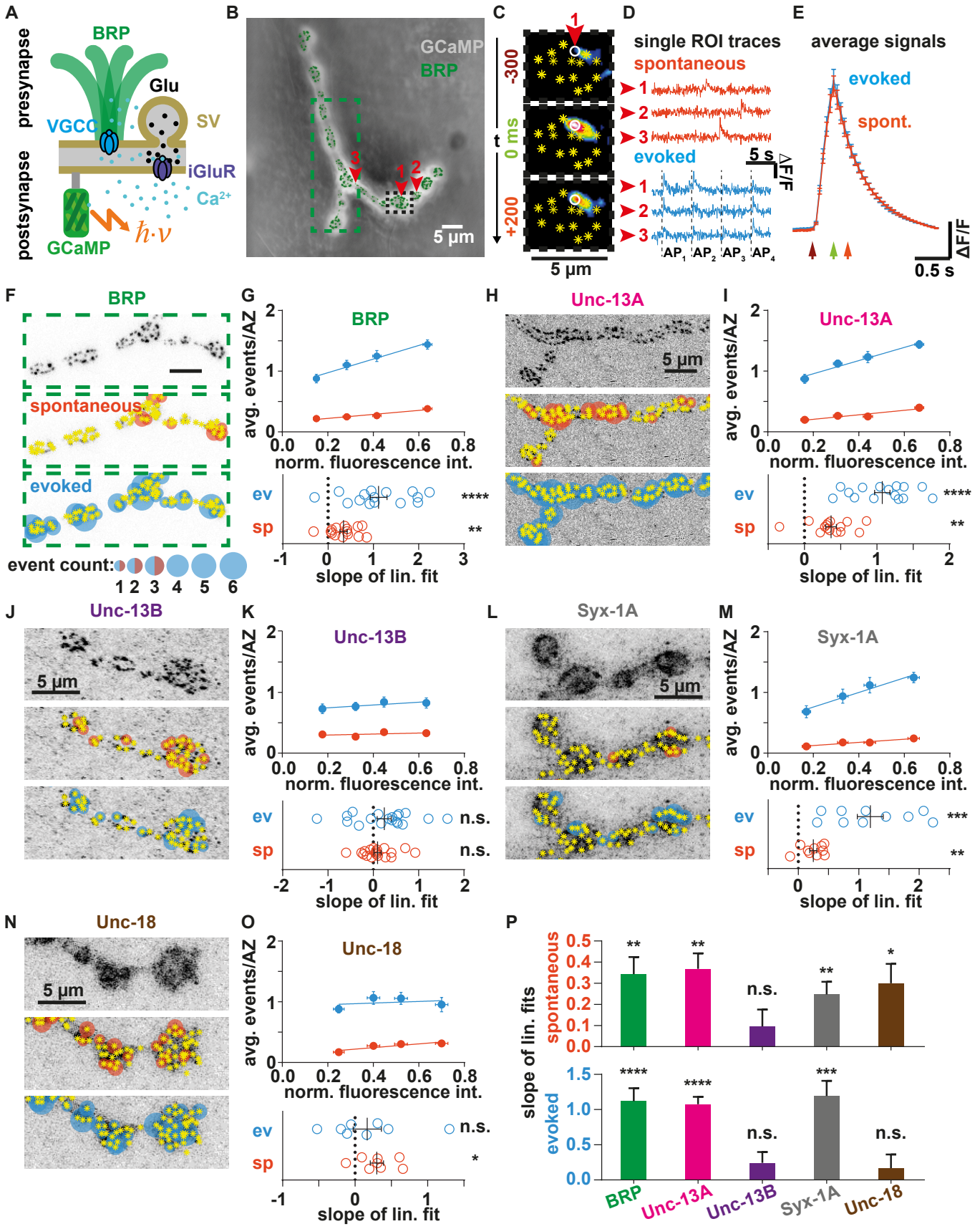

(*Drosophila* isoform Syx-1A) and the auxiliary protein (M)Unc18 (ROP in Drosophila), a member of the Sec-1/(M)Unc18 like (SM) protein family. As we previously reported in Reddy-Alla et al. (2017), we saw a scaling of AP-evoked activity only with Syx-1A AZ levels (**Figure 1 L+M**), but not with Unc18 (**Figure 1 N+O**, cells reused and reanalyzed from Reddy-Alla et al., 2017). We here expanded this analysis to include spontaneous activity, which revealed a positive correlation with both Syx-1A and Unc18 AZ levels.

Thus, our investigation of AZ activity in both NT release modes reveals overlapping as well as distinct relations among essential components of the SV release machinery. While the levels of BRP, Unc13A and Syx-1A all predict activity levels in both transmission modes, only spontaneous (but not AP-evoked) activity scales with Unc18 levels. Interestingly, while initially scaling with AP-evoked activity, high levels of Unc18 seemed to attenuate it (seen in an initial rise followed by saturation of activity as a function of Unc18 levels; **Figure 1 O**). This could mean that high Unc18 levels possibly favor binding Syx-1A in its closed conformation, which is incompatible with SV fusion (Misura et al., 2000). Low to intermediate levels might predominantly exert a facilitatory effect on AP-evoked SV release by facilitating the formation of the ternary SNARE complex (Südhof and Rothman, 2009).

Voltage-gated ion channels differentially influence spontaneous NT release

AP-evoked NT release crucially depends on voltage-gated ion channels. Voltage-gated sodium channels (VGSCs) are essential to initiate and propagate the AP along the neuronal cell membrane (Hodgkin and Huxley, 1952; Hille, 1968), while VGCCs function downstream at presynaptic terminals to locally elevate the Ca^{2+} concentration which triggers SV fusion by activating the vesicular Ca^{2+} sensor synaptotagmin-1 (Syt-1; Yoshihara et al., 2003; Südhof, 2012). Because our above findings indicate that many proteins predict both NT modes to a similar extent, we wondered whether spontaneous activity, just like AP-evoked release, may also be triggered by local Ca^{2+} elevations. This would align with findings that Syt-1 also controls spontaneous transmission (Littleton et al., 1993; Xu et al., 2009), and the application of exogenous Ca^{2+} buffers reduces spontaneous NT release (Schneggenburger and Rosenmund, 2015). This could explain why we find that spontaneous activity scales with BRP (**Figure 1 G**), as its levels correlate with VGCC abundance (Fouquet et al., 2009; Böhme et al., 2016; Fulterer et al., 2018). We therefore wondered whether spontaneous activity may depend on voltage gated ion channels, by stochastic gating of either VGCCs directly or via VGSCs, potentially leading to subtle fluctuations in the membrane potential that open some VGCCs (Magee and Johnston, 1995; Kavalali and Plummer, 1996; Kavalali et al., 1997).

We first tested for a role of VGSCs by blocking them with the specific antagonist Tetrodotoxin (TTX) (Nakamura et al., 1965) and by measuring synaptic activity in electrophysiological recordings (two-electrode voltage clamp, TEVC). While TTX (1 µM) effectively blocked all AP-evoked SV release (**Figure 2 A+B**), this did not reduce the frequency (or amplitude) of spontaneous 'miniature Excitatory Junction Currents' (mEJCs; **Figure 2 C-E**), suggesting that spontaneous transmission is independent of VGSCs. We further verified these observations with GCaMP-imaging, where fluorescence amplitudes and frequencies of spontaneous release events remained similar in the presence of TTX (**Figure 2 F-H**) and spontaneous activity was still strictly predicted by local Unc13A levels (**supplementary Figure S2 A&B**). Thus, consistent with a large body of work, spontaneous neurotransmission is maintained upon VGSC block, but still depends on priming proteins (i.e. Unc13A) needed for both transmission modes.

Next, we tested whether VGCCs played a role for spontaneous NT release by blocking Ca^{2+} influx with $CdCl_2$ (Cadmium chloride, 740.7 µM). Akin to TTX, this inhibited all AP-evoked SV release (**Figure 2 I+J)** but unlike TTX it led to a strong reduction of the frequency of spontaneous NT release (**Figure 2 M**) (without affecting mEJC amplitudes; **Figure 2 K+L**). We verified this with the GCaMP assay, seeing no significant change in amplitudes but an even stronger decrease in frequency (**Figure 2 N-P**). This observation is consistent with spontaneous activity being triggered by Ca^{2+} influx through stochastically gating VGCCs (as described for rat hippocampal synapses; Ermolyuk et al., 2013), and that SV exocytosis can be triggered by single VGCC opening (investigated at frog NMJs by simulations based on freeze-fracture EM-derived VGCC positions; Shahrezaei et al., 2006).

Neurotransmission in both release modes targets overlapping postsynaptic receptors

So far, we have shown that both AP-evoked and spontaneous transmission are concomitantly predicted by presynaptic AZ protein levels (BRP, Unc13A and Syx-1A) and depend on VGCCs. Next, we wondered whether the same NT receptors detect both transmission modes (**Figure 3 B**), or whether they are dedicated to either transmission mode (**Figure 3 A**), as implied by previous studies (Atasoy et al., 2008; Peled et al., 2014). We tested this by stimulating AP-evoked NT release in the presence of the use-dependent glutamate receptor blocker Philanthotoxin (PhTx; Davis and Müller, 2015), and asked whether this also affected spontaneous transmission (**Figure 3 C**). This would only be the case if NT receptors responded to both transmission modes, because the same receptors sensing spontaneous NT release would have been

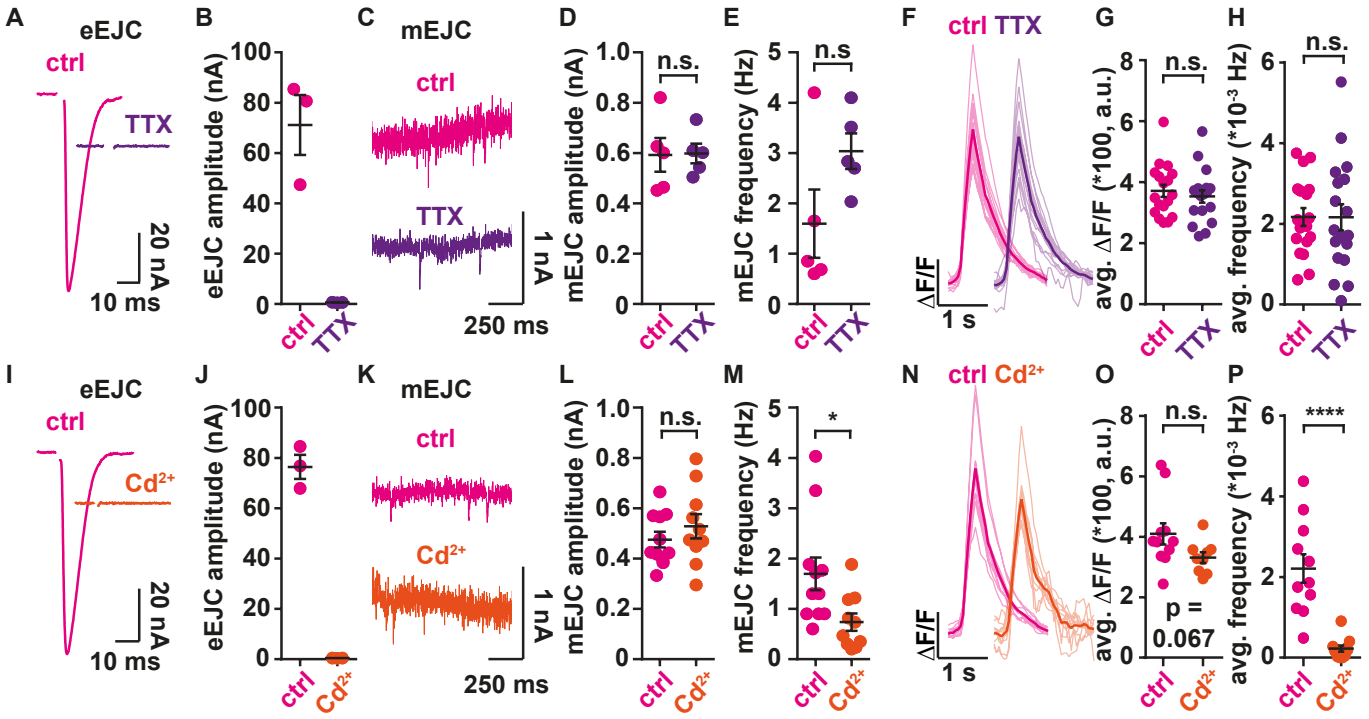

Figure 2. Voltage-gated channel block differentially influences spontaneous neurotransmission. (A+I) Representative eEJC traces of ctrl cells (magenta) and cells treated with 1 µM TTX (purple) or 740.7 µM Cd^{2+} (orange). (B+J) Cell-wise (N = 3 animals) quantification of experiment shown in A+I (B: ctrl 71.14±11.93 nA, TTX 0.6131±0.08289 nA; J: ctrl 76.43±4.798 nA, Cd^{2+} 0.4375±0.01550 nA). (C+K) Representative mEJC traces of ctrl cells (magenta) or cells treated with 1 µM TTX (purple) or 740.7 µM Cd^{2+} (orange). (D+L) Cell-wise (D: ctrl N = 5; TTX N = 5; L: ctrl N = 11; Cd^{2+} N = 10 animals) quantification of mEJC amplitudes (D: ctrl 0.5925±0.06691 nA, TTX 0.5983±0.03879 nA; L: ctrl 0.4754±0.03126 nA, Cd^{2+} 0.5282±0.04835 nA); unpaired t-test: ctrl vs. TTX: p = 0.9423; ctrl vs. Cd^{2+}: p = 0.3618. (E+M) Cell-wise (E: ctrl N = 5; TTX N = 5; M: ctrl N = 11; Cd^{2+} N = 10 animals) quantification of mEJC frequencies (D: ctrl 1.597±0.6769 Hz, TTX 3.037±0.3551 Hz; L: ctrl 1.695±0.3255 Hz, Cd^{2+} 0.7383±0.1734 Hz); unpaired t-test: ctrl vs. TTX: p = 0.0964; ctrl vs. Cd^{2+}: p = 0.0209. (F+N) Single cell (faint) and average (solid) traces of spontaneous event GCaMP-fluorescence. (G+O) Cell-wise (G: ctrl N = 18; TTX N = 18; O: ctrl N = 11; Cd^{2+} N = 9 animals) quantification of GCaMP event amplitudes (G: ctrl 371.7±20.18 a.u., TTX 353.5±20.45 a.u.; O: ctrl 409.4±35.19 a.u., Cd^{2+} 330.9±18.01 a.u.); unpaired t-test: ctrl vs. TTX: p = 0.5305; Mann-Whitney-Test: ctrl vs. Cd^{2+}: p = 0.0668. (H+P) Cell-wise (H: ctrl N = 18; TTX N = 18; P: ctrl N = 11; Cd^{2+} N = 11 animals) quantification of GCaMP event frequency (H: ctrl 0.002170±0.0002246 Hz, TTX 0.002162±0.0003297 Hz; O: ctrl 0.002210±0.0003540 Hz, Cd^{2+} 0.0002248±0.00007827 Hz); Mann-Whitney-Test: ctrl vs. TTX: p = 0.7123; Mann-Whitney-Test: ctrl vs. Cd^{2+}: p < 0.0001. All averaged data shown is represented as mean±SEM. n.s. not significant; * p<0.05; **** p<0.0001. Refer to statistics table for details on mean values and testing.

blocked by the AP-evoked NT release (**Figure 3 A&B**).

We initially monitored baseline spontaneous transmission in electrophysiological current-clamp experiments for 30 s before and after the application of PhTx, which (as expected) significantly reduced miniature Excitatory Junction Potential (mEJP) amplitudes (**Figure 3 D**). Then, in half of the animals, the efferent nerve was stimulated with an AP train (10 Hz over 10 s; **Figure 3 F**) suitable to block gluatamate receptors in the presence of PhTx (**supplementary Figure S3 A**). The other half of the animals received no AP stimulation (but there was a corresponding wait time of 10 s) (**Figure 3 E**). In both groups, spontaneous mEJPs were then recorded for another 30 s. If spontaneous and AP-evoked activity were exclusively sensed by non-overlapping postsynaptic receptors, the AP-stimulation should have no effect on spontaneous transmission (**Figure 3 A**). Contrasting this, we observed a clear decrease of mEJP frequency (but not amplitude) only in the group receiving the AP stimulations (**Figure 3 F**). Notably, neither PhTx application alone nor stimulation alone affected mEJP frequencies (**supplementary Figure S3 B&C**), proving that the effect was due to the use-dependent NT receptor block. A previous study using a similar approach at the *Drosophila* NMJ concluded that there was no effect of use-dependent NT receptor block across transmission modes (Peled et al., 2014). However, those experiments were compared across different groups of animals (which is less sensitive) and over a much longer time (25 min vs. 10 s here) where compensatory, homeostatic mechanisms are known to take place with this treatment (Frank et al., 2006; Davis and Müller, 2015; Harris and Littleton, 2015; Newman et al., 2017). As this homeostasis elicits marked functional changes which, among

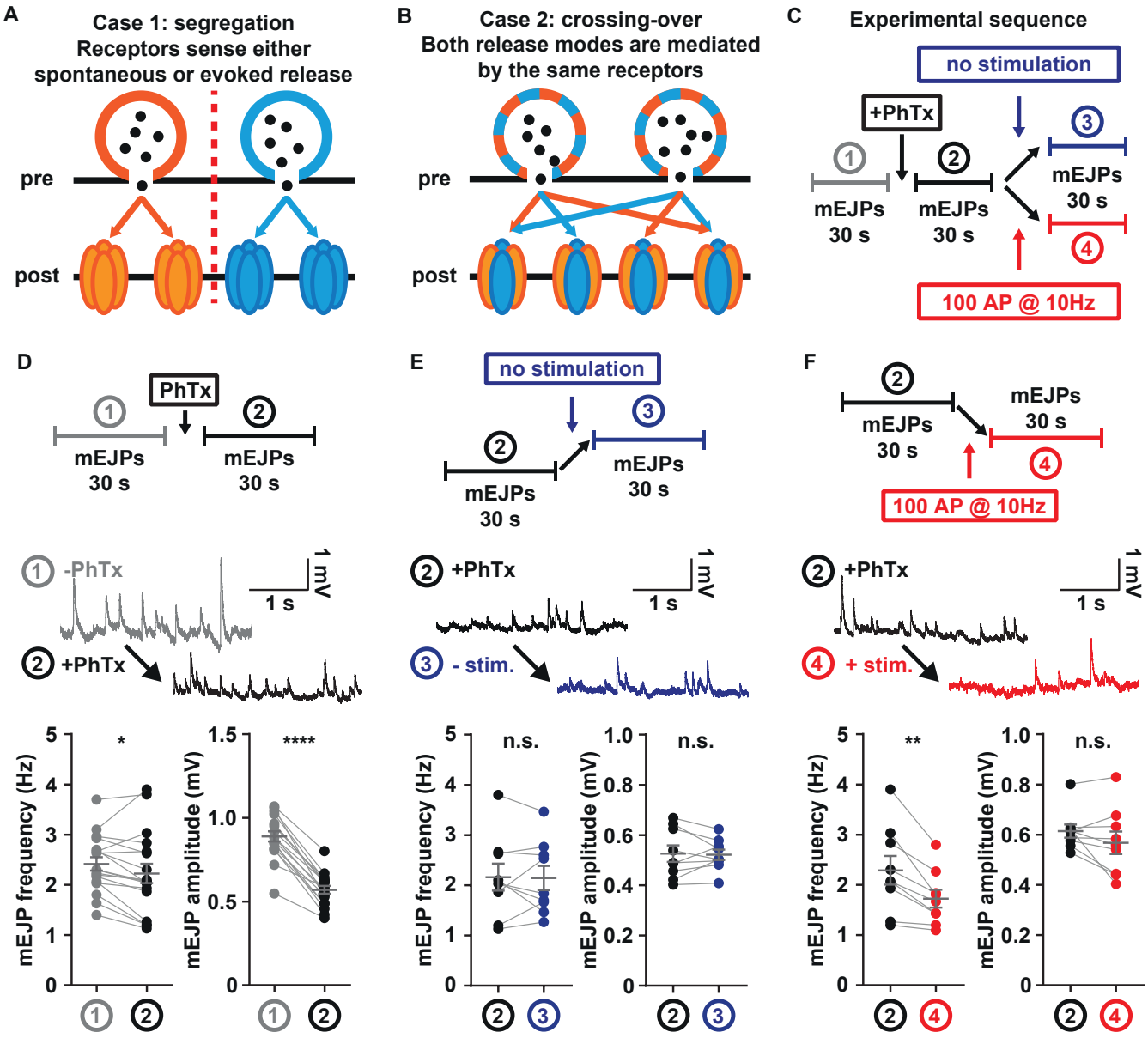

Figure 3. Spontaneous and evoked neurotransmission target overlapping receptors at the postsynapse. (A)&(B) Cartoon of two possible scenarios. (A) Spontaneous (orange) and evoked (blue) release are mediated by different vesicle pools and postsynaptic receptors. (B) Postsynaptic receptors are responsible for sensing both release modes equally and no different vesicle pools are used. (C) Schematic depiction of experimental setup: After 30 s mEJP baseline recordings, all larvae are equally treated with 4 µM PhTx (for details see method section), and another 30 s of mEJPs are recorded. Then, only one group (4, red) undergoes stimulation at 10 Hz over 10 s, the other (3, blue) receives no stimulation. Another 30 s of mEJPs are recorded after that, resulting in traces like those shown in (D-F). (D) Quantification before and after PhTx application of mEJP frequency (-PhTx.: 2.417±0.1329 Hz; +PhTx: 2.226±0.1917 Hz; p = 0.0435, paired parametric t-test) and amplitude (-PhTx: 0.8902±0.03051 mV; +PhTx: 0.5702±0.02297 mV; p < 0.0001, paired parametric t-test) (N = 18 animals) (E) Quantification after PhTx application and without stimulation of mEJP frequency (+PhTx.: 2.163±0.2705 Hz; -stim.: 2.144±0.2429 Hz; p = 0.8962, paired parametric t-test) and amplitude (+PhTx: 0.5261±0.03291 mV; -stim.: 0.5218±0.02073 mV; p = 0.8328, paired parametric t-test) (N = 9 animals) (F) Quantification after PhTx application and with stimulation of mEJP frequency (+PhTx.: 2.289±0.2863 Hz; +stim.: 1.726±0.179 Hz; p = 0.0027, paired parametric t-test) and amplitude (+PhTx: 0.6144±0.02594 mV; +stim.: 0.5675±0.04475 mV; p = 0.2031, Wilcoxon matched-pairs signed rank test) (N = 9 animals). All averaged data shown is represented as mean±SEM. n.s. not significant; * p<0.05; **/## p<0.01; ***/### p<0.001; **** p<0.0001. Refer to statistics table for details on mean values and testing.

other proteins, involve BRP, Unc13A, VGCCs and Syx-1, this makes interpretations difficult (Gratz et al., 2019; Goel et al., 2019; Böhme et al., 2019). Our analysis achieves higher sensitivity by contrasting the spontaneous activity of the same NMJ before and after AP-stimulation in a strictly paired fashion, which revealed a clear effect. Our finding does not rule out that some dedicated pathways may also exist, but it clearly indicates that NT receptors are shared and used for both transmission modes.

SVs engaging in spontaneous and evoked release originate from the same active zones and SV pools

It was previously reported that spontaneous and AP-evoked transmission originate from distinct AZs (Melom et al., 2013; Peled et al., 2014). However, the common use of postsynaptic receptors and the similar dependence on the presynaptic release machinery (shown above) could also imply that the same AZs contribute to both transmission modes. We tested this by investigating whether AP-evoked and spontaneous NT release were correlated at single AZs (**Figure 4**). In our typical recording paradigm, we sequentially measure spontaneous activity (100 s) before assessing AP-evoked activity from the same AZs (36 APs at 0.2 Hz) (**Figure 4 A**). The insert in **Figure 4 A** illustrates the positions of NT release mapped during either episode and shows a substantial number of AZs that exhibit mixed (spontaneous and AP-evoked) activity. It is worth noting that the absolute numbers will depend heavily on the acquisition time and stimulus number, which must be balanced in the experiment to prevent rundown and/or fluorescence bleaching. When analyzing events in a single cell (**Supplementary Figure S4-1 C**), we saw no obvious correlation ($R^2 = 0.014$) between the number of spontaneous and AP-evoked events, agreeing with previous findings (Melom et al., 2013). However, sampling across all AZs is problematic due to the limited acquisition time and the overall low activity per single AZ. The situation became clearer when considering the mean AP-evoked activity as a function of spontaneous events per AZ in the same cell. This revealed a considerably higher correlation ($R^2 = 0.792$; **Supplementary Figure S4-1 C**). The effect became obvious when furthermore considering the mean per-AZ activity in many animals (N = 59 animals), which revealed a near-perfect correlation ($R^2 = 0.97$; **Figure 4 C**) between both release modes. This implies that NT release per AZ is highly heterogeneous, but that AZs participate in both transmission modes to a similar degree.

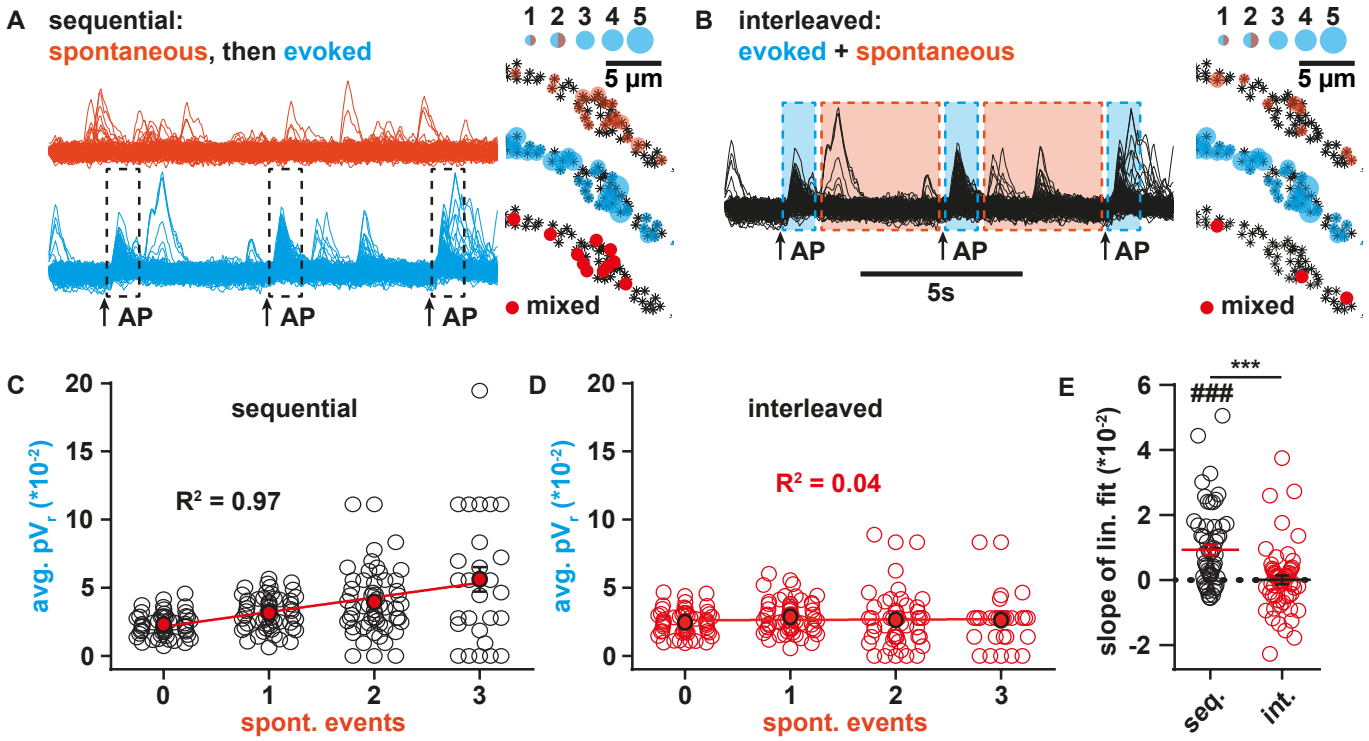

Figure 4. Spontaneous and evoked synaptic vesicle release are linked at individual active zones. (A) Sequence of experimental procedure for "sequential" experiment: spontaneous events (top, orange) are recorded for 100 s, and then the motoneuron is stimulated 36 times at 0.2 Hz to quantify evoked release (bottom, blue). "Mixed" AZs showing both modes of release can then be quantified (right). Asterisks signify positions of AZs defined by anti-BRP IHC. Size of overlaid circles corresponds to number of measured events. (B) Sequence of experimental procedure for "interleaved" experiment: the motoneuron is stimulated 36 times at 0.2 Hz to quantify evoked release (shaded blue), and spontaneous events are measured in between stimuli (shaded orange). "Mixed" AZs showing both modes of release can then be quantified (right). Asterisks signify positions of AZs defined by anti-BRP IHC. Size of overlaid circles corresponds to number of measured events (C) "Sequential" experiment: Cell-wise (N = 59 animals) quantification of NMJs by spontaneous events frequency vs. average pVr per cell; Black hollow dots represent single NMJs, red dots represent means; red line is a linear fit through the means, $R^2 = 0.965$. (D) "Interleaved" experiment: Cell-wise (N = 59 animals) quantification of NMJs by spontaneous event frequency vs. average pVr per cell; Red hollow dots represent single NMJs, red dots represent means; red line is a linear fit through the means, $R^2 = 0.0358$. (E) Cell-wise (N = 59 animals) quantification of linear fit slopes. Significant difference from zero: seq. 0.009312±0.001608; $p<0.0001$; int. 0.00005444±0.001309; $p = 0.967$. Wilcoxon matched-pairs signed rank test of seq. vs. int.: $p = 0.0002$. All mean values are represented as mean±SEM. Refer to statistics table for details on mean values and testing.

Our analysis does not rule out that very specialized synapses (i.e. those engaging in only one transmission mode) may exist as well. In fact, survival analysis and exponential extrapolation allowed us to estimate the fraction of AZs that may exclusively engage in spontaneous synaptic transmission. Around 27% of AZs showing spontaneous activity (during the first recording episode) may exclusively operate in transmission (**Supplementary Figure S4-1 E**), which constitutes ~6% of all BRP-positive AZs (**Supplementary Figure S4-1 F**). However, this number likely represents an upper estimate based on extrapolation. Unfortunately, due to the limited acquisition time of our experiment, it is not possible to measure this exactly. Sampling of more events in longer experiments could improve the estimate, but also adds uncertainty due to possible problems with photo-bleaching and rundown of synaptic activity.

Thus, our results argue that spontaneous and AP-evoked transmission coexist at the vast majority of AZs, and that there is overlap in the respective presynaptic release machinery (BRP, Unc13A, Syx-1A, and VGCCs), and postsynaptic receptors. However, an additional central question has been whether the same or distinct SV pools are utilized in both release modes (Alabi and Tsien, 2012; Kavalali, 2015). To study this, we tested whether AP-evoked activity led to cross-depletion of spontaneous activity at single AZs. For this, we once again analyzed the single-AZ recordings in which AP stimuli were applied (**Figure 4 A**), but this time also quantified the spontaneous activity in-between the stimuli in an "interleaved" analysis (**Figure 4 B**). Indeed, AP-stimulation resulted in overall fewer spontaneous events (while amplitudes were unaffected) and fewer (27% less) AZs were seen in the "mixed" category (solid red circles in the example in **Figure 4 A&B**) (**Supplementary Figure S4-1 A,B,D**). Moreover, unlike for spontaneous events recorded in isolation, where AZ BRP levels predicted spontaneous activity (**Figure 1 G**, **supplementary Figure S4-2 A,C**), this transmission mode no longer correlated with BRP levels in the "interleaved" analysis (**supplementary Figure S4-2 B&C**). Notably, the correlation between transmission modes vanished as well (**Figure 4 D**), consistent with previous analysis of spontaneous NT release between APs (Melom et al., 2013; Peled et al., 2014). Thus, interleaved AP-stimulation reduces spontaneous activity and the correlation between transmission modes at single AZs, likely due to SV depletion. This is consistent with both modes drawing from the same SV pool.

Conclusions & Outlook

Taken together, our results argue that the vast majority of AZs at the Drosophila NMJ share mechanisms to engage in either release mode while a small subset may be limited to spontaneous activity. It is tempting to speculate that these features relate to a developmental trajectory, with nascent AZs containing the essential machinery required to engage in NT release, yet lacking some of the more specialized machinery to tune activity to APs. Clearly, this spontaneous activity may be essential to guide further functional AZ maturation. While this remains speculation, we show that at most AZs, both release modes coexist, utilize the same molecular presynaptic machinery (SV priming and fusion proteins, VGCCs, likely organized by AZ scaffolding proteins), draw on the same SV pool, and activate the same NT receptors.

Data and software availability

All ImageJ and MATLAB code used in this paper will be made available by the corresponding author (A.M.W., awalter@fmp-berlin.de) upon reasonable request.

Author contributions

A.T.G. and M.J. performed Ca^{2+}-imaging experiments and pharmacology, immunohistochemistry, confocal microscopy, and analyzed the data. A.T.G. and A.M.W. developed MATLAB and ImageJ code for image processing and data analysis. A.W.M. and M.J. performed electrophysiology and pharmacology, and analyzed the data. A.T.G. and A.M.W. conceived the study and wrote the manuscript with input from all co-authors.

Acknowledgments

We would like to thank Sabine Hahn for excellent technical assistance. A.T.G. was supported by a Cluster of Excellence NeuroCure PhD-fellowship within the international graduate school Medical Neurosciences (Charité Universitätsmedizin Berlin). M.J. was funded by a PhD-fellowship from the Einstein Center for Neurosciences Berlin. Grants from Deutsche Forschungsgemeinschaft (DFG) included TRR186 and an Emmy-Noether grant to A.M.W.

Competing Interests

All authors confirm the absence of any financial or non-financial competing interests.

Methods

Animal rearing and preparation

Experiments making use of genetically modified invertebrate animals have been registered with and approved by the respective authorities (Landesamt für Gesundheit und Soziales LaGeSo, Berlin), and were performed in accordance with German laws and regulations on biosafety. Animals were bred and maintained at standard laboratory conditions (Sigrist et al., 2003) on semi-defined fly medium (Bloomington recipe). Male and female flies were used for all experiments. Wild type *w1118* flies were used for the experiments shown in **Figure 3**. The following fly strain was used for all other experiments: *Mhc-myrGCaMP5G/+;* (Reddy-Alla et al., 2017). Third instar larvae were dissected as described in Qin et al., 2005 in standard Ca^{2+}-free, hemolymph-like solution HL-3 (composition in mM: 70 NaCl, 5 KCl, 20 $MgCl_2$, 10 $NaHCO_3$, 5 Trehalose, 115 Sucrose, 5 HEPES; Stewart et al., 1994; low Mg^{2+}-solution used for PhTx-electrophysiology experiments contained 10 mM $MgCl_2$), adjusted to pH=7.2. Dissection was performed using fine insect pins on Sylgard-184 (Dow Corning, Midland MI, USA), by opening the dorsal body wall from posterior to anterior, removing all internal organs, and severing the motoneurons from the CNS without damaging the underlying body wall muscles, then removing the brain. For experimentation, the dissected larvae were then transferred to recording chambers on the respective recording setups, as detailed in the sections explaining electrophysiology and live calcium imaging.

Electrophysiology

All electrophysiological experiments were performed at room temperature using sharp glass electrodes (borosilicate glass with filament, 0.86x1.5x80 nm, Science products, Hofheim, Germany) pulled with a Flaming Brown Model P-97 pipette puller (Sutter Instruments, CA, USA). Stimulating suction electrodes were pulled on a DMZ-Universal Puller (Zeitz-Instruments GmbH, Germany) and fire polished using a CPM-2 microforge (ALA Scientific, NY, USA). All recordings were acquired using Clampex software (v10.5/10.6). Analysis for all electrophysiological datasets was performed with Clampfit (v10.5/10.6.2.2) and Graphpad Prism 6 software. mEJPs were further filtered with a 500 Hz Gaussian low-pass filter. A single mEJP template was generated for each cell and used to identify individual mEJPs, and to calculate the mean mEJP amplitude and frequency per cell.

Two-electrode voltage clamp experiments to determine VGCC role in spontaneous SV release

TEVC recordings were performed at room temperature from muscle 4 of abdominal segments A2-A4 (**Figure 2**). Pipettes were filled with 3 mM KCl solution and exhibited resistances between 20 to 30 MΩ. Signals were recorded using a 5 KHz low-pass filter at a sampling frequency of 20 KHz using the Digidata 1440A digitizer (Molecular devices, Sunnyvale, CA, USA) with Clampex (v10.6) software and Axoclamp 900A amplifier (Axon instruments, Union City, CA, USA) with Axoclamp software. Only cells with resting membrane potentials below -49 mV and membrane resistances above 4 MΩ prior to measurements were included in the datasets. TEVC recordings shown in **Figure 2 (A-E and I-M)** were performed at 1.5 mM extracellular $CaCl_2$. For eEJC recordings, specimens were acclimated in the recording chamber for 2 minutes prior to recording in bath solution. For recordings shown in **Figure 2 A-E**, the bath solution contained 1 µM TTX (purple) or the equivalent volume of dH_2O in controls (magenta). Recordings shown in **Figure 2 I-M** were obtained in the presence of 740.7 µM $CdCl_2$ (orange) or the equivalent volume of dH_2O as control (magenta). Cells were clamped at a holding potential of -70 mV and stimulated using a suction electrode as follows. APs were evoked in motoneurons using a S48 stimulator (Grass Technologies, USA) by giving a short (300 µs) depolarizing pulse (8 V stimulation strength). eEJC amplitudes were determined by quantifying the minimal current following an AP. The presence of $CdCl_2$ strongly affected the membrane potential (depolarization). As this electrophysiological investigation of the Ca^{2+}-dependence of spontaneous activity was performed in conjunction with GCaMP recordings in other animals (**Figure 2 F-H and N-P**) where the membrane potential was not manipulated, we aimed to perform TEVC experiments at similar conditions, therefore recording at a holding potential of -55 mV.

Current clamp experiments to determine receptor sensitivity to different SV release modes

For current clamp experiments using PhTx to determine postsynaptic receptor field sensitivity to both release modes (**Figure 3**), the Sylgard block and completed larval preparation was placed in the recording chamber which was filled with 2 ml HL3 (0.4 mM CaCl2, 10 mM MgCl2). Recordings were performed at room temperature in current clamp mode at muscle 6 in segments A2/A3 as previously described (Zhang and Stewart, 2010) using an Axon Digidata 1550A digitizer, Axoclamp 900A amplifier with HS-9A x0.1 headstage (Molecular Devices, CA, USA) and on a BX51WI Olympus microscope with a 40X LUMPlanFL/IR water immersion objective. Sharp intracellular recording electrodes were made with a resistance of 20-35 MΩ and back-filled with 3 M KCl. Cells were only considered with a membrane potential below -60 mV and membrane resistances greater than 4 MΩ. Recordings were acquired using Clampex software (v10.5) and sampled at 10-50 kHz, filtering with a 5 kHz low-pass filter. eEJPs were recorded by stimulating the appropriate nerve at 10 Hz, 100 times (8 V, 300 µs pulse) using an ISO-STIM 01D stimulator (NPI Electronic, Germany).

Spontaneous mEJPs for analysis shown in **Figure 3 (D-F)** were recorded for 30 seconds. 1 ml of solution was then removed without disturbing the preparation or electrodes and 1 ml of HL3 added containing PhTx-433 (Sigma-

Aldrich, MO, USA), mixing gently with the pipette to a final bath concentration of 4 µM PhTx. Spontaneous mEJPs were recorded immediately, again for 30 seconds. Stimulation was performed at 10 Hz for 10 seconds to measure eEJPs or, in the case of control recordings, 10 seconds passed without stimulation. Finally, mEJPs were recorded for 30 seconds.

Pharmacology

Philanthotoxin (PhTx-433) used for experiments in **Figure 3** was obtained from Sigma Aldrich (subsidiary of Merck KGaA, Darmstadt, Germany) and diluted to a stock concentration of 4 mM in dH_2O. In experiments, it was used at a concentration of 4 µM in HL-3 by applying it directly to the bath (see electrophysiology method section). Tetrodotoxin-citrate (TTX) used for experiments shown in **Figure 2** was obtained from Tocris (subsidiary of Bio-Techne, Minneapolis, MN, USA) and diluted (w/v) in dH_2O to a stock concentration of 1 mM. In GCaMP experiments, it was used at a concentration of 1 µM in HL-3 (5 µL 1 mM TTX/dH_2O stock in 4.6 mL HL-3 and 0.4 mL dH_2O, and a corresponding amount of dH_2O in controls), and imaging began after 2 minutes of incubation time. Cadmium dichloride ($CdCl_2$) used for experiments shown in **Figure 2** was obtained from Sigma Aldrich and diluted to a stock concentration of 10 mM in dH_2O, and used at a final concentration of 740.7 µM in HL-3 (1.12 mL 10 mM $CdCl_2$/dH_2O stock in 14 mL HL-3 and a corresponding amount of dH_2O in controls); imaging began after 2 minutes of incubation time. Control experiments were performed using the same amounts of the respective solvent (TTX: dH_2O, $CdCl_2$: dH_2O, PhTx: dH_2O).

Live Calcium-Imaging

GCaMP live imaging experiments were conducted in 2 mL HL-3 containing 1.5 mM $CaCl_2$ (except for Ca^{2+}-titration **supplementary Figure S1-1 C**: 0.4, 0.75, 1.5, 3, 6, 12 mM) on an Olympus BX51WI epifluorescence microscope, using a water immersion LUMFL 60x 1.10 w objective. A Lambda DG-4 (Sutter Instrument Company, Novato CA, USA) white light source was used to illuminate the samples through a GFP excitation/emission filter set. For experiments in **Figure 1 F-I**, **supplementary Figure S4-2 A-C**, and **supplementary Figure S1-1 C**, a newer light source of the same model was used in combination with an Olympus ND25 neutral density filter. Images were acquired in camera-native 16-bit grayscale using an Orca Flash v4 sCMOS camera (Hamamatsu Photonics, Hamamatsu, Japan) under constant illumination with an exposure of 50 ms per frame, resulting in an effective imaging frame rate of 20 Hz. For analysis shown in **Figures 1, 2,** and **4**, spontaneous events were recorded from 1b NMJs in muscle 4, abdominal segments 2-4, for 100 s (120 s in the case of TTX and Cd^{2+} experiments shown in **Figure 2**). For experiments involving the imaging of AP-evoked events in **Figures 1, 2** and **4**, the efferent motoneuronal bundle innervating the same muscle was sucked into a polished glass capillary containing bath HL-3. The glass capillary was held in place by a patch electrode holder (npi electronic, Tamm, Germany), and contained a chlorided silver wire electrode, which connected to a pipette holder (PPH-1P-BNC, npi electronic, Tamm, Germany). After recording of spontaneous events, 36 single stimuli were applied as a square depolarization pulse of 300 µs at 7 V, 0.2 Hz for 180 s using a connected S48 stimulator (Grass Technologies, now part of Natus Medical Inc., Pleasanton, CA, USA). Imaging start/end was controlled by µManager software (version 1.4.20, https://micro-manager.org), and stimulation was administered through software (Clampex 10.5.0.9, Molecular Devices, San Jose, CA, USA) controlling a DA/AD converter (DigiData 1440A, Molecular Devices, San Jose, CA, USA). All videos acquired in 16-bit were then converted to 8-bit using ImageJ (version 1.48q). See section Image processing and analysis for further procedures and details.

Immunohistochemistry

After live imaging experiments, larval tissue was fixated for 7 min at -20°C using fresh Methanol for experiments involving IHC stainings against Unc13A, or for 10 min at RT using fresh 4% PFA in 0.1 mM PBS for all other experiments (i.e. involving IHC for BRP, Syx-1A, ROP, Unc13B). Fixated samples (max. 8 per 1.5 mL sample cup) were then stored in 1 mL 1xPBS until all samples had been collected, but 6 hours at most. Then, off-target epitope blocking was performed in 1xPBS containing 0.05% Triton-X100 (PBS-T) and 5% normal goat serum (NGS) (total volume: 1000 µL) for 45 min on a wheel at RT, 17 rpm. Immediately after, the mix was replaced by an identical mixture and the respective first antibody was added at the following concentrations: mouse Syntaxin-1A 8C3 (1:40, Developmental Studies Hybridoma Bank, University of Iowa, Iowa City, IA, USA), mouse Unc18/ROP (1:500, Developmental Studies Hybridoma Bank, University of Iowa, Iowa City, IA, USA), guinea pig Unc13A (1:500) (Böhme et al., 2016), rabbit Unc13B (1:1000) (Böhme et al., 2016), mouse $BRP^{C\text{-}term}$ (1:1000, Developmental Studies Hybridoma Bank, University of Iowa, Iowa City, IA, USA), rabbit $BRP^{last200}$ (1:1000) (Ullrich et al., 2015). Samples were incubated with the primary antibody overnight at 4°C on a sample wheel. Afterwards, samples were washed four times in PBS-T for 30 min at RT. Secondary antibodies were applied (4 h, RT) in PBS-T containing 5% NGS at the following concentrations: donkey anti guinea pig DyLight 405 (1:500, Jackson ImmunoResearch, West Grove, PA, USA), goat anti mouse Cy3 (1:500, Jackson ImmunoResearch), goat anti rabbit Cy3 (1:500, Jackson ImmunoResearch, West Grove, PA, USA). After this, they were washed with PBS for 30 min and finally mounted on 26x76 mm glass slides (Paul Marienfeld GmbH, Lauda-Königshofen, Germany) in VectaShield (Vector Laboratories, subsidiary of Maravai Life Sciences, San Diego, CA, USA) under 18x18 mm cover glass slides (Carl Roth GmbH, Karlsruhe, Germany) using clear nail polish to seal off the sides of the cover glass slide. The samples were then stored at 4°C and imaged within a week as described in the confocal microscopy and image processing section.

Confocal microscopy and image processing

Confocal imaging of immunohistochemically stained samples was performed on a Leica SP8 confocal quadruple solid-state laser scanning system (excitation wavelengths: 405, 488, 552, 635 nm), and operating on LAS X software (Leica Microsystems, Wetzlar, Germany) with a 63x 1.4 NA oil immersion objective at room temperature. Pixel edge length was 100 nm at a zoom factor of 1.8 and a z-step size of 0.5 µm for all datasets. Care was taken to choose fluorophores with non-overlapping excitation/emission spectra (see immunohistochemistry section), and confocal GCaMP images were always acquired without additional IHC at 488 nm excitation. Single z-stack images from all channels were exported from the proprietary .lif-format into TIF images using LAS AF Lite software (version 2.6.3, Leica Microsystems, Wetzlar, Germany) and converted to 8-bit grayscale maximal projections using ImageJ/Fiji software (version 1.52i).

Image processing and analysis

Stabilization of live-imaging videos

As further analysis of GCaMP live-imaging videos was highly reliant on a stable position of the NMJ over time, all 2D-translational movement (in x,y-direction) of the muscle during the recording had to be corrected for. This was done as shown in Reddy-Alla et al., 2017, and is described in the following. Converting videos of mhc-myr-GCaMP5G from 16-bit to 8-bit grayscale was done in ImageJ.

After conversion from 16-bit to 8-bit, the 8-bit multipage .TIF-video file ('stack') was loaded into MATLAB and a subregion of the first frame, containing the whole GCaMP-positive 1b NMJ, was chosen as a reference for the registration process using the MATLAB function *getrect*. Using the MATLAB function *normxcorr2*, every subsequent frame was then 2D-translated by a simple *x,y*-shift until the highest cross-correlation between pixel values of the current frame and the first frame was achieved. This procedure was repeated for all pairs of the first frame and succeeding frames. For this procedure, all images were Gaussian filtered (MATLAB function *imgaussfilt*) with a sigma value of 5 for noise reduction.

Alignment of confocal images to live-imaging videos

Next, we compensated for fixative-induced anisotropic deformation, orientation and size changes in confocal images by registering them to GCaMP-videos in ImageJ using the plugin "TurboReg" (Biomedical Imaging Group, EPFL, Switzerland; Thévenaz et al., 1998). An affine transformation that used three reference points in each image applied *x,y*-translation, rotation, and *x,y*-shearing where necessary to get the optimal overlay between GCaMP-signal in confocal and live-imaging. The necessary transformation found for the confocal GCaMP image was then applied identically to all other channels.

Quantification of single AZ protein- and activity-levels

In order to quantify protein and activity levels on the level of single AZs, we first defined ROIs in the confocal BRP channel by applying the ImageJ function *find maxima* using threshold values between 10 and 20. Circular ROIs with a diameter of 650 nm were centrally overlaid at all *x,y*-positions found with this procedure. The integrated density (sum of intensities of all pixels whose sub-pixel center lay within the borders of the circle) in all ROIs was then saved for each confocal frame and live-imaging frame in .xls-format for later analysis in MATLAB. Additionally, a file with all corresponding *x,y*-coordinates of all ROIs was saved as a text file. Further, to correct for unspecific background fluorescence decay due to photobleaching, we shifted all ROIs to a region without GCaMP fluorescence and generated another .xls-file containing the fluorescence values in these ROIs over time. These values were later subtracted from the corresponding fluorescence signal in the original ROIs.

We then loaded these files into MATLAB for further analysis. First, we determined all inter-AZ distances (all distances between every possible pair of AZs) using the squared Euclidean distance as shown in equation (1).

$$(1)\quad dist(ROIa, ROIb) = sz_{px} * \sqrt{(d_x(ROIa, ROIb))^2 + (d_y(ROIa, ROIb))^2}$$

In equation (1), *ROIa* and *ROIb* are any of the determined ROIs, sz_{px} is the physical pixel edge length of 0.10833 µm, and d_x and d_y are the vertical or horizontal pixel shift values in x or y, respectively, between both compared ROIs. This resulted in a diagonally symmetrical matrix of all possible inter-AZ distances. This distance was then used to exclude detecting another event within 2.5 µm (evoked activity measurements) or 1000 µm (spontaneous activity measurements) around one event in the same frame. We added another layer of security to exclude the detection of the same event twice by only considering the ROI with the highest amplitude within the given distance threshold and a single frame (each frame representing 20 ms of recording time).

Single AZ protein levels were normalized to a range between 0 and 1 as shown in equation (2). This procedure accounted for inter-experimental variability and allowed the direct comparison of different proteins.

$$(2)\quad Signal_{norm} = \frac{Signal - \min(Signal)}{\max(Signal) - \min(Signal)}$$

The GCaMP fluorescence over time of each ROI was corrected for photobleaching as described before, by subtracting the fluorescence measured in the corresponding background ROI. We then performed a linear fit on each single fluorescence trace over time (separately for spontaneous and AP-evoked activity recordings), yielding two parameters reflecting its slope and y-intercept (MATLAB function *polyfit*). Using these parameters (slope *s* and y-intercept *int*), we performed a baseline correction

for each time step *t* and each *ROI* as shown in equation (3).

(3) $Fluo_{GCaMP,corr}(t, ROI) = Fluo_{GCaMP}(t, ROI) - (t * s(ROI) + int(ROI))$

A custom procedure was then used to detect single peaks in the resulting fluorescence traces. All fluorescence traces were filtered by a 1D-filter using the MATLAB function *filter* (filter width: 5 frames). We then manually evaluated all instances in the fluorescence trace where the mean of the unfiltered signal over three consecutive frames exceeded a threshold of four times the SD of the filtered signal. As stated above, a circular distance threshold of 2.5 µm (evoked activity measurements) or 1000 µm (spontaneous activity measurements) around each event was enforced to avoid unspecific detection of close by events in a single frame. When analyzing evoked activity measurements, we only considered events that were detected within 1 s of the stimulus.

In order to generate activity maps as those shown in **Figure 1 (panels F,H,J,L, and N)**, we counted the number of detected events in each ROI and overlaid an IHC image of the respective protein at the NMJ with circles of corresponding sizes. The average signals shown in **Figure 1, panel E** were generated by averaging all detected events in each cell, and then averaging over all cell means.

The correlation of normalized protein levels and average activity levels per AZ shown in **Figure 1 (panels G,I,K,M, and O)** was done as follows. First, we counted the number of events for each AZ as done for the activity maps. We then sorted the list of event numbers and the list of AZ intensities by ascending intensity. Then, the lists were binned into four bins so that each bin contained the same amount of AZs. In each bin, we then averaged the fluorescence of all AZs and the corresponding number of events, yielding the average number of events per AZ intensity bin. For the graphs shown in **Figure 4 (C&D)** and **supplementary Figure S4-2 (panels A&B)** we further divided the spontaneous events per AZ by the recording time (100 s) and the evoked events per AZ by the number of stimuli (36 APs).

Spontaneous event detection between evoked events

Besides the "sequential" way of analyzing spontaneous activity measurements and then evoked activity measurements as described above, we also quantified spontaneous events that happened between stimuli ("interleaved") as shown in **Figure 4 (panel D)** and supplementary **Figure S4-2 (panel B)**. For this, we altered the procedure described above by one detail. While everything else happened as in our conventional approach to measure spontaneous activity, we suppressed the detection of evoked events and instead quantified SV release between stimuli by creating an exclusion list. This list included all time points 200 ms before and 500 ms after the stimulus, within which no fluorescence peaks would be considered as a signal. To account for the differing time over which spontaneous events were recorded (100 s in sequential analysis vs. 154.8 s in interleaved analysis), we divided all activity levels by the respective recording time.

Survival analysis

To analyze how many spontaneously active ROIs would "survive", or maintain their exclusively spontaneous state by not showing any evoked activity in the evoked activity measurement (**supplementary Figure S4-1 E**), we proceeded as follows. We loaded the results from the analysis of spontaneous and evoked activity measurements (described above) containing all activity time points and AZ identities of spontaneous or evoked events into MATLAB. We then first found the number and identity of all AZs showing spontaneous activity. We created a data vector containing as many data points as we had frames in the evoked activity recording (3600 over 180 s) and filled all positions with the number of AZs showing spontaneous activity we had found. Then, we found all time points of evoked events in these AZs and subtracted 1 from the previously created vector at the time points of the evoked event to the end of the vector, resulting in a decreasing amount of exclusively spontaneously active AZs over the time of the evoked activity measurement. For each cell, we then set the initial amount of exclusively spontaneously active AZs in that cell to 1 (100 %).

Automated spontaneous event detection

For the automated detection of spontaneous vesicle fusion without respect to AZ positions shown in **Supplementary Figures S1-1 C** and **S1-3** we developed a set of custom MATLAB code. Single steps and results of the whole procedure on a single event are shown in **Supplementary Figure S1-2**. Stabilized 8-bit grey scale multipage .TIF-video files (**Figure S1-2 A**) were loaded into MATLAB, where the user could then manually select an area of the video with the NMJ of interest. Using the MATLAB function *bwboundaries*, a logical mask was then generated to find all pixels within the manually selected ROI. The chosen area was then extended by 20 pixels to each side, generating a rectangular selection taken from the original video. This cropped video was then further processed by slightly reducing noise using the *medfilt3* function (**Figure S1-2 B**), which smoothes noise in 3D arrays by taking the median grey value in a 3x3x3 pixel neighborhood. Next, the background was subtracted to leave only transient increases in fluorescence. For this, a maximum projection of 10 closely preceding frames was generated for every frame of the video, which was then subtracted from the current frame, where every resulting negative value was set to 0 (**Figure S1-2 C**). To avoid removing parts of an event, a 'lag' of 5 frames was included before the currently observed frame, resulting in a sequence of frames from the 15th to 6th before the current frame for the background subtraction. Every iteration of this process resulted in a single frame that was devoid of any basal GCaMP signal and excessive noise, only leaving transient fluorescence peaks that deviated from the brightest features of the last

15th through 6th frames. In addition to this background-subtracted video, another one was generated with the only difference being that here, instead of the maximum projection of 10 frames, an average projection of the same 10 frames was used to subtract the background. This video was then used for the exact determination of events by a 2D-Gaussian fit as described further down. A Gaussian filter (function *imgaussfilt* with a sigma of 3 pixels) was then applied to the resulting video for further noise removal (**Figure S1-2 D**). This was necessary for the next step, in which regions of connected (continuously bright) pixels above a threshold grey value of 2, and within the manual selection, were identified (**Figure S1-2 E**). For each of the identified regions, the median x,y-coordinates were found and temporarily defined as the location of the event (**Figure S1-2 F**). Detected events within 10 pixels of the edge of the video were removed, as they represented noise and were located outside the manual NMJ selection. A Gaussian fit was then performed on the second background-subtracted video, where the average of the 15th to 6th preceding frame was subtracted from the current frame (**Figure S1-2 G**), as follows. A 2D-Gaussian was simulated (the 'simulated image', **Figure S1-2 H**) and fit to a maximal projection of six frames of an event (the 'temporary image'). An optimization procedure with the MATLAB function *fminsearch* was used to find the best parameters for the center x,y-coordinate of the Gaussian, its amplitude, its sigma value, and the baseline. An initial value of 20 was chosen for all five parameters. As a measure of the quality of the fit, a cost function was used that calculated the difference between the temporary image and the simulated image by subtracting them. As the success of *fminsearch* depends, among other factors, on the initial parameters, the optimization was additionally repeated twice with the best fit values of the previous run. The same optimization procedure with a global optimization algorithm yielded the same results at vastly longer processing times.

The analysis of spontaneous event amplitudes over increasing calcium concentrations shown in **Supplementary Figure S1-1 C** was performed in *Mhc-myrGCaMP5G/+* larvae with the script described above at $[Ca^{2+}]_{ext.}$ of 0.4, 0.75, 1.5, 3, 6 and 12 mM in HL3 by exchanging the bath solutions between recordings in one animal. The nonlinear fit on the cell-wise means was performed by assuming a Hill-relationship, where binding of Ca^{2+} to the sensor occurs with cooperativity h, and half-maximal fluorescence is reached at a concentration of $[Ca^{2+}]_{ext.}$ (K_A) as shown in equation (4). In that equation, F_{max} is the asymptotic maximal value of fluorescence at high $[Ca^{2+}]_{ext.}$, and C is a baseline correction to allow a baseline fluorescence different from 0.

$$(4)\ F([Ca^{2+}]_{ext}) = F_{max} * \frac{[Ca^{2+}]_{ext}{}^{h}}{K_A{}^{h} + [Ca^{2+}]_{ext}{}^{h}} + C$$

References

Alabi, A. A. and Tsien, R. W. (2012). Synaptic vesicle pools and dynamics. Cold Spring Harbor perspectives in biology *4*, a013680.

Atasoy, D., Ertunc, M., Moulder, K. L., Blackwell, J., Chung, C., Su, J., and Kavalali, E. T. (2008). Spontaneous and evoked glutamate release activates two populations of NMDA receptors with limited overlap. Journal of Neuroscience *28*, 10151–10166.

Böhme, M. A., Beis, C., Reddy-Alla, S., Reynolds, E., Mampell, M. M., Grasskamp, A. T., Lützkendorf, J., Bergeron, D. D., Driller, J. H., Babikir, H., et al. (2016). Active zone scaffolds differentially accumulate Unc13 isoforms to tune Ca(2+) channel-vesicle coupling. Nature neuroscience *19*, 1311–1320.

Böhme, M. A., Grasskamp, A. T., and Walter, A. M. (2018). Regulation of synaptic release-site Ca2+ channel coupling as a mechanism to control release probability and short-term plasticity. FEBS letters *592*, 3516–3531.

Böhme, M. A., McCarthy, A. W., Grasskamp, A. T., Beuschel, C. B., Goel, P., Jusyte, M., Laber, D., Huang, S., Rey, U., Petzoldt, A. G., et al. (2019). Rapid active zone remodeling consolidates presynaptic potentiation. Nat Commun *10*, 1–16.

Brenner, S. (1974). The Genetics of CAENORHABDITIS ELEGANS. Genetics *77*, 71–94.

Brose, N., Rosenmund, C., and Rettig, J. (2000). Regulation of transmitter release by Unc-13 and its homologues. Current opinion in neurobiology *10*, 303–311.

Chang, H., Ciani, S., and Kidokoro, Y. (1994). Ion permeation properties of the glutamate receptor channel in cultured embryonic Drosophila myotubes. The Journal of physiology *476*, 1–16.

Cornelisse, L. N., Tsivtsivadze, E., Meijer, M., Dijkstra, T. M. H., Heskes, T., and Verhage, M. (2012). Molecular machines in the synapse: overlapping protein sets control distinct steps in neurosecretion. PLoS computational biology *8*, e1002450.

Davis, G. W. and Müller, M. (2015). Homeostatic control of presynaptic neurotransmitter release. Annual review of physiology *77*, 251–270.

Dittman, J. S. (2019). Unc13: a multifunctional synaptic marvel. Current opinion in neurobiology *57*, 17–25.

Ermolyuk, Y. S., Alder, F. G., Surges, R., Pavlov, I. Y., Timofeeva, Y., Kullmann, D. M., and Volynski, K. E. (2013). Differential triggering of spontaneous glutamate release by P/Q-, N- and R-type Ca2+ channels. Nature neuroscience *16*, 1754–1763.

Fouquet, W., Owald, D., Wichmann, C., Mertel, S., Depner, H., Dyba, M., Hallermann, S., Kittel, R. J., Eimer, S., and Sigrist, S. J. (2009). Maturation of active zone assembly by Drosophila Bruchpilot. The Journal of cell biology *186*, 129–145.

Frank, C. A., Kennedy, M. J., Goold, C. P., Marek, K. W., and Davis, G. W. (2006). Mechanisms underlying the rapid induction and sustained expression of synaptic homeostasis. Neuron *52*, 663–677.

Fulterer, A., Andlauer, T. F. M., Ender, A., Maglione, M., Eyring, K., Woitkuhn, J., Lehmann, M., Matkovic-Rachid, T., Geiger, J. R. P., Walter, A. M., et al. (2018). Active Zone Scaffold Protein Ratios Tune Functional Diversity across Brain Synapses. Cell reports *23*, 1259–1274.

Goel, P., Dufour Bergeron, D., Böhme, M. A., Nunnelly, L., Lehmann, M., Buser, C., Walter, A. M., Sigrist, S. J., and Dickman, D. (2019). Homeostatic scaling of active zone scaffolds maintains global synaptic strength. The Journal of cell biology *218*, 1706–1724.

Gratz, S. J., Goel, P., Bruckner, J. J., Hernandez, R. X., Khateeb, K., Macleod, G. T., Dickman, D., and O'Connor-Giles, K. M. (2019). Endogenous Tagging Reveals Differential Regulation of Ca2+ Channels at Single Active Zones during Presynaptic Homeostatic Potentiation and Depression. Journal of Neuroscience *39*, 2416–2429.

Groemer, T. W. and Klingauf, J. (2007). Synaptic vesicles recycling spontaneously and during activity belong to the same vesicle pool. Nature neuroscience *10*, 145–147.

Guerrero, G., Reiff, D. F., Rieff, D. F., Agarwal, G., Ball, R. W., Borst, A., Goodman, C. S., and Isacoff, E. Y. (2005). Heterogeneity in synaptic transmission along a Drosophila larval motor axon. Nature neuroscience *8*, 1188–1196.

Harris, K. P. and Littleton, J. T. (2015). Transmission, Development, and Plasticity of Synapses. Genetics *201*, 345–375.

Hille, B. (1968). Pharmacological modifications of the sodium channels of frog nerve. The Journal of general physiology *51*, 199–219.

Hodgkin, A. L. and Huxley, A. F. (1952). A quantitative description of membrane current and its application to conduction and excitation in nerve. The Journal of physiology *117*, 500–544.

Kaeser, P. S. and Regehr, W. G. (2014). Molecular mechanisms for synchronous, asynchronous, and spontaneous neurotransmitter release. Annual review of physiology *76*, 333–363.

Kavalali, E. T. (2015). The mechanisms and functions of spontaneous neurotransmitter release. Nature reviews. Neuroscience *16*, 5–16.

Kavalali, E. T. and Plummer, M. R. (1996). Multiple voltage-dependent mechanisms potentiate calcium channel activity in hippocampal neurons. Journal of Neuroscience *16*, 1072–1082.

Kavalali, E. T., Zhuo, M., Bito, H., and Tsien, R. W. (1997). Dendritic Ca2+ channels characterized by recordings from isolated hippocampal dendritic segments. Neuron *18*, 651–663.

Kittel, R. J., Wichmann, C., Rasse, T. M., Fouquet, W., Schmidt, M., Schmid, A., Wagh, D. A., Pawlu, C., Kellner, R. R., Willig, K. I., et al. (2006). Bruchpilot promotes active zone assembly, Ca2+ channel clustering, and vesicle release. Science *312*, 1051–1054.

Littleton, J.T., Stern, M., Schulze, K., Perin, M., and Bellen, H. J. (1993). Mutational analysis of Drosophila synaptotagmin demonstrates its essential role in Ca2+-activated neurotransmitter release. Cell *74*, 1125–1134.

Magee, J. C. and Johnston, D. (1995). Synaptic activation of voltage-gated channels in the dendrites of hippocampal pyramidal neurons. Science *268*, 301–304.

Melom, J. E., Akbergenova, Y., Gavornik, J. P., and Littleton, J. T. (2013). Spontaneous and evoked release are independently regulated at individual active zones. Journal of Neuroscience *33*, 17253–17263.

Misura, K. M., Scheller, R. H., and Weis, W. I. (2000). Three-dimensional structure of the neuronal-Sec1-syntaxin 1a complex. Nature *404*, 355–362.

Muhammad, K., Reddy-Alla, S., Driller, J. H., Schreiner, D., Rey, U., Böhme, M. A., Hollmann, C., Ramesh, N., Depner, H., Lützkendorf, J., et al. (2015). Presynaptic spinophilin tunes neurexin signalling to control active zone architecture and function. Nature communications *6*, 8362.

Nakamura, Y., Nakajima, S., and Grundfest, H. (1965). The action of tetrodotoxin on electrogenic components of squid giant axons. The Journal of general physiology *48*, 975–996.

Newman, Z. L., Hoagland, A., Aghi, K., Worden, K., Levy, S. L., Son, J. H., Lee, L. P., and Isacoff, E. Y. (2017). Input-Specific Plasticity and Homeostasis at the Drosophila Larval Neuromuscular Junction. Neuron *93*, 1388-1404.e10.

Pang, Z. P., Bacaj, T., Yang, X., Zhou, P., Xu, W., and Südhof, T. C. (2011). Doc2 supports spontaneous synaptic transmission by a Ca(2+)-independent mechanism. Neuron *70*, 244–251.

Peled, E. S. and Isacoff, E. Y. (2011). Optical quantal analysis of synaptic transmission in wild-type and rab3-mutant Drosophila motor axons. Nature neuroscience *14*, 519–526.

Peled, E. S., Newman, Z. L., and Isacoff, E. Y. (2014). Evoked and spontaneous transmission favored by distinct sets of synapses. Current Biology *24*, 484–493.

Qin, G., Schwarz, T., Kittel, R. J., Schmid, A., Rasse, T. M., Kappei, D., Ponimaskin, E., Heckmann, M., and Sigrist, S. J. (2005). Four different subunits are essential for expressing the synaptic glutamate receptor at neuromuscular junctions of Drosophila. Journal of Neuroscience *25*, 3209–3218.

Ramirez, D. M. O. and Kavalali, E. T. (2011). Differential regulation of spontaneous and evoked neurotransmitter release at central synapses. Current opinion in neurobiology *21*, 275–282.

Reddy-Alla, S., Böhme, M. A., Reynolds, E., Beis, C., Grasskamp, A. T., Mampell, M. M., Maglione, M., Jusyte, M., Rey, U., Babikir, H., et al. (2017). Stable Positioning of Unc13 Restricts Synaptic Vesicle Fusion to Defined Release Sites to Promote Synchronous Neurotransmission. Neuron *95*, 1350-1364.e12.

Rizo, J. (2018). Mechanism of neurotransmitter release coming into focus. Protein science : a publication of the Protein Society *27*, 1364–1391.

Rizo, J. and Rosenmund, C. (2008). Synaptic vesicle fusion. Nature structural & molecular biology *15*, 665–674.

Sakamoto, H., Ariyoshi, T., Kimpara, N., Sugao, K., Taiko, I., Takikawa, K., Asanuma, D., Namiki, S., and Hirose, K. (2018). Synaptic weight set by Munc13-1 supramolecular assemblies. Nature neuroscience *21*, 41–49.

Schneggenburger, R. and Rosenmund, C. (2015). Molecular mechanisms governing Ca(2+) regulation of evoked and spontaneous release. Nature neuroscience *18*, 935–941.

Shahrezaei, V., Cao, A., and Delaney, K. R. (2006). Ca2+ from one or two channels controls fusion of a single vesicle at the frog neuromuscular junction. Journal of Neuroscience *26*, 13240–13249.

Sigrist, S. J., Reiff, D. F., Thiel, P. R., Steinert, J. R., and Schuster, C. M. (2003). Experience-dependent strengthening of Drosophila neuromuscular junctions. Journal of Neuroscience *23*, 6546–6556.

Stewart, B., Atwood, H. L., Renger, J. J., Wang, J., and Wu, C. F. (1994). Improved stability of Drosophila larval neuromuscular preparations in haemolymph-like physiological solutions. Journal of comparative physiology. A, Sensory, neural, and behavioral physiology *175*, 179–191.

Südhof, T. C. (2012). Calcium control of neurotransmitter release. Cold Spring Harbor perspectives in biology *4*, a011353.

Südhof, T. C. (2013). Neurotransmitter release: the last millisecond in the life of a synaptic vesicle. Neuron *80*, 675–690.

Südhof, T. C. and Rothman, J. E. (2009). Membrane fusion: grappling with SNARE and SM proteins. Science (New York, N.Y.) *323*, 474–477.

Thévenaz, P., Ruttimann, U. E., and Unser, M. (1998). A pyramid approach to subpixel registration based on intensity. IEEE transactions on image processing : a publication of the IEEE Signal Processing Society *7*, 27–41.

Ullrich, A., Böhme, M. A., Schöneberg, J., Depner, H., Sigrist, S. J., and Noé, F. (2015). Dynamical Organization of Syntaxin-1A at the Presynaptic Active Zone. PLoS computational biology *11*, e1004407.

Walter, A. M., Haucke, V., and Sigrist, S. J. (2014). Neurotransmission: spontaneous and evoked release filing for divorce. Current Biology *24*, R192-4.

Xu, J., Pang, Z. P., Shin, O.-H., and Südhof, T. C. (2009). Synaptotagmin-1 functions as a Ca2+ sensor for spontaneous release. Nature neuroscience *12*, 759–766.

Yoshihara, M., Adolfsen, B., and Littleton, J. T. (2003). Is synaptotagmin the calcium sensor? Current opinion in neurobiology *13*, 315–323.

Zhang, B. and Stewart, B. (2010). Electrophysiological recording from Drosophila larval body-wall muscles. Cold Spring Harbor protocols *2010*, pdb.prot5487.

Supplementary Material

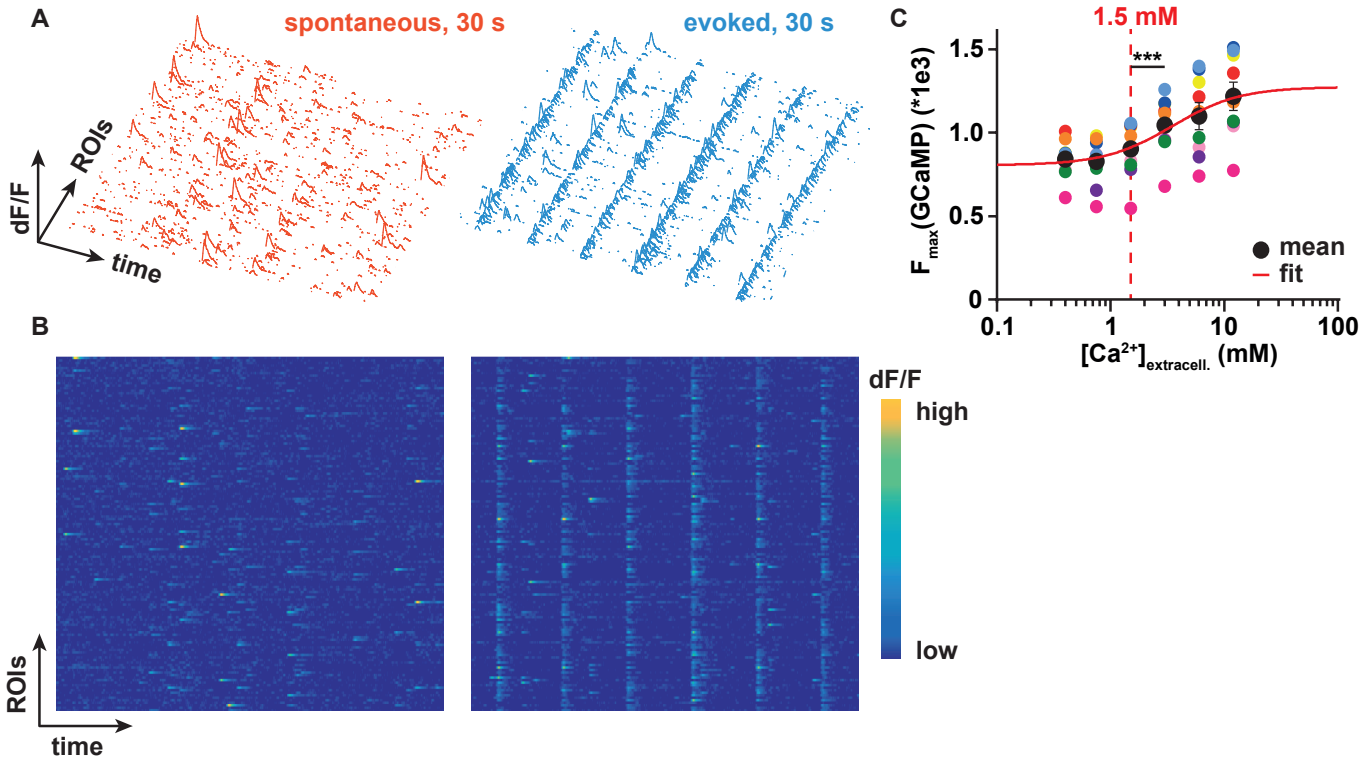

Supplementary Figure S1-1. Single AZ fluorescence traces in both transmission modes and non-saturating spontaneous event amplitudes. (A) 3D representation of 30 s of spontaneous (orange) and evoked (blue) event amplitudes over all ROIs in one NMJ **(B)** 2D color map representation of data shown in (A). **(C)** Quantification of spontaneous event amplitudes over six extracellular Ca^{2+} concentrations (0.4, 0.75, 1.5, 3, 6, 12 mM) shows no saturation at physiological 1.5 mM $[Ca^{2+}]_{ext.}$ (N = 9 cells&animals). Red line represents hill curve fit on individual values. Data is shown as cell-wise mean (colored dots) or mean±SEM (black).

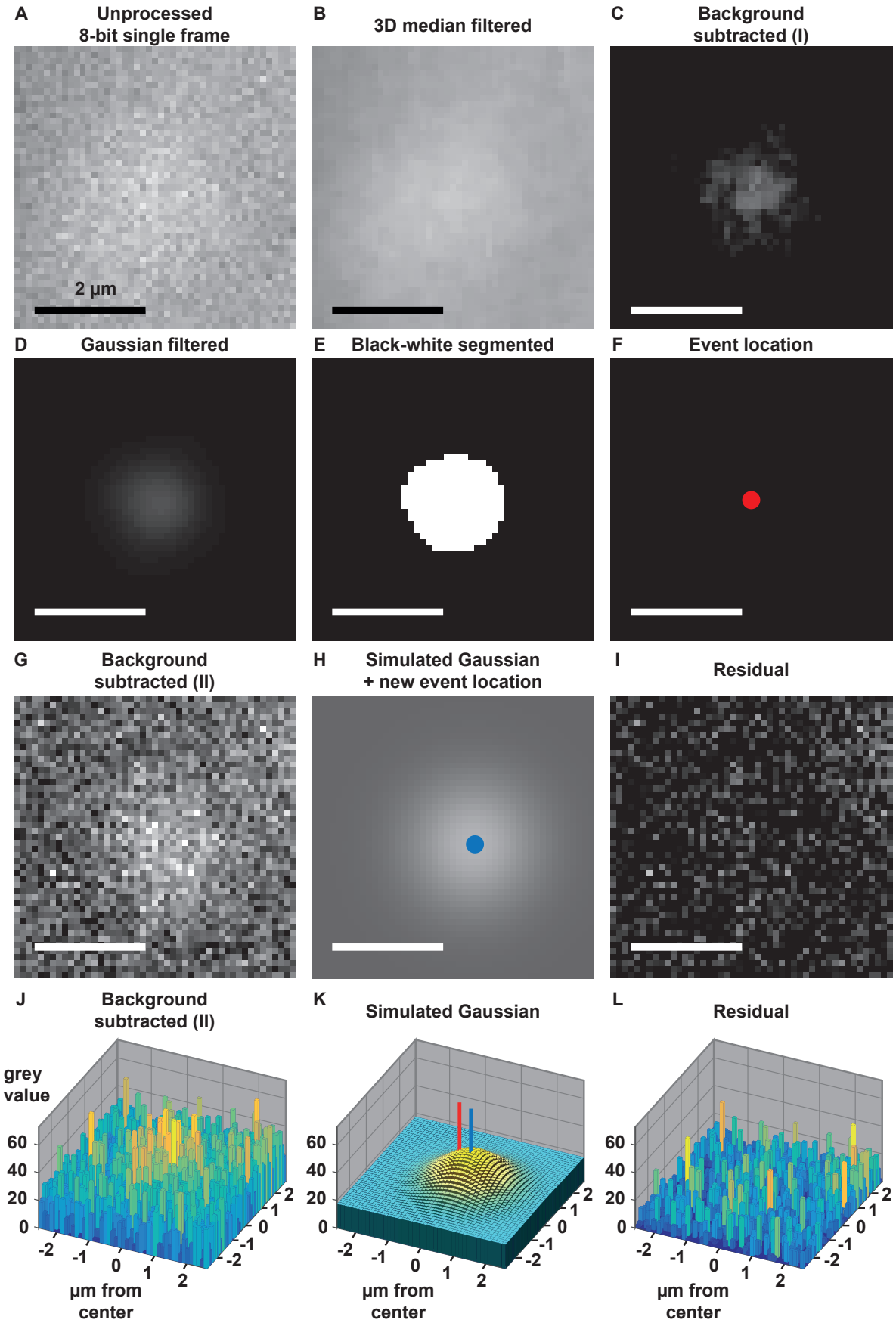

Supplementary Figure S1–2. Sequence of the event detection algorithm. (A) 47x47 pixel cutout from the original, 8-bit video showing a typical spontaneous event. **(B)** Image from A after 3D median filtering for noise reduction. **(C)** Image from B after subtraction of brightest features of the 10th through 6th preceding frames. **(D)** Image from C after application of a Gaussian filter for noise reduction. **(E)** Image from D segmented into grey values below or equal to 2 (black) or greater (white). **(F)** Determined location of the event. **(G)** Maximum projection of 6 frames from original video A after subtraction of average features of the 10th through 6th preceding frames. **(H)** 2D Gaussian fit to G. **(I)** Residual of Gaussian fit: Result of subtracting H from G. **(J)-(L)** 3D representations of images in G-I. Scale bar: 2 µm

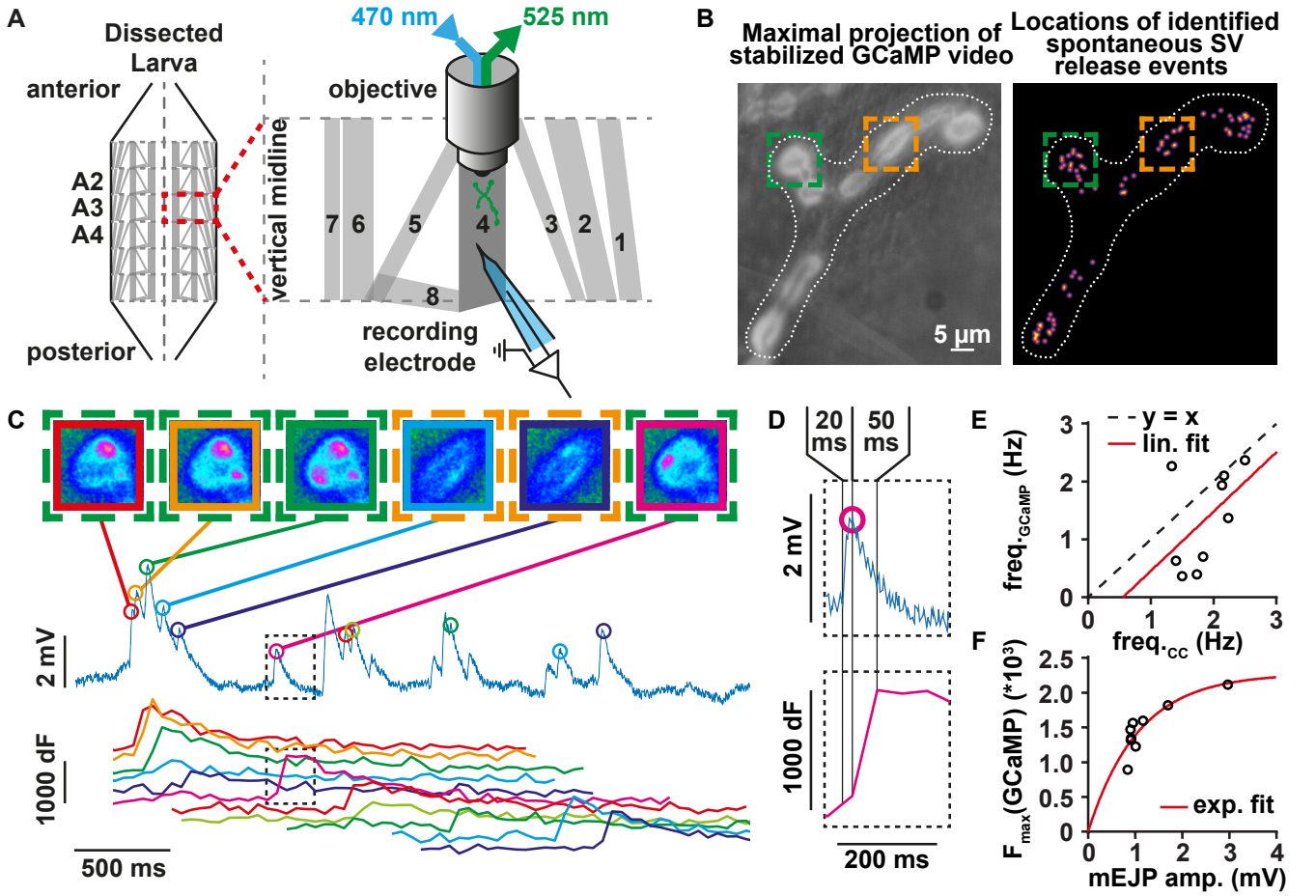

Supplementary Figure S1–3. Concurrent electrophysiological and optical measurements. **(A)** Scheme of the experimental setup; current clamp recordings and GCaMP fluorescence measurements are performed in the same muscle 4 NMJ. **(B)** Spontaneous event detection in GCaMP fluorescence assay independent of BRP (see methods section and **supp. Figure S1-2** for details). Two ROIs over active boutons are marked in green and orange. **(C)** Events detected in current-clamp recordings and GCaMP fluorescence assay coincide to a large degree. Spontaneous events in bouton ROIs marked in **B** are observable with high spatial and temporal resolution **(D)** Blow-up of black ROI in **C** to show details of the temporal quality of current-clamp and fluorescence measurements. **(E)** Cell-wise (N = 9 cells&animals) spontaneous event frequencies measured in current-clamp recordings plotted against frequencies measured in fluorescence recordings. Linear fit on cell means in red, dashed black line represents x = y. **(F)** Cell-wise (N = 9 cells&animals) mEJP amplitudes measured in current-clamp plotted against maximal fluorescence amplitudes measured in fluorescence assay. Exponential fit on cell means in red. Scale bar in **B**: 5 µm

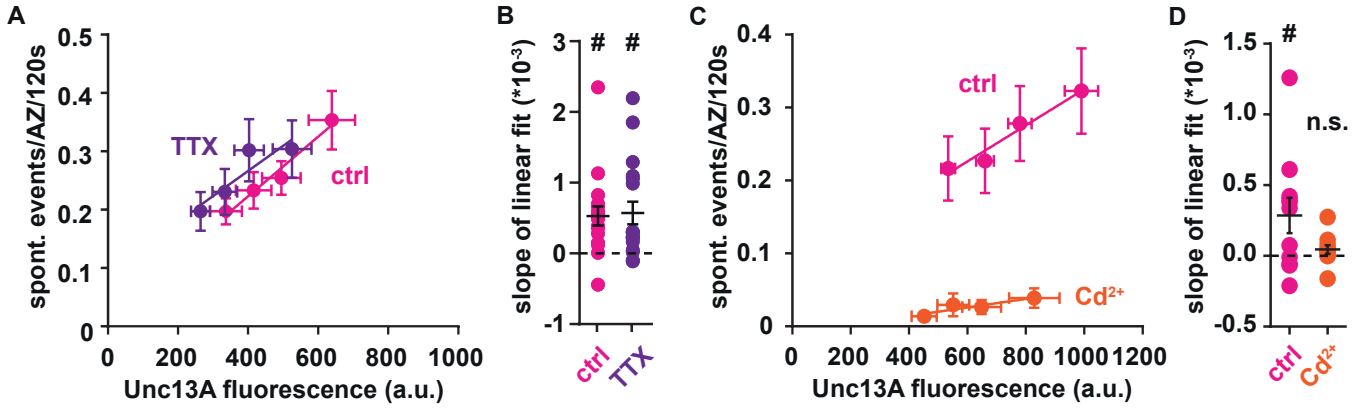

Supplementary Figure S2. Dependence of spontaneous activity under pharmacological block of VGSCs or VGCCs. **(A)** Binned absolute Unc13A fluorescence values plotted against binned single AZ spontaneous activity levels in either control (magenta) or TTX (purple) conditions. **(B)** Quantification of slopes on individual cells (N = 18 animals) **(C)** Binned absolute Unc13A fluorescence values plotted against binned single AZ spontaneous activity levels in either control (magenta) or Cd^{2+} (orange) conditions **(D)** Quantification of slopes on individual cells (N = 11 animals). All mean values are represented as mean±SEM. Comparison in B&D: One sample t-test against hypothetical slope of 0. # $p<0.05$; n.s. not significant. Refer to statistics table for details on mean values and testing.

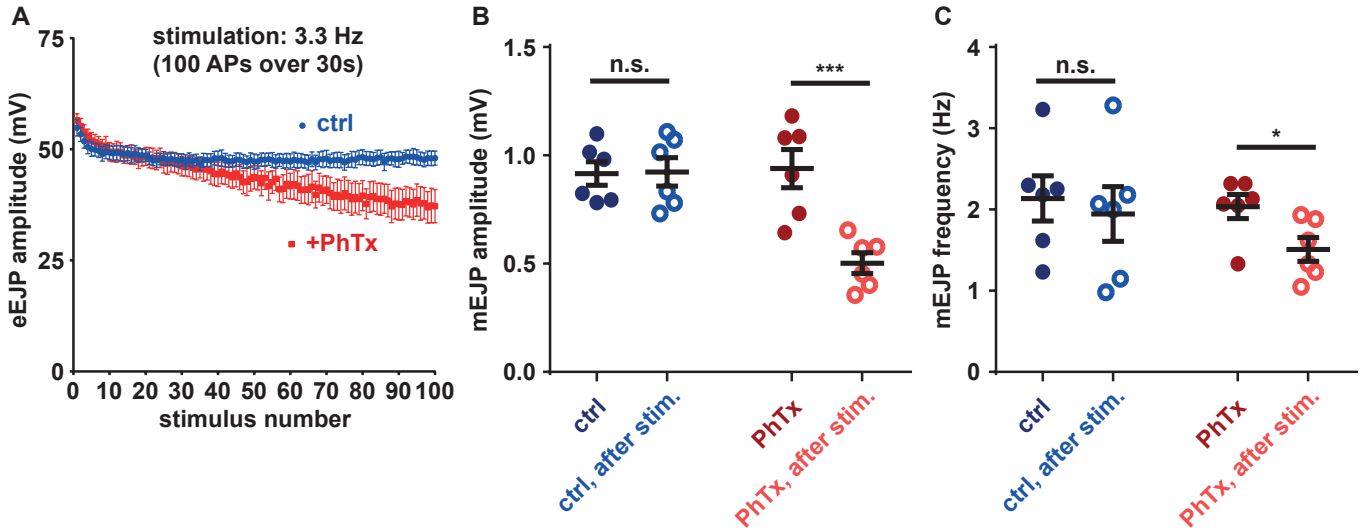

Supplementary Figure S3. Current clamp measurements of PhTx and AP-stimulation influence on mEJPs/eEJPs. **(A)** Sequential quantification of eEJP amplitudes over 100 stimuli applied at 3.3 Hz in either control (ctrl, blue) or PhTx (red, 4 µM PhTx) treatment. **(B)** Quantification of mEJP amplitudes before and after application of 100 stimuli at 3.3 Hz, in either ctrl (blue - ctrl: 0.9160±0.05442 mV; light blue - ctrl, after stim: 0.9233±0.06565 mV; p = 0.9089) or PhTx (red - PhTx: 0.9389±0.08801 mV; light red - PhTx, after stim: 0.5025±0.04765 mV; p = 0.0003) conditions (N = 6 cells&animals) **(C)** Quantification of mEJP frequency, same conditions as in (B) (blue - ctrl: 2.136±0.2787 Hz; light blue - ctrl, after stim: 1.944±0.3378 Hz; p = 0.0591; red - PhTx: 2.036±0.1485 Hz; light red - PhTx, after stim: 1.508±0.1471 Hz; p = 0.0208) (N = 6 cells&animals). Comparison in panels B and C: paired parametric t-test; *p<0.05; ***p<0.001; n.s. not significant. All mean values are represented as mean±SEM. Refer to statistics table for details on mean values and testing.

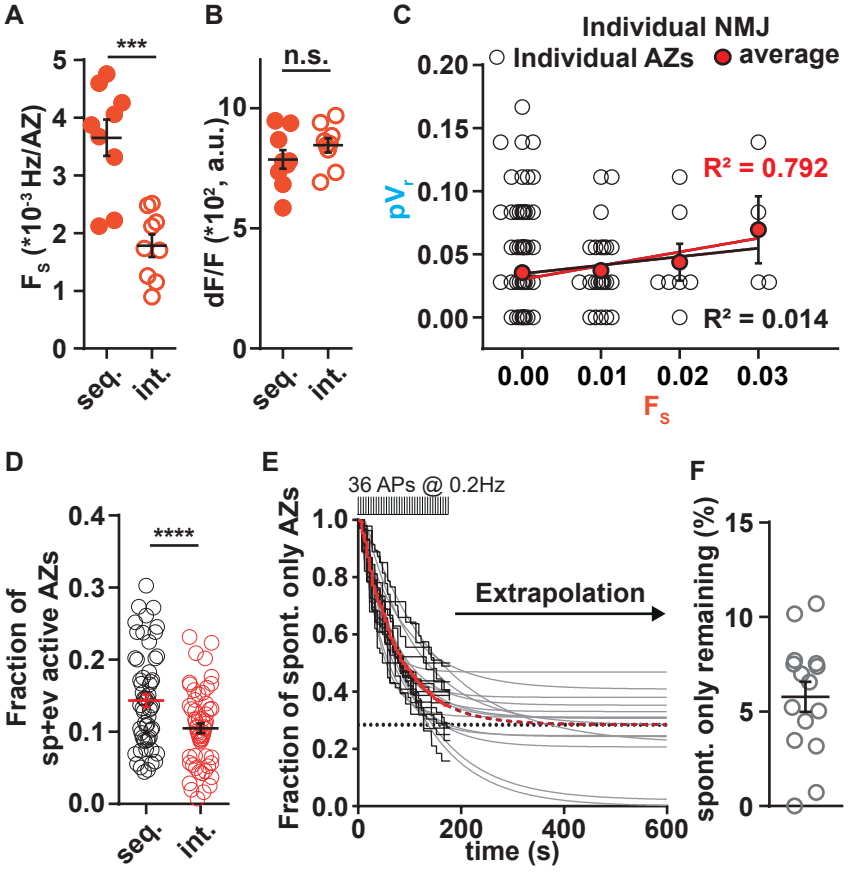

Supplementary Figure S4–1. (A) Cell-wise quantification of spontaneous event frequency per AZ. Paired parametric t-test of seq. (0.003654±0.0003165) vs. int. (0.001784±0.0001964): p = 0.0003. (N = 9 animals) **(B)** Cell-wise spontaneous event amplitude quantification. Paired parametric t-test of seq. (786.8±39.04 dF/F) vs. int (845.5±29.48 dF/F): p = 0.1274. (N = 9 animals) **(C)** Single NMJ AZ-wise analysis of spontaneous event frequency vs SV release probability (N = 148 AZs, N = 1 animal) Black hollow dots represent single AZs; Black line: linear fit through all replicates, $R^2 = 0.014$; red line: linear fit through mean values (red dots), $R^2 = 0.792$. **(D)** Cell-wise quantification (N = 59 animals) of AZs active in both spontaneous and AP-evoked NT release either in sequential (black, mean: 0.1433±0.008586) or interleaved (red, mean: 0.1048±0.006805) measurement. p<0.0001 **(E)** Cell-wise (N =15 animals) survival analysis of all exclusively spontaneously active AZs during application of 36 APs at 0.2 Hz. (plateau value: 0.2661±0.04037). A fraction of 1 represents all AZs spontaneously active before AP application. **(F)** Fraction of exclusively spontaneously active AZs in relation to all AZs (mean value: 0.05774±0.007911). All mean values are represented as mean±SEM. Comparison in panels A, B and D: paired parametric t-test; ***p<0.001; ****p<0.0001; n.s. not significant. Refer to statistics table for details on mean values and testing.

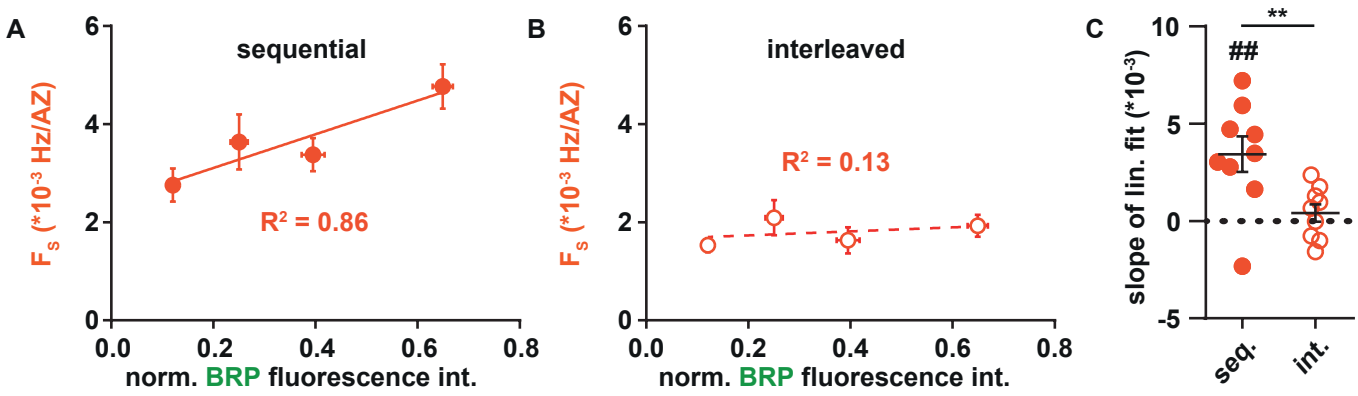

Supplementary Figure S4–2. (**A**) "Sequential" experiment: Binned normalized BRP fluorescence plotted against spontaneous event frequency per AZ in these bins. Solid line: linear fit on mean values, $R^2 = 0.8552$ (N = 9 animals). (**B**) "Interleaved" experiment: Binned normalized BRP fluorescence plotted against spontaneous event frequency per AZ in these bins. Dashed line: linear fit on mean values, $R^2 = 0.1283$ (N = 9 animals). (**C**) Cell-wise (N = 9 animals) quantification of linear fit slopes. Significant difference from zero: seq. 0.003435±0.0009145; p=0.0056; int. 0.0004099±0.0004456; p = 0.3846. Paired parametric t-test of seq. vs. int.: p = 0.0041. **/## p<0.01; All mean values are represented as mean±SEM. Refer to statistics table for details on mean values and testing.

Figure	Panel	Group	Measure	Mean	SEM	Test type	Comment	alpha of test against 0	N (animals)	R² of lin. fit on means	R² of lin. fit on indiv. values	slope of lin. fit on means	slope of lin. fit on indiv. values
1	G	BRP	norm. fluorescence intensity (BRP)	0.1501747	0.0133355				15				
				0.283389	0.016424				15				
				0.415631	0.018312				15				
				0.638101	0.019565				15				
			avg. spontaneous events/AZ	0.218978	0.0292645				15	0.9315	0.1613	0.3298 ± 0.06325	0.3430 ± 0.08084
				0.2483379	0.03778524				15				
				0.2678991	0.03624079				15				
				0.3813965	0.03961334				15				
			avg. evoked events/AZ	0.8784386	0.07004075				15	0.9727	0.3193	1.124 ± 0.1332	1.117 ± 0.1850
				1.103367	0.07644235				15				
				1.24902	0.08996777				15				
				1.439836	0.07600868				15				
			slopes of linear fits on evoked activity	1.117	0.185	One sample t-test against 0		< 0.0001	15				
			slopes of linear fits on spont. activity	0.343	0.08084			0.0008	15				

Figure	Panel	Group	Measure	Mean	SEM	Test type	Comment	alpha of test against 0	N (animals)	R² of lin. fit on means	R² of lin. fit on indiv. values	slope of lin. fit on means	slope of lin. fit on indiv. values
1	I	Unc13A	norm. fluorescence intensity (Unc13A)	0.1622362	0.0173113				15				
				0.307401	0.018919				15				
				0.440075	0.020381				15				
				0.665783	0.019603				15				
			avg. spontaneous events/AZ	0.1979672	0.02489092				15	0.8846	0.1981	0.3710 ± 0.09799	0.3686 ± 0.07304
				0.2646663	0.03863161				15				
				0.2533061	0.03663702				15				
				0.3969627	0.04275438				15				
			avg. evoked events/AZ	0.87284	0.07232647				15	0.969	0.3493	1.084 ± 0.1943	1.075 ± 0.1054
				1.124079	0.05934022				15				
				1.231124	0.09132861				15				
				1.438935	0.06324529				15				
			slopes of linear fits on evoked activity	1.075	0.1054	One sample t-test against 0		< 0.0001	15				
			slopes of linear fits on spont. activity	0.3686	0.07304			0.0002	15				

Figure	Panel	Group	Measure	Mean	SEM	Test type	Comment	alpha of test against 0	N (animals)	R² of lin. fit on means	R² of lin. fit on indiv. values	slope of lin. fit on means	slope of lin. fit on indiv. values
1	K	Unc13B	norm. fluorescence intensity (Unc13B)	0.176638	0.009345				19				
				0.32257	0.011295				19				
				0.447253	0.013443				19				
				0.633093	0.014828				19				
			avg. spontaneous events/AZ	0.3090562	0.04134119				19	0.253	0.007589	0.08181 ± 0.09939	0.09543 ± 0.08016
				0.2729507	0.03275595				19				
				0.3464497	0.03653378				19				
				0.3284572	0.0349623				19				
			avg. evoked events/AZ	0.7303309	0.07986292				19	0.7504	0.01319	0.2307 ± 0.09409	0.2418 ± 0.1545
				0.7687393	0.06644706				19				
				0.8414298	0.08246355				19				
				0.8263869	0.08459458				19				
			slopes of linear fits on evoked activity	0.2418	0.1545	One sample t-test against 0		0.2493	19				
			slopes of linear fits on spont. activity	0.09543	0.08016			0.1349	19				

Supplementary Data relating to Figure 1, panels G,I,K

Figure	Panel	Group	Measure	Mean	SEM	Test type	Comment	alpha of test against 0	N (animals)	R² of lin. fit on means	R² of lin. fit on indiv. values	slope of lin. fit on means	slope of lin. fit on indiv. values
1	M	Syx-1A	norm. fluorescence intensity (Syx-1A)	0.169753	0.018402				10				
				0.32985	0.023114				10				
				0.448273	0.025404				10				
				0.641375	0.025084				10				
			avg. spontaneous events/AZ	0.111662	0.02180399				10				
				0.1774151	0.02380485				10				
				0.1751061	0.02952431				10				
				0.243055	0.0294237				10				
			avg. evoked events/AZ	0.682342	0.09892222				10				
				0.9380794	0.1156975				10				
				1.119013	0.1267532				10				
				1.245341	0.08642571				10				
			slopes of linear fits on evoked activity	1.191	0.2158	One sample t-test against 0		0.0004	10				
			slopes of linear fits on spont. activity	0.247	0.0597			0.0025	10				

Figure	Panel	Group	Measure	Mean	SEM	Test type	Comment	alpha of test against 0	N (animals)	R² of lin. fit on means	R² of lin. fit on indiv. values	slope of lin. fit on means	slope of lin. fit on indiv. values
1	O	Unc18	norm. fluorescence intensity (Unc18)	0.24851	0.023503				8				
				0.400879	0.027758				8				
				0.521641	0.028349				8				
				0.700445	0.027386				8				
			avg. spontaneous events/AZ	0.1703719	0.03166767				8	0.8005	0.2431	0.3091 ± 0.09957	0.3002 ± 0.09131
				0.2746125	0.01719362				8				
				0.3040119	0.04153982				8				
				0.3151339	0.03549303				8				
			avg. evoked events/AZ	0.8794593	0.06368656				8	0.08101	0.006478	0.1317± 0.2979	0.1669 ± 0.1948
				1.063754	0.1048829				8				
				1.057098	0.09773384				8				
				0.9535489	0.1182448				8				
			slopes of linear fits on evoked activity	0.1669	0.1948	One sample t-test against 0		0.42	8				
			slopes of linear fits on spont. activity	0.3002	0.09131			0.0133	8				

Figure	Panel	Group	Measure	Mean	SEM	Test type	Comment	alpha of test against 0	N (animals)	R² of lin. fit on means	R² of lin. fit on indiv. values	slope of lin. fit on means	slope of lin. fit on indiv. values
1	P	BRP	slope of linear fits on spont. activity	0.343	0.08084	One sample t-test against 0		0.0008	15				
		Unc13A		0.3686	0.07304			0.0002	15				
		Unc13B		0.09543	0.08016			0.1349	19				
		Syx-1A		0.247	0.0597		reanalyzed data from Reddy-Alla et al., 2017	0.0025	10				
		Unc18		0.3002	0.09131			0.0133	8				
1	P	BRP	slope of linear fits on evoked activity	1.117	0.185	One sample t-test against 0		< 0.0001	15				
		Unc13A		1.075	0.1054			< 0.0001	15				
		Unc13B		0.2418	0.1545			0.2493	19				
		Syx-1A		1.191	0.2158		reanalyzed data from Reddy-Alla et al., 2017	0.0004	10				
		Unc18		0.1669	0.1948			0.42	8				

Supplementary Data relating to Figure 1, panels M,O,P

Figure	Panel	Group	Measure	Mean	SEM	Significance level/alpha	Test type	N (animals)
S1-1	C	0.4 mM $[Ca^{2+}]_{ext}$	mean GCaMP5G spontaneous event amplitude	843.5276	38.74352			9
		0.75 mM $[Ca^{2+}]_{ext}$		827.7138	47.4679			
		1.5 mM $[Ca^{2+}]_{ext}$		903.2866	58.19328	0.0039	non-parametric paired t-test	
		3 mM $[Ca^{2+}]_{ext}$		1044.243	59.1905			
		6 mM $[Ca^{2+}]_{ext}$		1100.524	80.43235			
		12 mM $[Ca^{2+}]_{ext}$		1218.499	84.52728			

Supplementary Data relating to Supplementary Figure S1-1

Figure	Panel	Measure	Group	Mean	SEM	Significance level/alpha	Test type	Comment	N (animals)
2	B	eEJC amplitude (nA)	ctrl	71.14	11.93				3
			TTX	0.6131	0.08289				
2	D	mEJC amplitude (nA)	ctrl	0.5925	0.06691	0.9423	unpaired parametric t-test		5
			TTX	0.5983	0.03879				
2	E	mEJC frequency (Hz)	ctrl	1.597	0.6769	0.0964	unpaired parametric t-test		
			TTX	3.037	0.3551				
2	G	average GCaMP fluorescence amplitude	ctrl	371.7	20.18	0.5573	unpaired non-parametric t-test		18
			TTX	353.5	20.45				
2	H	avg. spont. event frequency (Hz/AZ)	ctrl	0.00217	0.0002246	0.7123	unpaired non-parametric t-test		
			TTX	0.002162	0.0003297				
2	J	eEJC amplitude (nA)	ctrl	76.43	4.798				3
			Cd	0.4375	0.0155				
2	L	mEJC amplitude (nA)	ctrl	0.4754	0.03126	0.3618	unpaired parametric t-test		11
			Cd	0.5282	0.04835				10
2	M	mEJC frequency (Hz)	ctrl	1.695	0.3255	0.0209	unpaired parametric t-test		11
			Cd	0.7383	0.1734				10
2	O	average GCaMP fluorescence amplitude	ctrl	409.4	35.19	0.0668	unpaired non-parametric t-test		11
			Cd	330.9	18.01			2 animals showed no events	9
2	P	avg. spont. event frequency (Hz/AZ)	ctrl	0.00221	0.000354	< 0.0001	unpaired non-parametric t-test		11
			Cd	0.0002248	0.00007827				

Supplementary Data relating to Figure 2

Figure	Panel	Group	Measure	Mean	SEM	Test type	Comment	alpha of test against 0	N (animals)	R² of lin. fit on means	R² of lin. fit on indiv. values	slope of lin. fit on means	slope of lin. fit on indiv. values
S2	A	ctrl	Unc13A fluorescence	336.5736	45.83423		1 value per bin		18	0.9692	0.1386	0.0005109 ± 0.00006443	0.0005291 ± 0.0001355
				415.9869	50.57554								
				495.1338	55.25953								
				639.061	66.22487								
S2	A	ctrl	avg. spontaneous events/AZ	0.1971101	0.02229648		1 value per bin						
				0.2331693	0.03115313								
				0.2543244	0.02861136								
				0.3534747	0.05023948								
S2	A	TTX	Unc13A fluorescence	264.1649	27.26155		1 value per bin			0.8107	0.04814	0.0004298 ± 0.0001469	0.0005733 ± 0.0001600
				333.4852	35.13753								
				402.9435	42.05859								
				525.5592	55.30049								
S2	A	TTX	avg. spontaneous events/AZ	0.1971751	0.03317349		1 value per bin						
				0.2305532	0.03940564								
				0.3018868	0.05330624								
				0.3040288	0.04922991								
S2	B	ctrl	slope of linear fits	0.0005291	0.0001355	one sample t-test against 0		0.0011					
		TTX	slope of linear fits	0.0005733	0.00016			0.0023					
S2	C	ctrl	Unc13A fluorescence	533.8755	23.93425		1 value per bin		11	0.9589	0.06499	0.0002476 ± 0.00003623	0.0002854 ± 0.0001248
				659.9739	30.54895								
				779.6198	40.01649								
				990.3765	56.97451								
S2	C	ctrl	avg. spontaneous events/AZ	0.2165222	0.04387565		1 value per bin						
				0.2269964	0.04430959								
				0.2780659	0.05132264								
				0.3226849	0.05851287								
S2	C	Cd	Unc13A fluorescence	451.5756	42.95469		1 value per bin			0.816	0.04561	0.00005818 ± 0.00001954	0.00004567 ± 0.00003085
				551.3224	54.7773								
				648.4687	66.50378								
				828.731	86.30315								
S2	C	Cd	avg. spontaneous events/AZ	0.01373182	0.005438797		1 value per bin						
				0.02952527	0.01554948								
				0.02653209	0.009663778								
				0.03877882	0.01334082								
S2	D	ctrl	slope of linear fits	0.0002854	0.0001248	one sample t-test against 0		0.0453					
		Cd	slope of linear fits	0.00004567	0.00003085			0.1696					

Supplementary Data relating to Supplementary Figure S2

Figure	Panel	Measure	Group	Mean	SEM	Significance evel/alpha	Test type	Comment	N (animals)
3	D	mEJP frequency (Hz)	before PhTx	2.417	0.1329	0.0435	paired parametric t-test		18
		mEJP frequency (Hz)	after PhTx	2.226	0.1917				18
3	D	mEJP amplitude (mV)	before PhTx	0.8902	0.03051	< 0.0001	paired parametric t-test		18
		mEJP amplitude (mV)	after PhTx	0.5702	0.02297				18
3	E	mEJP frequency (Hz)	after PhTx	2.163	0.2705	0.8962	paired parametric t-test		9
		mEJP frequency (Hz)	no stim	2.144	0.2429				9
3	E	mEJP amplitude (mV)	after PhTx	0.5261	0.03291	0.8328	paired parametric t-test		9
		mEJP amplitude (mV)	no stim	0.5218	0.02073				9
3	F	mEJP frequency (Hz)	after PhTx	2.289	0.2863	0.0027	paired parametric t-test		9
		mEJP frequency (Hz)	stim	1.726	0.179				9
3	F	mEJP amplitude (mV)	after PhTx	0.6144	0.02594	0.2031	Wilcoxon matched-pairs signed rank test	Group "after PhTx" matched with "stimulation" group failed D'Agostino & Pearson omnibus normality test	9
		mEJP amplitude (mV)	stim	0.5675	0.04475				9

Supplementary Data relating to Figure 3

Figure	Panel	Measure	Group	Mean	SEM	Significance evel/alpha	Test type	N (animals)
S3	B	mEJP amplitude (mV)	ctrl	0.916	0.05442	0.9089	paired parametric t-test	6
		mEJP amplitude (mV)	ctrl after stim	0.9233	0.06565			6
S3	B	mEJP amplitude (mV)	PhTx	0.9389	0.08801	0.0003	paired parametric t-test	6
		mEJP amplitude (mV)	PhTx after stim	0.5025	0.04765			6
S3	C	mEJP frequency (Hz)	ctrl	2.136	0.2787	0.0591	paired parametric t-test	6
		mEJP frequency (Hz)	ctrl after stim	1.944	0.3378			6
S3	C	mEJP frequency (Hz)	PhTx	2.036	0.1485	0.0208	paired parametric t-test	6
		mEJP frequency (Hz)	PhTx after stim	1.508	0.1471			6

Supplementary Data relating to Supplementary Figure S3

Figure	Panel	Measure	Group	Mean	SEM	Significance evel/alpha	Test type	Comment	alpha of test against 0	N (animals)	R^2 of lin. fit on means	R^2 of lin. fit on indiv. values	slope of lin. fit on means	slope of lin. fit on indiv. values
4	C	Cell-wise avg. pV_r	sequential	0.02295727	0.001079352	-	-	1 value per bin; same cells as G	-	59	0.965	0.1701	0.01073 ± 0.001444	0.01011 ± 0.001572
				0.03152708	0.00156973					59				
				0.03941979	0.003070061					58				
				0.05608464	0.009086707					28				
4	D	Cell-wise avg. pV_r	interleaved	0.02464688	0.001164756	-	-	1 value per bin; same cells as F	-	59	0.03576	0.0007365	0.0002399 ± 0.0008808	0.000396 ± 0.001025
				0.02862246	0.001537988					59				
				0.02644304	0.002703864					54				
				0.02617293	0.00367214					30				
4	E	slopes of linear fits	sequential	0.009312	0.001608	0.0002	Wilcoxon matched-pairs signed rank test	Both datasets failed the D'Agostino & Pearson omnibus normality test	< 0.0001	59				
			interleaved	0.00005444	0.001309				0.967	59				

Supplementary Data relating to Figure 4

Figure	Panel	Measure	Group	Mean	SEM	Significance level/alpha	Test type	alpha of test against 0	N (animals)	n (AZs)	R^2 of lin. fit on means	R^2 of lin. fit on indiv. values	slope of lin. fit on means	slope of lin. fit on indiv. values
S4-1	A	event frequency per AZ	sequential	0.003654	0.0003165	0.0003	paired parametric t-test		9					
			interleaved	0.001784	0.0001964				9					
S4-1	B	event amplitude	sequential	786.8	39.04	0.1274	paired parametric t-test		9					
			interleaved	845.5	29.48				9					
S4-1	C	pV_r (F_s = 0.000)	-	0.035	0.004				1	110	0.7922	0.01435	1.089±0.3943	0.6731±0.4617
		pV_r (F_s = 0.010)		0.037	0.006					27				
		pV_r (F_s = 0.020)		0.044	0.015					7				
		pV_r (F_s = 0.030)		0.069	0.027					4				
S4-1	D	fraction of AZs active in sp+ev	sequential	0.1433	0.008586	<0.0001	paired parametric t-test		59					
			interleaved	0.1048	0.006805									
S4-1	E	mean of exp. fit plateaus	-	0.2661	0.04037				15					
S4-1	F	percentage of spont. only AZs	-	0.05774	0.007911			<0.0001	15					

Supplementary Data relating to Supplementary Figure S4-1

Figure	Panel	Measure	Group	Mean	SEM	Significance evel/alpha	Test type	Comment	alpha of test against 0	N (animals)	R^2 of lin. fit on means	R^2 of lin. fit on indiv. values	slope of lin. fit on means	slope of lin. fit on indiv. values
S4-2	A	norm. BRP fluorescence int.	sequential	0.12099	0.01057	-	-	1 value per bin; same cells as D	-	9	0.8552	0.2243	0.003435 ± 0.0009997	0.003435 ± 0.001096
				0.250263	0.016963				-					
				0.395396	0.022727				-					
				0.649276	0.020024				-					
S4-2	A	event frequency per AZ	sequential	0.002756667	0.000337701	-	-	1 value per bin; same cells as D	-	9				
				0.003636111	0.000561103				-					
				0.003377889	0.000336608				-					
				0.004769556	0.000452645				-					
S4-2	B	norm. BRP fluorescence int.	interleaved	0.12099	0.01057	-	-	1 value per bin; same cells as C	-	9	0.1283	0.01096	0.0004097 ± 0.0007551	0.0004097 ± 0.0006676
				0.250263	0.016963				-					
				0.395396	0.022727				-					
				0.649276	0.020024				-					
S4-2	B	event frequency per AZ	interleaved	0.001531444	0.000144109	-	-	1 value per bin; same cells as C	-	9				
				0.002090778	0.000358016				-					
				0.001631	0.000265414				-					
				0.001927556	0.000224158				-					
S4-2	C	slopes of linear fits	sequential	0.003435	0.0009145	0.0041	paired parametric	-	0.0056	9				
			interleaved	0.0004099	0.0004456				0.3846	9				

Supplementary Data relating to Supplementary Figure S4-2

3 Discussion

3.1 Preface

Recent years and decades have seen a surge in technological advances that continually serve to dissect the properties of neuronal signal transmission, building on the fundamental findings of previous decades. Progress across many disciplines has yielded ever more performant approaches for elaborate bioinformatics applications (e.g. machine learning in tumor diagnosis: Fauw et al., 2018), highly precise genetic tools to watch cellular processes unfold in real time (e.g. GFP: Prasher et al., 1992; Chalfie et al., 1994), as well as super-resolution microscopy techniques (e.g. STED: Hell and Wichmann, 1994; Hell and Kroug, 1995; Klar and Hell, 1999; STORM: Rust et al., 2006; PALM: Betzig et al., 2006).

In this cumulative work encompassing six publications (Böhme et al., 2016; Reddy-Alla et al., 2017; Böhme et al., 2018; Böhme et al., 2019; Kobbersmed et al., 2020; Schuhmacher et al., 2020) and a manuscript in preparation (Grasskamp et al.), I have listed and described my efforts (and those of my colleagues and collaborators) to utilize these technologies and methods directly or indirectly, and to the best of my capabilities. As it is inherent in science that the need for further research never ceases, and because results can often be interpreted in several ways, this dissertation makes no claim to completeness or infallibility. The published and unpublished work presented was conducted with the aim to further our knowledge of neurobiology and cellular signal transmission. Ideally, science should be a self-correcting process of reproducibility testing and peer review. Yet, it is never certain whether published work in even the highest-ranking journals can be taken for granted. With the following section, I will put my work into the context of other published results that contradict or support what I have found. I aim to discuss what inconsistencies, curiosities, or changes in perspective may arise when comparing our published work with that of others. I will further try to explain why these contradictions exist and how likely it is that they will turn into agreement in the future.

3.2 Computational challenges in model choice & optimization procedures

3.2.1 The principles of parsimony

The presented computational work spans almost all sections of my thesis, which is why I want to put special emphasis on discussing how it was used and what purposes that served. Furthermore, the necessary prerequisites for the combination of biological data and computer models are explained. For five of the seven presented manuscripts, I have employed algorithmic optimization procedures to build a computer model that agrees with the respective experimental data. As implied in my choice of a cover quote (“All models are wrong, but some are useful” - Box and Draper, 1987), any of these models

have to be viewed as an approximation of reality in the cell, and our simulations and mathematical models show our most reasonable interpretation at the point of publication. The principle of parsimony is popularly known as Ockham's razor (after William of Ockham, circa 1288 – 1347), although its exact origins are disputed. It specifies that, of all models explaining the observed experimental data reasonably well, only the simplest should be accepted. A model will eventually most likely agree with the data if it is sufficiently complex, even using the wrong assumptions. Overfitting, the explanation of an observation by too many adjustable parameters, contradicts parsimonious considerations. For these reasons, we always strove to reduce the degrees of freedom in our models as far as possible. All procedures discussed in this section were performed in MATLAB.

When determining the distances of Unc13A and Unc13B to the active zone center in Böhme et al., 2016, we restricted ourselves to only optimizing the physically necessary parameters of the model, like the number of releasable vesicles, coupling distances of the proteins, and Ca^{2+} influx. Interestingly, we had to add one parameter enhancing Ca^{2+} influx in the *unc13A*^{null} mutant to get our model to agree with the data. This fits an increasing abundance of the *Drosophila* calcium channel Cac in the *unc13A*^{null} mutant (observed with immunohistochemical stainings in Böhme et al., 2016, supplementary Figure 6). This also generated a testable hypothesis, namely that an increased Ca^{2+} current might counteract the decreasing SV release in the mutant, and this might be addressed in future studies. In principle, a mechanism of increasing Ca^{2+} influx to counterbalance synaptic disturbances exists, as shown previously by Müller and Davis (2012. Likewise, an increase in calcium channel abundance under similar circumstances has been shown by our lab (Böhme et al., 2019). In this case, we found it justified to add one degree of freedom to the model and explain synaptic transmission in two genotypes simultaneously.

Our most objectively rigorous way of model selection is shown in Schuhmacher et al. (2020). Here, we modeled lipid kinetics in living cells based on optical measurements of fluorescent sensor recruitment to the cellular membrane after lipid liberation by uncaging. The mathematical model was built assuming the presence of four parameters: two to explain bidirectional translocation over the lipid bilayer membrane, one to trace lipid metabolism, and finally one to explain sensor association and dissociation. We found that for one of the lipid species, stearoyl-oleoylglycerol (SOG), we could remove the kinetic parameter for lipid movement from the inside to the outside of the cell at virtually no loss of model quality. Therefore, we calculated the difference in Akaike's information criterion (AIC, Akaike, 1974) for both versions of our model, one including the parameter and the other excluding it. It became obvious from these calculations that we could not justify removing this parameter when fitting our model to data from experiments with stearoyl-arachidonylglycerol (SAG) or dioctanoylglycerol (DOG).

This illustrates that different experimental conditions can be explained by different models. However, an overarching model concurrently explaining all observations in the same experiment is preferable and will yield the most value. If no model can perform well enough to achieve this, then it is possible that one of the experimental conditions is not sufficiently determined and needs to be reassessed. A mutually beneficial feedback mechanism between model and experiment may therefore help in determining not only the structure of the model, but also the necessary experimental measurements. Testable hypotheses yielded from a well-determined experiment and an appropriate model will supposedly lead to a gain in knowledge regarding the initial research question(s).

3.2.2 Comparing model and data: the cost of simulations

A crucial factor in reproducing experimental data with computational calculations is the definition of the loss, commonly referred to as cost. This value is used to measure how much model simulations deviate from observed experimental data: a bigger deviation incurs a higher cost, and the model's value in approximating reality consequently decreases. It is therefore a measure of agreement between computer model and experiment, and the goal is to minimize the cost and hence maximize the agreement. Several approaches exist to do so. The simplest form used in our optimizations is the residual sum of squares (RSS) loss function. Generally, it can be expressed as the sum of squared errors: $RSS = \sum_{k=1}^{n_{total}} (model(k) - data(k))^2$ where n_{total} is the number of compared data points. In its simplicity, it serves as a good choice for linear problems like the minimization of distances performed in Böhme et al. (2019). Because we wanted to use the RSS value in the calculation of Akaike's information criterion (as described earlier), we also used this cost function for the modeling in Schuhmacher et al. (2020). As we sought to understand how the standard deviation of the data would influence the quality of the fit, we also tested another loss function, known as the reduced Chi square statistic: $X^2_{red.} = \sum_{k=1}^{n_{total}} \frac{(model(k) - data(k))^2}{\sigma^2(k)}$. Here, the squared error is divided by the squared standard deviation, or variance σ^2. A high variance will lead to a lower cost than a low variance, giving a higher "weight" to well-defined (low variance) parts of the data. The optimization will hence force the model to agree more with those well-defined parts of the data. This means that the cost for deviations between experiment and model is higher when the experimental data is well-defined. Vice-versa, deviations between experiment and model are tolerated when experimental values are not well-determined. However, we found that this loss function worked worse for our approach, as variances were not as well defined as expected in the supposedly relevant regions of the data. A simpler and comparably rigorous method of computing the loss function can be applied according to Pearson's Chi square statistic, expressed as $X^2 = \sum_{k=1}^{n_{total}} \frac{(model(k) - data(k))^2}{data(k)}$ (Pearson, 1900; Burnham and Anderson, 2004:199; Bolboacă et al., 2011). We have used this loss function for two of the presented publications, Kobbersmed et al. (2020) and Böhme et al. (2016). However, an alternate form was used in Böhme et al. (2016) to include weights, and to normalize to model

and data: $X^2 = \sum_{k=1}^{n_{total}} w_k * \left[\left(\frac{\text{data}(k)-model(k)}{model(k)} + \frac{\text{data}(k)-model(k)}{\text{data}(k)}\right) * 0.5\right]^2$. Here, w_k represents the weight according to how many data points were present in the compared experimental data. This was necessary to ensure the equally distributed quality of the model regarding all experiments that we built the model on. We combined several experiments to optimize our model to, and we therefore had to ascertain that all data points of all experiments would be regarded with the same importance.

3.2.3 Choosing the right optimization approach

Having found the qualitatively appropriate variables and a way of cost estimation for the model, another obstacle for this type of computational endeavor presents itself. The variables must be tuned towards numerical values that produce the best-possible agreement with the data. This can be achieved by an optimization procedure, and there are numerous ways to perform one. An optimization procedure is, in the simplest sense, an iterative change of variables and concurrent comparison of the simulated data with the observed data. If a set of variables produces better agreement with the data than another set of variables, then the optimization should proceed in this direction. The most naïve way of estimating variables is to figuratively throw a very big dice and sample them randomly from an infinite range of numbers. Luckily, this infinite range can be somewhat constrained in most cases, and this least informed choice is only needed at the beginning of the optimization.

Once an initial estimate has been made, a solver algorithm calculates all further steps. From then on, the choice of the solver will crucially influence whether the outcome is useful or not. Depending on the problem at hand, an optimization can easily return a result that does not represent the overall best possible solution. If one looks at all possible solutions as part of a “solution space”, then this result can be called a local optimum. One can think of this problem as two holes of different depth dug into the ground bordering on each other, with the best solution being the bottom of the deeper hole. A golf ball dropped from above will likely end up at the bottom of one of the holes, but this very much depends on its initial position over the holes, and the height of the border between them. Gravity dictates the direction of the golf ball’s descent into the hole, and the procedural improvement of parameters by a solver can be imagined in a similar fashion. With each step in the solver procedure, it is evaluated whether the step has taken the model into a direction where it fits the data better. If that is the case, the solver will continue along this gradient by iterating steps and evaluations, making it a gradient based approach.

Many solvers can generally only be trusted to find a “local” solution. This is akin to the golf ball ending up at the deepest point of the shallower hole, while the deepest point of the deeper hole would further decrease its potential energy in relation to the earth’s center of gravity, and represents the best possible solution (or the global solution). The local solution is therefore only the best solution

in respect to its proximal neighborhood. However, certain measures exist to ensure finding a global optimum beyond reasonable doubt. Firstly, the range of initial parameters ideally must cover all values that could possibly lie within the realm of solutions if no well-founded estimate exists. Secondly, the search for the best solution should be started from as many different points as possible, analogous to dropping as many golf balls as possible. This will increase the likelihood of the initial step to be closer to the global solution and decreases the number of steps that need to be taken. Only if these prerequisites are met and many of the found solutions cluster at a certain value can one be reasonably certain to have found the best, global solution.

In some cases, computational effort limits the possibilities to explore large numbers of solutions. In the modeling part of our publication Böhme et al. (2016), where we investigated differential Unc13A/B accumulation at the AZ, a major temporal bottleneck was imposed by the combination of optimization and the simulation of calcium currents. This latter part took place outside of MATLAB in a program kindly provided by Victor Matveev (CalC, Matveev et al., 2002). This software is capable of elaborately calculating buffered spatial and temporal diffusion of Ca^{2+} ions, and was therefore used to simulate the Ca^{2+} concentration changes induced by the arrival of an AP at the synapse, leading to SV exocytosis and neurotransmission (see introduction). However, its speed over many repetitions depends greatly on the complexity of the problem at hand. As our optimization procedure included several variables describing Ca^{2+} influx, we had to run the software iteratively for every step of the optimization. The calculation of Ca^{2+} influx depended on several free parameters (5 out of 9), which had to be optimized together with physical distances of Unc13 isoforms and SV pools sizes. However, the latter parameters were only needed to determine SV exocytosis by taking into account the Ca^{2+} amounts calculated before. Therefore, this latter step could be uncoupled from Ca^{2+} calculations. In future attempts using more computer power to reproduce or expand this study, one could therefore generate a library of pre-determined calculations to source from and narrow down the region of calcium influx parameters that must be evaluated. This would decrease the complexity of the problem quite considerably, as Ca^{2+} dynamics could be sourced from the lookup table instead of having to be calculated iteratively, saving time in the optimization procedure and allowing further evaluations of the model, e.g. in respect to other proteins like the calcium sensors responsible for evoked and/or spontaneous release.

Luckily, other parameters were strictly constrainable as e.g. the distances of vesicles to the AZ center were likely on the scale of tens to a few hundreds of nanometers. Additionally, the maximum number of available vesicles can be roughly constrained by volume calculations. The average diameter of SVs at the *Drosophila* NMJ has been reported to range between 34.9 (Zhan et al., 2016) and 42.7 nm (Stevens et al., 2012), resulting in volumes between 22257.4 – 40764.5 nm^3 (or 22.3 - 40.7 zeptoliters). Our whole AZ simulation space of 540x540x400 nm^3 (a volume of $116.64x10^6$ nm^3 or 116640 zeptoliters) could then possibly only hold a few thousand spherical SVs, depending on the space effectively

available and the density of sphere packing. The highest density of sphere packing according to the Kepler conjecture (published in 1611 by Johannes Kepler, 1571 – 1630 as "*De nive sexangula*"), is a complex issue debated among mathematicians until very recently (Hales et al., 2017). Assuming the reported maximum density of η_{Kepler}=74.048 % (meaning any number of perfect spheres can at most take up 74.048% of a volume unit in three-dimensional Euclidean geometry), a maximum of 3882 SVs could exist in the given volume ($\frac{0.74048*1.1664*10^{-16}L}{2.22574*10^{-20}\frac{L}{SV}} = 3882.375\ SV$). Furthermore, one of our main assumptions (which later turned out to be too simplistic, an issue discussed later) was that SVs could only be released at two distinct distances from the AZ center, additionally constraining the upper limit of available SVs by an order of magnitude. Further parameters describing the behavior of the calcium sensor of SV release could be fixed to values taken from the literature, resulting in a model which at that time was our best estimate of SV release at the *Drosophila* NMJ.

When the computational effort of simulating a problem is low, algorithmic ambitions can increase correspondingly. The genetic algorithm, which we used for one of our recent publications (Böhme et al., 2019), is an interesting approach in optimization. It is a so-called metaheuristic based on the evolutionary principles of natural selection and reproductive fitness (Goldberg, 1989). While it does not guarantee finding a global optimum in itself, it enables the search for it over a very large part of the parameter space, analogous to dropping hundreds of golf balls on a hilly golf course. However, as golf balls have not been observed to reproduce, this analogy ends here. At the start of using the genetic algorithm, a "population" is defined, containing a theoretically unlimited number of "individuals". Every individual in this population represents a randomly chosen set of variables, making up the first "generation". Now, these individuals are evaluated for their fitness, or agreement with the data. Like in evolution as established primarily by Charles Darwin (1809 – 1882; Darwin, 1859), a greater fitness increases their likelihood of passing down their traits to their progeny. The fittest individuals are therefore chosen to exchange variables with a certain amount of mutation, effectively reproducing and generating the next generation. This process is then repeated until all individuals of the current generation have comparable fitness and it cannot be increased any further.

We chose this approach for our recently published work Böhme et al. (2019) as the problem was comparably simple in terms of computational effort. The project aimed to find structural and mechanistic correlates of homeostatic plasticity, the dynamic scaling of connection strength in response to challenges, in the presynapse. To facilitate this, we categorized super-resolution microscopy images of single AZs by how many high-intensity clusters we found in an automated approach. By concurrent rotation of at most a few hundred images in each category, we wanted to minimize the distances between intensity maxima in the images to reveal the underlying geometrical pattern of release sites. The parameter boundaries for this problem were comparably easy to choose: it would not make sense to rotate a single image by more than 180 degrees in either direction. The angle of rotation was also the only parameter we needed to optimize, but an angle had to be found for each individual image.

Therefore, we chose a population size of 500 individuals, effectively representing 500 different sets of rotated images. The initial, randomly chosen population was then allowed to iteratively mutate and cross, resulting in a comparably homogeneous population of the fittest individuals after several hundred generations. Due to the well-defined and non-stochastic nature of the problem, we could then be reasonably certain that the resulting rotation angles represented the best attainable solution.

Having learned from the previous modeling approaches, we went another step further for the model optimization shown in Schuhmacher et al. (2020), a project designed to quantitatively determine lipid kinetics in membranes and cells. When starting to work on the project, we soon found that the genetic algorithm would not arrive at meaningful solutions, as it showed many non-feasible pseudo-solutions and was very slow overall. This was partly because the parameters K_d, k_{in} and k_{out} had to stay in a certain relation to each other, and extreme cases would slow down and mislead the algorithm. Therefore, we employed a search heuristic that is designed to find global solutions. Similar to the genetic algorithm, the multistart search algorithm randomly generates many different initial parameter sets, 10000 in our case. It then employs local solvers such as the nonlinear multi-variable function solver *fmincon* to find as many local solutions and returns the best one. In contrast to the genetic algorithm, the local solutions do not iteratively influence each other, but rather represent many independent solutions. Because our model sufficiently fit the data with only four parameters (as described above: two parameters to explain bidirectional translocation over the lipid bilayer membrane, one to trace lipid metabolism, and one to explain sensor affinity), we could then explore and visualize the parameter space to show that we had found the global solution for each DAG species.

From our observations, it became obvious that one must execute great caution when choosing model constraints, parameters, and an appropriate optimization algorithm to yield a meaningful and representative result. We tailored our approach to each of the problems we encountered and can claim with reasonable certainty that we have fulfilled these requirements. However, even after following the necessary steps, we can never be truly sure that the obtained solution is the one that explains the data correctly. This is due to the simple fact that all our mathematical models and simulations are based on hypotheses and previous observations by ourselves as well as other groups and colleagues. This does not imply that we have likely chosen wrong paths in our models, but it reflects the conditions for virtually all approaches to replicate experimental data *in silico*. Similarly, the quote by Box and Draper (1987) may sound too fatalistic – all models may be wrong, but this is inherent in the word "model". A pillow case can be seen as a model to approximate the shape of the encased pillow, and it will do so better than encasing the pillow in an inflated balloon, but it will normally not show the exact shape of the pillow down to its creases and fibers.

Therefore, until a better solution can be presented, our published results shall serve as our best

approximation. With the described prerequisites in mind, the following sections partly aim to discuss how each individual project benefitted from our computational efforts.

3.3 Lipid-protein interactions: The role of lipid structure in cellular signaling

A large fraction of every cellular membrane is composed of lipids, and many organelles depend on the integrity of their own lipid membrane. At the outer cell membrane, a semi-symmetrical lipid bilayer of exposed polar, hydrophilic headgroups and inwardly oriented apolar, hydrophobic tails constitutes an important barrier between intra- and extracellular space, maintaining a vital separation of ions and proteins (Trimble and Grinstein, 2015). Where necessary, substances that cannot diffuse through the membrane like water can cross through specialized channels and transporters. In addition to proteins that act in cellular signaling cascades, the highly diverse class of lipid molecules plays a major role in pathways that affect the physiological parameters of the cell. Our lab has previously shown (without my involvement) that the membranous phospholipid phosphatidylinositol 4,5-bisphosphate $PI(4,5)P_2$ is a potent factor in enhancing exocytosis of secretory vesicles (Walter et al., 2017). Other labs have also seen a role of $PI(4,5)P_2$ in the maintenance of neurotransmission (Di Paolo et al., 2004). A vast bouquet of other lipids has been implicated in the cellular processes necessary for proper neurotransmission (reviewed in Puchkov and Haucke, 2013 and Postila and Róg, 2020).

3.3.1 Production and roles of diacylglycerol in the cell

By catalyzing the hydrolysis of $PI(4,5)P_2$, the GPCR-dependent enzyme class of phospholipase C aids in metabolizing the phospholipid into inositol 1,4,5-trisphosphate (IP_3) and diacylglycerol (DAG) (Bill and Vines, 2020), when a ligand (like a neurotransmitter or hormone) binds to the G-protein coupled receptor and activates the second messenger signaling cascade. IP_3 then serves to induce the release of Ca^{2+} from intracellular stores (specifically the endo- or sarcoplasmic reticulum), leading to a varied host of downstream consequences, and playing decisive roles in cell proliferation (Kania et al., 2017).

The other product of this metabolic process, DAG, was of more interest to my work. As it constitutes the hydrophobic remainder of the $PI(4,5)P_2$ tail groups after PLC-mediated cleavage, it remains anchored in the membrane and serves to recruit another class of signaling molecules to the membrane, namely protein kinase C (PKC; Igumenova, 2015). It can also be metabolized by diacylglycerol kinases (DGK) into phosphatidic acid (PA), from which it can in turn be synthesized by phosphatidate-phosphohydrolase, or it can be turned into triacylglycerol (TAG) by acyltransferases (Eichmann and Lass, 2015). It becomes obvious that the ways of lipid metabolism are various due to complex and partly redundant mechanisms, and I refer the interested reader to Eichmann and Lass (2015) for further elaborations. Interestingly, like phorbol esters (PMA/PdBu), DAG also binds to Unc13

(see introduction) via its C1-domain and enhances neurotransmission (Rhee et al., 2002), again underlining the role of lipid signaling in neuronal function. PKC is a signaling molecule that, by way of phosphorylation, can modulate function of other proteins (such as iGluRs (Correia et al., 2003) and Munc-18 (Fujita et al., 1996; Genç et al., 2014)) and lead to diverse modes of cellular long-term signaling, exerting important roles in cell proliferation.

The structure of DAG itself can vary widely, as the composition of the two fatty acid chain groups is not narrowly defined (Eichmann and Lass, 2015). However, it is not clear to this day what physiological implications such a variability of DAG side chain structures could have, although qualitative influences on signaling have been shown (Nadler et al., 2013). In order to understand how differences in side chain composition of these lipids as cellular signaling molecules would change their kinetics and the effect on downstream signaling molecules, Milena Schuhmacher and André Nadler from the Max Planck Institute of Molecular Cell Biology and Genetics (MPI-CBG) in Dresden approached our lab to collaborate on computational analysis. They had further developed an experimental assay conceptually close to the one already used in previous collaborative work (Walter et al., 2017), where intracellular caged PI(4,5)P_2 (rendered biologically inactive with a negatively charged coumarin cage) was acutely uncaged by a UV-spectrum laser flash to turn it into its biologically active form. We were not the first to make use of photochemical probes to investigate signaling cascades, as the concept of caged compounds in cell biology research has existed for several decades (Adams and Tsien, 1993; Nadler et al., 2013; Höglinger et al., 2014).

3.3.2 Quantitative determination of lipid-protein interactions and lipid dynamics through mathematical modeling

The novelty of the approach we took for Schuhmacher et al. (2020) lay in the fact that we combined a refined experimental assay (a GFP-bound sensor that was based on the DAG-binding C1 domain of PKCγ and contained a nucleus export sequence (NES); PKCγ-C1-GFP-NES), with a mathematical model that would allow us to decipher individual steps in the lifetime of DAG after uncaging. Caged DAG species (listed below) were employed in this experiment, and they could be spatially and temporally controlled because they would only translocate from the exterior to the interior of the cell upon UV-flash. This degree of control is a prerequisite for a relaxation study, in which a biophysical or chemical process is started from a known state (all caged DAG being on the outside of the cell in this case) and observed until all processes are in equilibrium or all educts have been metabolized. To derive kinetic parameters and lipid-protein affinities from the experiments, the setup had to be strictly quantitative. The quantitative nature of the experiments conducted by our colleagues was ensured by two calibration experiments. Firstly, the intracellular concentration of the sensor was derived from a calibration of known concentrations of the sensor and the corresponding fluorescence strength

in vitro. Secondly, the amount of loaded DAG was determined by another calibration experiment making use of the inherent fluorescence of the coumarin cage and known lipid concentrations. These two values, the amount of caged DAG loaded on the outer leaflet of the membrane and the amount of available sensor in the cell, were the known variables in our model.

The experimental assay made use of four caged DAG species: the naturally occurring forms stearoyl-arachidonylglycerol (SAG) and stearoyl-oleoylglycerol (SOG), as well as the short-chain form dioctanoylglycerol (DOG) not normally observed in the cell (and a non-PKCγ-C1 recruiting isomer of dioleoylglycerol (1,3-DOG) to control for nonspecific PKCγ-C1 recruitment and photobleaching of the probe). The three caged DAG species capable of recruiting PKCγ-C1 only differed among each other in length and fatty acid saturation degree of their acyl chains. When uncaging the lipids at the membrane, they were able to translocate to the inner membrane leaflet and recruit the fluorescent sensor. The experimental readout was therefore the decrease and recovery in fluorescence in an intracellular region of interest (ROI) after uncaging.

Our hypothesis was that, through different membrane translocation kinetics, dwell times at the place of uncaging, and differential metabolization, the different DAG forms should differ in their PKCγ-C1-recruitment properties. Due to the large role PKCs play in cellular signaling, this could then have implications for other cell biological processes, like malignant cell proliferation (Garg et al., 2014). PKC has also been shown to play a role in the establishment of long-term potentiation, a process implied in long-term memory formation and maintenance (Linden and Routtenberg, 1989). This builds an intriguing bridge to the results shown in Böhme et al. (2019), where *Drosophila* Unc18 (ROP) was shown to only cluster to the presynaptic active zone during genetically induced (i.e. long-lasting) presynaptic plasticity. It is possible that PKC activity plays a role here as Barclay et al. (2003), Wierda et al. (2007), and Genç et al. (2014) have shown interaction between the two molecules, and this calls for further investigation. The serine at position 313 in murine and human Unc18 is essential for phosphorylation by PKC (Barclay et al., 2003). It is further evolutionarily highly conserved and present in *Drosophila* Unc18 (position 322 on ROP, Uniprot ID Q07327) as per my own preliminary sequence alignments not shown here. This notion could be tested by site-directed mutagenesis of the protein and interaction studies like co-immunoprecipitation. Furthermore, the importance of this interaction for long-lasting synaptic plasticity in *Drosophila* could be tested by artificially expressing the modified protein in *unc-18*$^{\text{null}}$ (as used in Weimer et al., 2003) and *gluRIIA*$^{\text{null}}$ double-mutant animals. Alternatively, should these double-mutants prove too unhealthy for experimentation (i.e. by dying in the early embryonic or larval stages), acute genetic interference with the glutamate receptors could be performed in *unc-18*$^{\text{null}}$ mutants partially rescued with the modified protein, e.g. by temperature-controlled expression of GluRIIA-RNAi (interfering RNA suppressing the translation of a specific protein, here glutamate receptor subunit IIA) through gal80$^{\text{ts}}$ (Yoshihara and Ito, 2012). However, achieving this genotype is rather complicated and not guaranteed to work, and other

approaches should be explored. This could include the targeted modification of Unc18 with CRISPR/Cas9 (Bier et al., 2018) in *glurIIA*^{null} mutant animals.

To quantify the differential PKC recruitment using the experimental data, and to understand why recruitment was different, we developed a mathematical model based on the processes that were supposed to happen after uncaging. We then determined the sought-for rate constants (see Figure 5 in Schuhmacher et al., 2020): Uncaging would allow the bidirectional movement of the lipid through the membrane bilayer (rate constants k_{in} and k_{out}). Further, after translocation to the inner leaflet, it would be able to bind the fluorescent sensor with a certain affinity K_d. This establishes one of two important assumptions of our model, namely that binding and unbinding of the sensor would be in chemical equilibrium. Binding and unbinding rates would therefore always occur at the same ratio. This enabled us to describe the lipid-protein affinity as a single parameter, the equilibrium constant. When unbound from the sensor and present on the intracellular side of the membrane, DAG could then be irreversibly metabolized (k_{met}). This poses the other prerequisite of the model, stating that DAG bound to the fluorescent sensor would be shielded from metabolism. Without the latter assumption, metabolism rates could not be precisely determined, as there would be a convolution of fluorescence recovery and concurrent metabolism. Turning all reactions into differential equations (describing changes of concentrations over time), we used an algorithm to compare simulations and experiments (see modeling section of this discussion).

As the experiment included the uncaging of DAG at nine different laser powers (0-40 %) to capture the dose-dependence of uncaging and sensor recruitment, our modeling approach was expected to yield a well-defined description of the data after some fine tuning. Fitting the model consisting of four parameters on a single response curve would have led to an underdetermination of the result, leading to many different combinations of parameters that could explain the data similarly well.

Once we had determined the parameters in this *in vitro* experiment that did not necessarily reflect physiological conditions, we were able to simulate cellular signaling processes as they occur in nature, but which cannot be readily observed. Using the best fit parameters we found, we performed *in silico* experiments of PLC cleaving $PI(4,5)P_2$, yielding IP_3 and DAG with a time constant of 100 s, as determined by ATP stimulation experiments not discussed here. One of the most interesting findings of this analysis was that of the three tested DAG species, only SAG would form a relatively stable pool on the outer membrane leaflet. The implications of this species-specific behavior are unclear, but it is conceivable that it might influence signaling proteins on the outer leaflet, or simply delay its metabolism and therefore regulate the time it can be active. Testing this hypothesis could be

done in an “inverse” experimental setup: an extracellular sensor (like the one used here, but externally applied instead of genetically expressed) could be used to detect the outer leaflet pool of SAG after its controlled intracellular production or uncaging.

3.3.3 Possible confounders of our approach

As explained in the respective section, an optimization approach laying claim to completeness must explore as much of the parameter space as possible, and ideally all of it. Therefore, we chose boundaries on our model that we thought would reflect this. For the rate of DAG translocating into the cell, we allowed a maximum of 1000 per second. As this was only the rate constant, it had to be multiplied with the available amount of DAG after uncaging, e.g. $1.93x10^6$ molecules for SAG at 20 % laser power, yielding $1.93x10^9$ molecules in the first second. This means that at this upper rate limit, every single liberated SAG molecule would have to cross the membrane 1000 times in one second, leaving 500 µs for each flip- or flop-movement. While realistic estimates on rates are hard to find and greatly depend on the lipid composition of the membrane, it is believed to happen far slower than this in naturally occurring, heterogeneous lipid bilayer membranes. In a study employing fluorescently tagged DAG and mathematical modeling, the half time of DAG flipping back and forth through the membrane once was around 70 ms (Bai and Pagano, 1997). However, similar studies mostly employ unnaturally homogeneous and symmetrical lipid membrane systems not comparable to the typical cell membrane (Siontorou et al., 2017). We chose the boundaries for all other parameters on similar scales.

While the found best fit values simulated the experimental results with satisfactory accuracy, we had to objectively ascertain that we could not find better results. Therefore, we performed an analysis showing how unique our solutions were in a large space of other parameter sets. Using the acquired best fit values, we searched the parameter space for better-fitting combinations of the three parameters k_{in}, k_{out} and k_{met}. Changing them by factors over a range of 0.01 to 100 yielded no better results (supplementary figure S5-2 of Schuhmacher et al., 2020). This however depended on a singular K_d value and still leaves the possibility of further exploration by future studies. It also has to be taken into account that for SOG, which yielded a best fit for k_{out} of essentially zero, simple multiplication would not show a useful part of the parameter space, which is why we repeated the analysis on a different range (absolute rather than relative) of parameters shown in the same figure.

We knew that our model would depend on the quality of the data. This includes its variability, and our model would only be useful if the same analysis would hold true for other datasets. As more datasets were not at our disposal, we applied a bootstrapping approach. Generally, this approach randomly draws different subsets from the available data to generate artificial variation between datasets and aims to simulate the variation expected from repeatedly performing the experiment. We used bootstrapping

to draw random subsets and then repeated the fit on these datasets to determine whether parameter values would cluster around those found for the whole dataset, and that was indeed the case (Figure 5 of Schuhmacher et al., 2020). While this bootstrapping approach served to confirm the sensitivity and accuracy of our model, future approaches would benefit from higher temporal resolution of sensor recruitment and could also include further analysis of the downstream effects induced by acyl chain group differences. For the role of SAG on the outer leaflet of the cell membrane, it should be verified that the prediction of our model holds true. As stated earlier, this might be achieved by the combination of an extracellular sensor with the induced production or uncaging of SAG.

Lastly, we have not considered in our model that the uncaged DAG might not only recruit the fluorescently labelled PKCγ-C1 domain, but also other downstream signaling molecules. This is hard to implement, as we have no readily available way of measuring this unspecific effect. If there were another decisively large pool of PKCs binding to the uncaged DAG, the determined rate constants would be altered proportionally, while the relative differences between them (both inter- and intra-species) should stay the same. However, as the experiment involved the overexpression of the PKCγ-C1-GFP-NES sensor, we can be relatively certain that the major target of the uncaged DAG was this recombinant protein.

3.4 Synaptic release sites and active zone geometry

3.4.1 Unc13: paralyzing worms and electrifying researchers

Not long after its discovery through ethyl-methane-sulfonate mutagenization screens in *Caenorhabditis elegans* (Brenner, 1974), the synaptic protein (M)Unc13 started to be of particular interest to the neuroscientific community. The protein has since been extensively investigated (beautifully reviewed by Dittman, 2019), and research has made it very clear that it plays a key role in SV release at the synapses of worms, flies, and mammals (Maruyama and Brenner, 1991; Betz et al., 1998; Aravamudan et al., 1999; Augustin et al., 1999; Richmond et al., 1999; Shin et al., 2010), although it has been present in organisms without nervous systems that emerged hundreds of millions of years ago (Dittman, 2019). Its phorbol ester binding C1 (Betz et al., 1998) and phospholipid/calcium binding C2 (Shin et al., 2010) domains, in addition to the Syx-1 interaction motif MUN (Ma et al., 2011; Yang et al., 2015) hint strongly towards its functional integration in synaptic release mechanisms. Likewise, it serves as the guiding thread through all publications except one shown here (Böhme et al., 2016; Reddy-Alla et al., 2017; Böhme et al., 2018; Böhme et al., 2019; Kobbersmed et al., 2020; Grasskamp et al., in preparation).

3.4.2 Modeling SV coupling distances based on Unc13 isoforms

In our work Böhme et al. (2016), we have shown that two N-terminally different isoforms of the protein Unc13 (Unc13A and Unc13B) regulate release of SVs at the *Drosophila* AZ by mediating their position in regard to the AZ center (the VGCC cluster, source of AP-induced calcium influx) at two distances (76.8 and 145 nm). This was made possible through the combination of genetics, electrophysiology, super-resolution imaging and mathematical modeling. In the mathematical model that optimized simulated data based on experimental observations (detailed in the mathematical modeling section), we postulated that synapses lacking the more closely coupling A isoform try to make up for this lack by upregulating the influx of calcium during an AP (action potential, see introduction). Indeed, immunohistochemical analysis showed increases in the levels of *Drosophila* Ca_v2 homologue Dmca1A or Cac (supplementary Figure 6 of Böhme et al. 2016). Furthermore, this testable hypothesis fits what has been observed by other labs (Zhao et al., 2011; Gratz et al., 2019), but remains to be directly verified. Measurements using presynaptically expressed GCaMP or Oregon Green BAPTA (or other conditionally fluorescent Ca^{2+}-indicators) delivered to the presynaptic compartment through the motoneuron could be useful in doing so.

In our modeling approach, we have based the exclusively confined localization of releasable SVs in a perimeter around the AZ center on former work by colleagues (Nakamura et al., 2015). In their perimeter release model, distances between the calcium sensor for release (Syt-1 located on SVs) and the closest VGCC were estimated to range between 20-30 nm based on measures of synaptic properties under controlled calcium buffering conditions, and mathematical modeling. Using this assumption in our model, we were able to reproduce synaptic short-term plasticity over a range of $[Ca^{2+}]_{ext.}$. However, we found it rather troubling to reach the high facilitation values observed at low $[Ca^{2+}]_{ext.}$. In a recent approach (described in a later section), we found that the perimeter release model is not applicable at the *Drosophila* NMJ (Kobbersmed et al., 2020). In short, we had to consider a broad distribution rather than a singular radius for SV localization. Our model from Böhme et al. (2016) then failed to reproduce the results using this distribution due to the depletion of closely coupled SVs during the first release phase, and a lower availability of SVs for release for the second phase of the PPR experiment.

3.4.3 Nailing down the release site

This strong indicator for a role of Unc13 in coupling distance regulation (as observed for the AZ-specific Unc13L and the less clearly localized Unc13S in *C. elegans* by Zhou et al., 2013) then led us to determine it as the protein generating the release site in Reddy-Alla et al. (2017). This molecular correlate had been sought for over several decades, since José del Castillo and Bernard Katz had found that synaptic signal transmission events are made up of quantal release events (Fatt and

Katz, 1952; del Castillo and Katz, 1954). Statistical fluctuation analysis has then made clear that the amount of release events is limited by a defined number of release sites (Clements and Silver, 2000; Scheuss and Neher, 2001; Clements, 2003; Neher, 2010). In our study, we used an N-terminal mutant of Unc13A to show how SV positions follow this aberrantly localized mutant. In addition, I applied the genetically encoded green-fluorescent calcium indicator GCaMP5 to show how spontaneous and evoked SV release scaled with single-AZ BRP levels when Unc13A was present, and less so when it was not (Reddy-Alla et al., 2017), indicating that SV positioning at (and release from) the release site depended on Unc13A while BRP played a less pronounced role in this, or more upstream of the process. The finding that evoked SV release scaled with BRP levels was not new, as it had been shown before (Peled and Isacoff, 2011; Muhammad et al., 2015). In addition to showing that spontaneous release also depended on BRP and Unc13A levels, we showed that this was due to Unc13A by making use of the *unc13A*^{null} mutant. Not long after our study had been published, the role of Unc13 as the release site generating molecule could be shown in mammalian synapses as well (Sakamoto et al., 2018).

3.4.4 Addition of Unc13 to the release machinery under physiological challenge

A defining property of the synapse is its ability to respond to changing demand for its activity by plastically increasing or decreasing its connection strength. This mechanism termed synaptic plasticity ensures the viability and maintenance of synaptic connection strength under challenges. A naturally occurring compound has helped in investigating this: The *Philanthus* genus of solitary wasps preys on different bee species by injecting them with a paralyzing venom. A polyamine compound identified in the venom of *P. triangulum*, δ-philanthotoxin (PhTX-433, Piek, 1982; Eldefrawi et al., 1988), has been useful to research in synapse physiology and plasticity as it partially blocks postsynaptic ionotropic glutamate receptors persistently and use-dependently in *Drosophila* (Frank et al., 2006). To a similar end, the NMDA-receptor blocking compound Dizocilpine/MK-801 (Clineschmidt et al., 1982) is used to study the mechanism in mammalian synapses (Atasoy et al., 2008). In both cases, plasticity consists of an increase in presynaptic NT release to counteract the decrease in postsynaptic NT sensing to maintain signaling at physiological levels. It is still unclear how postsynaptic disturbances are retrogradely communicated to the presynapse, and how much of the plastic response is based on post- vs presynaptic alterations (e.g. by dynamically replacing blocked postsynaptic receptors). In our publication Böhme et al. (2019) my colleagues and I have elucidated a presynaptic mechanism of homeostatic plasticity. Electrophysiology, genetics, pharmacology, computational analysis, and super-resolution microscopy have enabled us to define the role of Unc13A in this vital pathway.

Processing high numbers of STED images acquired by my colleague Mathias Böhme and building on existing analysis, I showed that AZs contain geometrically ordered “packages” or “clusters” of Unc13A, BRP, and RBP, but not of Syx-1A or Unc-18 (although Syx-1A clusters had been postulated before by Ullrich et al., 2015). Additionally, synapses incorporated more clusters of these proteins when challenged to upregulate their signaling capability by PhTX within 10 minutes, or on a longer time scale when postsynaptic ionotropic glutamate receptors were genetically ablated. Expressing mutant versions of the kinesin-dependent transport adaptor protein Aplip1 (involved in transporting RBP to the AZ; Siebert et al., 2015) or the serine-arginine protein kinase srpk79D (suppressing the ectopic axonal formation of AZs; Johnson et al., 2009; Nieratschker et al., 2009) inhibited this effect, implying the need for protein transport in this rapid remodeling mechanism. Where this transport originates is unclear as yet, and invites further investigation into the role of microtubules and the actin cytoskeleton. A role for actin polymerization has been shown in our work, but without relating this role to the origin of transport. It is conceivable that extrasynaptic pools of inactive protein can be recruited during synaptic challenge. Interestingly, mutant flies lacking BRP did not show this active zone remodeling, but could still adapt to the challenge. However, in the chronic model lacking GluRIIA, AZ remodeling was necessary for plastic maintenance of synaptic strength. This shows that there are possibly two or more partly redundant mechanisms to ensure homeostatic plasticity on a presynaptic level.

3.5 Short-term plasticity in light of heterogeneous coupling distances

Some information about how a resting (e.g. naïve in regard to previous stimulation) synapse will respond to repetitive stimulation can be gathered by taking into account the initial release probability of a single SV (pV_r). This synaptic property is termed short-term plasticity and crucially influences its ability to uphold transmission when facing increased demand (Stevens and Wang, 1995). Under high-frequency stimulation, SV release can either decrease (short-term depression, STD) or increase (short-term facilitation, STF). This mainly depends on the availability and replenishment of SVs in the readily releasable pool and their coupling distances (Böhme et al., 2018). Synapses with many closely coupled SVs typically exhibit STF, while those with more distantly coupled or overall few SVs will show STD. STP also depends on the levels of basal and residual calcium, and present buffers (reviewed in Fioravante and Regehr, 2011). An appropriate measure for this is the paired pulse ratio (PPR) which is achieved by stimulating twice at defined inter-stimulus intervals (ISI) of few tens of ms, and dividing the strength of the second response by that of the first. Facilitating synapses will show a high PPR (>1) at short ISIs, while STD will lead to a low PPR (<1) at short ISIs. A high PPR then informs that the synapse had a lower initial pV_r (assuming similar pV_r for all SVs of the RRP), and its capability to release SVs rapidly increased after the first stimulus, while the opposite case is true for a low PPR. For our published work in Kobbersmed et al. (2020), we investigated this behavior at the *Drosophila* NMJ due to new findings we wanted to integrate into our computational model of the synapse, as explained below.

My contribution to this work, apart from initiating calcium simulations and building on the model from Böhme et al. (2016) by exploring SV replenishment and a second sensor, encompassed the experimental investigation of changes in presynaptic calcium influx over varying $[Ca^{2+}]_{ext.}$, as experiments investigating STP were also conducted at different $[Ca^{2+}]_{ext.}$. This approach allowed us to predict the temporal and spatial development of Ca^{2+} transients induced by APs, and how Ca^{2+}-dynamics and STP are affected by $[Ca^{2+}]_{ext.}$.

3.5.1 Heterogeneously distributed coupling distances in our model

As we found out that Unc13A constitutes the release site determining molecule (Reddy-Alla et al., 2017), and that the positioning of docked SVs as observed in EM follows the same distribution as this protein, we had to revise our model of calcium-driven SV release built for the computational work shown in Böhme et al. (2016). In that model we had assumed that all SVs were positioned circularly around the AZ center either at Unc13A or Unc13B distribution maxima derived from STED analysis. This assumption was partly based on earlier work by Nakamura et al. (2015), who proposed the "perimeter release model" of distinct SV-VGCC coupling distances, and on work of others (Meinrenken et al., 2002; Vyleta and Jonas, 2014; Keller et al., 2015). However, the observation that Unc13A distribution and localizations of docked SVs were near identical led us to the conclusion that we had to adapt our model to this distribution data, and we did so for the work published in Kobbersmed et al. (2020).

3.5.2 Different approaches to explain experimentally observed STF

Simulating the Ca^{2+}-dependence of NT release necessitates the presence of a suitable model. We started with the allosteric single-sensor model by Lou et al. (2005) which explains SV release by five-step calcium binding to Syt-1, with each step increasing pV_r. It became immediately obvious that the model, while capable of reproducing initial pV_r, not only failed to reproduce the experimentally observed facilitation, but led to strong depression at all simulated $[Ca^{2+}]_{ext.}$ (Figure 4 of Kobbersmed et al., 2020). We then investigated whether this could be solved by including SV replenishment (starting at 183 s^{-1} (Miki et al., 2016) and yielding 165.53 s^{-1} as the best fit) from an infinite pool that would act between stimuli, as done before by other labs (Wölfel et al., 2007; Miki et al., 2016). While this rescued the depression at higher $[Ca^{2+}]_{ext.}$, facilitation was still far below the experimental observation at low $[Ca^{2+}]_{ext.}$. Stochastic simulations performed by the first author allowed the comparison of experimental and modelled variances. Experimentally, these had been measured by my colleague Meida Jusyte over different $[Ca^{2+}]_{ext.}$. Analyzing release variance and comparing it to mean amplitudes at the respective $[Ca^{2+}]_{ext.}$ allows the determination of parameters such as the quantal size q, the number of release sites N, and the release probability pV_r as the measured

postsynaptic response (measured as the current I) is a product of these: $I = pV_r*q*N$ (Scheuss and Neher, 2001; Clements, 2003). As this fluctuation analysis allows the measurement of parameters that will vary with repetitive stimulation, it is an appropriate way of quantifying calcium-dependent STP. Stochastic simulations (stochasticity stemmed from SV choice, not VGCC gating) of this experiment showed excessive variance at high $[Ca^{2+}]_{ext.}$, further indicating that this model would not be able to explain the data. This is supposedly mainly due to the fact that, with equal replenishment rates over all $[Ca^{2+}]_{ext.}$, closely coupled SVs will be replenished in a similar fashion, leading to the same STP behavior over all $[Ca^{2+}]_{ext.}$. In our model shown in Böhme et al. (2016), we had not made the comparison to experimental fluctuation analysis, and the model was sufficient to explain experimental STF as it mainly relied on enough calcium bridging the singular coupling distances to either Unc13A or Unc13B and therefore increasing the pV_r of SVs remaining after the first stimulus.

Our next attempt to reproduce STF made use of the previous observations that a second release sensor may regulate SV release in a calcium dependent manner (Wen et al., 2010; Bacaj et al., 2013), and may do so especially after the first, synchronous release phase and therefore act on the subsequent release probability of SVs. This would require a slow onset and a high affinity for residual calcium. We therefore optimized kinetics of this second sensor but found that there was no situation in which it would act considerably during the second release phase without also influencing the first and releasing SVs asynchronously. Therefore, while it did slightly improve STF at low $[Ca^{2+}]_{ext.}$, we found that a second release sensor acting in conjunction with Syt-1 to enhance later phases of SV release by increasing pV_r of remaining SVs did not explain what we measured at the *Drosophila* NMJ. It is therefore our opinion that neither a replenishment rate alone nor a second sensor operating on the fusion reaction will lead to sufficient STF. Mechanisms based on an activity-dependent increase in pV_r were not sufficient in facilitating release between rapidly succeeding stimuli, but a calcium-dependent mechanism acting on the unpriming rate of SVs achieved this.

3.5.3 Differential facilitation requires a calcium-dependent mechanism

The above findings gave us the opportunity to explore a third possibility of a mechanism that leads to STF at low $[Ca^{2+}]_{ext.}$. We knew it was necessary to drastically upregulate the availability of SVs after an initial release phase when $[Ca^{2+}]_{ext.}$ was low, and this effect needed to decrease with higher $[Ca^{2+}]_{ext.}$ Such an effect could act on the rate with which SVs are primed for release. Therefore, we speculated that, in conjunction with rapid vesicle replenishment, a pathway might exist which would restrict SV unpriming at higher $[Ca^{2+}]_{ext.}$. This would effectively lead to a high initial pV_r at high $[Ca^{2+}]_{ext.}$ and a low initial pV_r at low $[Ca^{2+}]_{ext.}$, explaining the high facilitation at low $[Ca^{2+}]_{ext.}$ which we see in experiments. Importantly, it would do so not only close to the VGCC cluster, but at all coupling distances.

Taken together, these findings agree reasonably well with what has been reported by colleagues, while they expand the view of synaptic STP by an interesting dimension. Future studies will need to address the exact nature of this calcium dependent mechanism regarding its molecular correlates. Apart from synaptotagmin-7, it has been described that replenishment may be dependent on actin and myosin (Miki et al., 2016). However, it is unclear how these would regulate unpriming in a calcium-dependent fashion. A promising candidate for calcium-dependent maintenance of the RRP, as well as for the activation of release sites, which we have found to be nearly equally valid (although slightly more complex) to the calcium-dependent unpriming model, is calmodulin. This calcium-activated protein can bind to the primary release site determining factor Unc13 (Junge et al., 2004) and its binding might stabilize an inactivated form of the release site as loss of binding leads to an increased initial pV_r (Lipstein et al., 2013; Lipstein et al., 2017).

3.6 On the relations between evoked and spontaneous neurotransmission

My main experimental project presented in this thesis revolved around the question whether and how evoked and spontaneous SV release modes differ in terms of mechanistic and functional properties (Grasskamp et al., in preparation). Therefore, the last part of my discussion is dedicated to the investigation of this question over the last decades. Many groups have spent a significant amount of work on it (Atasoy et al., 2008; Hua et al., 2010; Peled and Isacoff, 2011; Melom et al., 2013) and hence, different opinions on this matter are easy to encounter. Generally, these opinions can be divided into two factions: one follows the notion that spontaneous release is uncoupled from evoked release and has its own biological functional role; the other notion is that spontaneous SV release is merely a byproduct of the machinery controlling evoked release, a synaptic “leak” so to say. While my results point mainly towards the latter, compelling arguments can be made for both sides. It is important to note that, while the synaptic proteins essential for SV exocytosis are very well conserved over animal phyla and even fungi (reviewed in Burkhardt, 2015), the function of spontaneous release may not be. Therefore, it is not necessarily a contradiction to find one role for it in mammalian and vertebrate synapses, and another or none in invertebrates. Additionally, as I will elaborate, the role and necessity for spontaneous release can even vary within the same organism, depending on the synapse type.

3.6.1 Investigating neurotransmission at single *Drosophila* NMJ synapses

Using a GCaMP-fluorescence based optophysiological assay developed by Peled and Isacoff (2011) and improved by Akerboom et al. (2012), Melom et al. (2013), Peled et al. (2014), and Newman et al. (2017), we investigated single AZs in different stages of maturity for their mechanisms of quantal spontaneous and evoked SV release events (Reddy-Alla et al., 2017 and Grasskamp et al.,

in preparation). The green fluorescent calcium sensor GCaMP can be expressed in the postsynaptic muscle using the UAS/Gal4 system (Brand and Perrimon, 1993; Phelps and Brand, 1998) and a myristoylation sequence for membrane targeting (Melom et al., 2013; Muhammad et al., 2015). In our studies (Reddy-Alla et al., 2017 and Grasskamp et al., in preparation), we wanted to make sure that the protein was constantly expressed in the postsynaptic muscle. Therefore, we used a form of the protein that was constitutively expressed in the muscle (work performed by my colleague Christina Beis). Type 1 NMJs of 3rd instar larvae exhibit a large heterogeneity in the maturity of single synapses (Guerrero et al., 2005). This allows the concurrent measurement of synaptic activity in structurally different active zones. The assay depends on the permeability of postsynaptic ionotropic glutamate receptors for calcium (Chang et al., 1994). These receptors are activated by glutamate and quisqualate but not by either NMDA, AMPA, or kainate (Han et al., 2015). Furthermore, they mainly exist in two compositions at the fly NMJ, consisting of either GluRIIA or GluRIIB in a heterotetramer with C/D/E subunits (Qin et al., 2005) in conjunction with the accessory subunit neto (Kim et al., 2012).

This assay exhibits an inherent detection threshold, only enabling the detection of events that pass it by showing a minimum fluorescence brightness. The detection threshold is also the reason we cannot make statements about the dependence of spontaneous SV exocytosis on extracellular calcium concentrations. However, we did use a calcium titration experiment to show that we do not hit a fluorescence ceiling (i.e. saturation of the sensor and limited dynamic range) at 1.5 mM $[Ca^{2+}]_{ext.}$, and therefore likely observe quantal events.

Another caveat of this assay stems from the uncertainty of the calcium source that triggers GCaMP fluorescence transients. Influx of calcium through gating iGluRs may trigger initial fluorescence but may also lead to further release of calcium from internal stores (like the sarcoplasmic reticulum), possibly cloaking the real time course of single SV release events. However, even considering this possible confounder, the on- and offset of the GECIs (GCaMP6: Kobbersmed et al., 2020; GCaMP5: Reddy-Alla et al., 2017 and Grasskamp et al., in preparation) used in our experiments were fast enough to alleviate the doubts imposed by this because these sensors exhibit kinetics suitable for this type of experiment (Dana et al., 2019), as on- and offset of fluorescence signals happen within a few 100 ms. Further, the identical shape of the average fluorescence signal in spontaneous and AP-evoked experiments confirms the quantal quality of the assay.

Lastly, it must be taken into consideration that any calcium binding protein may act as a calcium buffer. This is apparently especially relevant when expressing the sensor GCaMP6m presynaptically, as it can then decrease SV release probability and alter short term plasticity in central synapses (Singh et al., 2018). Therefore, one should exercise caution in basing SV release analysis on presynaptically expressed GCaMP or other calcium binding proteins. As our only experiment involving presynaptic GCaMP (Kobbersmed et al., 2020) did not measure SV release but merely calcium-influx dependent increases in fluorescence strength, this caveat does not play into our analysis. In our experiments

involving postsynaptic GCaMP expression, SV release should not be hindered by postsynaptic calcium buffering. Still, development of the muscle might be altered by this, albeit supposedly to a minor extent due to the high affinity of GCaMP for calcium in the low hundred nM range (Akerboom et al., 2012; Chen et al., 2013), and its confined localization at the membrane.

3.6.2 Synchronous and asynchronous neurotransmitter release

The synchronous release of many SVs after nerve stimulation can happen within fractions of a millisecond after the arrival of the AP at the presynapse, and lead to a postsynaptic response within 1-2 milliseconds (Fatt and Katz, 1951; Borst and Sakmann, 1996). However, AP-evoked neurotransmitter release through SV exocytosis is not necessarily this strictly temporally coupled to the stimulus. Asynchronous SV release can persist for several hundred milliseconds after the end of the stimulus (Hefft and Jonas, 2005) (Reviewed in: Rozov et al., 2019 and Kaeser and Regehr, 2014), but is not prevalent at the wild type *Drosophila* NMJ. The calcium sensor synaptotagmin-7 has been implicated in specifically regulating asynchronous release (Wen et al., 2010; Bacaj et al., 2013). However, earlier reports on its calcium dependence have been contradictory (Maximov et al., 2008) which the lab claims may be due to developmental compensation ("earlier experiments involved constitutive KOs that may have elicited developmental compensation" - Maximov et al., 2008), and its role remains disputed. A protein containing two calcium-binding C_2-like domains, Doc2, is another candidate for the calcium-dependent regulation of asynchronous release (Yao et al., 2011). However, it is more strongly implicated in the regulation of spontaneous release as described after this section. In addition, the N-terminal mutant of Unc13A has been shown to lead to asynchronous release due to the erratic redistribution of release sites over the AZ (Reddy-Alla et al., 2017). As the experiments shown in Grasskamp et al. (in preparation) happened in absence of any of these mutations, and nerve stimulation was independent of the CNS, it is sufficiently certain that the SV release events I observed represent what is commonly viewed as spontaneous release. Moreover, and however unlikely, the possibility to detect asynchronous instead of spontaneous release adds to the importance of measuring spontaneous activity before AP-evoked activity as shown in figure 4 of the manuscript.

3.6.3 Properties of spontaneous neurotransmission

Spontaneous, single SV neurotransmission events happening without any preceding stimulus have been famously observed by Paul Fatt and Bernard Katz as early as 1950 (Fatt and Katz, 1950) with an elaboration shortly after (Fatt and Katz, 1952). These quantal packages of neurotransmitter were then determined to underlie the compound response measured in the postsynapse (del Castillo and Katz, 1954). Since then, few putative roles of this NT mode in physiology have been found. These include the modulation of evoked release events via interneurons (Carter and Regehr, 2002),

the maintenance of synapses (McKinney et al., 1999) and their function (Sutton et al., 2006), and an influence on NMJ development (Huntwork and Littleton, 2007; Ataman et al., 2008; Choi et al., 2014).

Spontaneous SV release can be directly influenced by pharmacological agents, for example phorbol esters which target PKC (PMA/TPA: Publicover, 1985, PDBu: Malenka et al., 1987), cyclic GMP targeting PKG (Arancio et al., 1995), and forskolin scaling PKA activity by formation of cyclic AMP (Capogna et al., 1995). These essential signaling proteins have been implicated in the modulation of long-term potentiation (LTP) (PKC: Linden and Routtenberg, 1989, PKA: Frey et al., 1993, Nayak et al., 1998, PKG: Son et al., 1998), which is thought to be the major neural correlate in memory formation and consolidation. However, little is known about whether the observed increased spontaneous release frequency has any causal relationship with the induction of LTP or is simply a side effect of enhanced signaling.

Unlike evoked SV exocytosis, spontaneous SV release is not unequivocally accepted to depend on or scale with increasing $[Ca^{2+}]_{ext.}$ concentrations, although it has been shown to depend on intracellular calcium levels (Nosyreva and Kavalali, 2010; Wierda and Sørensen, 2014). Previous work shows a direct correlation (Xu et al., 2009) and indicates a role for the G-protein coupled calcium-sensing receptor CaSR (Vyleta and Smith, 2011). In our experiments, we could not show this scaling as the calcium dependent fluorescence assay prohibits such an analysis; the more extracellular calcium we add to the hemolymph-like extracellular solution, the more events we are likely to see due to an inherent detection threshold (as the maximum fluorescence of single events increases). This problem could be circumvented by employing iGluSnfr, a fluorescent glutamate indicator (Marvin et al., 2013). Electrophysiological measurements in the *Drosophila* NMJ may not be a valid approach to measure this as the assay lacks crucial spatial resolution and would not differentiate between individual synapses that might show decreased spontaneous SV release and those that show elevated release.

If spontaneous release depended on calcium concentration spikes induced by Ca^{2+} influx through VGCCs, then it is conceivable that this effect is mediated by a calcium sensor such as Syt-1, as has been postulated (Xu et al., 2009; Bai et al., 2016). However, a common notion is that Syt-1 acts as a clamp on spontaneous SV release (Yoshihara and Littleton, 2002), questioning its role as a sensor for spontaneous release. In Xu et al., 2009, it was argued that the increased spontaneous NT release upon Syt-1 deletion was due to the activation of a second sensor. A molecule harboring two calcium binding C_2 domains (double C_2-like domain containing protein beta, Doc2β) has been shown to mediate spontaneous release (Groffen et al., 2010). Although later results contested its calcium dependence by rescuing spontaneous release with a Doc2β mutant lacking calcium binding domains (Pang et al., 2011), a growing body of evidence indicates that this sensor does act in calcium dependent spontaneous SV exocytosis (Courtney et al., 2018; Bourgeois-Jaarsma et al., 2019). At frog NMJs,

single VGCCs can trigger SV release (Shahrezaei et al., 2006). Interestingly, the stochastic gating of VGCCs has been shown to account for as much as 50% of all spontaneous glutamate release at central mammalian synapses (Ermolyuk et al., 2013), further indicating a role for extracellular calcium in spontaneous SV release, and fitting our observations that the blockage of calcium entry via cadmium decreases spontaneous NT.

Based on these findings by other groups, spontaneous release can easily be conceived as a calcium dependent initiator and consolidator of pre-/postsynaptic coupling and synapse maintenance at nascent or immature connections. At NMJs of late-stage *Drosophila* larvae, however, neurotransmission is supposedly a recurring and regular constant simply due to the sustained movement of the foraging larva. Therefore, it is as easily imaginable that spontaneous release is indeed a byproduct of the developed machinery dedicated to fast and efficient evoked SV release in this specific case. We did see a small subset of AZs (~6% of all investigated AZs) that showed no participation in AP-evoked release over the course of the experiment ("survival analysis" in Grasskamp et al., in preparation). Despite their low relative abundance, it would be interesting to investigate their molecular composition to determine whether these synapses are simply in an early developmental stage, or if they serve as a potentially vital "pool" of spontaneously active AZs. It remains to be investigated whether *Drosophila* CNS dendrites require the spontaneous presynaptic release of NT as a "ping signal" to maintain the connection at sparsely used synapses.

3.6.4 The dependence of spontaneous release on synaptic factors

It is a well-documented and consistent observation that AP-evoked release probability scales with levels of BRP at the fly NMJ (Kittel et al., 2006; Wagh et al., 2006), with evidence at the single synapse level (Peled et al., 2014; Muhammad et al., 2015; Reddy-Alla et al., 2017). The situation is less clear for spontaneous, AP-independent SV release. As shown in Reddy-Alla et al. (2017) and Grasskamp et al. (in preparation), we do see a marked scaling between several AZ proteins (including BRP) and spontaneous activity at individual synapses. Interestingly, we could show a scaling of spontaneous activity with Unc18/ROP levels, but no such relation of evoked release. It has been shown before that Unc18 can bind syntaxin-1 in its closed, inactive conformation and therefore inhibit SNARE complex assembly (Misura et al., 2000). This may explain why, for AZs containing the highest levels of Unc18, evoked activity is reduced compared to those AZs with intermediate levels of Unc18. It might be further interesting to know if the used antibody against Syx-1A is selective for the open conformation, which could explain the high dependence of both release modes on high levels of Syx-1A seen in our experiments. However, the wide distribution of Syx-1A IHC-signal outside of AZs implies mixed selectivity for closed and open conformation, but this needs to be verified. An antibody selective for the closed conformation should then show similarly (i.e. similar to Unc18)

attenuated influence of high Syx-1A levels. A constitutively open form of Syx-1A, like the one used in *C. elegans* (Hammarlund et al., 2007), could additionally be used to test this hypothesis.

Furthermore, we could show a near-perfect positive correlation between spontaneous and evoked activity at the average synapse, implying the use of shared SV pools in both release modes. Preceding studies have not found the dependence of spontaneous activity on the scaffold protein BRP (Peled et al., 2014) or on release probability (Melom et al., 2013; Peled et al., 2014). In fact, the dependence of spontaneous release on BRP levels was shown to be strongly negative in Peled et al., 2014. This seeming contradiction is easily explained by the experimental setup and way of analysis, as described below.

The positive correlation of spontaneous SV release with levels of synaptic release determinants like Syx-1A, Unc13A and BRP as previously shown for evoked release (Reddy-Alla et al., 2017) is a seemingly intuitive notion, if spontaneous release is indeed as calcium-dependent as we postulate, and largely relies on the same synaptic machinery as evoked release. As BRP acts in the recruitment of SVs to the AZ (Scholz et al., 2019), higher levels of BRP should lead to higher numbers of SVs close to the central VGCC. Congruently, we show a decrease in electrophysiologically and optically quantified spontaneous NT event frequency when blocking VGCCs with $CdCl_2$, but not when blocking VGSCs with TTX (figure 2 in Grasskamp et al., in preparation). Upon stochastic opening of VGCCs, these closely-coupled SVs might be the first to be released, even with minute increases in intracellular calcium levels. Super-resolution live imaging studies could be used to test this hypothesis in conjunction with high acquisition speed and fluorescent tags of SVs (e.g. by tagging the vesicular glutamate transporter vGlut) or the pH-dependent pHluorin fluorescence assay. If this positional dependence of spontaneous release was the case, SV release would be heavily reliant on the naivety of a single synapse in regard to previous evoked events. Therefore, the observed negative correlation between BRP levels and spontaneous activity found by Peled et al. (2014) is likely due to the method of measurement. Additionally, we have acquired experimental evidence not shown in this thesis indicating that the used *rab3*^{null} genotype is exacerbating this effect through unknown molecular mechanisms. Peled et al. argue that the concentration of evoked release at the subset of BRP-rich AZs in this genotype allows the dissection of spontaneous release at those AZs without BRP, but it is unclear how those AZs are defined. Without a reliable marker for AZs lacking BRP, it seems hard to conclude how spontaneous release is regulated there. In the study, results in figure 4 were acquired by evoking SV release once at $t \approx 1.2$ s (section “Single-pulse stimulation” in supplementary method description) and then imaging miniature transmission events after that, for a total time of 4-13 s. Our data (shown in Reddy-Alla et al., 2017 figure S2 panel E) indicates that 46.4% of all analyzed AZs will engage in AP-evoked SV release over the course of the whole experiment, with 16.6% showing both AP-evoked and spontaneous release. This latter, lower number is heavily dependent on the timeframe of the experiment and therefore likely represents a low estimate. A study by Atasoy et al. (2008)

even shows an overlap in 79% of observed synapses, although they warn of an overestimation due to selection bias. If SV pools are shared between the two modes, it is therefore imperative to separate the measurements of AP-evoked and spontaneous release. In our experiments using wild type flies, we have measured spontaneous release before stimulating release. To corroborate our suspicion, we compared this to measurements of spontaneous release in between stimuli applied every 5 s. We found a strong decrease in the dependence of spontaneous activity on BRP levels, indicating a sharing of SV pools between the release modes (Figure 4 in Grasskamp et al., in preparation) as well as confirming the notion that spontaneous SV release scales with BRP levels when measured at naïve synapses. It might of course influence this conclusion if a considerable amount of spontaneous release happened outside of BRP-positive AZs. Still, as BRP is so well characterized as the AZ marker in *Drosophila*, we have used it as the universal marker for AZ locations and did not see evidence for a large amount of extrasynaptic spontaneous SV release.

3.6.5 Postsynaptic crossover of release mode detection

Apart from the degree of interdependence between AP-evoked and spontaneous release on the presynaptic level, it has been postulated that postsynaptic sensing of NT is specific to either release mode (Atasoy et al., 2008; Peled et al., 2014). Both cited studies employed a similar approach to investigate this: use-dependent glutamate receptor blockers (PhTx by Peled et al. or MK-801 by Atasoy et al.) were applied and it was tested whether stimulation of glutamate release would have an effect on the detection of miniature NT events that markedly differs from the non-stimulation cohort. Both studies concluded that this was not the case, indicating the existence of non-overlapping subpopulations of glutamate receptors on the postsynapse. Using the approach chosen by Peled et al., albeit with 100x higher stimulation frequency (10 Hz instead of 0.1 Hz), we contest this view for the case of *Drosophila* NMJ 1b bouton synapses. These experiments were conducted by my colleague Anthony McCarthy. In figure 1 of the study by Peled et al., mEPSP amplitudes decrease drastically with PhTx treatment, regardless of the presence of stimulation. However, this conclusion is not supported by our data, as we added another control. We compared mEPSP amplitudes under +PhTx, +stimulation as well as +PhTx, -stimulation conditions to those under +PhTx instead of to those under –PhTx conditions. This was necessary as the high initial decrease of synaptic transmission upon PhTx treatment would otherwise cloak the effect brought about by stimulation. Glutamate activating a glutamate receptor will allow PhTx to block further activation. Hence, an initial drop in mEPSP amplitudes and, to a lower extent, frequencies is apparent when comparing –PhTX with +PhTx conditions, showing the necessity for our intermittent analysis. The authors do state that they are aware of this possible confounder. However, its extent may have been underestimated and hence led to different conclusions than ours. Lastly, the study used PhTx (which induces homeostatic mechanisms within few minutes; Davis and Müller, 2015; Böhme et al., 2019) over a long time period of 25 minutes, while our experiments were conducted within 40 seconds

after PhTx application. To my understanding, the additional control, the shorter timeframe of the experiment and the higher stimulation applied in our case should explain the discrepancy between results. The study in mammalian hippocampal synapses by Atasoy et al. came to the conclusion that PSDs with areas above 0.2 μm² allow the spatially separated detection of glutamate released at the same AZ by distinct receptor fields. It remains unclear how regulated dispersion of NT in the synaptic cleft, or the suggested spatially distinct positioning of SVs at the AZ, would be mediated. Rather than activating distinct sets of postsynaptic receptors, the specific effects of spontaneous release in maturation and signaling may be mediated by a dose-dependent effect of NT release on the same receptors.

4 Conclusions and outlook

The merging of computational and experimental methods provides a powerful way of developing and testing hypotheses. By my own experimental work, and by complementing the experimental work of my colleagues with mathematical models and optimizations, I have contributed to the characterization of the *Drosophila* NMJ in some detail.

In doing so, we have determined that SV release at the active zone is mediated by two distinctly located isoforms of Unc13, namely Unc13A and Unc13B (Böhme et al., 2016). We could show that the experimentally determined coupling distances of these proteins (Unc13A: ~70 nm; Unc13B: ~120 nm) were in sufficient agreement with our semi-complex model (Unc13A: 76.8 nm; Unc13B: 145 nm). Furthermore, our model generated the testable hypothesis that AP-induced calcium influx through the VGCC would be increased by a factor of 1.72 in *unc13A*^{null} mutants (Böhme et al., 2016), which is very well in line with known synaptic compensation mechanisms (Zhao et al., 2011; Gratz et al., 2019).

We then went on to provide further proof for the fact that Unc13 is the decisive protein in defining the SV release site (Reddy-Alla et al., 2017). This release site determinant had been sought after over the last decades, and our observations were confirmed at central mammalian synapses shortly after our work had been published (Sakamoto et al., 2018). Using single-AZ fluorescence imaging, my experimental contribution to this work served to show that spontaneous and AP-evoked NT release quantitatively depended on the presence of Unc13A (Reddy-Alla et al., 2017).

Further elaborating on the critical role of Unc13A in synaptic release, we then investigated its role in the maintenance of synaptic homeostasis. We found that its acute recruitment to the AZ is essential to compensate for signal transmission disturbances (Böhme et al., 2019). Pharmacological as well as genetic disturbance of postsynaptic NT sensing led to presynaptic increases in Unc13A levels. Additionally, genetic removal of Unc13A, as well as its genetically induced mislocalization, abolished signal potentiation. Building on previous unpublished work from our lab, I developed a

computational method of counting Unc13A clusters and could show its dynamic incorporation into the AZ upon neurotransmission decrease. This gave us insight into the fine structure of the *Drosophila* NMJ synapse and provided evidence for the role of Unc13 in transmission strength maintenance and scaling, even influencing short-term memory formation. It remains to be seen how this translates to memory formation and consolidation in mammals, and might pose a promising target for therapeutics aiming at the alleviation of memory loss. Furthermore, from a therapeutic perspective and in the context of neuromuscular signaling, it seems especially interesting that Unc13 is heavily implicated in the risk of amyotrophic lateral sclerosis (ALS) and associated with frontotemporal dementia (FTD) (Diekstra et al., 2014), and a gain of function variant has been shown to cause dyskinesia in a human patient (Lipstein et al., 2017). If the current pace of developments in personalized medicine persists, this protein might soon be a target for acute genetic rescue, possibly involving the revolutionary CRISPR/Cas9 system.

After our attempts to accurately model neurotransmission at the fly synapse (Böhme et al., 2016), it became increasingly clear that a central assumption of our model was an oversimplification, although this does not disqualify our initial findings. We had assumed that SVs would be positioned in relation to the VGCC cluster as proposed by Nakamura et al. (2015), where a perimeter around the VGCC cluster sharply defines the SV-VGCC coupling distances. While this may hold true for central mammalian synapses, it is evident from super-resolution analysis in *Drosophila* (Böhme et al., 2016; Reddy-Alla et al., 2017) that Unc13A and SV positions follow a near-identical (in regard to each other and when 2D-EM distribution data was integrated over the circular area of the AZ) broad distribution in regard to VGCCs at the AZ center as shown in Kobbersmed et al. (2020). While the peak of both distributions is where we proposed it to reside (~76 nm) we could not reproduce short-term facilitation with our model when assuming this distribution. Importantly, this was also not possible when including a facilitation sensor mainly acting on subsequent SV release. Instead, it was necessary to introduce a rapid, calcium-dependent mechanism blocking unpriming, which served to overfill the pool of readily releasable SVs that had been depleted with the first stimulus.

In a related project, my computational work served to decipher the effects of structural differences in small lipids on cellular signaling (Schuhmacher et al., 2020). Photochemically liberating caged DAG compounds at the outer membrane leaflet of cultured cells in the presence of an intracellular fluorescent sensor allowed building a kinetic model and determining single lipid kinetics. Subtle structural differences turned out to heavily influence cellular localization and the recruitment of a fluorescently tagged PKC-C1 domain to the membrane after uncaging. This is likely to affect the properties of neuronal signal transmission as well (Postila and Róg, 2020), as has already been shown by others (Di Paolo et al., 2004) and our lab (Walter et al., 2017). Future studies might combine the uncaging of DAG at neuronal cells *in vitro* or *in vivo*, with kinetic quantifications and long-term optical or electrophysiological assays to determine the details of lipid influence on SV exocytosis.

This might be promising for future attempts to link metabolic diseases and neural symptoms.

My main experimental project attempted to dissect the molecular determinants of evoked and spontaneous SV release with respect to their functional overlap (Grasskamp et al, in preparation). I made use of the genetically encoded fluorescent calcium sensor GCaMP (Nakai et al., 2001; Akerboom et al., 2012) to quantify single synapse SV release. With the help and expertise of my colleagues I could show that, while some molecular components (like Unc18/ROP and voltage-gated sodium channels) influence only either mode, many signaling factors are shared between the two release modes. This includes SV pools, the scaffold molecules BRP, Unc13A, and Syntaxin 1A, as well as voltage gated calcium channels and postsynaptic glutamate receptors. It is conceivable that future studies might apply this concept in central synapses with more detail than is available so far, although many studies have already pointed at the function of spontaneous release in synapse maintenance (McKinney et al., 1999; Sutton et al., 2006), potentiation of evoked release (Kombian et al., 2000), and development (Choi et al., 2014). It would be interesting to correlate the number of release sites seen in super-resolution microscopy with results from the GCaMP assay. Further, spontaneous voltage changes in the membrane leading to spontaneous calcium influx and SV release could be imaged using genetically encoded voltage sensors like Arclight (Jin et al., 2012). To uncouple the assay from the calcium-dependent GCaMP, one could target the fluorescent glutamate indicator iGluSnfr (Marvin et al., 2013) to the postsynaptic membrane. As mentioned before, our findings are restricted to frequently firing NMJ synapses, and results might differ from those found at central synapses.

The further advancement of available methods in neuroscience, and their diligent use, will inevitably bring forth a great number of insights into the molecular underpinnings of synaptic signal transmission. Likewise, fundamental research in “simpler” organisms like *Drosophila* will play a considerable role in the determination of physiologically relevant components of the synapse and neurological disease risk factors. With my work, I hope to have contributed to this process to the best of my abilities and remain confident in its value to the scientific community.

References

Ackermann F, Waites CL, Garner CC (2015) - *Presynaptic active zones in invertebrates and vertebrates*, EMBO reports 16(8):923–938. doi:10.15252/EMBR.201540434.

Adams SR and Tsien RY (1993) - *Controlling cell chemistry with caged compounds*, Annual review of physiology 55:755–784. doi:10.1146/ANNUREV.PH.55.030193.003543.

Akaike H (1974) - *A new look at the statistical model identification*, IEEE Transactions on Automatic Control 19(6):716–723. doi:10.1109/TAC.1974.1100705.

Akerboom J, Chen T-W, Wardill TJ, Tian L, Marvin JS, Mutlu S, Calderón NC, Esposti F, Borghuis BG, Sun XR, Gordus A, Orger MB, Portugues R, Engert F, Macklin JJ, Filosa A, Aggarwal A, Kerr RA, Takagi R, Kracun S, Shigetomi E, Khakh BS, Baier H, Lagnado L, Wang SS-H, Bargmann CI, Kimmel BE, Jayaraman V, Svoboda K, Kim DS, Schreiter ER, Looger LL (2012) - *Optimization of a GCaMP calcium indicator for neural activity imaging*, The Journal of Neuroscience 32(40):13819–13840. doi:10.1523/JNEUROSCI.2601-12.2012.

Akerboom J, Rivera JDV, Guilbe MMR, Malavé ECA, Hernandez HH, Tian L, Hires SA, Marvin JS, Looger LL, Schreiter ER (2009) - *Crystal structures of the GCaMP calcium sensor reveal the mechanism of fluorescence signal change and aid rational design*, Journal of Biological Chemistry 284(10):6455–6464. doi:10.1074/JBC.M807657200.

Alabi AA and Tsien RW (2012) - *Synaptic vesicle pools and dynamics*, Cold Spring Harbor perspectives in biology 4(8):a013680. doi:10.1101/CSHPERSPECT.A013680.

Alberts, B (2008) - *Molecular biology of the cell*. 5th ed. New York: Garland Science.

Albertson DG and Thomson JN (1976) - *The pharynx of Caenorhabditis elegans*, Philosophical transactions of the Royal Society of London. Series B, Biological sciences 275(938):299–325. doi:10.1098/RSTB.1976.0085.

Allen JA, Halverson-Tamboli RA, Rasenick MM (2007) - *Lipid raft microdomains and neurotransmitter signalling*, Nature Reviews Neuroscience 8(2):128–140. doi:10.1038/NRN2059.

Ammar MR, Kassas N, Chasserot-Golaz S, Bader M-F, Vitale N (2013) - *Lipids in Regulated Exocytosis: What are They Doing?*, Frontiers in endocrinology 4:125. doi:10.3389/FENDO.2013.00125.

Andreae LC, Fredj NB, Burrone J (2012) - *Independent vesicle pools underlie different modes of release during neuronal development*, The Journal of Neuroscience 32(5):1867–1874. doi:10.1523/JNEUROSCI.5181-11.2012.

Arancio O, Kandel ER, Hawkins RD (1995) - *Activity-dependent long-term enhancement of transmitter release by presynaptic 3',5'-cyclic GMP in cultured hippocampal neurons*, Nature 376(6535):74–80. doi:10.1038/376074A0.

Aravamudan B, Fergestad T, Davis WS, Rodesch CK, Broadie K (1999) - *Drosophila UNC-13 is essential for synaptic transmission*, Nature Neuroscience 2(11):965–971. doi:10.1038/14764.

Aristotle and Ogle, W (1911) - *De partibus animalium, tr*. Oxford: Clarendon Press (The works of Aristotle translated into English).

Aristotle and Peck, AL (1943) - *Generation of animals, with an English translation by A.L. Peck*. Cambridge: Harvard University Press.

Ataman B, Ashley J, Gorczyca M, Ramachandran P, Fouquet W, Sigrist SJ, Budnik V (2008) - *Rapid Activity-Dependent Modifications in Synaptic Structure and Function Require Bidirectional Wnt Signaling*, Neuron 57(5):705–718. doi:10.1016/J.NEURON.2008.01.026.

Atasoy D, Ertunc M, Moulder KL, Blackwell J, Chung C, Su J, Kavalali ET (2008) - *Spontaneous and evoked glutamate release activates two populations of NMDA receptors with limited overlap*, The Journal of Neuroscience 28(40):10151–10166. doi:10.1523/JNEUROSCI.2432-08.2008.

Augustin I, Rosenmund C, Südhof TC, Brose N (1999) - *Munc13-1 is essential for fusion competence of glutamatergic synaptic vesicles*, Nature 400(6743):457–461. doi:10.1038/22768.

Augustine GJ and Kasai H (2007) - *Bernard Katz, quantal transmitter release and the foundations of presynaptic physiology*, The Journal of physiology 578(Pt 3):623–625. doi:10.1113/JPHYSIOL.2006.123224.

Bacaj T, Wu D, Yang X, Morishita W, Zhou P, Xu W, Malenka RC, Südhof TC (2013) - *Synaptotagmin-1 and synaptotagmin-7 trigger synchronous and asynchronous phases of neurotransmitter release*, Neuron 80(4):947–959. doi:10.1016/J.NEURON.2013.10.026.

Bahi A, Fizia K, Dietz M, Gasparini F, Flor PJ (2012) - *Pharmacological modulation of mGluR7 with AMN082 and MMPIP exerts specific influences on alcohol consumption*

and preference in rats, Addiction biology 17(2):235–247. doi:10.1111/J.1369-1600.2010.00310.X.

Bai H, Xue R, Bao H, Zhang L, Yethiraj A, Cui Q, Chapman ER (2016) - *Different states of synaptotagmin regulate evoked versus spontaneous release*, Nature Communications 7(1):1–9. doi:10.1038/NCOMMS10971.

Bai J and Pagano RE (1997) - *Measurement of spontaneous transfer and transbilayer movement of BODIPY-labeled lipids in lipid vesicles*, Biochemistry 36(29):8840–8848. doi:10.1021/BI970145R.

Baluska F, Volkmann D, Barlow PW (2004) - *Eukaryotic cells and their cell bodies: Cell Theory revised*, Annals of botany 94(1):9–32. doi:10.1093/AOB/MCH109.

Barclay JW, Craig TJ, Fisher RJ, Ciufo LF, Evans GJO, Morgan A, Burgoyne RD (2003) - *Phosphorylation of Munc18 by protein kinase C regulates the kinetics of exocytosis*, Journal of Biological Chemistry 278(12):10538–10545. doi:10.1074/JBC.M211114200.

Basu J, Betz A, Brose N, Rosenmund C (2007) - *Munc13-1 C1 domain activation lowers the energy barrier for synaptic vesicle fusion*, The Journal of Neuroscience 27(5):1200–1210. doi:10.1523/JNEUROSCI.4908-06.2007.

Bear, MF; Connors, BW; Paradiso, MA (2012) - *Neurowissenschaften:* Ein grundlegendes Lehrbuch für Biologie, Medizin und Psychologie. 3. Aufl., Nachdr. Heidelberg: Spektrum, Akad. Verl.

Bellen HJ, Tong C, Tsuda H (2010) - *100 years of Drosophila research and its impact on vertebrate neuroscience: a history lesson for the future*, Nature Reviews Neuroscience 11(7):514–522. doi:10.1038/NRN2839.

Bennett MR (1999) - *The early history of the synapse: from plato to sherrington*, Brain Research Bulletin 50(2):95–118. doi:10.1016/S0361-9230(99)00094-5.

Betts JG, Young KA, Wise JA, Johnson E, Poe B, Kruse DH, Korol O, Johnson JE, Womble M, DeSaix P (2013) - *Anatomy and Physiology*. OpenStax. Houston, TX, USA. Available online under https://openstax.org/details/books/anatomy-and-physiology, last updated: 17.02.2020, last checked: 08.03.2020.

Betz A, Ashery U, Rickmann M, Augustin I, Neher E, Südhof TC, Rettig J, Brose N (1998) - *Munc13-1 Is a Presynaptic Phorbol Ester Receptor that Enhances Neurotransmitter Release*, Neuron 21(1):123–136. doi:10.1016/S0896-6273(00)80520-6.

Betzig E, Patterson GH, Sougrat R, Lindwasser OW, Olenych S, Bonifacino JS, Davidson MW, Lippincott-Schwartz J, Hess HF (2006) - *Imaging intracellular fluorescent proteins at nanometer resolution*, Science 313(5793):1642–1645. doi:10.1126/SCIENCE.1127344.

Bier E, Harrison MM, O'Connor-Giles KM, Wildonger J (2018) - *Advances in Engineering the Fly Genome with the CRISPR-Cas System*, Genetics 208(1):1–18. doi:10.1534/GENETICS.117.1113.

Bill CA and Vines CM (2020) - *Phospholipase C*, Advances in experimental medicine and biology 1131:215–242. doi:10.1007/978-3-030-12457-1_9.

Bock O (2013) - *Cajal, Golgi, Nansen, Schäfer and the neuron doctrine*, Endeavour 37(4):228–234. doi:10.1016/J.ENDEAVOUR.2013.06.006.

Böhme MA, Beis C, Reddy-Alla S, Reynolds E, Mampell MM, Grasskamp AT, Lützkendorf J, Bergeron DD, Driller JH, Babikir H, Göttfert F, Robinson IM, O'Kane CJ, Hell SW, Wahl MC, Stelzl U, Loll B, Walter AM, Sigrist SJ (2016) - *Active zone scaffolds differentially accumulate Unc13 isoforms to tune Ca(2+) channel–vesicle coupling*, Nature Neuroscience 19(10):1311–1320. doi:10.1038/NN.4364.

Böhme MA, Grasskamp AT, Walter AM (2018) - *Regulation of synaptic release-site Ca2+ channel coupling as a mechanism to control release probability and short-term plasticity*, FEBS letters 592(21):3516–3531. doi:10.1002/1873-3468.13188.

Böhme MA, McCarthy AW, Grasskamp AT, Beuschel CB, Goel P, Jusyte M, Laber D, Huang S, Rey U, Petzoldt AG, Lehmann M, Göttfert F, Haghighi P, Hell SW, Owald D, Dickman D, Sigrist SJ, Walter AM (2019) - *Rapid active zone remodeling consolidates presynaptic potentiation*, Nature Communications 10(1085). doi:10.1038/S41467-019-08977-6.

Bolboacă SD, Jäntschi L, Sestraş AF, Sestraş RE, Pamfil DC (2011) - *Pearson-Fisher Chi-Square Statistic Revisited*, Information 2(3):528–545. doi:10.3390/INFO2030528.

Borroni MV, Vallés AS, Barrantes FJ (2016) - *The lipid habitats of neurotransmitter receptors in brain*, Biochimica et biophysica acta 1858(11):2662–2670. doi:10.1016/J.BBAMEM.2016.07.005.

Borst JG and Sakmann B (1996) - *Calcium influx and transmitter release in a fast CNS synapse*, Nature 383(6599):431–434. doi:10.1038/383431A0.

Bourgeois-Jaarsma Q, Verhage M, Groffen AJ (2019) - *Doc2b Ca2+ binding site mutants enhance synaptic release at rest at the expense of sustained synaptic strength*, Scientific reports 9(1):14408. doi:10.1038/S41598-019-50684-1.

Box, GEP and Draper, NR (1987) - *Empirical model-building and response surfaces* (Wiley series in probability and mathematical statistics : Applied probability and statistics).

Bracciali A, Brunelli M, Cataldo E, Degano P (2008) - *Stochastic models for the in silico simulation of synaptic processes*, BMC bioinformatics 9 Suppl 4:S7. doi:10.1186/1471-2105-9-S4-S7.

Brand AH and Perrimon N (1993) - *Targeted gene expression as a means of altering cell fates and generating dominant phenotypes*, Development (Cambridge, England) 118:401–415. PMID:8223268.

Breitwieser GE (2008) - *Extracellular calcium as an integrator of tissue function*, The international journal of biochemistry & cell biology 40(8):1467–1480. doi:10.1016/J.BIOCEL.2008.01.019.

Brenner S (1974) - *The genetics of Caenorhabditis elegans*, Genetics 77:71–94. PMID:4366476.

Brock, DC and Moore, GE (2006) - *Understanding Moore's law:* Four decades of innovation. Philadelphia, Pa.: Chemical Heritage Foundation.

Brose N, Petrenko AG, Südhof TC, Jahn R (1992) - *Synaptotagmin: a calcium sensor on the synaptic vesicle surface*, Science 256(5059):1021–1025. doi:10.1126/SCIENCE.1589771.

Brose N, Rosenmund C, Rettig J (2000) - *Regulation of transmitter release by Unc-13 and its homologues*, Current opinion in neurobiology 10(3):303–311. doi:10.1016/S0959-4388(00)00105-7.

Burkhardt P (2015) - *The origin and evolution of synaptic proteins - choanoflagellates lead the way*, The Journal of experimental biology 218(Pt 4):506–514. doi:10.1242/JEB.110247.

Burnham, KP and Anderson, DR (2004) - *Model Selection and Multimodel Inference:* A Practical Information-Theoretic Approach. 2. Aufl. New York, NY: Springer-Verlag New York, Inc.

Bykhovskaia M and Vasin A (2017) - *Electrophysiological analysis of synaptic transmission in Drosophila*, Wiley interdisciplinary reviews. Developmental biology 6(5). doi:10.1002/WDEV.277.

Cao G, Platisa J, Pieribone VA, Raccuglia D, Kunst M, Nitabach MN (2013) - *Genetically targeted optical electrophysiology in intact neural circuits*, Cell 154(4):904–913. doi:10.1016/J.CELL.2013.07.027.

Capogna M, Gähwiler BH, Thompson SM (1995) - *Presynaptic enhancement of inhibitory synaptic transmission by protein kinases A and C in the rat hippocampus in vitro*, The Journal of Neuroscience 15(2):1249–1260. doi:10.1523/JNEUROSCI.15-02-01249.1995.

Carafoli E and Krebs J (2016) - *Why Calcium? How Calcium Became the Best Communicator*, Journal of Biological Chemistry 291(40):20849–20857. doi:10.1074/JBC.R116.735894.

Carmeliet E (2019) - *From Bernstein's rheotome to Neher-Sakmann's patch electrode. The action potential*, Physiological reports 7(1):e13861. doi:10.14814/PHY2.13861.

Carter AG and Regehr WG (2002) - *Quantal events shape cerebellar interneuron firing*, Nature Neuroscience 5(12):1309–1318. doi:10.1038/NN970.

Casares D, Escribá PV, Rosselló CA (2019) - *Membrane Lipid Composition: Effect on Membrane and Organelle Structure, Function and Compartmentalization and Therapeutic Avenues*, International journal of molecular sciences 20(9). doi:10.3390/IJMS20092167.

Chalfie M, Tu Y, Euskirchen G, Ward WW, Prasher DC (1994) - *Green fluorescent protein as a marker for gene expression*, Science 263(5148):802–805. doi:10.1126/SCIENCE.8303295.

Chang H, Ciani S, Kidokoro Y (1994) - *Ion permeation properties of the glutamate receptor channel in cultured embryonic Drosophila myotubes*, The Journal of physiology 476(1):1–16. doi:10.1113/JPHYSIOL.1994.SP020107.

Chen T-W, Wardill TJ, Sun Y, Pulver SR, Renninger SL, Baohan A, Schreiter ER, Kerr RA, Orger MB, Jayaraman V, Looger LL, Svoboda K, Kim DS (2013) - *Ultrasensitive fluorescent proteins for imaging neuronal activity*, Nature 499(7458):295–300. doi:10.1038/NATURE12354.

Choi BJ, Imlach WL, Jiao W, Wolfram V, Wu Y, Grbic M, Cela C, Baines RA, Nitabach MN, McCabe BD (2014) - *Miniature neurotransmission regulates Drosophila synaptic structural maturation*, Neuron 82(3):618–634. doi:10.1016/J.NEURON.2014.03.012.

Clements JD (2003) - *Variance–mean analysis: a simple and reliable approach for investigating*

synaptic transmission and modulation, Journal of Neuroscience Methods 130(2):115–125. doi:10.1016/J.JNEUMETH.2003.09.019.

Clements JD and Silver RA (2000) - *Unveiling synaptic plasticity: a new graphical and analytical approach*, Trends in Neurosciences 23(3):105–113. doi:10.1016/S0166-2236(99)01520-9.

Clineschmidt BV, Martin GE, Bunting PR (1982) - *Anticonvulsant activity of (+)-5-methyl-10, 11-dihydro-5H-dibenzo[a, d]cyclohepten-5, 10-imine (MK-801), a substance with potent anticonvulsant, central sympathomimetic, and apparent anxiolytic properties*, Drug Development Research 2(2):123–134. doi:10.1002/DDR.430020203.

Cobb M (2002) - *Timeline: exorcizing the animal spirits: Jan Swammerdam on nerve function*, Nature Reviews Neuroscience 3(5):395–400. doi:10.1038/NRN806.

Correia SS, Duarte CB, Faro CJ, Pires EV, Carvalho AL (2003) - *Protein kinase C gamma associates directly with the GluR4 alpha-amino-3-hydroxy-5-methyl-4-isoxazole propionate receptor subunit. Effect on receptor phosphorylation*, Journal of Biological Chemistry 278(8):6307–6313. doi:10.1074/JBC.M205587200.

Courtney NA, Briguglio JS, Bradberry MM, Greer C, Chapman ER (2018) - *Excitatory and Inhibitory Neurons Utilize Different Ca2+ Sensors and Sources to Regulate Spontaneous Release*, Neuron 98(5):977-991.e5. doi:10.1016/J.NEURON.2018.04.022.

Crawford DC and Kavalali ET (2015) - *Molecular underpinnings of synaptic vesicle pool heterogeneity*, Traffic (Copenhagen, Denmark) 16(4):338–364. doi:10.1111/TRA.12262.

Crivellato E and Ribatti D (2007) - *Soul, mind, brain: Greek philosophy and the birth of neuroscience*, Brain Research Bulletin 71(4):327–336. doi:10.1016/J.BRAINRESBULL.2006.09.020.

Dana H, Sun Y, Mohar B, Hulse BK, Kerlin AM, Hasseman JP, Tsegaye G, Tsang A, Wong A, Patel R, Macklin JJ, Chen Y, Konnerth A, Jayaraman V, Looger LL, Schreiter ER, Svoboda K, Kim DS (2019) - *High-performance calcium sensors for imaging activity in neuronal populations and microcompartments*, Nature methods 16(7):649–657. doi:10.1038/S41592-019-0435-6.

Darwin, C (1859) - *On the origin of species by means of natural selection or The preservation of favoured races in the struggle for life*. Dover thrift ed.

Davis GW (2013) - *Homeostatic signaling and the stabilization of neural function*, Neuron 80(3):718–728. doi:10.1016/J.NEURON.2013.09.044.

Davis GW and Müller M (2015) - *Homeostatic control of presynaptic neurotransmitter release*, Annual review of physiology 77:251–270. doi:10.1146/ANNUREV-PHYSIOL-021014-071740.

del Castillo J and Katz B (1954) - *Quantal components of the end-plate potential*, The Journal of physiology 124(3):560–573. doi:10.1113/JPHYSIOL.1954.SP005129.

Di Paolo G, Moskowitz HS, Gipson K, Wenk MR, Voronov S, Obayashi M, Flavell R, Fitzsimonds RM, Ryan TA, Camilli P de (2004) - *Impaired PtdIns(4,5)P2 synthesis in nerve terminals produces defects in synaptic vesicle trafficking*, Nature 431(7007):415–422. doi:10.1038/NATURE02896.

Diekstra FP, van Deerlin VM, van Swieten JC, Al-Chalabi A, Ludolph AC, Weishaupt JH, Hardiman O, Landers JE, Brown RH, van Es MA, Pasterkamp RJ, Koppers M, Andersen PM, Estrada K, Rivadeneira F, Hofman A, Uitterlinden AG, van Damme P, Melki J, Meininger V, Shatunov A, Shaw CE, Leigh PN, Shaw PJ, Morrison KE, Fogh I, Chiò A, Traynor BJ, Czell D, Weber M, Heutink P, Bakker PIW de, Silani V, Robberecht W, van den Berg LH, Veldink JH (2014) - *C9orf72 and UNC13A are shared risk loci for amyotrophic lateral sclerosis and frontotemporal dementia: a genome-wide meta-analysis*, Annals of neurology 76(1):120–133. doi:10.1002/ANA.24198.

Díez-Arazola R, Meijer M, Bourgeois-Jaarsma Q, Cornelisse LN, Verhage M, Groffen AJ (2020) - *Doc2 proteins are not required for the increased spontaneous release rate in synaptotagmin-1 deficient neurons*, The Journal of Neuroscience. doi:10.1523/JNEUROSCI.0309-19.2020.

Dittman JS (2019) - *Unc13: a multifunctional synaptic marvel*, Current opinion in neurobiology 57:17–25. doi:10.1016/J.CONB.2018.12.011.

DongM, MasuyerG, StenmarkP (2019) - *Botulinum and Tetanus Neurotoxins*, Annual review of biochemistry 88:811–837. doi:10.1146/ANNUREV-BIOCHEM-013118-111654.

Dunst S and Tomancak P (2019) - *Imaging Flies by Fluorescence Microscopy: Principles, Technologies, and Applications*,

Genetics 211(1):15–34. doi:10.1534/GENETICS.118.300227.

Eichmann TO and Lass A (2015) - *DAG tales: the multiple faces of diacylglycerol--stereochemistry, metabolism, and signaling*, Cellular and molecular life sciences : CMLS 72(20):3931–3952. doi:10.1007/S00018-015-1982-3.

Eldefrawi AT, Eldefrawi ME, Konno K, Mansour NA, Nakanishi K, Oltz E, Usherwood PN (1988) - *Structure and synthesis of a potent glutamate receptor antagonist in wasp venom*, Proceedings of the National Academy of Sciences of the United States of America 85(13):4910–4913. doi:10.1073/PNAS.85.13.4910.

Erecińska M and Silver IA (1994) - *Ions and energy in mammalian brain*, Progress in Neurobiology 43(1):37–71. doi:10.1016/0301-0082(94)90015-9.

Ermolyuk YS, Alder FG, Surges R, Pavlov IY, Timofeeva Y, Kullmann DM, Volynski KE (2013) - *Differential triggering of spontaneous glutamate release by P/Q-, N- and R-type Ca2+ channels*, Nature Neuroscience 16(12):1754–1763. doi:10.1038/NN.3563.

Fatt P and Katz B (1950) - *Some observations on biological noise*, Nature 166(4223):597–598. doi:10.1038/166597A0.

Fatt P and Katz B (1951) - *An analysis of the end-plate potential recorded with an intracellular electrode*, The Journal of physiology 115(3):320–370. doi:10.1113/JPHYSIOL.1951.SP004675.

Fatt P and Katz B (1952) - *Spontaneous subthreshold activity at motor nerve endings*, The Journal of physiology 117(1):109–128. doi:10.1113/JPHYSIOL.1952.SP004735.

Fauw J de, Ledsam JR, Romera-Paredes B, Nikolov S, Tomasev N, Blackwell S, Askham H, Glorot X, O'Donoghue B, Visentin D, van den Driessche G, Lakshminarayanan B, Meyer C, Mackinder F, Bouton S, Ayoub K, Chopra R, King D, Karthikesalingam A, Hughes CO, Raine R, Hughes J, Sim DA, Egan C, Tufail A, Montgomery H, Hassabis D, Rees G, Back T, Khaw PT, Suleyman M, Cornebise J, Keane PA, Ronneberger O (2018) - *Clinically applicable deep learning for diagnosis and referral in retinal disease*, Nature medicine 24(9):1342–1350. doi:10.1038/S41591-018-0107-6.

Fioravante D and Regehr WG (2011) - *Short-term forms of presynaptic plasticity*, Current opinion in neurobiology 21(2):269–274. doi:10.1016/J.CONB.2011.02.003.

Fodstad H (2001) - *The neuron theory*, Stereotactic and functional neurosurgery 77(1-4):20–24. doi:10.1159/000064596.

Frank CA, Kennedy MJ, Goold CP, Marek KW, Davis GW (2006) - *Mechanisms underlying the rapid induction and sustained expression of synaptic homeostasis*, Neuron 52(4):663–677. doi:10.1016/J.NEURON.2006.09.029.

Frey U, Huang YY, Kandel ER (1993) - *Effects of cAMP simulate a late stage of LTP in hippocampal CA1 neurons*, Science 260(5114):1661–1664. doi:10.1126/SCIENCE.8389057.

Fujita Y, Sasaki T, Fukui K, Kotani H, Kimura T, Hata Y, Südhof TC, Scheller RH, Takai Y (1996) - *Phosphorylation of Munc-18/n-Sec1/rbSec1 by protein kinase C: its implication in regulating the interaction of Munc-18/n-Sec1/rbSec1 with syntaxin*, Journal of Biological Chemistry 271(13):7265–7268. doi:10.1074/JBC.271.13.7265.

Gallegos LL and Newton AC (2008) - *Spatiotemporal dynamics of lipid signaling: protein kinase C as a paradigm*, IUBMB life 60(12):782–789. doi:10.1002/IUB.122.

Garg R, Benedetti LG, Abera MB, Wang H, Abba M, Kazanietz MG (2014) - *Protein kinase C and cancer: what we know and what we do not*, Oncogene 33(45):5225–5237. doi:10.1038/ONC.2013.524.

Genç Ö, Kochubey O, Toonen RFG, Verhage M, Schneggenburger R (2014) - *Munc18-1 is a dynamically regulated PKC target during short-term enhancement of transmitter release*, eLife 3:e01715. doi:10.7554/ELIFE.01715.

Geppert M, Goda Y, Hammer RE, Li C, Rosahl TW, Stevens CF, Südhof TC (1994) - *Synaptotagmin I: A major Ca2+ sensor for transmitter release at a central synapse*, Cell 79(4):717–727. doi:10.1016/0092-8674(94)90556-8.

Goldberg, DE (1989) - *Genetic algorithms in search, optimization, and machine learning*. Reading, Mass., Wokingham: Addison-Wesley.

Gratz SJ, Goel P, Bruckner JJ, Hernandez RX, Khateeb K, Macleod GT, Dickman D, O'Connor-Giles KM (2019) - *Endogenous Tagging Reveals Differential Regulation of Ca2+ Channels at Single Active Zones during Presynaptic Homeostatic Potentiation and Depression*, The Journal of Neuroscience 39(13):2416–2429. doi:10.1523/JNEUROSCI.3068-18.2019.

Grienberger C and Konnerth A (2012) - *Imaging calcium in neurons*, Neuron 73(5):862–885.

doi:10.1016/J.NEURON.2012.02.011.

Groffen AJ, Martens S, Díez Arazola R, Cornelisse LN, Lozovaya N, Jong APH de, Goriounova NA, Habets RLP, Takai Y, Borst JG, Brose N, McMahon HT, Verhage M (2010) - *Doc2b is a high-affinity Ca2+ sensor for spontaneous neurotransmitter release*, Science 327(5973):1614–1618. doi:10.1126/SCIENCE.1183765.

Guerrero G, Reiff DF, Rieff DF, Agarwal G, Ball RW, Borst A, Goodman CS, Isacoff EY (2005) - *Heterogeneity in synaptic transmission along a Drosophila larval motor axon*, Nature Neuroscience 8(9):1188–1196. doi:10.1038/NN1526.

Hales T, Adams M, Bauer G, Dang TD, Harrison J, Le Hoang T, Kaliszyk C, Magron V, McLaughlin S, Nguyen TT, Nguyen QT, Nipkow T, Obua S, Pleso J, Rute J, Solovyev A, Ta THA, Tran NT, Trieu TD, Urban J, Vu K, Zumkeller R (2017) - *A formal proof of the Kepler conjecture*, Forum of Mathematics, Pi 5:207. doi:10.1017/FMP.2017.1.

Hallermann S, Kittel RJ, Wichmann C, Weyhersmüller A, Fouquet W, Mertel S, Owald D, Eimer S, Depner H, Schwärzel M, Sigrist SJ, Heckmann M (2010) - *Naked dense bodies provoke depression*, The Journal of Neuroscience 30(43):14340–14345. doi:10.1523/JNEUROSCI.2495-10.2010.

Hammarlund M, Palfreyman MT, Watanabe S, Olsen S, Jorgensen EM (2007) - *Open syntaxin docks synaptic vesicles*, PLoS biology 5(8):e198. doi:10.1371/JOURNAL.PBIO.0050198.

Han TH, Dharkar P, Mayer ML, Serpe M (2015) - *Functional reconstitution of Drosophila melanogaster NMJ glutamate receptors*, Proceedings of the National Academy of Sciences of the United States of America 112(19):6182–6187. doi:10.1073/PNAS.1500458112.

Han Y, Kaeser PS, Südhof TC, Schneggenburger R (2011) - *RIM determines Ca^{2}+ channel density and vesicle docking at the presynaptic active zone*, Neuron 69(2):304–316. doi:10.1016/J.NEURON.2010.12.014.

Hardie RC (2007) - *TRP channels and lipids: from Drosophila to mammalian physiology*, The Journal of physiology 578(Pt 1):9–24. doi:10.1113/JPHYSIOL.2006.118372.

Häusser M (2000) - *The Hodgkin-Huxley theory of the action potential*, Nature Neuroscience 3 Suppl:1165. doi:10.1038/81426.

He T and Lnenicka GA (2011) - *Ca^{2}+ buffering at a drosophila larval synaptic terminal*, Synapse (New York, N.y.) 65(7):687–693. doi:10.1002/SYN.20909.

Hefft S and Jonas P (2005) - *Asynchronous GABA release generates long-lasting inhibition at a hippocampal interneuron-principal neuron synapse*, Nature Neuroscience 8(10):1319–1328. doi:10.1038/NN1542.

Hell SW and Kroug M (1995) - *Ground-state-depletion fluorscence microscopy: A concept for breaking the diffraction resolution limit*, Applied Physics B Lasers and Optics 60(5):495–497. doi:10.1007/BF01081333.

Hell SW and Wichmann J (1994) - *Breaking the diffraction resolution limit by stimulated emission: stimulated-emission-depletion fluorescence microscopy*, Optics letters 19(11):780–782. doi:10.1364/OL.19.000780.

Helmholtz H von (1850) - *Vorläufiger Bericht über die Fortpflanzungs-Geschwindigkeit der Nervenreizung*. Available online under http://vlp.mpiwg-berlin.mpg.de/references?id=lit29168.

Herculano-Houzel S, Avelino-de-Souza K, Neves K, Porfírio J, Messeder D, Mattos Feijó L, Maldonado J, Manger PR (2014) - *The elephant brain in numbers*, Frontiers in neuroanatomy 8:46. doi:10.3389/FNANA.2014.00046.

Heuser JE (1989) - *Review of electron microscopic evidence favouring vesicle exocytosis as the structural basis for quantal release during synaptic transmission*, Quarterly journal of experimental physiology (Cambridge, England) 74(7):1051–1069. doi:10.1113/EXPPHYSIOL.1989.SP003333.

Hodgkin AL and Huxley AF (1939) - *Action Potentials Recorded from Inside a Nerve Fibre*, Nature 144(3651):710–711. doi:10.1038/144710A0.

Hodgkin AL and Katz B (1949) - *The effect of sodium ions on the electrical activity of giant axon of the squid*, The Journal of physiology 108(1):37–77. doi:10.1113/JPHYSIOL.1949.SP004310.

Höglinger D, Nadler A, Schultz C (2014) - *Caged lipids as tools for investigating cellular signaling*, Biochimica et biophysica acta 1841(8):1085–1096. doi:10.1016/J.BBALIP.2014.03.012.

Hua Y, Sinha R, Martineau M, Kahms M, Klingauf J (2010) - *A common origin of synaptic vesicles undergoing evoked and spontaneous fusion*, Nature Neuroscience 13(12):1451–1453. doi:10.1038/NN.2695.

Hudry B, Viala S, Graba Y, Merabet S (2011) - *Visualization of protein interactions in living*

Drosophila embryos by the bimolecular fluorescence complementation assay, BMC biology 9:5. doi:10.1186/1741-7007-9-5.

Huntwork S and Littleton JT (2007) - *A complexin fusion clamp regulates spontaneous neurotransmitter release and synaptic growth*, Nature Neuroscience 10(10):1235–1237. doi:10.1038/NN1980.

Hyman SE (2005) - *Neurotransmitters*, Current biology : CB 15(5):R154-8. doi:10.1016/J.CUB.2005.02.037.

Igumenova TI (2015) - *Dynamics and Membrane Interactions of Protein Kinase C*, Biochemistry 54(32):4953–4968. doi:10.1021/ACS.BIOCHEM.5B00565.

Jahn R and Fasshauer D (2012) - *Molecular machines governing exocytosis of synaptic vesicles*, Nature 490(7419):201–207. doi:10.1038/NATURE11320.

Jan LY and Jan YN (1976) - *L-glutamate as an excitatory transmitter at the Drosophila larval neuromuscular junction*, The Journal of physiology 262(1):215–236. doi:10.1113/JPHYSIOL.1976.SP011593.

Jin L, Han Z, Platisa J, Wooltorton JRA, Cohen LB, Pieribone VA (2012) - *Single action potentials and subthreshold electrical events imaged in neurons with a fluorescent protein voltage probe*, Neuron 75(5):779–785. doi:10.1016/J.NEURON.2012.06.040.

Johnson EL, Fetter RD, Davis GW (2009) - *Negative regulation of active zone assembly by a newly identified SR protein kinase*, PLoS biology 7(9):e1000193. doi:10.1371/JOURNAL.PBIO.1000193.

Jones EG (2007) - *Neuroanatomy: Cajal and after Cajal*, Brain Research Reviews 55(2):248–255. doi:10.1016/J.BRAINRESREV.2007.06.001.

Junge HJ, Rhee J-S, Jahn O, Varoqueaux F, Spiess J, Waxham MN, Rosenmund C, Brose N (2004) - *Calmodulin and Munc13 Form a Ca2+ Sensor/Effector Complex that Controls Short-Term Synaptic Plasticity*, Cell 118(3):389–401. doi:10.1016/J.CELL.2004.06.029.

Kaeser PS and Regehr WG (2014) - *Molecular mechanisms for synchronous, asynchronous, and spontaneous neurotransmitter release*, Annual review of physiology 76:333–363. doi:10.1146/ANNUREV-PHYSIOL-021113-170338.

Kaeser PS and Regehr WG (2017) - *The readily releasable pool of synaptic vesicles*, Current opinion in neurobiology 43:63–70. doi:10.1016/J.CONB.2016.12.012.

Kandel ER (2012) - *The molecular biology of memory: cAMP, PKA, CRE, CREB-1, CREB-2, and CPEB*, Molecular brain 5:14. doi:10.1186/1756-6606-5-14.

Kandel ER (2014) - *A place and a grid in the sun*, Cell 159(6):1239–1242. doi:10.1016/J.CELL.2014.11.033.

Kania E, Roest G, Vervliet T, Parys JB, Bultynck G (2017) - *IP3 Receptor-Mediated Calcium Signaling and Its Role in Autophagy in Cancer*, Frontiers in oncology 7:140. doi:10.3389/FONC.2017.00140.

Keller D, Babai N, Kochubey O, Han Y, Markram H, Schürmann F, Schneggenburger R (2015) - *An Exclusion Zone for Ca2+ Channels around Docked Vesicles Explains Release Control by Multiple Channels at a CNS Synapse*, PLoS computational biology 11(5):e1004253. doi:10.1371/JOURNAL.PCBI.1004253.

Keshishian H, Broadie K, Chiba A, Bate M (1996) - *The drosophila neuromuscular junction: a model system for studying synaptic development and function*, Annual review of neuroscience 19:545–575. doi:10.1146/ANNUREV.NE.19.030196.002553.

Khelashvili G and Weinstein H (2015) - *Functional mechanisms of neurotransmitter transporters regulated by lipid-protein interactions of their terminal loops*, Biochimica et biophysica acta 1848(9):1765–1774. doi:10.1016/J.BBAMEM.2015.03.025.

Kim Y-J, Bao H, Bonanno L, Zhang B, Serpe M (2012) - *Drosophila Neto is essential for clustering glutamate receptors at the neuromuscular junction*, Genes & development 26(9):974–987. doi:10.1101/GAD.185165.111.

Kittel RJ, Wichmann C, Rasse TM, Fouquet W, Schmidt M, Schmid A, Wagh DA, Pawlu C, Kellner RR, Willig KI, Hell SW, Buchner E, Heckmann M, Sigrist SJ (2006) - *Bruchpilot promotes active zone assembly, Ca2+ channel clustering, and vesicle release*, Science 312(5776):1051–1054. doi:10.1126/SCIENCE.1126308.

Klar TA and Hell SW (1999) - *Subdiffraction resolution in far-field fluorescence microscopy*, Optics letters 24(14):954–956. doi:10.1364/OL.24.000954.

Kobbersmed JRL, Grasskamp AT, Jusyte M, Böhme MA, Ditlevsen S, Sørensen JB, Walter AM (2020) - *Rapid regulation of vesicle priming explains synaptic facilitation despite heterogeneous vesicle:Ca2+ channel distances*, eLife 9. doi:10.7554/ELIFE.51032.

Kombian SB, Hirasawa M, Mouginot D, Chen X, Pittman QJ (2000) - *Short-term potentiation*

of miniature excitatory synaptic currents causes excitation of supraoptic neurons, Journal of neurophysiology 83(5):2542–2553. doi:10.1152/JN.2000.83.5.2542.

Leys SP (2015) - *Elements of a 'nervous system' in sponges*, The Journal of experimental biology 218(Pt 4):581–591. doi:10.1242/JEB.110817.

Linden DJ and Routtenberg A (1989) - *The role of protein kinase C in long-term potentiation: a testable model*, Brain Research Reviews 14(3):279–296. doi:10.1016/0165-0173(89)90004-0.

Lipstein N, Sakaba T, Cooper BH, Lin K-H, Strenzke N, Ashery U, Rhee J-S, Taschenberger H, Neher E, Brose N (2013) - *Dynamic control of synaptic vesicle replenishment and short-term plasticity by Ca(2+)-calmodulin-Munc13-1 signaling*, Neuron 79(1):82–96. doi:10.1016/J.NEURON.2013.05.011.

Lipstein N, Schaks S, Dimova K, Kalkhof S, Ihling C, Kölbel K, Ashery U, Rhee J, Brose N, Sinz A, Jahn O (2012) - *Nonconserved Ca(2+)/calmodulin binding sites in Munc13s differentially control synaptic short-term plasticity*, Molecular and cellular biology 32(22):4628–4641. doi:10.1128/MCB.00933-12.

Lipstein N, Verhoeven-Duif NM, Michelassi FE, Calloway N, van Hasselt PM, Pienkowska K, van Haaften G, van Haelst MM, van Empelen R, Cuppen I, van Teeseling HC, Evelein AMV, Vorstman JA, Thoms S, Jahn O, Duran KJ, Monroe GR, Ryan TA, Taschenberger H, Dittman JS, Rhee J-S, Visser G, Jans JJ, Brose N (2017) - *Synaptic UNC13A protein variant causes increased neurotransmission and dyskinetic movement disorder*, The Journal of clinical investigation 127(3):1005–1018. doi:10.1172/JCI90259.

Littleton JT, Stern M, Perin M, Bellen HJ (1994) - *Calcium dependence of neurotransmitter release and rate of spontaneous vesicle fusions are altered in Drosophila synaptotagmin mutants*, Proceedings of the National Academy of Sciences of the United States of America 91(23):10888–10892. doi:10.1073/PNAS.91.23.10888.

Littleton JT, Stern M, Schulze K, Perin M, Bellen HJ (1993) - *Mutational analysis of Drosophila synaptotagmin demonstrates its essential role in Ca2+-activated neurotransmitter release*, Cell 74(6):1125–1134. doi:10.1016/0092-8674(93)90733-7.

Lou X, Scheuss V, Schneggenburger R (2005) - *Allosteric modulation of the presynaptic Ca2+ sensor for vesicle fusion*, Nature 435(7041):497–501. doi:10.1038/NATURE03568.

Lydiard RB (2003) - *The role of GABA in anxiety disorders*, The Journal of clinical psychiatry 64 Suppl 3:21–27. PMID:12662130.

Ma C, Li W, Xu Y, Rizo J (2011) - *Munc13 mediates the transition from the closed syntaxin-Munc18 complex to the SNARE complex*, Nature Structural & Molecular Biology 18(5):542–549. doi:10.1038/NSMB.2047.

MacDermott AB, Role LW, Siegelbaum SA (1999) - *Presynaptic ionotropic receptors and the control of transmitter release*, Annual review of neuroscience 22:443–485. doi:10.1146/ANNUREV.NEURO.22.1.443.

Macleod GT, Hegström-Wojtowicz M, Charlton MP, Atwood HL (2002) - *Fast calcium signals in Drosophila motor neuron terminals*, Journal of neurophysiology 88(5):2659–2663. doi:10.1152/JN.00515.2002.

Madeira F, Park YM, Lee J, Buso N, Gur T, Madhusoodanan N, Basutkar P, Tivey ARN, Potter SC, Finn RD, Lopez R (2019) - *The EMBL-EBI search and sequence analysis tools APIs in 2019*, Nucleic acids research 47(W1):W636-W641. doi:10.1093/NAR/GKZ268.

Magdziarek M, Bolembach AA, Stepien KP, Quade B, Liu X, Rizo J (2020) - *Re-examining how Munc13-1 facilitates opening of syntaxin-1*, Protein science : a publication of the Protein Society. doi:10.1002/PRO.3844.

Makarova M, Rycek L, Hajicek J, Baidilov D, Hudlicky T (2019) - *Tetrodotoxin: History, Biology, and Synthesis*, Angewandte Chemie (International ed. in English) 58(51):18338–18387. doi:10.1002/ANIE.201901564.

Malenka RC, Ayoub GS, Nicoll RA (1987) - *Phorbol esters enhance transmitter release in rat hippocampal slices*, Brain Research 403(1):198–203. doi:10.1016/0006-8993(87)90145-4.

Martin TFJ (2012) - *Role of PI(4,5)P(2) in vesicle exocytosis and membrane fusion*, Sub-cellular biochemistry 59:111–130. doi:10.1007/978-94-007-3015-1_4.

Martin TFJ (2015) - *PI(4,5)P_2-binding effector proteins for vesicle exocytosis*, Biochimica et biophysica acta 1851(6):785–793. doi:10.1016/J.BBALIP.2014.09.017.

Maruyama IN and Brenner S (1991) - *A phorbol ester/diacylglycerol-binding protein encoded by the unc-13 gene of Caenorhabditis elegans*, Proceedings of the National Academy of Sciences of the United States

of America 88(13):5729–5733. doi:10.1073/PNAS.88.13.5729.

Marvin JS, Borghuis BG, Tian L, Cichon J, Harnett MT, Akerboom J, Gordus A, Renninger SL, Chen T-W, Bargmann CI, Orger MB, Schreiter ER, Demb JB, Gan W-B, Hires SA, Looger LL (2013) - *An optimized fluorescent probe for visualizing glutamate neurotransmission*, Nature methods 10(2):162–170. doi:10.1038/NMETH.2333.

Matveev V, Sherman A, Zucker RS (2002) - *New and Corrected Simulations of Synaptic Facilitation*, Biophysical Journal 83(3):1368–1373. doi:10.1016/S0006-3495(02)73907-6.

Maximov A, Lao Y, Li H, Chen X, Rizo J, Sørensen JB, Südhof TC (2008) - *Genetic analysis of synaptotagmin-7 function in synaptic vesicle exocytosis*, Proceedings of the National Academy of Sciences of the United States of America 105(10):3986–3991. doi:10.1073/PNAS.0712372105.

McKinney RA, Capogna M, Dürr R, Gähwiler BH, Thompson SM (1999) - *Miniature synaptic events maintain dendritic spines via AMPA receptor activation*, Nature Neuroscience 2(1):44–49. doi:10.1038/4548.

Meinrenken CJ, Borst JG, Sakmann B (2002) - *Calcium Secretion Coupling at Calyx of Held Governed by Nonuniform Channel–Vesicle Topography*, The Journal of Neuroscience 22(5):1648–1667. doi:10.1523/JNEUROSCI.22-05-01648.2002.

Melom JE, Akbergenova Y, Gavornik JP, Littleton JT (2013) - *Spontaneous and evoked release are independently regulated at individual active zones*, The Journal of Neuroscience 33(44):17253–17263. doi:10.1523/JNEUROSCI.3334-13.2013.

Menon KP, Carrillo RA, Zinn K (2013) - *Development and plasticity of the Drosophila larval neuromuscular junction*, Wiley interdisciplinary reviews. Developmental biology 2(5):647–670. doi:10.1002/WDEV.108.

Michelassi FE, Liu H, Hu Z, Dittman JS (2017) - *A C1-C2 Module in Munc13 Inhibits Calcium-Dependent Neurotransmitter Release*, Neuron 95(3):577-590.e5. doi:10.1016/J.NEURON.2017.07.015.

Miki T, Malagon G, Pulido C, Llano I, Neher E, Marty A (2016) - *Actin- and Myosin-Dependent Vesicle Loading of Presynaptic Docking Sites Prior to Exocytosis*, Neuron 91(4):808–823. doi:10.1016/J.NEURON.2016.07.033.

Misura KM, Scheller RH, Weis WI (2000) - *Three-dimensional structure of the neuronal-Sec1-syntaxin 1a complex*, Nature 404(6776):355–362. doi:10.1038/35006120.

Mittelstaedt T, Alvaréz-Baron E, Schoch S (2010) - *RIM proteins and their role in synapse function*, Biological chemistry 391(6):599–606. doi:10.1515/BC.2010.064.

Moghaddam N, Mailler-Burch S, Kara L, Kanz F, Jackowski C, Lösch S (2015) - *Survival after trepanation—Early cranial surgery from Late Iron Age Switzerland*, International Journal of Paleopathology 11:56–65. doi:10.1016/J.IJPP.2015.08.002.

Moore, GE (1965) - *Cramming more components onto integrated circuits*. New York: McGraw-Hill.

Moore GE (2020) - *Gordon Moore: The Man Whose Name Means Progress - IEEE Spectrum*. Available online under https://spectrum.ieee.org/computing/hardware/gordon-moore-the-man-whose-name-means-progress, last checked: 08.03.2020.

Moore JW (2010) - *A personal view of the early development of computational neuroscience in the USA*, Frontiers in computational neuroscience 4. doi:10.3389/FNCOM.2010.00020.

Muhammad K, Reddy-Alla S, Driller JH, Schreiner D, Rey U, Böhme MA, Hollmann C, Ramesh N, Depner H, Lützkendorf J, Matkovic T, Götz T, Bergeron DD, Schmoranzer J, Goettfert F, Holt M, Wahl MC, Hell SW, Scheiffele P, Walter AM, Loll B, Sigrist SJ (2015) - *Presynaptic spinophilin tunes neurexin signalling to control active zone architecture and function*, Nature Communications 6:8362. doi:10.1038/NCOMMS9362.

Müller M and Davis GW (2012) - *Transsynaptic control of presynaptic Ca^{2+} influx achieves homeostatic potentiation of neurotransmitter release*, Current biology : CB 22(12):1102–1108. doi:10.1016/J.CUB.2012.04.018.

Nadler A, Reither G, Feng S, Stein F, Reither S, Müller R, Schultz C (2013) - *The fatty acid composition of diacylglycerols determines local signaling patterns*, Angewandte Chemie (International ed. in English) 52(24):6330–6334. doi:10.1002/ANIE.201301716.

Nadler A, Yushchenko DA, Müller R, Stein F, Feng S, Mulle C, Carta M, Schultz C (2015) - *Exclusive photorelease of signalling lipids at the plasma membrane*, Nature Communications 6:10056. doi:10.1038/NCOMMS10056.

Nakai J, Ohkura M, Imoto K (2001) - *A high signal-to-noise Ca(2+) probe composed of a single green fluorescent protein*,

Nature biotechnology 19(2):137–141. doi:10.1038/84397.

Nakamura Y, Harada H, Kamasawa N, Matsui K, Rothman JS, Shigemoto R, Silver RA, DiGregorio DA, Takahashi T (2015) - *Nanoscale Distribution of Presynaptic Ca2+ Channels and Its Impact on Vesicular Release during Development*, Neuron 85(1):145–158. doi:10.1016/J.NEURON.2014.11.019.

Narahashi T (2008) - *Tetrodotoxin: a brief history*, Proceedings of the Japan Academy. Series B, Physical and biological sciences 84(5):147–154. doi:10.2183/PJAB.84.147.

Nayak A, Zastrow DJ, Lickteig R, Zahniser NR, Browning MD (1998) - *Maintenance of late-phase LTP is accompanied by PKA-dependent increase in AMPA receptor synthesis*, Nature 394(6694):680–683. doi:10.1038/29305.

Neher E (2010) - *What is Rate-Limiting during Sustained Synaptic Activity: Vesicle Supply or the Availability of Release Sites*, Frontiers in synaptic neuroscience 2:144. doi:10.3389/FNSYN.2010.00144.

Newman ZL, Hoagland A, Aghi K, Worden K, Levy SL, Son JH, Lee LP, Isacoff EY (2017) - *Input-Specific Plasticity and Homeostasis at the Drosophila Larval Neuromuscular Junction*, Neuron 93(6):1388-1404.e10. doi:10.1016/J.NEURON.2017.02.028.

Nieratschker V, Schubert A, Jauch M, Bock N, Bucher D, Dippacher S, Krohne G, Asan E, Buchner S, Buchner E (2009) - *Bruchpilot in ribbon-like axonal agglomerates, behavioral defects, and early death in SRPK79D kinase mutants of Drosophila*, PLoS genetics 5(10):e1000700. doi:10.1371/JOURNAL.PGEN.1000700.

Nosyreva E and Kavalali ET (2010) - *Activity-dependent augmentation of spontaneous neurotransmission during endoplasmic reticulum stress*, The Journal of Neuroscience 30(21):7358–7368. doi:10.1523/JNEUROSCI.5358-09.2010.

Owen, DM (2015) - *Methods in membrane lipids*. 2nd ed. New York: Humana Press : Springer (Methods in molecular biology, 1940-6029, Volume 1232).

Pandey UB and Nichols CD (2011) - *Human disease models in Drosophila melanogaster and the role of the fly in therapeutic drug discovery*, Pharmacological reviews 63(2):411–436. doi:10.1124/PR.110.003293.

Pang ZP, Bacaj T, Yang X, Zhou P, Xu W, Südhof TC (2011) - *Doc2 supports spontaneous synaptic transmission by a Ca(2+)-independent mechanism*, Neuron 70(2):244–251. doi:10.1016/J.NEURON.2011.03.011.

Pearson K (1900) - *X. On the criterion that a given system of deviations from the probable in the case of a correlated system of variables is such that it can be reasonably supposed to have arisen from random sampling*, The London, Edinburgh, and Dublin Philosophical Magazine and Journal of Science 50(302):157–175. doi:10.1080/14786440009463897.

Peled ES and Isacoff EY (2011) - *Optical quantal analysis of synaptic transmission in wild-type and rab3-mutant Drosophila motor axons*, Nature Neuroscience 14(4):519–526. doi:10.1038/NN.2767.

Peled ES, Newman ZL, Isacoff EY (2014) - *Evoked and spontaneous transmission favored by distinct sets of synapses*, Current biology : CB 24(5):484–493. doi:10.1016/J.CUB.2014.01.022.

Pellizzari R, Rossetto O, Schiavo G, Montecucco C (1999) - *Tetanus and botulinum neurotoxins: mechanism of action and therapeutic uses*, Philosophical transactions of the Royal Society of London. Series B, Biological sciences 354(1381):259–268. doi:10.1098/RSTB.1999.0377.

Peterlik D, Flor PJ, Uschold-Schmidt N (2016) - *The Emerging Role of Metabotropic Glutamate Receptors in the Pathophysiology of Chronic Stress-Related Disorders*, Current neuropharmacology 14(5):514–539. doi:10.2174/1570159X13666150515234920.

Petrone P, Niola M, Di Lorenzo P, Paternoster M, Graziano V, Quaremba G, Buccelli C (2015) - *Early medical skull surgery for treatment of post-traumatic osteomyelitis 5,000 years ago*, PloS one 10(5):e0124790. doi:10.1371/JOURNAL.PONE.0124790.

Phelps CB and Brand AH (1998) - *Ectopic Gene Expression inDrosophilaUsing GAL4 System*, Methods 14(4):367–379. doi:10.1006/METH.1998.0592.

Piek T (1982) - *δ-philanthotoxin, a semi-irreversible blocker of ion-channels*, Comparative Biochemistry and Physiology Part C: Comparative Pharmacology 72(2):311–315. doi:10.1016/0306-4492(82)90098-3.

Postila PA and Róg T (2020) - *A Perspective: Active Role of Lipids in Neurotransmitter Dynamics*, Molecular neurobiology 57(2):910–925. doi:10.1007/S12035-019-01775-7.

Prasher DC, Eckenrode VK, Ward WW, Prendergast FG, Cormier MJ (1992) - *Primary structure of the Aequorea victoria green-fluorescent protein*, Gene 111(2):229–233.

doi:10.1016/0378-1119(92)90691-H.

Publicover S (1985) - *Stimulation of spontaneous transmitter release by the phorbol ester, 12-O-tetradecanoylphorbol-13-acetate, an activator of protein kinase C*, Brain Research 333(1):185–187. doi:10.1016/0006-8993(85)90144-1.

Puchkov D and Haucke V (2013) - *Greasing the synaptic vesicle cycle by membrane lipids*, Trends in cell biology 23(10):493–503. doi:10.1016/J.TCB.2013.05.002.

Qin G, Schwarz T, Kittel RJ, Schmid A, Rasse TM, Kappei D, Ponimaskin E, Heckmann M, Sigrist SJ (2005) - *Four different subunits are essential for expressing the synaptic glutamate receptor at neuromuscular junctions of Drosophila*, The Journal of Neuroscience 25(12):3209–3218. doi:10.1523/JNEUROSCI.4194-04.2005.

Reddy-Alla S, Böhme MA, Reynolds E, Beis C, Grasskamp AT, Mampell MM, Maglione M, Jusyte M, Rey U, Babikir H, McCarthy AW, Quentin C, Matkovic T, Bergeron DD, Mushtaq Z, Göttfert F, Owald D, Mielke T, Hell SW, Sigrist SJ, Walter AM (2017) - *Stable Positioning of Unc13 Restricts Synaptic Vesicle Fusion to Defined Release Sites to Promote Synchronous Neurotransmission*, Neuron 95(6):1350-1364.e12. doi:10.1016/J.NEURON.2017.08.016.

Rhee J-S, Betz A, Pyott S, Reim K, Varoqueaux F, Augustin I, Hesse D, Südhof TC, Takahashi M, Rosenmund C, Brose N (2002) - *β Phorbol Ester- and Diacylglycerol-Induced Augmentation of Transmitter Release Is Mediated by Munc13s and Not by PKCs*, Cell 108(1):121–133. doi:10.1016/S0092-8674(01)00635-3.

Richmond JE, Davis WS, Jorgensen EM (1999) - *UNC-13 is required for synaptic vesicle fusion in C. elegans*, Nature Neuroscience 2(11):959–964. doi:10.1038/14755.

Rozov A, Bolshakov AP, Valiullina-Rakhmatullina F (2019) - *The Ever-Growing Puzzle of Asynchronous Release*, Frontiers in cellular neuroscience 13:28. doi:10.3389/FNCEL.2019.00028.

Rust MJ, Bates M, Zhuang X (2006) - *Sub-diffraction-limit imaging by stochastic optical reconstruction microscopy (STORM)*, Nature methods 3(10):793–795. doi:10.1038/NMETH929.

Sakamoto H, Ariyoshi T, Kimpara N, Sugao K, Taiko I, Takikawa K, Asanuma D, Namiki S, Hirose K (2018) - *Synaptic weight set by Munc13-1 supramolecular assemblies*, Nature Neuroscience 21(1):41–49. doi:10.1038/S41593-017-0041-9.

Scheuss V and Neher E (2001) - *Estimating Synaptic Parameters from Mean, Variance, and Covariance in Trains of Synaptic Responses*, Biophysical Journal 81(4):1970–1989. doi:10.1016/S0006-3495(01)75848-1.

Schoch S, Castillo PE, Jo T, Mukherjee K, Geppert M, Wang Y, Schmitz F, Malenka RC, Südhof TC (2002) - *RIM1alpha forms a protein scaffold for regulating neurotransmitter release at the active zone*, Nature 415(6869):321–326. doi:10.1038/415321A.

Scholz N, Ehmann N, Sachidanandan D, Imig C, Cooper BH, Jahn O, Reim K, Brose N, Meyer J, Lamberty M, Altrichter S, Bormann A, Hallermann S, Pauli M, Heckmann M, Stigloher C, Langenhan T, Kittel RJ (2019a) - *Complexin cooperates with Bruchpilot to tether synaptic vesicles to the active zone cytomatrix*, Journal of Cell Biology 218(3):1011–1026. doi:10.1083/JCB.201806155.

Scholz N, Ehmann N, Sachidanandan D, Imig C, Cooper BH, Jahn O, Reim K, Brose N, Meyer J, Lamberty M, Altrichter S, Bormann A, Hallermann S, Pauli M, Heckmann M, Stigloher C, Langenhan T, Kittel RJ (2019b) - *Complexin cooperates with Bruchpilot to tether synaptic vesicles to the active zone cytomatrix*, Journal of Cell Biology 218(3):1011–1026. doi:10.1083/JCB.201806155.

Schousboe A, Madsen KK, Barker-Haliski ML, White HS (2014) - *The GABA synapse as a target for antiepileptic drugs: a historical overview focused on GABA transporters*, Neurochemical research 39(10):1980–1987. doi:10.1007/S11064-014-1263-9.

Schuhmacher M, Grasskamp AT, Barahtjan P, Wagner N, Lombardot B, Schuhmacher JS, Sala P, Lohmann A, Henry I, Shevchenko A, Coskun Ü, Walter AM, Nadler A (2020) - *Live-cell lipid biochemistry reveals a role of diacylglycerol side-chain composition for cellular lipid dynamics and protein affinities*, Proceedings of the National Academy of Sciences of the United States of America:201912684. doi:10.1073/PNAS.1912684117.

Shahrezaei V, Cao A, Delaney KR (2006) - *Ca2+ from one or two channels controls fusion of a single vesicle at the frog neuromuscular junction*, The Journal of Neuroscience 26(51):13240–13249. doi:10.1523/JNEUROSCI.1418-06.2006.

Shin O-H, Lu J, Rhee J-S, Tomchick DR, Pang ZP, Wojcik SM, Camacho-Perez M, Brose N, Machius M, Rizo J, Rosenmund C, Südhof

TC (2010a) - *Munc13 C2B domain is an activity-dependent Ca2+ regulator of synaptic exocytosis*, Nature Structural & Molecular Biology 17(3):280–288. doi:10.1038/NSMB.1758.

Shin O-H, Lu J, Rhee J-S, Tomchick DR, Pang ZP, Wojcik SM, Camacho-Perez M, Brose N, Machius M, Rizo J, Rosenmund C, Südhof TC (2010b) - *Munc13 C2B domain is an activity-dependent Ca2+ regulator of synaptic exocytosis*, Nature Structural & Molecular Biology 17(3):280–288. doi:10.1038/NSMB.1758.

Siebert M, Böhme MA, Driller JH, Babikir H, Mampell MM, Rey U, Ramesh N, Matkovic T, Holton N, Reddy-Alla S, Göttfert F, Kamin D, Quentin C, Klinedinst S, Andlauer TF, Hell SW, Collins CA, Wahl MC, Loll B, Sigrist SJ (2015) - *A high affinity RIM-binding protein/Aplip1 interaction prevents the formation of ectopic axonal active zones*, eLife 4. doi:10.7554/ELIFE.06935.

Siegelbaum SA and Kandel ER (1991) - *Learning-related synaptic plasticity: LTP and LTD*, Current opinion in neurobiology 1(1):113–120. doi:10.1016/0959-4388(91)90018-3.

Silinsky EM and Searl TJ (2003) - *Phorbol esters and neurotransmitter release: more than just protein kinase C?*, British journal of pharmacology 138(7):1191–1201. doi:10.1038/SJ.BJP.0705213.

Singh M, Lujan B, Renden R (2018) - *Presynaptic GCaMP expression decreases vesicle release probability at the calyx of Held*, Synapse (New York, N.y.) 72(12). doi:10.1002/SYN.22040.

Siontorou CG, Nikoleli G-P, Nikolelis DP, Karapetis SK (2017) - *Artificial Lipid Membranes: Past, Present, and Future*, Membranes 7(3). doi:10.3390/MEMBRANES7030038.

Snyder SH (2009) - *Neurotransmitters, receptors, and second messengers galore in 40 years*, The Journal of Neuroscience 29(41):12717–12721. doi:10.1523/JNEUROSCI.3670-09.2009.

Son H, Lu Y-F, Zhuo M, Arancio O, Kandel ER, Hawkins RD (1998) - *The Specific Role of cGMP in Hippocampal LTP*, Learning & Memory 5(3):231–245. doi:10.1101/LM.5.3.231.

Stevens CF and Wang Y (1995) - *Facilitation and depression at single central synapses*, Neuron 14(4):795–802. doi:10.1016/0896-6273(95)90223-6.

Stevens RJ, Akbergenova Y, Jorquera RA, Littleton JT (2012) - *Abnormal synaptic vesicle biogenesis in Drosophila synaptogyrin mutants*, The Journal of Neuroscience 32(50):18054-67, 18067a. doi:10.1523/JNEUROSCI.2668-12.2012.

Südhof TC (2012) - *Calcium control of neurotransmitter release*, Cold Spring Harbor perspectives in biology 4(1):a011353. doi:10.1101/CSHPERSPECT.A011353.

Südhof TC (2013) - *Neurotransmitter release: the last millisecond in the life of a synaptic vesicle*, Neuron 80(3):675–690. doi:10.1016/J.NEURON.2013.10.022.

Sutton MA, Ito HT, Cressy P, Kempf C, Woo JC, Schuman EM (2006) - *Miniature neurotransmission stabilizes synaptic function via tonic suppression of local dendritic protein synthesis*, Cell 125(4):785–799. doi:10.1016/J.CELL.2006.03.040.

Tian L, Hires SA, Mao T, Huber D, Chiappe ME, Chalasani SH, Petreanu L, Akerboom J, McKinney SA, Schreiter ER, Bargmann CI, Jayaraman V, Svoboda K, Looger LL (2009) - *Imaging neural activity in worms, flies and mice with improved GCaMP calcium indicators*, Nature methods 6(12):875–881. doi:10.1038/NMETH.1398.

Trimble WS and Grinstein S (2015) - *Barriers to the free diffusion of proteins and lipids in the plasma membrane*, Journal of Cell Biology 208(3):259–271. doi:10.1083/JCB.201410071.

Turing AM (1937) - *On Computable Numbers, with an Application to the Entscheidungsproblem*, Proceedings of the London Mathematical Society s2-42(1):230–265. doi:10.1112/PLMS/S2-42.1.230.

Ullrich A, Böhme MA, Schöneberg J, Depner H, Sigrist SJ, Noé F (2015) - *Dynamical Organization of Syntaxin-1A at the Presynaptic Active Zone*, PLoS computational biology 11(9):e1004407. doi:10.1371/JOURNAL.PCBI.1004407.

van Meer G, Voelker DR, Feigenson GW (2008) - *Membrane lipids: where they are and how they behave*, Nature reviews. Molecular cell biology 9(2):112–124. doi:10.1038/NRM2330.

Verhage M and Sørensen JB (2008) - *Vesicle docking in regulated exocytosis*, Traffic (Copenhagen, Denmark) 9(9):1414–1424. doi:10.1111/J.1600-0854.2008.00759.X.

Voglis G and Tavernarakis N (2006) - *The role of synaptic ion channels in synaptic plasticity*, EMBO reports 7(11):1104–1110. doi:10.1038/SJ.EMBOR.7400830.

Vyleta NP and Jonas P (2014) - *Loose coupling between Ca2+ channels and release*

sensors at a plastic hippocampal synapse, Science 343(6171):665–670. doi:10.1126/SCIENCE.1244811.

Vyleta NP and Smith SM (2011) - *Spontaneous glutamate release is independent of calcium influx and tonically activated by the calcium-sensing receptor*, The Journal of Neuroscience 31(12):4593–4606. doi:10.1523/JNEUROSCI.6398-10.2011.

Wagh DA, Rasse TM, Asan E, Hofbauer A, Schwenkert I, Dürrbeck H, Buchner S, Dabauvalle M-C, Schmidt M, Qin G, Wichmann C, Kittel RJ, Sigrist SJ, Buchner E (2006) - *Bruchpilot, a protein with homology to ELKS/CAST, is required for structural integrity and function of synaptic active zones in Drosophila*, Neuron 49(6):833–844. doi:10.1016/J.NEURON.2006.02.008.

Walter AM, Böhme MA, Sigrist SJ (2018) - *Vesicle release site organization at synaptic active zones*, Neuroscience research 127:3–13. doi:10.1016/J.NEURES.2017.12.006.

Walter AM, Groffen AJ, Sørensen JB, Verhage M (2011) - *Multiple Ca2+ sensors in secretion: teammates, competitors or autocrats?*, Trends in Neurosciences 34(9):487–497. doi:10.1016/J.TINS.2011.07.003.

Walter AM, Haucke V, Sigrist SJ (2014) - *Neurotransmission: spontaneous and evoked release filing for divorce*, Current biology : CB 24(5):R192-4. doi:10.1016/J.CUB.2014.01.037.

Walter AM, Müller R, Tawfik B, Wierda KDB, Pinheiro PS, Nadler A, McCarthy AW, Ziomkiewicz I, Kruse M, Reither G, Rettig J, Lehmann M, Haucke V, Hille B, Schultz C, Sørensen JB (2017) - *Phosphatidylinositol 4,5-bisphosphate optical uncaging potentiates exocytosis*, eLife 6. doi:10.7554/ELIFE.30203.

Weimer RM, Richmond JE, Davis WS, Hadwiger G, Nonet ML, Jorgensen EM (2003) - *Defects in synaptic vesicle docking in unc-18 mutants*, Nature Neuroscience 6(10):1023–1030. doi:10.1038/NN1118.

Wells WA (2005) - *The discovery of synaptic vesicles*, Journal of Cell Biology 168(1):12–13. doi:10.1083/JCB1681FTA2.

Wen H, Linhoff MW, McGinley MJ, Li G-L, Corson GM, Mandel G, Brehm P (2010) - *Distinct roles for two synaptotagmin isoforms in synchronous and asynchronous transmitter release at zebrafish neuromuscular junction*, Proceedings of the National Academy of Sciences of the United States of America 107(31):13906–13911. doi:10.1073/PNAS.1008598107.

White JG, Southgate E, Thomson JN, Brenner S (1986) - *The structure of the nervous system of the nematode Caenorhabditis elegans*, Philosophical transactions of the Royal Society of London. Series B, Biological sciences 314(1165):1–340. doi:10.1098/RSTB.1986.0056.

Wierda KDB and Sørensen JB (2014) - *Innervation by a GABAergic neuron depresses spontaneous release in glutamatergic neurons and unveils the clamping phenotype of synaptotagmin-1*, The Journal of Neuroscience 34(6):2100–2110. doi:10.1523/JNEUROSCI.3934-13.2014.

Wierda KDB, Toonen RFG, Wit H de, Brussaard AB, Verhage M (2007) - *Interdependence of PKC-dependent and PKC-independent pathways for presynaptic plasticity*, Neuron 54(2):275–290. doi:10.1016/J.NEURON.2007.04.001.

Wölfel M, Lou X, Schneggenburger R (2007) - *A mechanism intrinsic to the vesicle fusion machinery determines fast and slow transmitter release at a large CNS synapse*, The Journal of Neuroscience 27(12):3198–3210. doi:10.1523/JNEUROSCI.4471-06.2007.

Xu J, Pang ZP, Shin O-H, Südhof TC (2009) - *Synaptotagmin-1 functions as a Ca2+ sensor for spontaneous release*, Nature Neuroscience 12(6):759–766. doi:10.1038/NN.2320.

Yang X, Wang S, Sheng Y, Zhang M, Zou W, Wu L, Kang L, Rizo J, Zhang R, Xu T, Ma C (2015) - *Syntaxin opening by the MUN domain underlies the function of Munc13 in synaptic-vesicle priming*, Nature Structural & Molecular Biology 22(7):547–554. doi:10.1038/NSMB.3038.

Yang Y, Liu N, He Y, Liu Y, Ge L, Zou L, Song S, Xiong W, Liu X (2018) - *Improved calcium sensor GCaMP-X overcomes the calcium channel perturbations induced by the calmodulin in GCaMP*, Nature Communications 9(1):1504. doi:10.1038/S41467-018-03719-6.

Yao J, Gaffaney JD, Kwon SE, Chapman ER (2011) - *Doc2 Is a Ca2+ Sensor Required for Asynchronous Neurotransmitter Release*, Cell 147(3):666–677. doi:10.1016/J.CELL.2011.09.046.

Yoshihara M and Ito K (2012) - *Acute genetic manipulation of neuronal activity for the functional dissection of neural circuits-a dream come true for the pioneers of behavioral genetics*, Journal of neurogenetics 26(1):43–52. doi:10.3109/01677063.2012.663429.

Yoshihara M and Littleton JT (2002) - *Synaptotagmin I Functions as a Calcium Sensor to Synchronize Neurotransmitter Release*, Neuron 36(5):897–908. doi:10.1016/S0896-6273(02)01065-6.

Zhai RG and Bellen HJ (2004) - *The architecture of the active zone in the presynaptic nerve terminal*, Physiology (Bethesda, Md.) 19:262–270. doi:10.1152/PHYSIOL.00014.2004.

Zhan H, Bruckner JJ, Zhang Z, O'Connor-Giles KM (2016) - *Three-dimensional imaging of Drosophila motor synapses reveals ultrastructural organizational patterns*, Journal of neurogenetics 30(3-4):237–246. doi:10.1080/01677063.2016.1253693.

Zhao C, Dreosti E, Lagnado L (2011) - *Homeostatic synaptic plasticity through changes in presynaptic calcium influx*, The Journal of Neuroscience 31(20):7492–7496. doi:10.1523/JNEUROSCI.6636-10.2011.

Zhou K, Stawicki TM, Goncharov A, Jin Y (2013) - *Position of UNC-13 in the active zone regulates synaptic vesicle release probability and release kinetics*, eLife 2:e01180. doi:10.7554/ELIFE.01180.

Acknowledgments

As a major chapter of my academic life is coming to its conclusion with this thesis, I want to give credit to those who contributed to its success for their support, be it of scientific or any other nature.

First and foremost, I'd like to express my sincere gratitude to my supervisor Dr. Alexander M. Walter for trusting his instincts and choosing to start his junior research group with me as his first doctoral student. His genuine enthusiasm and his professional support in planning and conducting my work have repeatedly proven to be of immeasurable value to its success. I especially appreciated the considerable effort he dedicated to ensuring a fair and professional, yet very friendly and pleasant atmosphere in the lab.

To my second reviewer, Prof. Dr. Stephan J. Sigrist, I am very grateful for supporting my work not only by generously sharing his resources, but also by discussing my results and giving constructive criticism. His agreement to co-supervise my work is greatly appreciated.

Furthermore, I want to sincerely thank Prof. Dr. Volker Haucke for including our group in his progress report seminar series, and for sharing his valuable opinions on my work, which has certainly helped me reconsider how I viewed my data.

This work would not have been half as fun or successful without the collegial atmosphere inside and outside the lab, especially due to my colleagues and friends. Thanks to the whole Walter, Owald & Sigrist labs for being so creative in making day-to-day lab work such a pleasant experience, and helping me with all questions and issues. I am especially grateful to Christina Beis, Meida, Anthony and Mathias for supporting my main project with their expertise and work, and for just being decent lab-mates during the whole time! Just as much, I want to thank Eva, Malou, and Torsten for many constructive coffee breaks. A special thank you goes to Sabine and Gabi for sharing my taste in music, which has more often than not salvaged my mood from beginning to end of my doctoral work. I am also very grateful to Meida, Anthony and Helge for helpful comments, proofing and proofreading. Thanks to Eric, Marc, Jason, Chengji, Niraja, Rukiye, Ina, Tina, Marta and Astrid (and everyone I may have forgotten) for the smiles and laughs.

I thank my friends outside the lab for providing the very much needed counterweight to my scientific endeavors. My heartfelt gratitude goes to my whole family for their unwavering support and love. I hope I at least partly succeeded in explaining what this support was for, and I will be happy to try further. To Christina, I thank you for your love and understanding during this demanding phase, you know how much that was worth to me.

Affidavit

I hereby affirm that this thesis (apart from the enclosed collaborative publications) was independently written by myself, using exclusively the listed sources. Parts of the text that have been taken from other literature verbatim or analogously have been marked as such by quoting the source(s). This dissertation has not been used to open a doctoral procedure elsewhere.

Hiermit versichere ich an Eides statt, dass die Anfertigung dieser Dissertationsschrift (abgesehen von den kollaborativen Publikationen) ausschließlich von mir selbst und nur unter Zuhilfenahme der angegebenen Quellen durchgeführt wurde. Textstellen, die sinngemäß oder im Wortlaut aus anderen Veröffentlichungen übernommen wurden, sind entsprechend durch Angabe der Quelle(n) gekennzeichnet. Diese Dissertation wurde des Weiteren bisher keinem anderen Prüfungsausschuss vorgelegt.

Berlin, den _____ _____

Andreas Till Grasskamp